Hydrogenated nanocrystalline silicon-based layers for silicon heterojunction and perovskite/c-Si tandem solar cells

Zhao, Y.

DOI
10.4233/uuid:d848c617-2eae-491d-aae1-d524495e9e65

Publication date
2023

Document Version
Final published version

Citation (APA)
Zhao, Y. (2023). *Hydrogenated nanocrystalline silicon-based layers for silicon heterojunction and perovskite/c-Si tandem solar cells*. [Dissertation (TU Delft), Delft University of Technology]. https://doi.org/10.4233/uuid:d848c617-2eae-491d-aae1-d524495e9e65

Hydrogenated nanocrystalline silicon-based layers for silicon heterojunction and perovskite/c-Si tandem solar cells

Yifeng ZHAO

赵一沣

Hydrogenated nanocrystalline silicon-based layers for silicon heterojunction and perovskite/c-Si tandem solar cells

Proefschrift

ter verkrijging van de graad van doctor
aan de Technische Universiteit Delft,
op gezag van de Rector Magnificus Prof.dr.ir. T.H.J.J. van der Hagen,
voorzitter van het College voor Promoties,
in het openbaar te verdedigen op vrijdag 15 December 2023 om 12:30 uur

door

Yifeng ZHAO

Master of Science in Sustainable Energy Technology
Delft University of Technology, the Netherlands
geboren te Cangxi, China

Dit proefschrift is goedgekeurd door de promotoren.

Samenstelling promotiecommissie bestaat uit:

Rector Magnificus	voorzitter
Prof. dr. A. W. Weeber	Technische Universiteit Delft, promotor
Prof. dr. ir. O. Isabella	Technische Universiteit Delft, promotor
Prof. dr. M. Zeman	Technische Universiteit Delft, promotor
Onafhankelijke leden:	
Prof. dr. F. C. Grozema	Technische Universiteit Delft
Prof. dr. P. Roca i Cabarrocas	École polytechnique
Prof. dr. S. De Wolf	King Abdullah University of Science and Technology
Dr. P. Delli Veneri	Agenzia nazionale per le nuove tecnologie, l'energia e lo sviluppo economico sostenibile
Prof. dr. ir. P. Bauer	Technische Universiteit Delft, reservelid

Keywords: Silicon heterojunction solar cells, perovskite/c-Si tandem solar cells, hydrogenated nanocrystalline silicon, hydrogenated nanocrystalline silicon oxide

Printed by: Ipskamp Printing

Illustrations: Designed by Y. Zhao utilizing DALL·E 3 along with Adobe Photoshop.

ISBN 978-94-6473-313-6

An electronic version of this dissertation is available at
`http://repository.tudelft.nl/`.

To my parents

To my loving family

To Yiran

Contents

Summary

Large-scale deployment of photovoltaic (PV) technology is imperative for realizing a future sustainable and electrified energy system. Over the past decades, technological advancements that enhance the efficiency of PV technologies have been one of the crucial aspects for significantly reducing the cost of PV-generated electricity. Among various crystalline silicon (c-Si) PV technologies, silicon heterojunction (SHJ) solar cells, which have achieved the highest efficiency of single-junction c-Si solar cells, hold great promise for advancing the energy transition facilitated by PV technologies even further. Moreover, notable efficiency enhancements, which are well beyond the theoretical efficiency limit of single-junction c-Si solar cells, have been experimentally demonstrated by combining SHJ solar cells with semi-transparent perovskite solar cells in tandem configurations. This thesis focuses on addressing the challenges of efficient deployments of doped hydrogenated nanocrystalline silicon-based (nc-Si:H-based) layers for high-efficiency front/back-contacted (FBC) SHJ solar cells and applications of FBC-SHJ bottom-cells in two-terminal (2T) and four-terminal (4T) tandem devices with perovskite top-cells, supported by advanced opto-electrical simulations.

Firstly, the development of transparent doped nc-SiO_x:H layers alongside various interfacial engineering techniques for their effective integration into FBC-SHJ solar cells is presented. We highlight the remarkable flexibility in tunning the opto-electrical properties of doped nc-SiO_x:H layers by adjusting their deposition conditions. In general, (*n*)-type nc-SiO_x:H layers offered a wider range of optical transparency for achieving low activation energies (E_a) as compared to the (*p*)-type counterparts. By implementing optimized interfacial engineering techniques developed for doped contact stacks based on nc-SiO_x:H layers in FBC-SHJ solar cells, we showcased a significant improvement in fill factor (*FF*) of more than $12\%_{abs.}$, raising it from 65.6% to 77.9%. Besides, the optical transparency of (*n*)nc-SiO_x:H-based window layers was demonstrated by an average 1.5 mA/cm^2 higher short-circuit current density (J_{SC}) as compared to (*n*)a-Si:H counterparts.

Afterwards, the design and optimization of efficient hole collectors based on bi-layer (*p*)-contact ((*p*)nc-SiO_x:H + (*p*)nc-Si:H) for high-efficiency SHJ solar cells are shown. Through a combination of theoretical understanding and experimental observations, several strategies were found to reduce the contact resistivities of (*p*)-type contact stacks. These strategies include using a thinner (*i*)a-Si:H layer, employing a (*p*)nc-SiO_x:H with a larger difference between the optical bandgap (E_{04}) and E_a, finding an appropriate thickness combination of (*p*)nc-SiO_x:H and (*p*)nc-Si:H, and applying the optimized hydrogen plasma treatments (HPTs). Optimizing these strategies contributed to achieving certified *FF*s well above 80% in both front and rear junction solar cells. In addition, the variation in the contact resistivity of (*p*)-type contact stacks was found to impact the distribution of lateral and vertical transport of holes on the illuminated side of solar cells. This was supported by device simulations which gave more insights into different com-

ponents of lateral contributions.

Subsequently, the opto-electrical properties of various (*n*)-layers, including (*n*)a-Si:H, (*n*)nc-Si:H and two types of (*n*)nc-SiO_x:H layers and their implementation (as thin as 2 nm) into rear junction FBC-SHJ solar cells are compared. A minimum thickness of around 8 nm was identified for (*n*)nc-SiO_x:H layers to maintain the passivation quality and be effective as the electron transport layer. On the other hand, the minimum thickness required for (*n*)nc-Si:H and (*n*)a-Si:H can be as thin as 3 to 4 nm. This difference could be associated with their dissimilar capability of incorporating active doping in such thin thicknesses (< 10 nm). Specifically, (*n*)a-Si:H was the most conductive layer, then followed by (*n*)nc-Si:H and (*n*)nc-SiO_x:H layers when they were deposited on (*i*)a-Si:H layers. Despite the high E_a of a 3-nm-thick (*n*)nc-Si:H layer, the solar cell endowed with this (*n*)-contact together with the optimized HPTs delivered a certified efficiency of 22.2% and a *FF* of 80.1%, and showed a 0.61 mA/cm^2 J_{SC} gain over the (*n*)a-Si:H counterpart mainly owing to the higher transparency of (*n*)nc-Si:H. Furthermore, we observed unexpected surface oxidation of (*n*)nc-Si:H likely induced by the TCO sputtering, which was not seen for (*n*)a-Si:H. To avoid this interfacial oxidation, an additional 2 nm (*n*)a-Si:H was added on top of this 3-nm-thick (*n*)nc-Si:H and significantly improved the *FF* from 78.6% to 80.0%.

With the optimized hole and electron collectors, the effects of (*i*)a-Si:H deposition temperature on the performance of SHJ solar cells are investigated. At the lower end of temperatures ranging from 140 °C to 200 °C, Fourier-transform infrared spectroscopy measurements revealed that these (*i*)a-Si:H films were less dense, thus hindering their surface passivation capabilities. However, after applying the additional HPTs on (*i*)a-Si:H layers, those layers deposited at lower temperatures exhibited significant improvements and better passivation qualities as compared to their counterparts deposited at higher temperatures. Conversely, although cells with (*i*)a-Si:H deposited at the lowest temperature (140 °C) exhibited the highest V_{OC}s, the related *FF*s were poorer as compared to their higher temperature counterparts. The optimum trade-off between V_{OC} and *FF* for the SHJ cells was found with temperatures ranging from 160 °C to 180 °C, resulting in independently certified efficiencies of 23.71%. With further improved (*p*)-layers that enabled a *FF* of 83.3%, an efficiency of 24.18% was achieved.

Furthermore, optical simulation-aided design and development of SHJ bottom sub-cells for high-efficiency 2T and 4T perovskite/SHJ tandem solar cells are presented. For front-flat and rear-textured 2T tandem devices, we developed and compared various (*i*)a-Si:H passivating layers for (100)-oriented flat c-Si surfaces. These (*i*)a-Si:H passivating layers include (*i*)a-Si:H mono-layer, (*i*)a-Si:H bi-layer and (*i*)a-Si:H bi-layer combined with an HPT. Afterwards, they were combined with (*n*)a-Si:H, (*n*)nc-Si:H, and (*n*)nc-SiO_x:H layers for SHJ bottom-cell applications. A long minority-carrier lifetime of 16.9 ms was achieved when combining (*i*)a-Si:H bi-layers with (*n*)nc-Si:H (extracted at the injection level of 10^{15} cm^{-3}) in a symmetrical configuration. Together with photostable mixed-halide perovskite top-cells developed by Eindhoven University of Technology, we demonstrated tandem efficiencies above 23% (a maximum of 25.1%) using all three types of (*n*)-layers. Experimental observations and optical simulations suggest that both (*n*)nc-SiO_x:H and (*n*)nc-Si:H are promising for high-efficiency tandem solar cell applications. This is attributed to minimized reflection at the interfaces between

the perovskite and SHJ sub-cells through optimized interference effects, demonstrating the applicability of such light management techniques to various tandem structures. Besides, thanks to the united efforts among the Netherlands Organization for Applied Scientific Research (TNO), Interuniversity Microelectronics Centre (imec), Eindhoven University of Technology and Delft University of Technology, we demonstrated a 4T tandem solar cell with an efficiency of 30.1% that features a certified semitransparent perovskite top-cell.

Last but not least, apart from concluding the main research findings obtained from this thesis, we also provide outlooks on future research topics that can advance further the development of SHJ solar cells. Especially, as an outlook beyond the classical FBC-SHJ solar cell architecture, we propose various novel SHJ-based solar cell architectures. Their potential performance was assessed and compared via rigorous opto-electrical simulations and a maximal efficiency of 27.60% was simulated for FBC-SHJ solar cells featuring localized contacts.

Samenvatting

Dutch translation by Youri Blom.

Grootschalige inzet van fotovoltaïsche (PV) technologie is noodzakelijk voor het realiseren van een duurzaam en geëlektrificeerd energiesysteem in de toekomst. In de afgelopen decennia zijn technologische ontwikkelingen die de efficiëntie van PV-technologieën verbeteren, een van de cruciale aspecten geweest om de kosten van door PV opgewekte elektriciteit aanzienlijk te verlagen. Van de verschillende kristallijn silicium (crystalline silicon in het Engels, c-Si) PV-technologieën hebben silicium heterojunctie (SHJ) zonnecellen, die het hoogste rendement hebben bereikt van enkelvoudige-junctie c-Si-zonnecellen, veel potentie om de energietransitie die wordt gefaciliteerd door PV-technologieën nog verder te bevorderen. Bovendien zijn significante efficiëntieverbeteringen, die veel verder gaan dan de theoretische efficiëntielimiet van enkelvoudige-junctie c-Si-zonnecellen, experimenteel aangetoond door SHJ-zonnecellen te combineren met semi-transparante perovskiet-zonnecellen in tandemconfiguraties. Dit proefschrift richt zich op het aanpakken van de uitdagingen van efficiënte implementaties van gedoteerde gehydrogeneerde nano-kristallijne silicium-gebaseerde (nc-Si:H-gebaseerde) lagen voor zeer efficiënte voor-/achterzijde gecontacteerde (front/back-contacted in het Engels, FBC) SHJ-zonnecellen en toepassingen van FBC-SHJ bodemcellen in tandempanelen met twee terminals (2T) en vier terminals (4T) met perovskiet-top-cellen, ondersteund door geavanceerde opto-elektrische computersimulaties.

Eerst wordt de ontwikkeling van transparante gedoteerde nc-SiO_x:H-lagen naast verschillende tussenlaag-gerelateerde engineeringtechnieken voor hun effectieve integratie in FBC-SHJ-zonnecellen gepresenteerd. We tonen de opmerkelijke flexibiliteit aan bij het afstemmen van de opto-elektrische eigenschappen van gedoteerde nc-SiO_x:H-lagen door hun depositie-omstandigheden aan te passen. Over het algemeen boden (*n*)-type nc-SiO_x:H-lagen een breder bereik van optische transparantie voor het bereiken van lage activeringsenergieën (E_a) in vergelijking met de (*p*)-type tegenhangers. Door geoptimaliseerde tussenlaag-gerelateerde engineeringtechnieken te implementeren die zijn ontwikkeld voor gedoteerde contactlaagstapelingen op basis van nc-SiO_x:H-lagen in FBC-SHJ-zonnecellen, hebben we een aanzienlijke verbetering van de vulfactor (fill factor in het Engels, *FF*) van meer dan $12\%_{\text{abs.}}$ laten zien waardoor deze is gestegen van 65,6% tot 77,9%. Bovendien werd de optische transparantie van (*n*)nc-SiO_x:H-gebaseerde vensterlagen aangetoond door een gemiddeld 1,5 mA/cm^2 hogere kortsluitstroomdichtheid (short-circuit current density in het Engels, J_{SC}) in vergelijking met (*n*)a-Si:H tegenhangers.

Daarna wordt het ontwerp en de optimalisering van efficiënte gatencollectoren op basis van het dubbellaagse (*p*)-contact ((*p*)nc-SiO_x:H + (*p*)nc-Si:H) voor hoog-efficiënte

SHJ-zonnecellen getoond. Door een combinatie van theoretisch inzicht en experimentele waarnemingen zijn verschillende strategieën gevonden om de contactweerstanden van (*p*)-type contactlagen te verminderen. Deze strategieën omvatten het gebruik van een dunnere (*i*)a-Si:H-laag, het gebruik van een (*p*)nc-SiO_x:H met een groter verschil tussen de optische bandgap (E_{04}) en E_a, het vinden van een geschikte laagdiktecombinatie van (*p*)nc-SiO_x:H en (*p*)nc-Si:H, en het toepassen van de geoptimaliseerde waterstofplasma-behandelingen (hydrogen plasma treatments in het Engels, HPTs). Het optimaliseren van deze strategieën heeft bijgedragen aan het behalen van gecertificeerde *FF*'s van ruim boven de 80% in voor- en achterzijde-junctie-zonnecellen. Bovendien bleek de variatie in de contactweerstand van (*p*)-type contactlaagstapelingen van invloed te zijn op de verdeling van lateraal en verticaal transport van gaten aan de belichte zijde van zonnecellen. Dit werd ondersteund door computersimulaties die meer inzicht gaven in de verschillende componenten van de laterale bijdragen.

Vervolgens worden de opto-elektrische eigenschappen van verschillende (*n*)-lagen, waaronder (*n*)a-Si:H, (*n*)nc-Si:H en twee soorten (*n*)nc-SiO_x:H-lagen en hun implementatie (zo dun als 2 nm) in achterzijde-junctie FBC-SHJ zonnecellen vergeleken. Een minimale dikte van ongeveer 8 nm is geïdentificeerd voor (*n*)nc-SiO_x:H-lagen om de passiveringskwaliteit te behouden en effectief te zijn als elektronen-transportlaag. Aan de andere kant kan de minimale dikte die nodig is voor (*n*)nc-Si:H en (*n*)a-Si:H lagen zo dun zijn als 3 tot 4 nm. Dit verschil komt mogelijk door hun ongelijke vermogen om hoge actieve doteringsconcentraties in dergelijke dunne lagen (<10 nm) te realiseren. (*n*)a-Si:H was de meest geleidende laag, gevolgd door (*n*)nc-Si:H en (*n*)nc-SiO_x:H lagen nadat zij op (*i*)a-Si:H lagen werden gedeponeerd. Ondanks de hoge E_a van deze 3 nm dikke (*n*)nc-Si:H-laag leverde de zonnecel voorzien van dit (*n*)-contact samen met de geoptimaliseerde HPTs een gecertificeerd rendement van 22,2% en een *FF* van 80,1% , en vertoonde een J_{SC}-winst van 0,61 mA/cm^2 ten opzichte van de (*n*)a-Si:H-tegenhanger, voornamelijk dankzij de hogere transparantie van (*n*)nc-Si:H. Verder zagen we onverwachte oxidatie aan het (*n*)nc-Si:H oppervlak waarschijnlijk geinduceerd door TCO-sputteren, wat niet werd waargenomen voor (*n*)a-Si:H. Om deze grensvlakoxidatie te voorkomen, werd een extra 2 nm (*n*)a-Si:H laag gedeponeerd bovenop deze 3 nm dikke (*n*)nc-Si:H laag en dit verbeterde de *FF* aanzienlijk van 78,6% naar 80,0%.

Met de geoptimaliseerde gaten- en elektronencollectoren, zijn de effecten van de (*i*)a-Si:H depositie-temperatuur op de prestaties van SHJ-zonnecellen onderzocht. Voor lagere temperaturen, variërend van 140 °C tot 200 °C, onthulden Fourier-transformatie infraroodspectroscopie-metingen dat deze (*i*)a-Si:H-films minder dicht waren, waardoor hun oppervlaktepassiverings-mogelijkheden werden belemmerd. Echter, na het uitvoeren van de extra HPTs op (*i*)a-Si:H-lagen, vertoonden de lagen, die bij lagere temperaturen werden gedeponeerd, significante verbeteringen en betere passiveringseigenschappen in vergelijking met hun tegenhangers die bij hogere temperaturen werden gedeponeerd. Omgekeerd, hoewel cellen met (*i*)a-Si:H gedeponeerd bij de laagste temperatuur (140 °C) de hoogste V_{OC}'s vertoonden, waren de bijbehorende *FF*'s slechter in vergelijking met hun tegenhangers gedeponeerd bij hogere temperaturen. De optimale combinatie van V_{OC} en *FF* voor de SHJ-cellen is gevonden bij temperaturen variërend van 160 °C tot 180 °C, resulterend in onafhankelijk gecertificeerde efficiënties van 23,71%. Met verder verbeterde (*p*)-lagen die een *FF* van 83,3% mogelijk maakten,

werd een efficiëntie van 24,18% behaald.

Verder worden met behulp van optische simulaties het ontwerp en de ontwikkeling van SHJ bodemcellen voor zeer efficiënte 2T- en 4T-perovskiet/SHJ-tandemzonnecellen gepresenteerd. Voor voorzijde-vlak en achterzijde getextureerde 2T tandem-cellen hebben we verschillende (*i*)a-Si:H passiveringslagen ontwikkeld en met elkaar vergeleken voor (100)-georiënteerde vlakke c-Si-oppervlakken. Deze (*i*)a-Si:H passiverende lagen bevatten een (*i*)a-Si:H monolaag, een (*i*)a-Si:H dubbellaag en een (*i*)a-Si:H dubbellaag gecombineerd met een HPT. Daarna werden ze gecombineerd met (*n*)a-Si:H-, (*n*)nc-Si:H- en (*n*)nc-SiO_x:H-lagen voor SHJ bodemcel-toepassingen. Een lange levensduur van minderheidsdragers van 16,9 ms werd bereikt bij het combineren van (*i*)a-Si:H dubbellagen met (*n*)nc-Si:H (bij een injectieniveau van 10^{15} cm^{-3}) in een symmetrische configuratie. Samen met fotostabiele mixed-halogenide perovskiet topcellen ontwikkeld door de Technische Universiteit Eindhoven, hebben we tandem-efficiënties van meer dan 23% (maximaal 25,1%) aangetoond met behulp van alle drie soorten (*n*)-lagen. Experimentele waarnemingen en optische simulaties suggereren dat zowel (*n*)nc-SiO_x:H als (*n*)nc-Si:H veelbelovend zijn voor zeer efficiënte tandem-zonneceltoepassingen. Dit wordt toegeschreven aan minimale reflecties op de grensvlakken tussen de perovskiet- en SHJ-subcellen door geoptimaliseerde interferentie-effecten, wat de toepasbaarheid van dergelijke lichtmanagementtechnieken op verschillende tandemstructuren aantoont. Bovendien hebben we dankzij de gezamenlijke inspanningen van TNO, Interuniversitair Micro-elektronica Centrum (imec), Technische Universiteit Eindhoven en Technische Universiteit Delft een 4T tandem-zonnecel gedemonstreerd met een efficiëntie van 30,1% en waarbij de semi-transparante topcel onafhankelijk gecertificeerd is.

Tenslotte, naast het concluderen van de belangrijkste onderzoeksresultaten die uit dit proefschrift zijn verkregen, werpen wij ook een blik op toekomstige onderzoeksthema's die de ontwikkeling van SHJ-zonnecellen kunnen bevorderen. Vooral als een vooruitblik op de klassieke FBC-SHJ-zonnecelarchitectuur, stellen we verschillende nieuwe op SHJ gebaseerde zonnecelarchitecturen voor. Hun potentiële prestaties werden beoordeeld en vergeleken via rigoureuze opto-elektrische simulaties en een maximale efficiëntie van 27,60% werd gesimuleerd voor FBC-SHJ-zonnecellen met lokale contacten.

1

Introduction

1.1 The indispensable energy transition: renewable energy on the upbeat

Global warming, an increasingly severe challenge for all humankind, is a true reality. An evident example of climate change is represented by the glacier retreat in Greenland.

Greenland, the largest island in the world, is the second-largest ice body worldwide with nearly 80% of its surface covered by ice [1]. As calculated, if all the ice of Greenland is melted, there is a global sea level rise of 7.2 meters [2]. Since the 1980s, the mass loss of the Greenland ice sheet has drastically increased nearly sixfold from 51 ± 17 Gt/year to 286 ± 17 Gt/year till 2018. This accelerated mass loss has contributed 13.7 ± 1.1 mm to the global sea level rise from 1972 to 2018 [3]. During this period, the global land-ocean temperature increased by 0.84 °C [4], which also increased the sea level through thermal expansion of the ocean [5]. Moreover, the ten warmest years in the past 2000-plus years have occurred in the recent decade, and this temperature rise is still happening [4]. Scientists have assessed the effects of global warming with evidence and indicated higher probabilities of negative impacts on our world, such as extreme temperatures, droughts, scarcity of drinking water and food, extreme precipitation and economic damage [6]. The root cause of global warming is the high emissions of heat-trapping greenhouse gases (GHGs) and insufficient capacity to process them, especially the rise of carbon dioxide (CO_2) concentrations due to our fossil fuel-based industry. Since the start of the industrial era around 1750, the atmospheric concentration of CO_2 has increased by 50%, which is even more than the natural evolution over a period of 20,000 years [4].

In an attempt to limit global warming to a minimum extent, Paris Agreement has been signed and entered into force with global efforts and collaborations in 2015. The goal of the Paris Agreement is to constrain the global temperature increment to be no more than 2 °C, and preferably 1.5 °C as compared to pre-industrial levels (1850-1900) [7]. Till 2022, the global temperature has increased by 1.05 °C since 1880 [4]. Therefore, to achieve this target set by Paris Agreement, human activity-induced CO_2 emissions have to be minimized. Figure 1.1 illustrates the projected total energy supply and CO_2 emis-

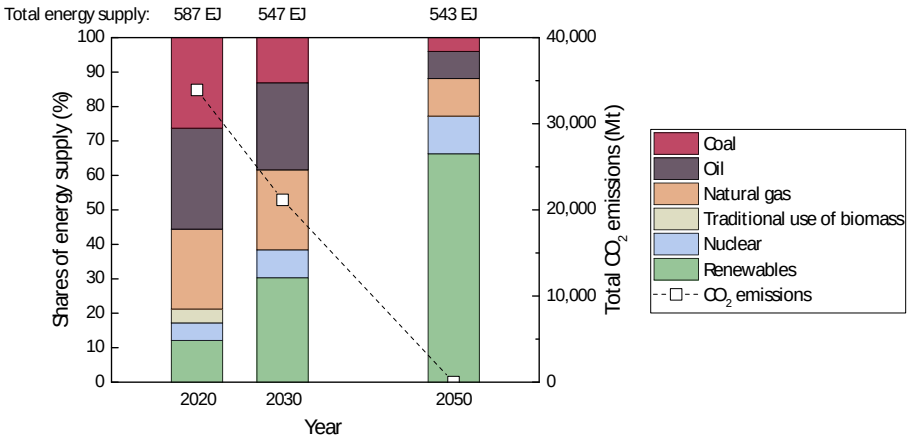

Figure 1.1: The projected total energy supply and CO_2 emissions for the Net-Zero emissions by 2050 scenario. Source from IEA [8].

sions for the International Energy Agency (IEA) Net-Zero emissions by 2050 scenario [8]. As seen in Figure 1.1, the current total energy supply heavily relies on fossil fuels such as coal, oil and natural gases. While in the Net-Zero emission by 2050 scenario, substantial progress has to be made to rapidly shift away from fossil fuels-dominated energy supply to renewable energy supply, which includes solar, wind, hydro, modern bioenergy and other renewables. According to the recent report from The Intergovernmental Panel on Climate Change (IPCC) [9], solar energy holds enormous potential among all renewable energy sources and offers the smallest economic cost to reduce net CO_2 emissions.

1.2 Photovoltaic solar cell technology

Solar energy is taking the lead in the energy transition and becoming the new king of electricity delivery among all available renewable energy sources [10]. In 2010, electricity generated by solar energy was negligible in all major power systems [11]. In 2021, around 6% and 3.72% of annual electricity production was from solar energy for Europe and the world, respectively [12, 13]. As more recently calculated by IEA Photovoltaic Power Systems Programme (PVPS), solar energy theoretically contributed 8.7% and 6.2% to the electrical demand of Europe and the world respectively by the end of 2022 [14]. While to meet the goal the world sets for 2050 (the Paris Agreement), at least 25% of electricity generation should be fulfilled with solar energy by 2050 according to the International Renewable Energy Agency (IRENA) [15]. Recently, research from Haegel and colleagues forecasts that over 40% of the world's electricity demand will be covered by solar energy in 2050 [11]. Furthermore, according to Ram, et al. [16], the significance of solar energy is also emphasized by its substantial contribution of 69% to the primary energy supply in a projected 100% renewable energy system for 2050.

The conversion of solar energy to useful electricity is achieved via Photovoltaic (PV) technology by using solar cells, whose basic working principle will be first elaborated

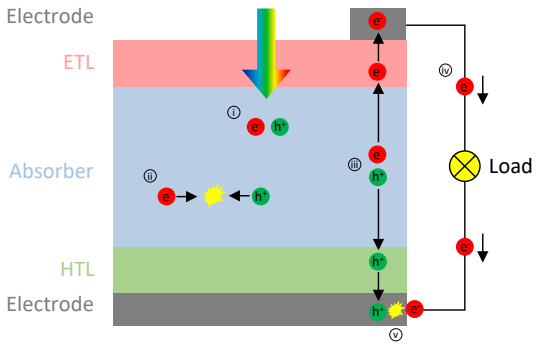

Figure 1.2: The schematic representation of the basic working principle of a solar cell. (i) Absorption of photons generates electron-hole pairs. (ii) In practice, electrons and holes may recombine. (iii) Preferably, selective transport and collection of electrons and holes are facilitated by the electron transport layer (ETL) and the hole transport layer (HTL), respectively. (iv) Mobile electrons transport through an external circuit and (v) recombine with holes. In the figure, e^- represents an electron and h^+ refers to a hole. Figure adapted from [18].

in this section. Subsequently, the diverse PV solar cell technologies and the market are briefly introduced.

1.2.1 The basic working principle and the efficiency limits of solar cells

Solar energy, or light, is electromagnetic radiation that consists of massless photons with different energies. The energy of a photon is given by $E = h\upsilon$, where h is Planck's constant, υ is the frequency of the light. A solar cell, which is mainly composed of semiconductor materials, can generate a potential difference upon its illumination to light. This phenomenon is referred to as the photovoltaic (PV) effect, which was first discovered by Alexandre-Edmond Becquerel back in 1839 [17]. The basic working principle of a solar cell is schematically illustrated in Figure 1.2.

As depicted in Figure 1.2, the energy conversion process in a solar cell can be comprehended as follows. Firstly, light is absorbed by an absorber, resulting in the generation of electron-hole pairs when the incident photons have sufficient energy equal to or larger than the bandgap (E_g) of the absorber (see Section 2.1.1 for the definition of E_g). Ideally, as the generated electrons and holes diffuse to (near) the surfaces of the absorber, they are selectively transported and collected towards the corresponding electrodes facilitated by the electron transport layer (ETL) and the hole transport layer (HTL), respectively. However, in practice, a portion of the generated electrons and holes undergo recombination (various recombination mechanisms are introduced in detail in Section 2.1.3), thus hindering the collection of generated charge carriers. Lastly, the generated electrons flow out of the solar cell, travelling through an external circuit containing a load, and eventually recombining with holes.

The performance of a solar cell is typically evaluated by its power conversion efficiency (η), which is the ratio of the maximum power generated by the solar cell to the total energy received from incident light. The η of a solar cell can be derived from the short-circuit current density (J_{SC}), the open-circuit voltage (V_{OC}) and the fill factor (FF)

of the cell extracted under standard test conditions (STC). The STC is defined by an irradiance of 1000 W/m^2, an AM 1.5G spectrum and a solar cell temperature of 25 °C. More details on characterizing these external parameters (J_{SC},V_{OC},FF and η) of a solar cell are presented in Section 3.2.2.

A solar cell cannot transform 100% of the incident solar energy into electricity. Apart from the fundamental thermodynamic limit that allows a maximum efficiency of around 85% (detailed discussion can be found in [18]), the Shockley-Queisser limit (or the detailed balance limit), which was developed back in 1961, predicted around 30% theoretical efficiency limit for single-junction solar cells [19]. Specifically, by considering only radiative recombination (see Section 2.1.3) in solar cells and using the 6000 K blackbody spectrum as the solar spectrum, they found a theoretical efficiency of 30% with an absorber featuring a bandgap of 1.1 eV and with a cell temperature of 300 K [19]. Further with measured global AM 1.5G solar spectrum and a cell temperature of 298.15 K (25 °C), maximum efficiencies were calculated to be 32.85% and 33.16% for absorbers with bandgaps of 1.15 eV and 1.34 eV, respectively [20]. With the addition of a perfect back reflector at the rear side of the solar cell, the highest efficiency of 33.77% with a bandgap of 1.34 eV was calculated [20]. For single-junction c-Si solar cells, a practical efficiency limit of 29.43% was recently reassessed considering additional factors, including but not limited to, non-radiative Auger recombination and bandgap narrowing occurring at high injection conditions [21].

1.2.2 Evolution of c-Si PV solar cell technologies

The PV industry is a technologically diverse market where different types of solar cells share the same basic working principle. Over the past decades, unprecedented cost reduction has been achieved for PV-generated electricity, which is already lower than fossil fuel-based electricity in large parts of the world [10, 22]. The cost reduction mainly originates from the gradual maturing of PV solar cell technologies, the continuous improvement in the efficiency of solar cells (modules), the progressive expansion of the production capacity and the decrease in manufacturing costs [23–25]. Among different factors that promote the advancement of the PV industry, uninterrupted technological innovations are of great importance. Nowadays, the commercial PV market is dominated by wafer-based crystalline silicon (c-Si) technologies. Thanks to the abundance of Si, processing maturity, high efficiency and long service time (over 25 years), c-Si technologies owned around 95% of the global annual PV production in 2021 [26]. In this section, different types of c-Si solar cells are briefly introduced and their schematic sketches are also provided in Figure 1.3.

Al-doped back surface field solar cells

Starting with the aluminium-doped back surface field (Al-BSF) solar cells, they feature simple architecture and were the main working horse of the PV industry in the past decades till 2013. As sketched in Figure 1.3 (a), typical Al-BSF solar cells use a positive-type ((*p*)-type) wafer as the substrate and feature a front-diffused homojunction phosphorus-doped n^+ emitter and a full-area rear Al-doped p^+ BSF [27]. The latter is formed during the firing process of screen-printed Al paste at the rear side of the solar cells. The front metal contact is also formed by screen printing with a subsequent

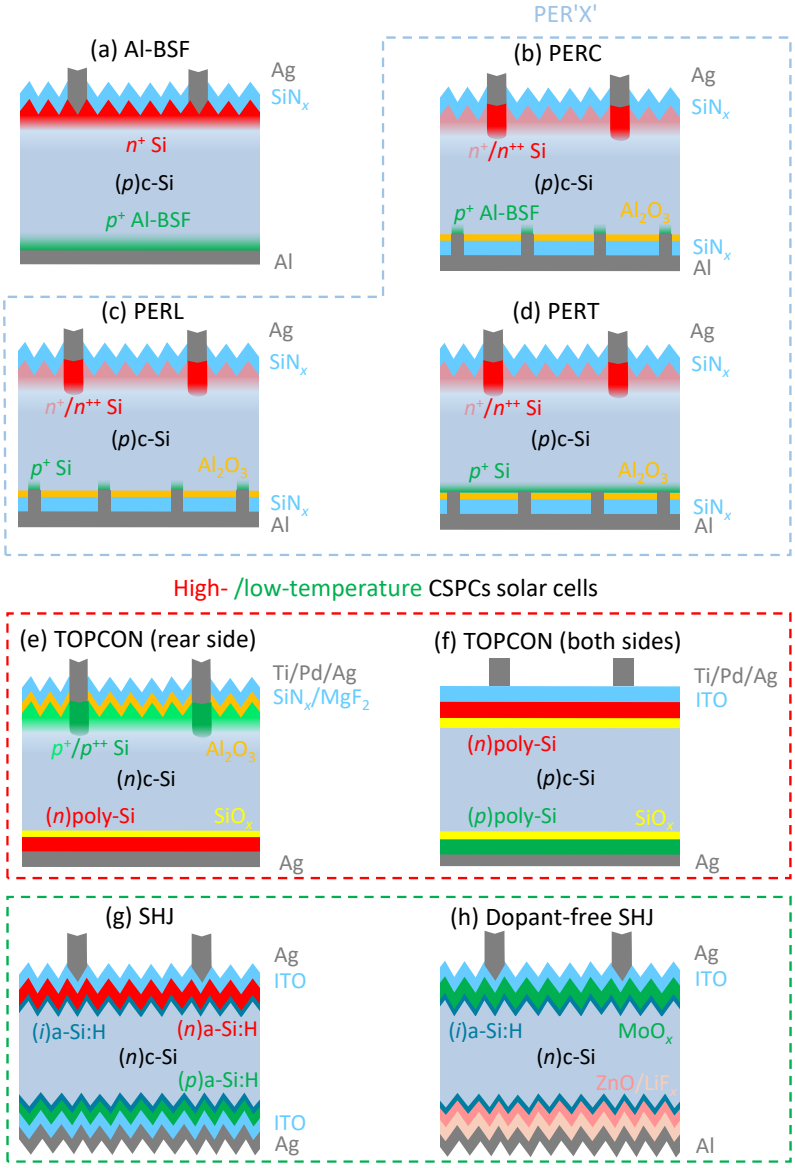

Figure 1.3: The schematic representations of the evolution of c-Si PV solar cell technologies: (a) Al-doped back surface field (Al-BSF) solar cells [27]; (b) Passivated emitter and rear cells (PERC) [28]; (c) Passivated emitter and rear locally diffused cells (PERL) [29]; (d) Passivated emitter and rear totally diffused cells (PERT) [30]; (e) Solar cell with a tunnel oxide passivating contact (TOPCon) on the rear side [31]; (f) Solar cell with TOPCon on both sides [32]; (g) Silicon heterojunction (SHJ) solar cells [30]; (h) Dopant-free SHJ solar cells [33]. The presented structures are typical device designs that are adapted from their corresponding references.

firing step, which allows the glass frit contained in the metal paste to etch away the front anti-reflecting SiO_2/SiN_x layer, thus forming direct contact between the metal and the n^+ emitter layer. In practice, co-firing of the front and rear sides is utilized for fabricating Al-BSF solar cells. Typically, the V_{OC} of Al-BSF solar cells is limited to below 650 mV. Such a low V_{OC} is mainly due to the full-area direct contact of metal and Si at the rear side, which results in high recombination losses of photogenerated electrons and holes at the metal-silicon interface. At this interface, a high density of defects introduces energy states that facilitate defect-assisted Shockley-Read-Hall recombination (more details can be found in Section 2.1.3). In addition to the low V_{OC}, Al-BSF solar cells also have high parasitic absorption and non-optimum internal reflection at the rear side [34]. The best Al-BSF solar cell has demonstrated a conversion efficiency of 20.29% [35]. Commercially, the Al-BSF cells exhibit efficiencies of around 20% [36].

Passivated emitter and rear cells

The recombination losses, especially at the rear side of Al-BSF solar cells, can be reduced by introducing a dielectric passivating layer between the Si absorber and rear metal contact. This type of solar cell is referred to as the passivated emitter and rear cells (PERC) as first reported in 1989 [37]. As seen from a typical commercial (p)-type PERC solar cell sketched in Figure 1.3 (b), the rear side features point contacts together with heavily doped p^+ regions, while the non-contacted surface is covered by a dielectric layer stack such as AlO_x/SiN_y with the double functions of suppressing the surface recombination and enhancing the internal reflectance [38, 39]. The point contacts can be formed by using laser ablation combined with screen-printed Al and a firing step. The non-contact area is protected by SiN_x which is resistant to the Al paste during the firing process. Comprehensive reviews about PERC solar cells can be found elsewhere [38, 40].

Instead of utilizing the Al-doped p^+ BSF, PERC-based architectures (PER'X') such as (p)-type passivated emitter rear locally diffused (PERL) [41] and (p)-type passivated emitter rear totally diffused (PERT) [42] solar cells, featuring either locally- or fully-diffused boron-doped regions, respectively, are also industrial appealing [23, 43]. In both (p)-type PERL and PERT, the contact regions are heavily doped with boron, while for PERT cells, non-contact regions are relatively less doped as compared to contact regions. Thanks to those boron-doped regions, the recombinations at the rear side can be suppressed and the contact resistance is also reduced around contacting areas. Overall, for the PER'X' family, a long-held record efficiency of 25% was achieved with a high V_{OC} of 706 mV back in 1999 [42, 44, 45]. In mass production till 2022, the PERC cells have efficiencies of about 24% [46].

Solar cells with carrier-selective passivating contacts

For both Al-BSF and PER'X' solar cells, although doping of wafers can partially reduce the recombination by minimizing the concentration of minority carriers at the metal/Si interface, it also introduces significant Auger recombination, free carrier absorption (FCA) and bandgap narrowing that limit their efficiencies [47–50]. To alleviate the direct contact between the metal and silicon wafer, solar cells with carrier-selective passivating contacts (CSPCs) are being developed. As the name suggests, stacks of thin-film layers are deposited on both sides of the wafer to passivate the surface defects of the wafer and selectively collect the photogenerated charge carriers. The prominent examples are

low-thermal budget silicon heterojunction (SHJ) solar cells [51] and high-thermal budget tunnel-oxide passivating contacts (TOPCon) [52] or doped polysilicon (poly-Si) on oxide junction (POLO) [53] solar cells (see Figure 1.3 (e) - (h)). For SHJ or TOPCon solar cells, optimized thin (< 10 nm) hydrogenated intrinsic amorphous silicon ((*i*)a-Si:H) layers or ultra-thin (< 2 nm) silicon oxide (SiO_x) layers are utilized, respectively, to provide excellent chemical passivation of c-Si substrates. Then, typically, doped a-Si:H and poly-Si layers, or their alloys with oxygen or carbon [54–66], are implemented to achieve carrier selectivity for SHJ and TOPCon solar cells, respectively. SHJ solar cells have reached a record efficiency of 26.81% [67] with a high V_{OC} of 751.4 mV in a front/back-contacted (FBC) configuration, and 26.7% in an interdigitated back-contacted (IBC) architecture [68]. Till the end of 2022, the best TOPCon solar cell efficiency has reached 26.4% [69] and POLO-IBC demonstrated an efficiency of 26.1% [70]. In production lines till 2022, solar cells with CSPCs deliver efficiencies of around 25% [71, 72].

These concepts of CSPCs entail the use of either doped a-Si:H or poly-Si layers which exhibit high parasitic absorption when placed at the illuminated side of the solar cells. Alternatively, dopant-free transition metal oxides (TMOs), which own higher transparency than the abovementioned silicon-based layers, can mitigate this optical loss while providing sufficient carrier selectivity. Materials with high work function (WF), such as molybdenum oxide (MoO_x) [73–76], tungsten oxide (WO_x) [77, 78] and vanadium oxide (VO_x) [79], can be used as hole transport layers (HTLs). Materials with low WF, such as lithium fluoride (LiF_x) [80], magnesium oxide (MgO_x) [81], magnesium fluoride (MgF_2) [82], titanium oxide (TiO_x) [83, 84], or strontium fluoride (SrF_2) [85] can be used as electron transport layers (ETLs) [27, 80]. In particular, in the Photovoltaic Materials and Devices (PVMD) group of Delft University of Technology, we implemented MoO_x as the HTL with standard (*i*)/(*n*)a-Si:H on the rear side in front-junction solar cells. With this structure, we demonstrated a record certified efficiency of 23.83% for this type of solar cells [86, 87]. As sketched in Figure 1.3 (h) [33], researchers presented a 21.4%-efficient solar cell with dopant-free contacts on both sides, where MoO_x/ITO/Ag and ZnO/LiF_x/Al contact stacks are used for hole and electron collections, respectively. Besides, both unencapsulated SHJ solar cells and encapsulated modules endowed with MoO_x were reported to retain over 95% of their initial efficiencies after standard damp heat stability tests [88–90], demonstrating the promising viability of this technology. Nevertheless, additional research is required for further progressing TMO-based SHJ solar cells.

Si-based tandem solar cells

High efficiencies achieved by solar cells with CSPCs are approaching the theoretical efficiency limit of a single-junction c-Si solar cell, which was calculated to be 29.43% [21]. This limitation is mainly due to the spectral mismatch between the absorption characteristics of the c-Si absorber and the broad solar spectrum (see Figure 1.4 (a)). Especially, photons with higher energy than 1.12 eV, which is the bandgap energy of c-Si, will generate charge carriers with excessive energy that will be eventually lost as heat. This is referred to as the thermalization loss as shown in Figure 1.4. To minimize this thermalization loss and overcome this efficiency limitation, high bandgap materials that absorb more efficiently the high energy photons can be stacked on top of c-Si solar cells to form

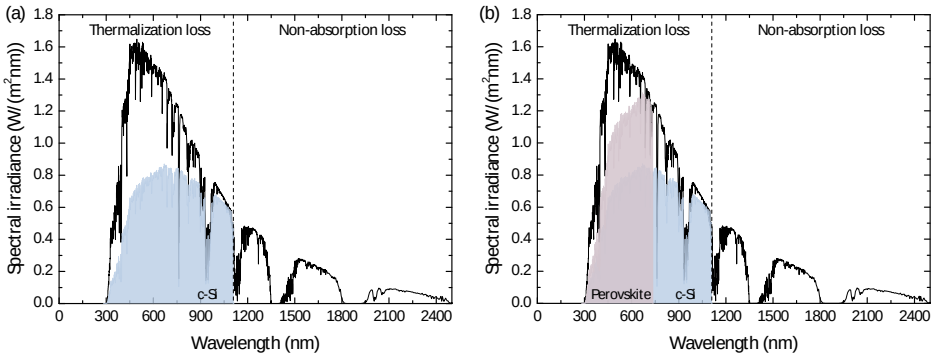

Figure 1.4: The spectral mismatch between the AM 1.5G solar spectrum and absorption characteristics of (a) a single-junction c-Si absorber (light blue, E_g = 1.12 eV), and (b) a tandem solar cell based on a c-Si absorber (light blue) and a perovskite (light purple, E_g = 1.69 eV).

tandem solar cells. As illustrated in Figure 1.4 (b), this architecture allows for better utilization of the solar spectrum. Typically, perovskite solar cells, which can be fabricated with low-cost materials and processes, are used as top sub-cells together with market-dominating c-Si solar cells as bottom sub-cells. The typical perovskite/c-Si tandem configurations are sketched in Figure 1.5.

As seen in Figure 1.5 (a), a monolithic two-terminal (2T) perovskite/c-Si tandem solar cell consists of a perovskite top sub-cell and a front/back-contacted c-Si bottom sub-cell that are electrically connected in series. This architecture allows a simple interconnection of sub-cells and low manufacturing costs. Due to the series connection, the current density of the tandem cell is limited by the sub-cell with the smaller current density. To enable high-efficiency 2T tandem solar cells, one has to ensure optimum current-matching conditions at the maximum power point (J_{MPP}). As highlighted by research on thin-film silicon tandem (micromorph) solar cells, *FF* values of tandem devices can be improved by slightly mismatching the J_{SC} of sub-cells [91]. Similarly, a more recent study on 2T perovskite/c-Si tandem solar cells also shows that the minimum *FF* of tandem devices was obtained when they featured nearly matched J_{SC} of both sub-cells [92]. This implies that a slightly lower $J_{SC,tandem}$ due to J_{SC} mismatching can be compensated by the increment of *FF*, thus resulting in a rather wide distribution of maximum tandem cell efficiency. The *FF* dependence on J_{SC} mismatching then becomes highly important when considering energy yield analysis as real-world environments mostly provide non-matching conditions. Nevertheless, J_{SC} matching is still a good first approximation to enable high-efficiency 2T perovskite/c-Si tandem solar cells. Moreover, the design of 2T tandem solar cells must also account for processing challenges as perovskite top sub-cells are processed using c-Si bottom sub-cells as substrates [93].

Another common tandem architecture is the four-terminal (4T) tandem solar cell. As shown in Figure 1.5 (c), the top and bottom sub-cells are electrically decoupled but optically coupled by an insulating layer in between. Therefore, mechanically stacked 4T tandem solar cells allow independent fabrication and operation of both sub-cells.

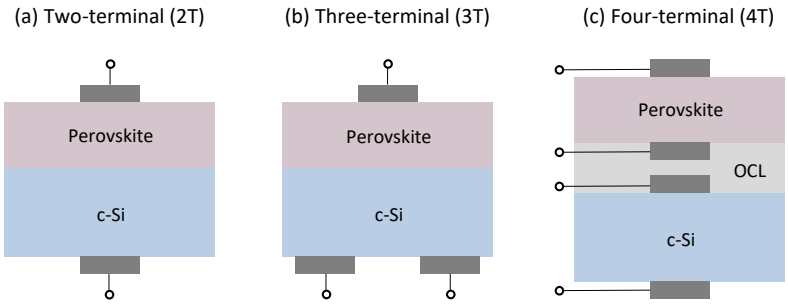

Figure 1.5: The schematic representations of typical (a) two-terminal (2T), (b) three-terminal (3T) and (c) four-terminal (4T) perovskite/c-Si tandem solar cells. For 2T and 3T tandem solar cells, sub-cells are monolithically stacked, while for the 4T solar cell, sub-cells are separated by an optical coupling layer (OCL).

However, as compared to 2T tandem solar cells, 4T tandem solar cells require additional transparent conductive oxide (TCO) layers, which can cause additional parasitic absorption losses. Besides, another substrate for the perovskite top sub-cell and more exterior electronics are needed for 4T tandem solar cells and modules, respectively, thus increasing the costs of the PV system [94]. Nevertheless, as 4T tandem solar cells do not require current matching, they are insensitive to spectrum variations and are expected to enable higher energy yield than the 2T counterparts [94]. However, some studies have indicated that spectrum variations do not significantly impact the energy yields of 2T tandem solar cells, resulting in comparable energy yields to 4T tandem solar cells under real-world conditions [95, 96]. Both tandem configurations can be adapted to bifacial designs, which are promising to provide a higher energy yield than their monofacial counterparts [94, 97, 98]. Especially, researchers have highlighted advantageous applications of bifacial 4T tandem solar cells over the 2T counterparts. This is primarily due to the better tolerance on albedo changes, the less sensitive requirement on the bandgap of the perovskite top sub-cells and theoretically higher energy yield that is more pronounced with higher albedos when using 4T tandem solar cells [98].

Keeping in mind the restrictions of 2T and 4T tandem solar cells, three-terminal (3T) tandem solar cells (Figure 1.5 (b)) that do not require current matching and avoid additional optical losses have also attracted considerable research interest [99–103]. Thanks to those advantages, the energy yield of a 3T tandem device is predicted to be more promising than the 2T and 4T tandem solar cells, as studied for selected locations in the United States [104]. However, 3-terminal tandem solar cells require a rather complicated c-Si bottom sub-cell (such as an IBC solar cell) and complex stringing at the module level [105–107].

All aforementioned tandem configurations are expected to feature theoretical efficiencies of over 40% [102, 108]. And till May of 2023, 2T, 3T and 4T tandem solar cells have achieved record efficiencies of 33.7% (area: 1.0035 cm^2), 29.56% (area: 24.5 cm^2), and 30.79% (area: 64 cm^2), respectively [109–112]. Challenges remain in scaling up and mitigating the instability of the perovskite sub-cells. Notably, perovskite modules have commenced mass production and have been deployed for field operations in utility-

1

scale solar farms [113]. Moreover, it has been reported that the first volume manufacturing line of perovskite/silicon tandem solar cells is set to initiate production in 2023 [114]. Altogether, thanks to the substantial research progress made on perovskite/c-Si tandem solar cells [115–118], the momentum of a further increase in cell efficiency is secured.

1.2.3 The c-Si PV market

The status of the c-Si PV market in 2022 and the market evolution predictions are presented in Figure 1.6 [43]. In fact, various c-Si cell technologies as introduced above and their different market shares reflect the overall evolution of mainly the efficiency of solar cells and the cost of production [119, 120]. It is predicted that Al-BSF cells will be phased out within 2023 [23, 43]. Due to the relatively straightforward upgrade from Al-BSF to PERC production lines and mature technology developments, the PV market is currently dominated by PERC solar cells with a total market share of around 80%. Nevertheless, PERC solar cells are projected to experience a decline in market share to slightly above 10% in the next decade, as more efficiency-promising TOPCon and SHJ solar cells are expected to undergo rapid growth. Other technologies such as back contact solar cells and Si-based tandem solar cells are believed to expand in the coming years gradually.

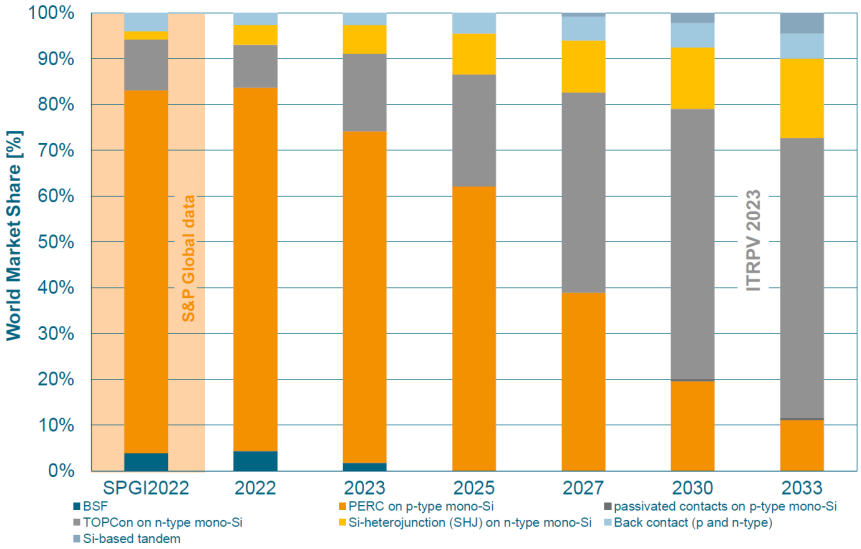

Figure 1.6: The market shares of different c-Si solar cell technologies in 2022 and predictions till 2033 [43]. The S&P Global (SPGI) data for 2022 is presented as a reference [121]. Different c-Si technologies are presented, namely, Al-doped back surface field (BSF), passivated emitter rear contact (PERC), tunnel oxide passivated contact (TOPCon), silicon heterojunction (SHJ), back contact and Si-based tandem solar cells.

Overall, continuous technological innovations and economies of scale strongly support the current success of the PV industry. In March of 2022, the world celebrated its first terawatt (TW) PV installation capacity [122]. In 2050, the world would require about 70 TW accumulative deployment of PV [11, 123]. To achieve this goal, PV solar cell tech-

nologies have to reduce or avoid the use of rare, expensive and toxic materials during manufacturing and also feature good recyclability after their service time [123]. Most importantly, solid political commitments and joint inter-governmental efforts are essential to ensure the realization of this common goal, providing a fair share for all.

1.2.4 A brief recap of the efficiency progression of SHJ solar cells

Among various c-Si solar cells, SHJ solar cell technology, which is also the focus of this PhD project, is a promising candidate to supply electricity with competitively low levelized cost of electricity (LCOE) thanks to its high efficiency [67], low temperature coefficient (efficiency change < -0.25%/°C as compared to around -0.35 to -0.45%/°C for diffused junction (Al-BSF and PER'X' solar cells) and around -0.28%/°C for TOPCon solar cells [124–126], high achievable bifaciality factor [127], simple and low-temperature processing related benefits (thinner wafers and low thermal budget) [128]. Here a summary of the certified record efficiency progression of low-thermal budget SHJ solar cells is illustrated in Figure 1.7.

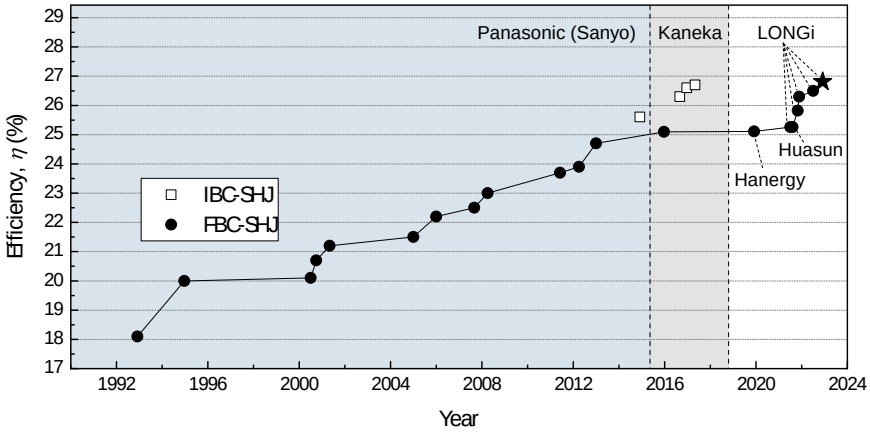

Figure 1.7: The certified record efficiency progression of low-thermal budget SHJ solar cells since the first 'HIT' solar cell was reported by Panasonic (Sanyo) [51, 67, 68, 109, 129–139]. Note that only the 'HIT' solar cell reported in 1992 was not certified. The star symbol represents the champion 26.81%-efficient FBC-SHJ solar cell. Both LONGi and Huasun achieved a certified efficiency of 25.26% in June and July of 2021, respectively, while LONGi's cell having an area of 244.53 cm^2 and Huasun's cell having an area of 274.5 cm^2, respectively.

The SHJ solar cells with (*i*)a-Si:H layers, also initially known as 'Heterojunction with Intrinsic Thin-layer' (HIT) solar cells were first introduced by Panasonic (Sanyo) with an efficiency of 18.1%, significantly marking better V_{OC} and *FF* values at cell level than those achieved in similar c-Si solar cell architectures without the (*i*)a-Si:H passivating layer [51]. Apart from the continuous developments from Panasonic (Sanyo) that resulted in an efficiency of 23.7% with a 98-µm-thin wafer (area: 100.7 cm^2) in 2011 [124, 134–137, 140], the high-efficiency SHJ solar cell technology also attracted numerous research interests from universities, research institutes and companies worldwide [27, 125, 141, 142], especially around the expiration period of 'core' SHJ patents [143]. Two years later,

in 2013, Panasonic (Sanyo) improved the efficiency to 24.7% by reducing the interface recombination of (*i*)a-Si:H/c-Si together with minimizing the resistive losses in the solar cells [138]. In 2014, they realized another jump in efficiency to 25.6% by implementing an IBC configuration [139]. Nevertheless, soon after, FBC-SHJ solar cell fabricated by Kaneka reached an efficiency of 25.1%, which also focused on recombination mitigation at the (*i*)a-Si:H/c-Si interface [129]. In 2017, Kaneka achieved an efficiency of 26.7% for an IBC-SHJ solar cell [68], which was a long-held record efficiency for single-junction c-Si solar cells until November 2022. At that time, LONGi announced a record-breaking efficiency of 26.81% for an FBC-SHJ solar cell (area: 274.4 cm^2), which features a J_{SC} of 41.5 mA/cm^2, a V_{OC} of 751.4 mV, a *FF* of 86.07% [67].

1.2.5 Motivation

The optimized opto-electrical performance, thus high efficiencies achieved for SHJ solar cells, must require a thorough theoretical understanding of device designs, experimental optimizations and careful processing. Tremendous efforts are being put internationally into the technology development and multi-gigawatt industrialization of SHJ solar cells and modules [27, 43, 125, 128, 141, 144–148]. However, the increasing demand of raw materials such as silver and indium, which are critical to this PV solar cell technology, has triggered comprehensive studies on the growth perspectives of this PV solar cell technology, from both the industrialization and sustainability standpoints [43, 148, 149]. Overall, to facilitate the mass implementation of SHJ cells that can contribute to the energy transition, it is crucial to develop SHJ solar cells with high efficiency while minimizing the consumption of scarce resources.

More specifically, as sketched in Figure 1.3 (g), typical FBC-SHJ solar cells feature layer stacks consisting of (*i*)a-Si:H passivating layers combined with doped a-Si:H layers. Electrically, these layer stacks should fulfil critical requirements to achieve high V_{OC} and *FF* of SHJ solar cells. These requirements include excellent surface passivation of the c-Si absorber, sufficient selectivity of photogenerated charge carriers, and low contact resistance with adjacent TCO layers. Apart from the necessity of optimized (*i*)a-Si:H passivating layers for achieving excellent chemical passivation of the c-Si surface, such requirements point to doped thin-film Si layers with minimum activation energy (E_a) for both electron and hole contacts, and favourably a wider E_g for hole collections [150, 151]. However, due to the moderate doping efficiency of a-Si:H films, their E_a is in the order of a few hundred millielectronvolts (meV) [152–154]. Attempts to reduce the E_a by increasing the doping in the a-Si:H films often result in increases in defect density, which deteriorate the effective collections of charge carriers [155].

Despite the limited doping efficiency of a-Si:H films, when the light illuminates the solar cells, part of the incident light will be parasitically absorbed by a-Si:H window layers. This leads to significant J_{SC} loss of SHJ solar cells because of the short diffusion length of charge carriers in such materials [128, 156]. One way to minimize this optical loss is to reduce the thicknesses of a-Si:H layers, which has revealed trade-offs between the optical and electrical performance of solar cells [51, 156, 157], thus limiting the overall efficiency of solar cells. Alternatively, a-Si:H can be alloyed with oxygen (O) or carbon (C) to become more transparent thanks to their widened E_g. Enhancing transparency often results in degraded electrical performance of solar cells, which restrains the effi-

ciency improvement [59, 158–161].

To quench the abovementioned material limitations, doped hydrogenated nanocrystalline silicon (nc-Si:H) that features superior opto-electrical properties over standard a-Si:H films is alternatively implemented in SHJ solar cells [67, 162–166]. As will be discussed later in detail (Section 2.4), nc-Si:H is a mixed-phase material that consists of nanocrystals embedded in the amorphous matrix. The existence of nanocrystals that can be efficiently doped allows a high conductivity within the material. Besides, nc-Si:H features lower absorption in the short-wavelength range [163, 164, 167] than a-Si:H, thus allowing less parasitic absorption when nc-Si:H is placed on the illuminated side of solar cells. The optical transparency can be further enhanced with its oxide alloys, or the so-called hydrogenated nanocrystalline silicon oxide (nc-SiO_x:H). Depending on the deposition conditions, nc-SiO_x:H features unique tunable opto-electrical properties, which in addition enable the flexibility to tailor the solar cell performance [168–175]. However, nc-Si:H-based materials exhibit substrate-dependent growth characteristics and thickness-dependent conductivity [176–178]. In SHJ solar cells with (*i*)a-Si:H passivating layers, it is challenging to facilitate prompt nucleations of nanocrystals and thus maintain excellent electrical properties within a thin nc-Si:H-based layer.

This thesis mainly focuses on addressing the challenges of efficient deployments of doped nc-Si:H-based layers for high-efficiency SHJ solar cells. Moreover, to deliver higher efficiencies than single-junction SHJ solar cells without adding substantial cost, the development of tandem solar cells that combine SHJ bottom sub-cells with perovskite top sub-cells is also a topic of this thesis.

1.2.6 Aim and outline

This thesis aims at understanding and developing high-efficiency SHJ solar cells utilizing doped nc-Si:H-based CSPCs, as well as their applications as bottom sub-cells in tandem devices with perovskite top sub-cells. Firstly, the tunable opto-electrical properties of doped nc-SiO_x:H layers were explored, and various approaches to effectively implementing these layers into SHJ solar cells were evaluated. Then, rigorous opto-electrical simulation-guided design and optimization of charge carrier collectors based on nc-SiO_x:H and nc-Si:H for high-efficiency SHJ solar cells were conducted. The investigation of critical requirements for optimizing the (*i*)a-Si:H layers was also carried out. Eventually, the optimized SHJ bottom sub-cells were combined with perovskite top sub-cells forming high-efficiency 2T and 4T tandem solar cells.

Following the introductory chapter that emphasizes the significance of PV solar cell technology for energy transition, particularly the high-efficiency SHJ solar cell technology, this thesis is structured as follows:

• In **Chapter 2**, the basic principles underlying the physics of SHJ solar cells are introduced. Carrier generation and recombination in solar cells are first presented. Then, typical FBC-SHJ device structures, mechanisms of selective transport and collection of charge carriers, properties of a-Si:H and nc-Si:H-based layers and key aspects of implementing them for high-efficiency SHJ solar cells are briefly reviewed and discussed.

• In **Chapter 3**, the experimental process and equipment used for fabricating FBC-SHJ solar cells are described. Following this, the main characterization setups for assessing opto-electrical and structural properties of thin-film layers, passivation quality,

contact resistivity, device external parameters and spectral response are mentioned together with brief introductions on their working principles.

• In **Chapter 4**, an evaluation of different strategies to improve opto-electrical parameters of SHJ contact stacks founded on highly transparent nc-SiO_x:H layers is presented. In this chapter, we first explore the opto-electrical properties of doped nc-SiO_x:H layers and build up a database of material properties with nc-SiO_x:H layers. Aiming at the efficient application of nc-SiO_x:H layers for high-efficiency FBC-SHJ solar cells, we further investigate the effects of different interface treatments on the electrical properties of doped nc-SiO_x:H layers (stack) and the performance of solar cells.

• In **Chapter 5**, the design and optimization of hole collectors based on bi-layer (*p*)nc-SiO_x:H and (*p*)nc-Si:H for high-efficiency SHJ solar cells are shown. By following guidelines obtained from our device simulations, contact resistivities of doped contact stacks, especially, the (*p*)-type contact stacks with varied deposition conditions, different layer combinations and additional hydrogen plasma treatments (HPTs), are evaluated. The extracted contact resistivities of doped contact stacks are subsequently utilized to gain insights into the performance of solar cells.

• In **Chapter 6**, the implementation of ultra-thin electron collectors based on nc-Si:H together with HPTs for high-efficiency SHJ solar cells is demonstrated. The development of thin (*n*)-type window layers that are not thicker than 8 nm aims at minimizing losses induced by their parasitic absorption. The opto-electrical properties are compared among thin (*n*)a-Si:H, (*n*)nc-Si:H and two types of (*n*)nc-SiO_x:H with device-relevant conditions. Then, we apply these (*n*)-layers into FBC-SHJ solar cells, and we evaluate the performance and interfacial properties of those devices with different (*n*)-layers.

• In **Chapter 7**, the effects of (*i*)a-Si:H deposition temperature on high-efficiency SHJ solar cells are investigated. We present the optical and microstructural properties of (*i*)a-Si:H layers deposited under various temperatures, and the performance of solar cells is further evaluated by examining those properties. Through this study, the requirements for realizing an optimized (*i*)a-Si:H layer (stack) for high-efficiency SHJ solar cells are revealed.

• In **Chapter 8**, the optical simulation-aided design and development of SHJ bottom sub-cells for high-efficiency 2T and 4T perovskite/SHJ tandem solar cells are presented. The optimization of SHJ solar cells dedicated to 2T tandem applications is performed. Besides, optical simulations are employed to enable the optimization of device designs with respect to light management. Finally, high-efficiency 2T and 4T perovskite/SHJ tandem solar cells are demonstrated.

• In **Chapter 9**, the main results presented in this thesis are summarized and the outlooks on future research for developing high-efficiency SHJ solar cells as well as tandem solar cells are provided. Especially, as an outlook beyond the classical FBC-SHJ solar cell design, we propose and evaluate the potential performance of various novel SHJ-based solar cell architectures.

1.2.7 Main contributions to the field

The work endowed in this thesis primarily contributes to the advancement of research and technology development on efficient implementations of nc-Si:H-based contact

stacks for high-efficiency SHJ solar cells, through the engineering of material properties and heterointerfaces. The efficiencies of FBC-SHJ solar cells were improved from around 18% to over 24% within this thesis. The best device exhibited an efficiency of 24.18% with a *FF* of 83.3%. As compared to our lab-standard screen-printed devices, this best cell features reduced Ag consumption thanks to the use of Cu-electroplating and reduced TCO consumption by utilizing double-layer anti-reflection coatings (DLARCs). The developed contact stacks also serve as benchmarks for other SHJ-related solar cell research conducted in the PVMD group of Delft University of Technology. Moreover, this work also explored the application of these developed contact stacks for perovskite/SHJ tandem solar cells, leading to new possibilities for the progression towards highly performing tandem devices. The specific main contributions to the field are outlined as follows:

• **Overview of tunable opto-electrical properties of doped nc-SiO$_x$:H.** We explored and showcased the significant adjustability of the opto-electrical characteristics of doped nc-SiO$_x$:H layers by varying their deposition conditions. The high flexibility of tuning those material properties allows one to tailor the selective transport of charge carriers and thus the solar cell performance. In general, (*n*)-type nc-SiO$_x$:H layers offer a wider range of optical transparency for achieving acceptable low E_a values as compared to the (*p*)-type counterparts, indicating the relaxed optimization efforts and preferred implementation of (*n*)-type nc-SiO$_x$:H-based window layers for high-efficiency SHJ solar cells.

• **Heterointerfaces engineering for nc-SiO$_x$:H-based contact stacks.** We applied various heterointerface engineering techniques to facilitate prompt nucleations of nanocrystals in doped nc-SiO$_x$:H-based layers and to ensure less resistive doped-Si/TCO interfaces. These techniques include the use of oxygen-absent nc-Si:H seed layers, HPTs, doped a-Si:H capping layers, post-HPT and their various combinations. Beneficial effects were found on the electrical properties of layers (stack) and the *FF* of corresponding solar cells by applying these techniques.

• **Bi-layer (*p*)nc-SiO$_x$:H + (*p*)nc-Si:H hole collector.** We performed simulation-guided optimization of hole collectors by using (*p*)nc-SiO$_x$:H with (*p*)nc-Si:H. In particular, (*p*)nc-SiO$_x$:H preserves the passivation quality and enables sufficient band bending at c-Si/(*i*)a-Si:H interface, while (*p*)nc-Si:H enhances the transport of holes to ITO and the band bending as well. The contact resistivities of (*p*)-type contact stacks can be reduced by several means, including using a thinner (*i*)a-Si:H layer, employing a (*p*)nc-SiO$_x$:H with a larger difference between the optical bandgap and E_a, finding an appropriate thickness combination of (*p*)nc-SiO$_x$:H and (*p*)nc-Si:H, and applying the optimized HPTs. As a result of the reduced contact resistivities, the proposed bi-layer (*p*)-layer stack was efficiently utilized for improving the *FF* of SHJ solar cells. Moreover, the corroborative experimental and simulation results suggest that the contact resistivities of the (*p*)-contact stack located on the illuminated side can also affect the vertical and lateral transport of holes in solar cells.

• **Ultra-thin (*n*)nc-Si:H-based electron collector.** We demonstrated the successful application of an ultra-thin layer of only 3-nm-thick based on (*n*)nc-Si:H plasma growth conditions without the use of additional contact or buffer layers. Despite the high E_a of this thin (*n*)nc-Si:H layer, the solar cell endowed with it delivered a certified efficiency

of 22.2% with a *FF* above 80%. This cell featured a higher J_{SC} with comparable *FF* and V_{OC} as compared to the (*n*)a-Si:H counterparts. By using the optimized HPTs prior to the deposition of this thin (*n*)nc-Si:H layer, all external parameters of resulting solar cells were enhanced. Besides, we additionally identified unexpected oxidation at the (*n*)nc-Si:H/ITO interface, which can be mitigated by inserting a 2-nm-thick (*n*)a-Si:H. Thus, the proposed bi-layer (*n*)nc-Si:H/(*n*)a-Si:H electron collector led to further improved *FF* of solar cells.

• **Microstructural modifications of (*i*)a-Si:H.** We observed that (*i*)a-Si:H layers became hydrogen-rich and less dense when deposited at lower temperatures or combined with the HPTs. The (*i*)a-Si:H deposited at a lower temperature exhibited a more significant boost of minority carrier lifetime after applying the HPTs as compared to higher temperature counterparts. At the device level, we noticed a trade-off between V_{OC} and *FF* when varying deposition temperatures of (*i*)a-Si:H layers. This reveals critical criteria for optimizing (*i*)a-Si:H for high-efficiency SHJ solar cells: (i) excellent surface passivation quality to reduce losses induced by interface recombination and simultaneously (ii) less-defective (*i*)a-Si:H bulk to not disrupt the charge carrier collections. Particularly, the (*p*)-contact is more sensitive to the bulk quality of (*i*)a-Si:H layers than the (*n*)-contact. Furthermore, we noticed distinctive absorption peaks near Si-H wagging-rocking mode in the infrared spectra of (*i*)a-Si:H, which seemingly reveal microstructural properties of thin-film (*i*)a-Si:H layers.

• **SHJ bottom sub-cells for 2T perovskite/SHJ tandem solar cells.** We re-optimized the (*i*)a-Si:H passivating layer together with various doped layers on (100)-oriented flat c-Si surface, specially for their applications in front-flat and rear-textured 2T tandem solar cells. The adjustment of deposition parameters is necessary as the (100)-oriented flat c-Si surface is more prone to detrimental epitaxial growth as compared to the (111)-oriented counterparts. Together with researchers from Eindhoven University of Technology, efficiencies from 23% to 25% were demonstrated for tandem solar cells with bottom sub-cells featuring various (*n*)-layers, namely, (*n*)a-Si:H, (*n*)nc-Si:H and (*n*)nc-SiO_x:H. Moreover, observations from experimentally prepared devices and optical simulations suggest that both (*n*)nc-Si:H and (*n*)nc-SiO_x:H layers are promising for application in high-efficiency tandem solar cells. This is possible mainly thanks to their capability to minimize intermediate reflections between the perovskite and c-Si absorbers, demonstrating the applicability of such light management to various tandem structures.

• **SHJ bottom sub-cells for 4T perovskite/SHJ tandem solar cells.** As a result of joint efforts among the Netherlands Organization for Applied Scientific Research (TNO), Interuniversity Microelectronics Centre (imec), Eindhoven University of Technology and Delft University of Technology, we presented a 30.1%-efficient 4T tandem solar cell. This tandem solar cell comprises a semi-transparent perovskite top sub-cell with a certified efficiency of 19.7% and an FBC-SHJ bottom sub-cell with a filtered efficiency of 10.4%. The FBC-SHJ solar cell featured an optimized DLARC to enable minimized reflection to air in the single junction application. As revealed by optical simulations, when utilizing air as the OCL, this optimized DLARC in single junction SHJ solar cells can also contribute to the current generation in bottom sub-cells of 4T tandem solar cells.

2

Fundamentals of the physics of SHJ solar cells

The basic working principle of solar cells, as briefly introduced in Section 1.2.1, involves the generation and recombination of charge carriers, and also the selective transport and collection of charge carriers. To elaborate on this aspect, in this chapter, we first introduce in more detail the concepts of carrier generation and recombination in solar cells. Then, specifically, the fundamentals of SHJ solar cells including the typical device structures, mechanisms of selective transport and collection of charge carriers, and the properties of a-Si:H and nc-Si:H-based layers are briefly reviewed and discussed.

2.1 Basic working principles of solar cells

2.1.1 Electronic band structure of semiconductors

Semiconductors feature electronic band structures that are determined by their crystal properties. In an isolated atom, its electrons occupy the atomic orbitals that feature discrete energy levels. In a solid that consists of a significant number (e.g. the density of Si atoms in crystalline Si is around $5 \times 10^{22}\,\mathrm{cm}^{-3}$) of identical atoms, there are overlappings of atomic orbitals among adjacent atoms. As a result, each discrete quantized energy level splits into a large number of discrete energy levels. Due to the large number of atoms, the energy differences between adjacent levels are extremely small. Consequently, those energy levels are considered to be (quasi-)continuous and form the so-called energy bands with allowed energy states. The outermost valence electrons are mostly relevant for the formation of those energy bands. While the bandgap (E_g) describes the energy states that are excluded by those abovementioned energy bands due to their finite widths and forbids the occupation by electrons.

As illustrated in Figure 2.1 for a typical nondegenerate semiconductor with a temperature above absolute zero, the lower energy band of allowed states, or the valence band, is nearly full of electrons as electrons tend to fill the lowest available energy states. While the upper energy band of allowed states, or the conduction band, is almost empty of

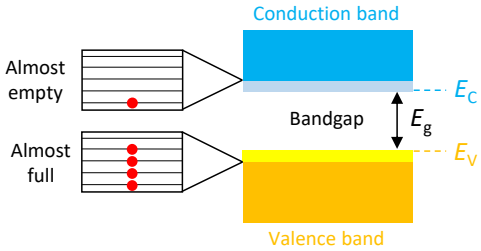

Figure 2.1: Allowed energy bands (valence band and conduction band) and the bandgap of a typical semiconductor when the temperature is above absolute zero degrees. The zoom-in (left) illustrates the closely 'spaced' energy levels either almost empty or occupied by electrons (red dots). E_C represents the lowest energy state in the conduction band. E_V represents the highest energy state in the valence band. The bandgap E_g is the energy difference between E_C and E_V. Figure adapted from [179].

electrons [179]. Thanks to the thermal energy that is sufficient for some electrons to undergo thermal excitation from the valence band to the conduction band, these electrons can occupy the energy states in the conduction band. The excitation of those negatively charged electrons results in the formation of an identical number of positively charged holes in the valence band. The movements of excited electrons in the conduction band and holes in the valence band are responsible for the conductivity of the semiconductor. When the temperature is at absolute zero, none of the electrons can jump from the valence band to the conduction band, thus no movable or free electrons and holes in the semiconductor and the material is not conductive in this case.

The operation of a semiconductor device depends on the concentrations of electrons in the conduction band and holes in the valence band that contribute to the charge transport. Under thermal equilibrium (an unperturbed state of a system) and for non-degenerate semiconductors, the total concentration of electrons in the conduction band (n) and holes in the valence band (p) can be expressed as (with Maxwell-Boltzmann approximation, the complete derivation can be found in [179]):

$$n = n_0 = N_C \exp\left(\frac{E_F - E_C}{k_B T}\right) \qquad \text{for} \quad E_C - E_F \geq 3 k_B T \tag{2.1}$$

$$p = p_0 = N_V \exp\left(\frac{E_V - E_F}{k_B T}\right) \qquad \text{for} \quad E_F - E_V \geq 3 k_B T \tag{2.2}$$

where n_0 and p_0 are the total concentration of electrons in the conduction band and holes in the valence band under thermal equilibrium, respectively. The N_C and N_V are the effective density of states function in the conduction and valence band, respectively. The k_B is Boltzmann's constant and T is the absolute temperature. The E_F is the Fermi energy or Fermi level, which is the electrochemical potential of the electrons in a material and represents the average energy of electrons in the material [18]. For an intrinsic semiconductor, its Fermi level approximately lies around the center of the bandgap. While the location of the Fermi level can be manipulated via doping to make semiconductors extrinsic ((n)-type or (p)-type). Dopant atoms such as phosphorus or boron add electrons to the conduction band or add holes to the valence band, while leaving fixed

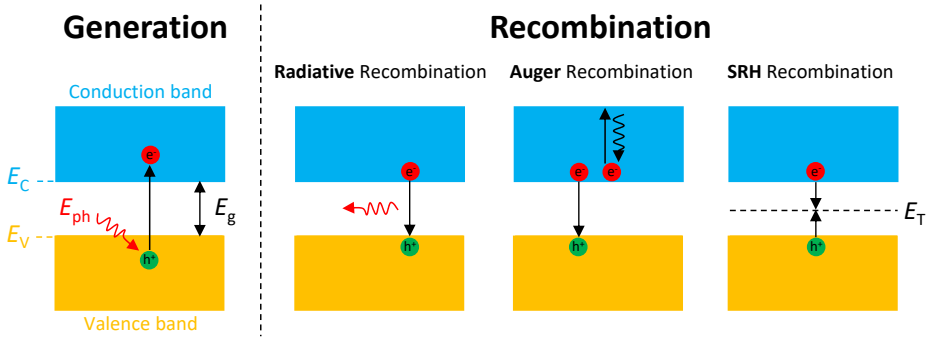

Figure 2.2: Illustrations of the generation process of an electron-hole pair via absorption of a photon (left) and different recombination mechanisms (right), namely, radiative recombination, Auger recombination and Shockley-Read-Hall (SRH) recombination. Figure adapted from [18].

positively or negatively charged ions in the material, respectively. Materials with sufficient doping concentrations or favored locations of Fermi level are critical for achieving efficient selective transport in solar cells which will be discussed in Section 2.3. Further, by multiplying equations 2.1 and 2.2, we obtain the following relation under thermal equilibrium:

$$np = n_0 p_0 = N_C N_V \exp(-\frac{E_g}{k_B T}) = n_i^2 \tag{2.3}$$

where n_i is the carrier concentration of an intrinsic semiconductor in which $n = n_0 = p = p_0 = n_i$. Equation 2.3 states that, under thermal equilibrium, the $n_0 p_0$ product is a constant for a certain (intrinsic or extrinsic) semiconductor at a given temperature. This equation is also known as the law of mass action.

2.1.2 Generation of excess charge carriers

As depicted in Figure 2.2, upon illumination with the light on a certain semiconductor, excess electrons can be excited from the valence band to the conduction band if the energy of the photons (E_{ph}) is not less than the E_g. In the meanwhile, excess holes (unoccupied states) are formed in the valence band. Both excess electrons in the conduction band and excess holes in the valence band can contribute further to charge transport. As the semiconductor is no longer under thermal equilibrium, the Fermi level will split into two quasi-Fermi levels that describe the occupation states in the conduction band with electrons (E_{Fn}) and in the valence band with holes (E_{Fp}). Then the total concentration of electrons in the conduction band (n) and holes in the valence band (p) can be expressed as:

$$n = n_0 + \Delta n = N_C \exp(\frac{E_{Fn} - E_C}{k_B T}) \tag{2.4}$$

$$p = p_0 + \Delta p = N_V \exp(\frac{E_V - E_{Fp}}{k_B T}) \tag{2.5}$$

where Δn and Δp are the concentrations of excess electrons and holes, respectively. By multiplying equations 2.4 and 2.5, and combining with equation 2.3, we obtain:

$$np = n_i^2 \exp\left(\frac{E_{Fn} - E_{Fp}}{k_B T}\right) = n_i^2 \exp\left(\frac{\mu_{eh}}{k_B T}\right) = n_i^2 \exp\left(\frac{q\mathrm{i}V_{OC}}{k_B T}\right) \tag{2.6}$$

The difference between the two quasi-Fermi levels ($E_{Fn} - E_{Fp}$) is the electrochemical energy of generated electron-hole pairs (μ_{eh}). By dividing the μ_{eh} with the elementary charge, we obtain the so-called implied open circuit voltage ($\mathrm{i}V_{OC}$), which represents the maximum possible potential that can be eventually extracted from a solar cell. As expected from equation 2.6, the $\mathrm{i}V_{OC}$ is related to the carrier concentrations that can be affected by recombination as will be elaborated in Section 2.1.3.

It is worth noting that for a certain type of semiconductors, or the so-called indirect bandgap semiconductors (such as c-Si), the position (crystal momentum) of the highest point of the valence band and the lowest point of the conduction band may not be aligned. Therefore, the excitation of electrons from the valence to the conduction band requires additional momentum that is provided by lattice vibrations (phonons). Differently, direct bandgap semiconductors (such as amorphous silicon, gallium arsenide, or generally most thin-film PV absorbers) feature aligned the highest point of the valence band and the lowest point of the conduction band. Due to the resulting different absorption coefficient, indirect bandgap semiconductors typically require thicker materials (often around hundreds of micrometers thick) to sufficiently absorb the light, especially for light with long wavelengths (lower energies), as compared to direct bandgap semiconductor counterparts (typically thinner than a few micrometers). It is worth mentioning that typical metal-halide perovskites also feature high absorption coefficients thanks to the direct transition from band to band [180], despite the direct-indirect character of the bandgap of methylammonium lead iodide ($CH_3NH_3PbI_3$) is also revealed [181].

2.1.3 Recombination mechanisms

In a real solar cell, not all photogenerated charge carriers can be successfully collected as those excited electrons tend to fall back to their initial energy levels. In other words, the electron-hole pair will recombine and release energy either in the form of a photon (band-to-band radiative recombination) or transferred to the third electron/hole or lattice vibrations (non-radiative recombination). In the following sections, different recombination mechanisms as illustrated in Figure 2.2 are introduced. Different recombination mechanisms can occur in parallel and the total recombination rate is the sum of all individual recombination rates.

Radiative recombination

Radiative recombination is the dominant mechanism in direct bandgap semiconductors, such as gallium arsenide. During this recombination process, an electron falls back from the conduction band to the valence band and recombines with a hole. In the meanwhile, a photon is emitted with an energy similar to the bandgap of the semiconductor that interacts weakly with the semiconductor. With continuous illumination and under steady-state conditions, the net radiative recombination rate (R_{rad}) is expressed as (derivation process can be found in [18]):

$$R_{\text{rad}} = \beta(np - n_0 p_0) \tag{2.7}$$

where β is the proportionality factor that can be calculated based on the absorption coefficient of the semiconductor [182, 183]. If there is no excess carrier, the R_{rad} is zero. Minority carrier lifetime (τ), which is defined as the average time that takes an excess minority carrier to recombine, is an important indicator for evaluating solar cell performance and in the case of an (n)-type semiconductor it can be expressed as:

$$\tau = \frac{\Delta p}{R} \tag{2.8}$$

where Δp is the concentration of excess holes and R is the recombination rate. Then, by substituting equation 2.8 to equation 2.7 and assuming $\Delta p = \Delta n$, we obtain the radiative recombination associated minority carrier lifetime as:

$$\tau_{\text{rad}} = \frac{1}{\beta(n_0 + p_0 + \Delta n)} \tag{2.9}$$

According to equation 2.9, for (n)-type and under low-injection conditions ($p_0 \ll n_0$, $\Delta n \ll n_0$), then a higher doping concentration N_{D} and thus a higher n_0 will reduce the τ_{rad}. While under high-injection conditions ($\Delta n \gg n_0$), the τ_{rad} is dominated by the Δn. Similar derivations can be made for a (p)-type semiconductor. For both typical c-Si and metal-halide perovskite absorbers, non-radiative recombination is dominant. Different mechanisms related to non-radiative recombination are discussed in the following section.

Auger recombination

As illustrated in Figure 2.2, the Auger recombination process involves three particles. During this process, the energy conservation of the recombining electron and hole is achieved by transferring the energy to another electron or hole instead of emitting light. As a consequence, a third electron (or hole) can be excited to higher energy levels in the conduction band (or deeper energy levels in the valence band). Eventually, the excited third electron (or hole) will relax back to the conduction band edge (or rise back to the valence band edge) through thermalization by transferring its energy to lattice vibration (phonon modes). Depending on whether electrons or holes are the majority carriers, the Auger recombination is dominated either by the electron-electron-hole (eeh) or electron-hole-hole (ehh) process, respectively. Traditionally, the total recombination rates of the two processes are expressed as [18]:

$$R_{\text{Aug}} = R_{\text{Aug,eeh}} + R_{\text{Aug,ehh}} = C_n n^2 p + C_p n p^2 \tag{2.10}$$

where C_n and C_p are the proportionality constants. For a highly doped ($N_{\text{D}} > 1 \times 10^{18}\,\text{cm}^{-3}$ [47]) (n)-type semiconductor and under low-injection conditions (assume $\Delta n = \Delta p$), by combining equations 2.8 and 2.10, the associated minority carrier lifetime can be then approximated as [47]:

$$\tau_{p,\text{Aug,low}} = \frac{1}{C_n N_{\text{D}}^2} \tag{2.11}$$

For high-injection conditions, the Auger lifetime can be approximated as [47]:

$$\tau_{p,\mathrm{Aug,high}} = \frac{1}{(C_n + C_p)\Delta n^2} \tag{2.12}$$

According to equations 2.11 and 2.12, the Auger recombination rate is higher with increased doping concentration at low-injection conditions and increased excess charge carrier generations at high-injection conditions.

Shockley-Read-Hall recombination

Different from the abovementioned two intrinsic recombination mechanisms, Shockley-Read-Hall (SRH) recombination is an extrinsic process. In realistic semiconductors, impurity atoms or lattice defects can generate defects within the crystal, forming discrete electronic energy states within the bandgap [179]. Those allowed energy states (E_T) or trap states facilitate the recombination of electrons and holes as illustrated in Figure 2.2 [184, 185]. More effective SRH recombination can happen through those trap states that have equal probabilities of capturing electrons and holes (e.g. around mid-gap). This process is usually non-radiative and the excess energy is dissipated in the form of lattice vibration or heat. The SRH recombination rate is obtained as (derivation process can be found in [18]):

$$R_\mathrm{SRH} = v_\mathrm{th} N_\mathrm{T} \frac{np - n_\mathrm{i}^2}{\frac{1}{\sigma_p}(n + n_1) + \frac{1}{\sigma_n}(p + p_1)} \tag{2.13}$$

with

$$n_1 = n_\mathrm{i}\exp(\frac{E_\mathrm{T} - E_\mathrm{Fi}}{k_\mathrm{B} T}), \quad p_1 = n_\mathrm{i}\exp(\frac{E_\mathrm{Fi} - E_\mathrm{T}}{k_\mathrm{B} T}),$$

where v_th is the thermal velocity (around 1×10^7 cm/s in Si at 300 K), σ_p and σ_n are the charge carrier capture cross-sections, N_T is the trap density, E_T is the trap energy, E_Fi is the intrinsic Fermi level. Then by combining equations 2.8 and 2.13, the SRH-associated minority carrier lifetime (τ_SRH) for an (n)-type semiconductor (assume $\Delta n = \Delta p$) can be expressed as (derivation process is not shown):

$$\tau_\mathrm{SRH} = \frac{\sigma_n(n_0 + \Delta n + n_1) + \sigma_p(p_0 + \Delta p + p_1)}{v_\mathrm{th}\sigma_n\sigma_p N_T(n_0 + p_0 + \Delta n)} \tag{2.14}$$

Considering low-injection conditions, then τ_SRH can be simplified as:

$$\tau_\mathrm{SRH,low} = \frac{1}{v_\mathrm{th}\sigma_n\sigma_p N_\mathrm{T}}(\sigma_n(1 + \frac{n_1}{n_0}) + \sigma_p\frac{p_1}{p_0}) \tag{2.15}$$

For high-injection conditions:

$$\tau_\mathrm{SRH,high} = \frac{\sigma_n + \sigma_p}{v_\mathrm{th}\sigma_n\sigma_p N_\mathrm{T}} \tag{2.16}$$

As seen from equations 2.15 and 2.16, the τ_SRH at both low-injection and high-injection conditions depend on the σ_n, σ_p and the N_T. Especially for low-injection conditions, the doping density (via n_0) and E_T (via n_1 and p_1) also affect the τ_SRH.

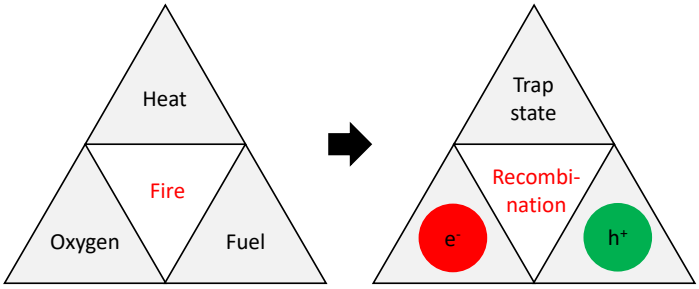

Figure 2.3: The three essential components for defect-assisted recombination (right) in analogy to the well-known fire triangle (left). The creation of this figure was inspired by Dr. Paul Procel.

As illustrated in Figure 2.3, in analogy to the well-known fire triangle (heat, oxygen and fuel), defect-assisted recombination also needs three essential components, namely, an electron, a hole and a trap state. Therefore, the effective reduction of defect-assisted recombination can be then achieved by minimizing the concentration of either one of the charge carrier types or reducing the density of the trap state. Especially with respect to the latter, monocrystalline silicon that has continuous and unbroken crystal lattice without any grain boundaries until the wafer edges is preferably used for high-efficiency c-Si solar cells as compared to multicrystalline silicon, which consists of many small random-oriented crystalline grains and many defects near those grain boundaries.

Surface recombination

Any real semiconductor device is not infinitely in size, therefore, there are abruptly terminated surfaces. On the surface, a vast amount of valence electrons cannot form covalent bonds resulting in so-called dangling bonds, which create allowed energy states within the bandgap that facilitate SRH recombination. Instead of forming discrete allowed energy states due to impurities or lattice defects as mentioned previously, a distribution of allowed energy states within the bandgap is formed due to the existence of surfaces. The surface recombination rate (R_{surface}) at a single-level surface state can be expressed as [186]:

$$R_{\text{surface}} = \frac{n_{\text{s}} p_{\text{s}} - n_{\text{i}}^2}{\frac{1}{S_{p0}}(n_{\text{s}} + n_1) + \frac{1}{S_{n0}}(p_{\text{s}} + p_1)} \tag{2.17}$$

with

$$S_{p0} = \sigma_p \nu_{\text{th}} N_{\text{sT}}, \quad S_{n0} = \sigma_n \nu_{\text{th}} N_{\text{sT}},$$

where S_{p0} (S_{n0}) is the surface recombination velocity parameters of holes (electrons), p_{s} (n_{s}) is the concentration of holes (electrons) at the surface, N_{sT} is the surface energy states per unit area. Moreover, by integrating over the bandgap at the interface, one can obtain the recombination rate that describes a continuum of independent (non-interacting) surface energy states [187, 188]. Surface recombination velocity (SRV, S) can be defined as [186]:

$$S = \frac{R_{\text{surface}}}{\Delta n_{\text{s}}} \tag{2.18}$$

where Δn_{s} is the excess carrier density at the surface. Considering realistic devices in which band bending exists near the wafer surfaces, an effective surface recombination velocity (S_{eff}) can be determined by replacing Δn_{s} and R_{surface} with $\Delta n(x = d)$ and $R_{\text{Surface}}(x = d)$ in equation 2.18, respectively. The $\Delta n(x = d)$ represents the excess minority carrier concentration at a virtual surface located at the edge of the surface space-charge region, which has a position of $x = d$. Strategies, as provided in Figure 2.3, can be also applied for minimizing the S_{eff} and different passivation mechanisms will be discussed in Section 2.1.4.

Effective minority carrier lifetime

In practice, effective minority carrier lifetime (τ_{eff}) that considers all the abovementioned bulk and surface recombination mechanisms in a semiconductor is typically measured. The τ_{eff} for symmetrical samples with non-diffused surfaces can be expressed as [189–192]:

$$\frac{1}{\tau_{\text{eff}}} = \frac{1}{\tau_{\text{B}}} + \frac{2S_{\text{eff}}}{W} \tag{2.19}$$

with

$$\frac{1}{\tau_{\text{B}}} = \frac{1}{\tau_{\text{Rad}}} + \frac{1}{\tau_{\text{Aug}}} + \frac{1}{\tau_{\text{SRH}}}$$

where τ_{B} is the minority carrier lifetime of bulk, W is the wafer thickness, S_{eff} represents the effective surface recombination velocity at the surface. It is worth noting equation 2.19 is only valid for samples with a sufficiently long τ_{B} that allows photogenerated charge carriers to reach both surfaces and with low S to avoid transport-limited profiles around the surfaces [191]. For high-quality c-Si wafers such as (n)-type float-zone (FZ) monocrystalline Si, the bulk recombination is minimized ($\tau_{\text{B}} \geq 2000\,\mu\text{s}$, typically much higher). Therefore, the τ_{eff} reflects mainly the surface passivation quality. It can be also seen from equation 2.19 that surface passivation is more crucial when a thinner wafer is used.

2.1.4 Surface passivation strategies

Passivation techniques that minimize surface recombination are critical to achieve high-efficiency solar cells. As discussed in Figure 2.3, two main surface passivation strategies are proposed: (i) reducing the density of surface trap states via chemical passivation; (ii) minimizing the concentration of either one of the charge carrier types through field-effect passivation. Accordingly, both passivation mechanisms are often jointly implemented to realize excellent surface passivation. Depending on the c-Si solar cell technology as already introduced in Figure 1.3, a thin dielectric layer stack (e.g., Al_2O_3/SiN_x [193] for PER'X' solar cells), a thin semiconductor layer stack (e.g., (i)a-Si:H/doped a-Si:H in SHJ solar cells [51]) or a combination of thin dielectric and semiconductor layers

(e.g., SiO_x/doped poly-Si in TOPCon solar cells [52, 53]) is typically deployed for high-efficiency solar cells. On the one hand, those layer stacks can saturate the surface dangling bonds by forming chemical bonds with oxygen, silicon and hydrogen atoms. On the other hand, the electric field (or band bending) near the c-Si surface induced by layers with either fixed charges, doping or proper work function results in the reduction of either type of charge carriers.

2.2 Typical architectures of front/back-contacted (FBC) SHJ solar cells

As introduced in Section 1.2.2, typical SHJ solar cells (see Figure 1.3 (g)) feature c-Si wafers sandwiched by layer stacks consisting of (*i*)a-Si:H and doped a-Si:H for chemical passivation and junction formation, respectively. On top of those a-Si:H layer stacks, transparent conductive oxide (TCO) layers are commonly needed. Due to the poor lateral conductivity of few-nanometer-thick doped a-Si:H layers, TCO is usually necessary for providing sufficient lateral conductance of charge carriers towards the front metal electrodes. Typically, around 75 nm of tin-doped indium oxide (ITO) that also serves as an anti-reflection coating (ARC) is applied for the stand-alone SHJ solar cells. While on the rear side, a thicker TCO is mainly used for enhancing the internal reflection thus maximizing the infrared response of the solar cells, and preventing metal diffusion or spiking [194–196]. Eventually, the overlaying metal contacts are deposited for extracting the charge carriers to the external circuit.

As illustrated in Figure 1.3, dominating industrial solar cells nowadays, such as PERC solar cells on (*p*)-type wafers (see Figure 1.6), generally feature a front junction (FJ) architecture. In this configuration, the minority carriers can be collected near their generation locations, thus reducing recombination-induced losses, which originate from insufficient diffusion length of minority charge carriers in the bulk of the wafer and high surface recombination rate at Si/metal interfaces. It is worth noting that PERC technology to date may not be limited by the wafer quality anymore as TOPCon solar cells with (*p*)-type wafers have demonstrated a record efficiency of 26.0% [197]. Nevertheless, thanks to both the use of high bulk quality of (*n*)-type c-Si wafers and excellent surface passivation, SHJ solar cells allow a high degree of flexibility when designing the device's polarity for achieving high efficiencies. Typical monofacial FJ and rear junction (RJ) FBC-SHJ solar cells with (*n*)-type c-Si substrates are shown in Figure 2.4. For both configurations, charge carriers (holes for FJ cells and electrons for RJ cells) are collected at the front side involving transporting through both vertical and lateral directions. While the carrier collection on the rear side is only associated with vertical transport due to the full coverage of metal electrodes.

It is widely reported that the rear junction SHJ solar cells exhibit more relaxed opto-electrical design requirements than their front junction counterparts. Specifically, there are fewer restrictions when choosing the front TCO (including its thickness) and the metal designs (e.g., the pitch size) in RJ solar cells, as they can benefit more from c-Si wafer-assisted lateral transport of majority carriers (electrons) [198, 199]. The reported beneficial effects for RJ solar cells over FJ solar cells can be mainly ascribed to that (i) (*n*)-type contact stacks (including c-Si/(*i*)a-Si:H/(*n*)-layer/TCO/Metal) generally exhibit

a lower contact resistance (ρ_c) from c-Si to TCO as compared to the (p)-type counterparts, while a lower ρ_c is critical for enabling c-Si wafer-assisted lateral transport; (ii) under typical illumination conditions (sufficiently high concentrations of both charge carrier types), the wafer sheet resistance for electrons is comparable and even lower to that of a typical 75-nm-thick TCO [200]; (iii) the sheet resistance for electrons is roughly three times lower than that of holes mainly due to the higher electron mobility than that of holes.

Besides, inherently from the symmetrical nature of SHJ solar cells, SHJ devices can be easily adapted to bifacial designs (see Figure 2.4) [124], which enables higher energy yield than a monofacial design and lesser usage of TCO and metals [200]. In bifacial designs, the abovementioned wafer-assisted lateral transport of charge carriers can be particularly interesting and critical, as both front and rear collections of charge carriers are accomplished by vertical and lateral transport of charge carriers.

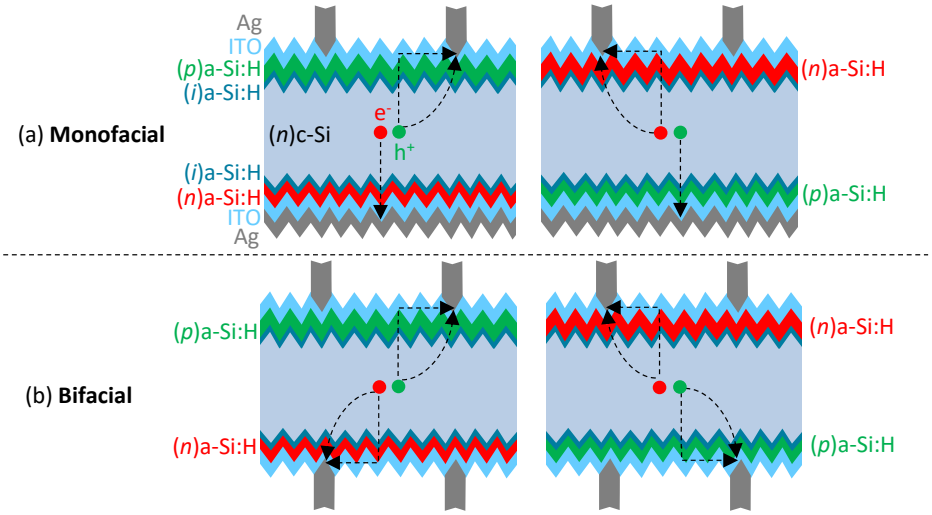

Figure 2.4: Schematic sketches of typical architectures of FBC-SHJ solar cells: (a) monofacial front junction (FJ, left) and rear junction (RJ, right) configurations; (b) bifacial configurations. The arrows indicate the transport of charge carriers.

2.3 Selective transport and collection of charge carriers in SHJ solar cells

Despite a low ρ_c from c-Si to TCO being critical for enhancing the wafer-assisted lateral transport of charge carriers, ρ_c also reflects the effectiveness of charge carrier transport across discontinuous interfaces due to different E_g or work function (WF) of adjacent materials. That is, ρ_c also provides insights into the transport mechanism of charge carriers [151, 201]. Besides, the effectiveness of this transport process also poses strong indications to the eventual performance of solar cells. A schematic energy band diagram

of an (*n*)-type SHJ solar cell including the main transport mechanisms of charge carriers from c-Si to TCO is illustrated in Figure 2.5 [151].

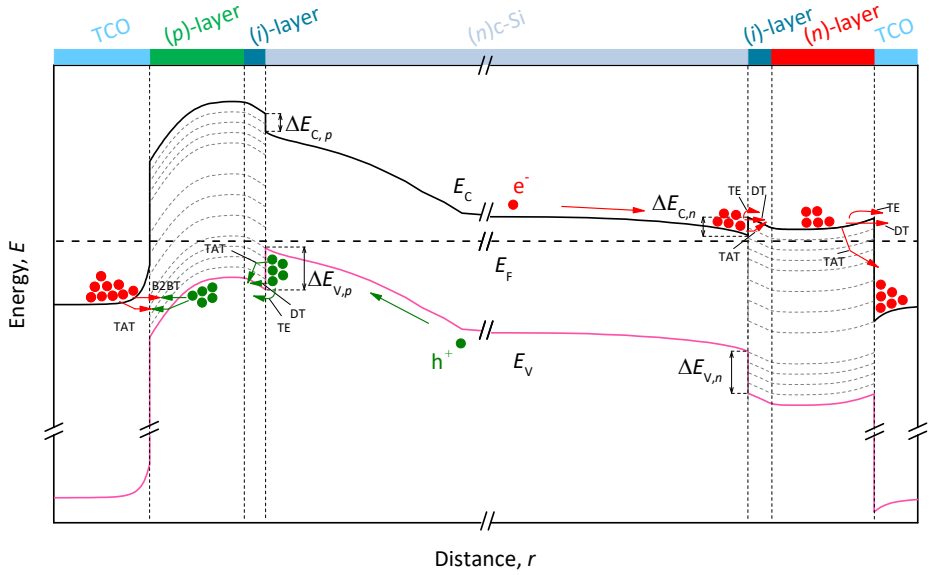

Figure 2.5: The schematic energy band diagram of a typical SHJ solar cell with an (*n*)-type c-Si wafer under dark and thermal equilibrium (the solid black line is the bottom of the conduction band; the solid pink line is the top of the valence band). The ΔE_C and ΔE_V represent the conduction and valence band offsets, respectively. The colored arrows in green and red are for the transport of holes and electrons, respectively. The corresponding transport mechanisms of charge carriers are thermionic emission (TE), direct tunnnelling (DT), trap-assisted-tunnelling (TAT) and band-to-band tunnelling (B2BT). The dashed lines indicate energy levels of different defect states within the bandgap. Those dashed lines also illustrate that the energy band bending can affect the energy levels of defect states. Figure adapted from [151].

The collection of negative charges is based on the transport of electrons towards the conduction band energy. A band bending is formed inside c-Si near the c-Si/(*i*)a-Si:H interface. The consequent band bending is determined by the properties of the (*n*)-type contact stack (c-Si/(*i*)-layer/(*n*)-layer/TCO/metal), which is affected by the relative Fermi level position in each compositional material [150, 151]. Accordingly, the transport of electrons is favored towards the c-Si/(*i*)a-Si:H interface. For a fixed c-Si wafer, a practical approach to improve band bending is to reduce the activation energy (E_a) of the (*n*)-layer, which is defined as the energy difference between the E_F and E_C for (*n*)-layers [150]. In the meanwhile, due to different E_g between the c-Si (1.12 eV) and the (*i*)a-Si:H (~1.7 eV), energy barriers or the so-called band offsets ($\Delta E_{C,n}$ for conduction band, $\Delta E_{V,n}$ for valence band) are formed at the c-Si/(*i*)a-Si:H interface. It is reported that for (*i*)a-Si:H with varied bulk hydrogen content (~12% – 24%), the conduction band offset (ΔE_C) is generally smaller (~0.22 – 0.31 eV) than the valence band offset (ΔE_V ~0.39 - 0.61 eV), and the latter is more sensitive to increase linearly with a higher hydrogen content of the (*i*)a-Si:H film [125, 202]. Thanks to both the band bending and the $\Delta E_{V,n}$, the diffusion of holes towards and across the c-Si/(*i*)a-Si:H interface (electron collection

side) is prevented. As a result, there are highly asymmetric concentrations of electrons and holes within the c-Si near the c-Si/(*i*)a-Si:H interface. The large difference in carrier concentration at c-Si interfaces suggests a high-quality selective contact [150, 203, 204].

Subsequently, the accumulated electrons near the c-Si/(*i*)a-Si:H interface can cross the potential barrier formed by the (*i*)a-Si:H/(*n*)-layer via thermionic emission (TE) [205], or with support of tunnelling processes such as direct tunnelling (DT) [205, 206] and trap-assisted-tunnelling (TAT) [151, 207–209]. Mainly depending on the WF and electronic properties of the (*n*)-layer and TCO, band bending and band offset are also present between adjacent materials. Typical TCO layers used in SHJ solar cells are (*n*)-type degenerate semiconductors, which have their E_F lying inside their conduction band. As both sides are (*n*)-type materials, electrons can move across the potential barriers formed at the (*n*)-layer/ITO interface via the conduction band with the abovementioned transport mechanisms as indicated in Figure 2.5 (TE, DT and TAT). Simulation studies suggest that the transport barrier from the (*n*)-layer to TCO can be minimized by using a TCO with a low WF (e.g, by increasing carrier concentration N_{TCO} of TCO), which is preferred due to the reduced WF mismatch between the TCO and the (*n*)-layer [150, 151, 210, 211]. Besides, an (*n*)-layer with a low E_a can enhance the band bending near the c-Si/(*i*)a-Si:H interface, and enable a reduced transport barrier from the (*n*)-layer to the TCO [151]. Eventually, electrons can be easily transported from TCO to the metal electrode thanks to the typical ohmic contact between TCO and metal electrode [200, 212].

The collection of positive charges is based on holes transporting up to the (*p*)-layer and electrons in the adjacent TCO layer. Holes are accumulated (due to band bending) while electrons are repelled near the c-Si/(*i*)a-Si:H interface (because of band bending and $\Delta E_{C,p}$). Similar to that of the electron collection, the accumulated holes can cross the (*i*)a-Si:H/(*p*)-layer interface via TE, DT and TAT, although the significance of the specific mechanisms varies for the transport of electrons and holes [151, 209]. A theoretical study from our group suggests that the band bending can be enhanced with a (*p*)-layer that exhibits a high E_g and a low E_a [150]. Note that at (*p*)-layer/TCO interface, charge exchange occurs via band-to-band tunnelling (B2BT) or TAT tunnelling processes [151, 213]. It is worth noting that a proper energy alignment between the valence band of the (*p*)-layer and the conduction band of TCO is essential to make B2BT possible [151, 214]. The energy alignment between the valence band of the (*p*)-layer and the conduction band of TCO is essential to discriminate if B2BT or TAT mechanism dominates the charge transfer. In the presence of the aforementioned energy alignment, the transport is mainly based on B2BT in direct energy transition between electrons from the TCO conduction band jumping into (*p*)-layer valence band energy state, and vice versa. In the absence of such energy alignment, the charge exchange is based on TAT mechanisms as indirect energy transitions or recombination of electrons from TCO with holes from c-Si at defect states inside the (*p*)-layer occur near the (*p*)-layer/TCO interface. In general, B2BT is preferred because it implies only direct energy transitions [151, 214]. While transport based on TAT happens through the energy states inside (*p*)-layer near (*p*)-layer/TCO interface in a form of capturing and emission (recombination) of charge carriers, and it is generally less efficient than the B2BT counterpart [151]. The proper energy alignment can be achieved by adjusting the E_a of the (*p*)-layer and/or the WF

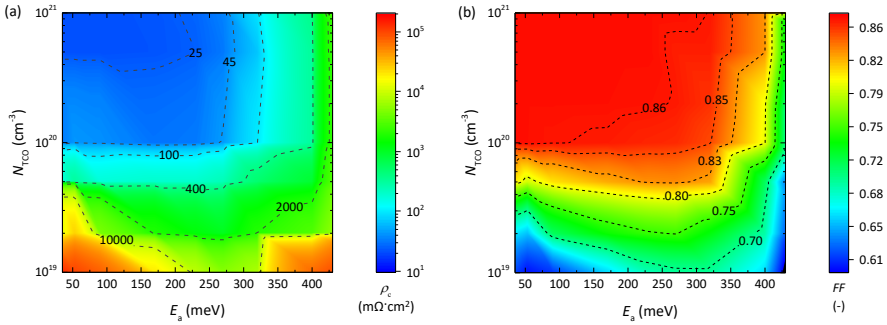

Figure 2.6: Contour plot of (a) ρ_c and (b) *FF* of IBC-SHJ solar cell as function of E_a and N_{TCO} at (*p*)-type contact stack. Figure adapted from [151].

of TCO. In particular, a (*p*)-layer with a low E_a enables more flexibility in the electronic properties of the TCO. Despite a low E_a required, the band bending near the c-Si/(*i*)a-Si:H interface can be also enhanced with a (*p*)-layer that exhibits a high E_g [150]. Due to the amorphous nature of typical Si-based thin-film layers used for SHJ solar cells, thus the existence of numerous energy states within their bandgap, transport via TAT is rather relevant in practical 'non-ideal' devices. More detailed discussions, including TAT via dangling bond states and tail states, can be found in [151]. In general, the optimization of hole collection requires more attentive effort than electron collection, this is due to (i) the inherently larger c-Si/(*i*)a-Si:H band offsets ($\Delta E_{V,p} > \Delta E_{C,n}$) for hole transport, and (ii) the more sensitive transport through (*p*)-layer/TCO interface that relies on tunnelling processes.

The transport of charge carriers across heterointerfaces is typically evaluated by the ρ_c [151, 201]. It has been proven experimentally that the minimization of ρ_c of SHJ contact stacks is essential for achieving high-efficiency SHJ solar cells [80, 164, 215]. The physical material parameters affecting ρ_c and thus the V_{OC} and *FF* of solar cells were assessed in a previous study [151], which constructed a detailed technology computer-aided design (TCAD) simulation framework replicating the transfer length method [216, 217]. As discussed before, the transport of charge carriers is ultimately driven by material properties that define the E_F of layers forming the contact stacks. For instance, for (*p*)-type contact stack, Figure 2.6 presents guidelines for improving the performance of SHJ solar cells with two practically accessible material properties, namely, E_a of doped layers and N_{TCO} of TCO. As seen in Figure 2.6, different combinations of these two parameters lead to various ρ_c values, which provide insight into distinct dominating transport mechanisms of charge carriers. More details on correlating various transport mechanisms (e.g., B2BT, TAT) and various combinations of E_a and N_{TCO} for both (*n*)- and (*p*)-type contact stacks can be found in the previous work [151]. As the simulation study suggests [151], the V_{OC} of solar cells is solely determined by the quality of the band bending inside the c-Si near its interface with (*i*)a-Si:H, whereas the *FF* is additionally influenced by the quality of the charge carrier transport at the doped-layer/TCO interface. Moreover, re-

ducing the E_a while increasing the N_{TCO} leads to a reduction of ρ_c of contact stacks, thus enhancing the *FF* of solar cells.

Last but not least, for a given solar cell under illumination, ideal selective contact stacks should first provide excellent surface passivation, thus allowing a maximized quasi-Fermi level splitting or a high iV_{OC} (see equation 2.6). This iV_{OC} then reflects the recombination losses of the c-Si absorber. Besides, ideal contact stacks should also ensure an eventual device V_{OC} to be the same as iV_{OC}, indicating an ideal selectivity [36, 218]. However, for realistic contact stacks, due to imperfect surface passivation, cells can feature lower iV_{OC} values as compared to the ideal case due to recombination, which limits the V_{OC} of devices. Moreover, the splitting of quasi-Fermi levels may not be maintained till the terminal electrodes, resulting in a voltage drop from iV_{OC} to V_{OC}. In this case, the device V_{OC} is limited by the extraction of the majority carriers through those contact stacks [36].

2.4 a-Si:H, nc-Si:H and their alloys for SHJ solar cells

As seen in Sections 2.2 and 2.3, Si-based thin-film stacks that consist of (*i*)a-Si:H and doped a-Si:H/nc-Si:H-based layers play a crucial role in achieving efficient SHJ solar cells. In this section, a concise literature review regarding the general properties of those materials and their relevance in the passivation, selective transport of charge carriers and light management in SHJ solar cells is presented.

2.4.1 Atomic structure and electronic band structure

Schematic illustrations of the atomic structure of c-Si, a-Si:H and nc-Si:H are presented in Figure 2.7. Different from c-Si that is tetrahedrally bonded with long-range periodic order, a-Si:H features a disordered covalent network consisting of Si-Si and Si-H bonds. Besides, a-Si:H also contains Si atoms that are not fourfold coordinated, such as under-coordinated (often referred to as 'dangling bonds') and over-coordinated (often referred to as 'floating bonds') bonds. The existence of hydrogen is critical for saturating the dangling bonds thus enabling reduced defect density as compared to the unhydrogenated a-Si [219–221]. The hydrogen can reside in the a-Si:H in different ways, such as forming bonds with Si atoms and/or presenting as isolated hydrogen molecules in the a-Si:H network [222]. Studies based on infrared absorption spectroscopy also revealed the non-homogeneous distribution and different configurations of defects in the material, such as monovacancies, divacancies and nanovoids [223, 224]. Instead of featuring only the amorphous phase, nc-Si:H (or also referred to as hydrogenated microcrystalline silicon, μc-Si:H) contains small crystalline grains embedded in the amorphous matrix, and features a certain volume fraction of voids [177, 225, 226]. The existence of crystalline grains gives rise to additional grain boundary defects, which can be well-passivated by hydrogen [225, 227]. Those Si-H hydrides at grain boundaries can be characterized by using infrared spectroscopy [227–229].

As a result of the different atomic structures between c-Si and a-Si:H, they also have different electronic band structures. Ideally, as for c-Si, it features a perfect crystalline lattice thus leading to a well-defined band gap of 1.12 eV. While in a-Si:H, due to the disordered amorphous network, there is the existence of band tails that represent expo-

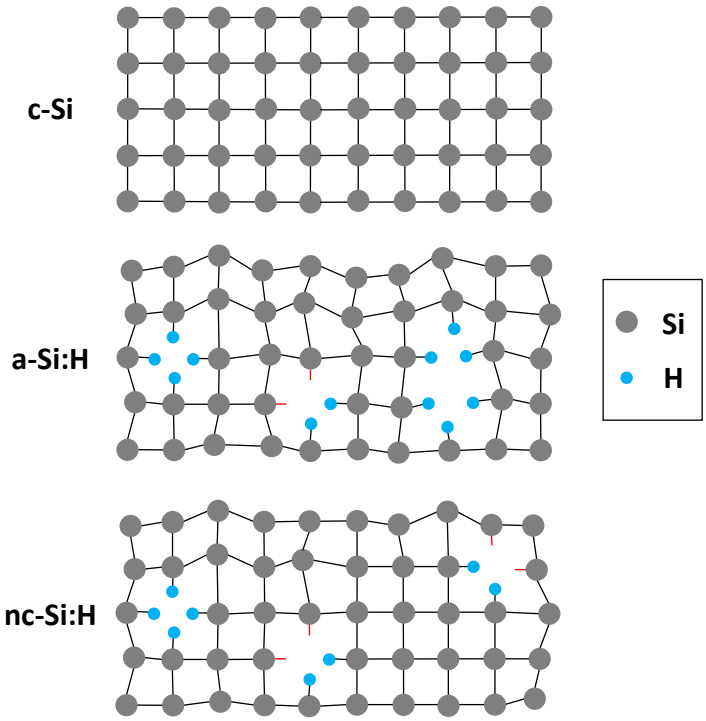

Figure 2.7: Schematic illustration of atomic structures of c-Si, a-Si:H and nc-Si:H. The grey and blue dots indicate silicon and hydrogen atoms, respectively. The red lines represent dangling bonds.

nential distributions of localised electronic states extending from the band edges into the bandgap. Those band tail states originate from energy states of electrons forming strained bonds in the material. Besides, around the mid-gap, there are defect states that are ascribed to the dangling bonds in the material. Charge carriers in both the band tail states and defect states have significantly reduced carrier mobility, therefore, the mobility gap is defined for a-Si:H (typically around 1.7 eV to 1.9 eV [18, 230]). Accordingly, mobility edges are often used instead of band edges for c-Si. Moreover, the disordered amorphous network (missing the k-selection rule) makes a-Si:H a direct bandgap semiconductor [18].

In practice, optical bandgaps are more frequently measured and reported. For amorphous semiconductors, their optical bandgaps are usually obtained by the Tauc plot (E_{tauc}) [231] or by equal to the energy at which the absorption coefficient reaches 10^4 cm^{-1} (E_{04}). As reported for a-Si:H [230, 232, 233], the extracted optical bandgap can be used as an indicative parameter for the mobility gap. Due to the mixed-phase compositions, the (mobility) bandgap of nc-Si:H may vary depending on the fraction of different material phases and the number of hydrogen atoms incorporated into the amorphous phase. Typically, E_{tauc} or E_{04} values ranging from around 1.8 to 2.3 eV were reported for nc-Si:H layers [234–238]. More discussions on the size effect of nanocrystals on the E_{tauc}

of nc-Si:H layers, which is linked to the quantum confinement effect in silicon nanocrystals, can be found in literature [234, 235, 237–240]. The difference in extracted E_{tauc} or E_{04} between a-Si:H and nc-Si:H suggests a potential preferred implementation of nc-Si:H layers as the window layer in SHJ solar cells.

2.4.2 Growth mechanisms

Both a-Si:H and nc-Si:H can be prepared via different deposition techniques, mainly chemical (e.g. chemical vapour deposition, CVD [152, 241–246]) and physical processes (e.g. sputtering [247–250]). As plasma-enhanced CVD (PECVD) (more details about PECVD are discussed in Section 3.1.2) is generally used for growing those Si-based thin-films nowadays, the growth mechanisms of those thin-films based on low temperature (around 200 °C) PECVD processing will be discussed. The advantages of PECVD over other deposition techniques are briefly discussed in [251].

a-Si:H

Silane (SiH_4) is commonly used as the precursor gas for depositing a-Si:H. In the PECVD reactor chamber, the dissociation of SiH_4 is triggered by accelerated electrons that gain energy from the applied electric field. Among different ions, radicals, and other species that exist in the plasma [251, 252], the (presumed) most abundant SiH_3 radical in the plasma that results in high-quality a-Si:H (low defect density), is considered to be the only film-growing precursor in the most popular a-Si:H growth model [253–256]. This model is schematically depicted in Figure 2.8.

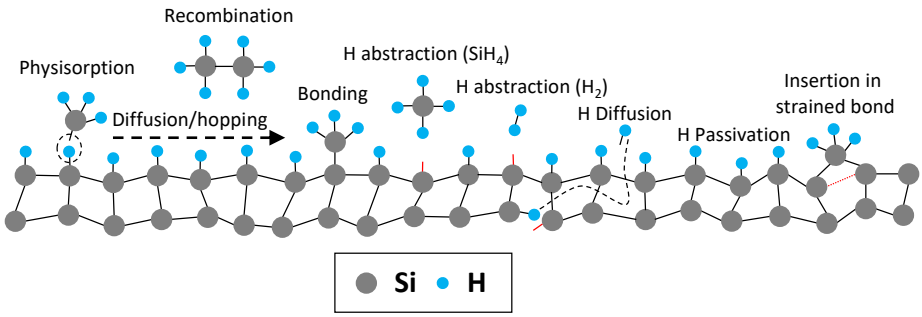

Figure 2.8: Schematic illustration of the a-Si:H growth model based on SiH_3 radical and atomic hydrogen. Figure adapted from [251, 257].

As illustrated in Figure 2.8, the SiH_3 radicals from the plasma can diffuse to the surface of the growing a-Si:H. As the surface is hydrogen-terminated, no chemical bond is formed when those radicals land on the surface. Instead, they are physisorbed on the surface and subsequently diffuse along the surface. While the radical is diffusing on the surface, it might: (i) abstract a hydrogen atom from the surface forming gaseous SiH_4 and leaving a dangling bond, which is the site for another SiH_3 radical to form a chemical bond with the surface; (ii) form a chemical bond with a surface dangling bond resulting

film growing; (iii) react with another SiH_3 and form gaseous Si_2H_6; (iv) desorb from the physisorbed site. Besides, as reported elsewhere [258], SiH_3 can also directly insert into strained Si-Si surface bonds, thus not relying on the available dangling bonds.

Nevertheless, this model does not consider the effect of atomic hydrogen in the plasma, which can be the product during the dissociation of SiH_4 and/or intentionally hydrogen-diluted SiH_4 plasma. As reported [259], atomic hydrogen from H_2 plasma can result in the abstraction of surface hydrogen thus increasing the density of the surface dangling bonds. Besides, atomic hydrogen can also passivate dangling bonds and break weak Si-Si bonds resulting in a structurally relaxed atomic network, and this is also often referred to as chemical annealing [260].

Overall, this model does not thoroughly reveal the growth mechanism of a-Si:H, especially when other radicals such as SiH_2 and SiH become abundant under certain process conditions [261]. Moreover, the limitations of this model and also interesting discussions on hydrogen-elimination during the film growth are given in [257, 262].

nc-Si:H

As compared to the deposition of a-Si:H, the role of hydrogen is more critical for obtaining a nc-Si:H layer as a highly hydrogen-diluted SiH_4 plasma is often required [263, 264]. Accordingly, higher deposition power is often applied to enable more efficient dissociation of H_2 to supply sufficient atomic hydrogen [265] as compared to a-Si:H deposition [251]. A few models on growth mechanisms of nc-Si:H have been proposed and they can be categorized into three main groups: (i) surface models including the surface diffusion model [266–268] and the selective etching model [269–271]; (ii) bulk models such as the chemical annealing model [271–273]; and (iii) growth model based on plasma-synthesised nanocrystals [274, 275].

Similar to the surface diffusion model as introduced for a-Si:H, the mobility of radicals on the surface of the growing film is further enhanced thanks to the high flux of atomic hydrogen impinging the surface, which improves the surface hydrogen coverage [276]. As a result, the radicals have higher probabilities to bond with sites featuring favorable energy, thus forming stable Si-Si bonds and eventually crystallites. As for the selective etching model, although there is simultaneous growth of both the amorphous and crystalline phases, atomic hydrogen is thought to preferentially etch the disordered amorphous phase rather than the crystalline phase on the surface, resulting in films with nanocrystals and voids that are not filled by a-Si:H [270].

However, using solely those surface models cannot explain experimentally observed low-temperature (around 200 to 250 °C) solid-phase crystallization of a-Si:H by post-deposition hydrogen plasma exposure. Specifically, by using the layer-by-layer deposition approach [271, 277] in which the a-Si:H deposition and hydrogen plasma were alternatively applied, the crystalline fraction of the film is increased and this crystallization is happening throughout the whole layer. This observation is explained by the chemical annealing model. That is, atomic hydrogen that penetrates the surface can diffuse in the Si network and lead to reactions, such as annihilating strained Si-Si bonds [260, 278], inserting into strained Si-Si bonds [273], breaking Si-H bonds and releasing energy [271, 279]. Consequently, those hydrogen-mediated cross-linking reactions can promote the rearrangement of the atomic structure and result formation of a crystallized network.

Apart from the abovementioned radicals and atomic hydrogen, energetic SiH_x^+ and H^+ ions, which drift to the surface of the growing film, can impact the growth of nc-Si:H [280]. It was observed that when depositing nc-Si:H layers on glass substrates, deposition conditions with a lower ion bombardment can result in a fully crystallized bulk likely due to reduced amorphization by energetic heavy SiH_x^+ ions [264]. However, there was an amorphous interlayer with the glass substrate. On the other hand, this initial amorphous layer disappeared when the film was deposited under high ion bombardment conditions. Here, the direct growth of nanocrystals on the glass substrate is ascribed to the more effective H^+ ion implantation, which leads to higher hydrogen content needed for nucleation at the initial growing phase [280]. Moreover, it is also reported that higher ion energy resulted in small-sized nanocrystals (a few nanometers) embedded in the porous and hydrogen-rich film, while smaller ion energy enabled larger grain sizes [229].

Notably, aside from growing nanocrystals via surface and/or bulk reactions as discussed previously, studies have indicated that the nanocrystals can be synthesised in plasma, resulting in direct nanocrystal deposition on the substrate [274, 275]. To allow the efficient generation of silicon nanocrystals in the plasma, the deposition conditions, such as pressure (or partial pressure of SiH_4), power and gas precursor compositions, need to be optimized. The optimized conditions should aim to increase the number of growth species (e.g. radicals) and enhance their residence time in the plasma [281, 282]. These together facilitate the formation of higher-order silane molecules (e.g. Si_2H_x, Si_3H_x), which serve as precursors for the generation of nanocrystals [283]. Subsequently, these higher-order silanes can accumulate and agglomerate, giving rise to the formation of nanocrystals. The presence of atomic hydrogen is reported to be crucial for the crystallization of the amorphous silicon cluster in the gas phase [284]. As these plasma-synthesised silicon nanocrystals can be positively charged, they can be accelerated towards the substrate, potentially leading to amorphization of the surface of the growing film. Therefore, it is crucial to ensure a soft landing of these nanocrystals on the substrate, not only to prevent amorphization of the already deposited film but also to preserve the structural integrity of these nanocrystals after landing [285]. As demonstrated in previous studies, this can be achieved by tuning the bias voltage and the substrate temperature [286, 287]. It is worth noting that the deposition conditions, which enable the formation of plasma-synthesised nanocrystals, are close to (or in the early stage of) the powder formation plasma regime (high power and high pressure). Precise control of the process, thereby avoiding detrimental powder formation, is necessary for obtaining high-quality films [281, 283].

To summarize, the growth of nc-Si:H layers involves mainly radicals, ions, atomic hydrogen and plasma-synthesised nanocrystals (if applicable), which allow the realization of materials with varied opto-electrical properties by tuning the deposition conditions. Comprehending the growth mechanisms of both a-Si:H and nc-Si:H layers assists in optimizing these layers with desired properties for their applications in SHJ solar cells.

2.4.3 Doped a-Si:H, nc-Si:H and nc-SiO_x:H

Despite the abovementioned intrinsic a-Si:H and nc-Si:H, doped layers with higher conductivities are often required to contribute to the selective transport of charge carriers as

discussed in Section 2.3. Both (*n*)-type and (*p*)-type a-Si:H and nc-Si:H can be prepared by adding the precursor gases containing, typically, phosphorus and boron during their depositions, respectively [152, 241, 288, 289]. The doping mechanism is commonly explained according to the autocompensation model [290], which reveals the unavoidable formation of dangling bonds when doping a-Si:H. As reported, dark conductivities (σ_d) of around 10^{-2} S/cm were achieved for both (*n*)- and (*p*)-type a-Si:H, whereas the optimized (*n*)-type layer exhibited a slightly higher optimized σ_d as compared to the (*p*)-type counterpart [241]. The corresponding minimum E_a is around 150 meV for (*n*)-type a-Si:H and approaching 200 meV for (*p*)-type a-Si:H [152, 241]. Further reduction of the E_a is hardly achievable, partially because the doping efficiency, which is the fraction of dopant atoms in fourfold coordination (active dopant atoms) over total dopant atoms, generally decreases with increasing dopant contents [290, 291].

With respect to efficient selective transport of charge carriers, nc-Si:H can feature more favorable electrical properties (e.g., lower achievable E_a) than doped a-Si:H. Thanks to the embedded nanocrystals, doped nc-Si:H layers allow higher doping efficiency than that of doped a-Si:H layers [291]. Typical optimized doped nc-Si:H can exhibit σ_d well above 1 S/cm and 10 S/cm for (*p*)-type and (*n*)-type layers, respectively, with values of E_a that are well below 100 meV [292, 293]. Excessive incorporation of doping gas precursors (e.g., diborane (B_2H_6) and phosphine (PH_3)) can result in the amorphization of the deposited films [293, 294]. Besides, hydrogen, which is more relevant for the growth of nc-Si:H, can also induce possible dopant passivation or dopant deactivation [295–297]. It is worth mentioning that unlike a-Si:H, due to the confirmed anisotropy properties in the growth direction of nc-Si:H layers [225, 298, 299] (see also Figure 2.10), these nc-Si:H layers can feature different conductivities in vertical and lateral directions.

When deploying doped nc-Si:H as the window layer of SHJ solar cells, it usually induces less parasitic absorption as compared to the a-Si:H mainly due to its lower absorption coefficients, especially, in the short wavelength range (around $\lambda < 600$ – 700 nm) [173]. Further reduction of parasitic absorption is possible by using oxygen–alloyed nc-Si:H (nc-SiO_x:H), which features further enhanced transparency while (potentially) maintaining good conductivity [173]. Besides, nc-SiO_x:H also has tunable opto-electrical properties by adjusting the deposition conditions, for example, by varying the CO_2 and H_2 flows during depositions [300]. This feature also allows one to tailor the selective transport of charge carriers with high flexibility [150].

2.4.4 Key aspects of their applications for SHJ solar cells

With respect to the applications of both a-Si:H and nc-Si:H layers into SHJ solar cells, the following aspects should be considered.

c-Si surface orientation: optimizing (*i*)a-Si:H passivating layer for (100) vs (111) orientations

For typical FBC-SHJ solar cells, c-Si wafers are double-side-textured mainly for improving the light management of solar cells. With respect to its application for 2-terminal (2T) perovskite/c-Si tandem solar cells, c-Si bottom sub-cells with a front-side-flat and rear-side-textured (single-side-textured, SST) morphology are often employed for de-

positing on their top solution process-based perovskite sub-cells. It should be noted that researchers have also successfully showcased efficient 2T tandem solar cells with solution-processed perovskite on double-side-textured c-Si bottom sub-cell [301]. In this thesis, SST <100> c-Si wafers were prepared with (100)-oriented flat front surface and (111)-oriented textured rear surface. Therefore, passivation optimizations of both surfaces are necessary for achieving high-efficiency single-junction and tandem applications.

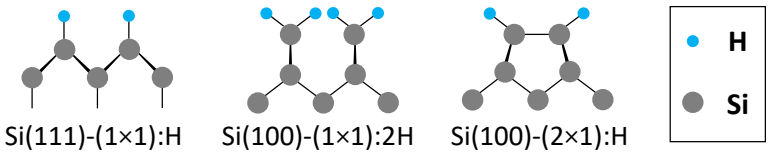

Figure 2.9: Schematic sketches of hydrogenated structures present on Si(111) and Si(100) surfaces. Figure adapted from [302, 303].

As compared to (111)-oriented surface, the passivation of (100)-oriented flat c-Si surface is rather challenging as it is prone to result in detrimental epitaxial growth, especially, when depositing high hydrogen diluted (*i*)a-Si:H layers [303–307]. Although it is still elusive to explain this difference between the (100) and (111) surfaces, possible origins are discussed here. Schematic illustrations of ideal c-Si surfaces with different orientations are given in Figure 2.9. As seen in Figure 2.9, (111) surface features one exposed bond and three back bonds per Si atom, while (100) surface has two exposed bonds and two back bonds per Si atom. For (100)-oriented surface, two bonds need to be formed for each atom of the growing film. That is, there is no rotation freedom for the bonded atom and thus benefiting the crystalline growth. While (111) surface allows a mono-layer bonded by a single back bond, which features rotation freedom and promotes the formation of the amorphous phase [306, 307]. Besides, as a result of two hydrogen-terminated bonds per surface atom for (100) surface instead of only one per surface atom for (111) surface, possible longer surface diffusion of radicals can facilitate crystal formation on (100) surface [307]. Moreover, as discussed in [303], an ideal (100) surface can easily form unique dimer bonds (see Figure 2.9, Si(100)-(2×1):H) and epitaxial growth happens as long dimer strings, which are perpendicular to the surface.

Substrate- and thickness-dependent growth of nc-Si:H

Typically, the growth of nc-Si:H layers, or the evolution of their compositions (nanocrystals and amorphous phase) depends on the nature of the substrate and the thickness of the nc-Si:H layer [176–178]. As reported by Roca i Cabarrocas, et al., [176], before the growth or nucleation of nanocrystals in the film, an amorphous incubation phase (around 15 nm) was first formed when depositing the nc-Si:H layer on the glass substrate. The gradual increment of the volume fraction of nanocrystals was seen after the nucleation with increasing film thickness and reached the steady state with a thickness of around 100 nm. Moreover, for a substrate coated with a-Si:H, the growth of nanocrystals was hardly observed even with a 100-nm-thick film deposited. Interestingly, the

amorphous incubation phase was mitigated by directly depositing the nc-Si:H layer on a c-Si substrate.

As discussed in works of literature [176, 263, 308], the transition from the amorphous incubation phase to the nucleation of the nanocrystals is assisted by a highly porous and hydrogen-rich layer. Indeed, such a transitional layer could promote structure relaxation mediated by the diffusion of hydrogen in the film, thus facilitating the formation of the crystallites. The proceeding growth of nanocrystals is then favored thanks to those existing crystallites. Therefore, various substrates that can affect differently the initial growth of the film are expected to result in either prompt or delayed nucleation of nanocrystals. Similar reasons can be applied to explain the thickness-dependent growth of nc-Si:H layer.

Overall, those substrate- and thickness-dependent growth characteristics of nc-Si:H layers become critically relevant when applying them in SHJ solar cells, which feature (*i*)a-Si:H passivating layer and might require limited thicknesses of nc-Si:H layers for the optimum device performance. Therefore, in this thesis, efforts have been devoted to facilitating fast nucleation of nanocrystals, which enable efficient band bending near the c-Si surface.

Microstructure of a-Si:H and nc-Si:H (nc-SiO$_x$:H) in SHJ solar cells

The microstructures of typical a-Si:H applied in SHJ solar cells are schematically depicted in Figure 2.10. As seen in Figure 2.10, a-Si:H layer (free from epitaxial growth) consists of three main components [309]. Starting from the substrate to the free surface, they are (i) the interface layer (around 1 to 2 nm) that is hydrogen-rich and highly porous, or also referred to as the Si-H_2 interface layer [309–311], (ii) the bulk layer that contains less hydrogen and is more compact than the interface layer as Si-H is the more dominant hydrides [262, 309, 311] and (iii) the surface layer (around 1 to 2 nm) with a high hydrogen content and void-rich (more fraction of Si-H_2 or Si-H_3 as compared to the bulk) [262, 309, 310]. Therefore, for SHJ solar cells that have relatively thin (*i*)a-Si:H (usually not thicker than 10 nm [312]), not only the microstructure properties of the bulk component but also that of the interface and the surface components are important for understanding the performance of the device. Especially, those microstructure properties can be tuned or affected by adjusting deposition conditions [313] or applying post-deposition plasma treatment [175].

Subsequential growth of doped nc-Si:H (nc-SiO$_x$:H) layer on (*i*)a-Si:H, applicable to this study, is also schematically drawn in Figure 2.10. As outlined in Section 2.4.2, nanocrystals can be produced via various mechanisms. Based on the microstructural characterization results presented in Chapter 6, we can dismiss the (insignificant) contribution of plasma-synthesized nanocrystals, as no instant nanocrystal growth on (*i*)a-Si:H layer was observed. Therefore, considering previously discussed substrate- and thickness-dependent growing characteristics of nc-Si:H (nc-SiO$_x$:H), their growth model consists of [176, 264]: the amorphous incubation layer, the nucleation phase of crystallites, the bulk layer with growing nanocrystals until reaching stationary growth, the surface layer including growth zone and surface roughness. Due to the amorphization induced by the impinging of energetic ions, the growth zone features slightly smaller nanocrystals and a higher amorphous fraction than the top surface of the bulk layer.

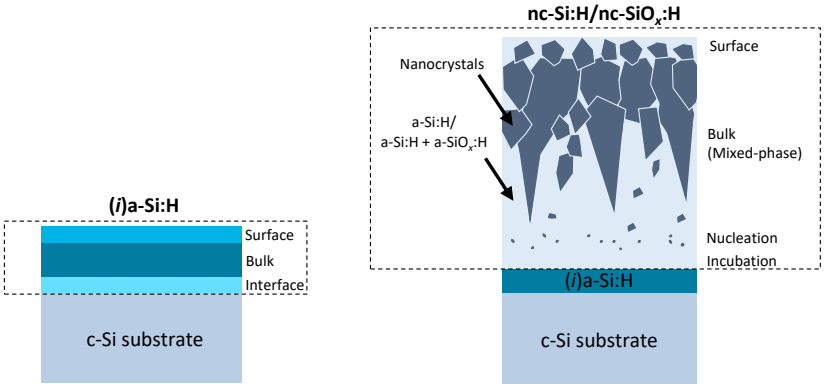

Figure 2.10: Schematic illustrations of (*i*)a-Si:H (left) and nc-Si:H/nc-SiO$_x$:H (right) deposited on c-Si and (*i*)a-Si:H passivated c-Si, respectively. The growth model presented for nc-Si:H/nc-SiO$_x$:H layers is representative of those prepared in this work. Figures adapted from [264, 309, 322].

The microstructure and the corresponding opto-electrical properties of nc-Si:H-based layers depend on the deposition conditions such as plasma excitation frequency [163, 314, 315], gas precursors [166, 173, 316], substrate temperature [163, 317, 318], power and pressure [170, 229, 319], and also importantly, the microstructural properties of the substrate modified by plasma treatment [312, 320, 321]. Understanding the microstructures of nc-Si:H layers underscores the significance of finely adjusting their deposition conditions and potentially applying pre- or post-deposition treatments, which are crucial to achieve layers with desired opto-electrical properties for SHJ solar cells. Furthermore, this understanding also plays a key role in comprehending the *J*-*V* characteristics of SHJ solar cells.

2.5 Conclusions

In this chapter, we briefly presented the fundamentals of the physics of SHJ solar cells. We first introduced carrier generation and recombination and highlighted the importance of minimizing surface recombination for SHJ solar cells. Then, typical architectures of FBC-SHJ solar cells were mentioned and compared. Through discussions on the mechanisms of selective transport and collection of charge carriers, we pointed out the preferred implementation of nc-Si:H-based contact stacks for high-efficiency SHJ solar cells. Subsequently, the microstructure, growth mechanisms and opto-electrical properties of a-Si:H and nc-Si:H-based layers were introduced. Lastly, we discussed the key aspects of applying both a-Si:H and nc-Si:H-based layers for high-efficiency SHJ solar cells, which are related to the device performance in terms of the passivation, selective transport of charge carriers and light management.

3

Experimental

In this chapter, the experimental process and tools used for the fabrication of FBC-SHJ solar cells are introduced first. Afterwards, we present the main characterization techniques utilized for thin-film layers and devices, where the latter can be dedicated samples for evaluating passivation quality, contact resistivity or solar cell performance.

3.1 Experimental process and equipment

3.1.1 Process flows for single-junction FBC-SHJ solar cells and bottom sub-cells for monolithic 2T perovskite/c-Si tandem solar cells

An overview of process flows for FBC-SHJ solar cells is presented in Figure 3.1. For fabricating FBC-SHJ solar cells as sketched in Figure 3.1 (b), we used 4-inch Topsil (*n*)-type double-side-polished float-zone (FZ) <100>-oriented c-Si wafers, which are 280 ± 20-µm thick with resistivities of 3 ± 2 $\Omega \cdot$ cm. To prepare double-side-textured (DST) FBC-SHJ solar cells, both sides of those wafers were randomly textured by diluted tetramethylammonium hydroxide (TMAH) solution with ALKA-TEX (GP Solar GmbH) as additives [323]. Then, those wafers were cleaned by sequentially dipping them into 99% room-temperature nitric acid (HNO_3), 69.5% 110 °C HNO_3, and then 0.55% hydrofluoric acid (HF) [324]. All Si-based thin-film layers were deposited via a multi-chamber radio-frequency (RF, 13.56 MHz) or very-high-frequency (VHF, 40.68 MHz) plasma-enhanced chemical vapor deposition (PECVD) cluster tool (Elettrorava S.p.A.). Besides, additional hydrogen plasma treatment (HPT) and VHF treatment were optionally applied on (*i*)a-Si:H layers (before depositions of doped Si layers). During PECVD depositions, we first deposited (*i*)a-Si:H/(*n*)-layer stack. Then with a short vacuum break, wafers were flipped for subsequent depositions of (*i*)a-Si:H/(*p*)-layer stack. After PECVD, RF magnetron sputtering (Polyteknic AS) was used for depositing TCO layers, such as ITO and tungsten-doped indium oxide (IWO) [325] on both sides of the wafers. For wafers that feature TCO layers deposited at room temperature, they were annealed in air at 180 °C for 5 minutes. Eventually, solar cells were finished with different metallization approaches, namely, Ag screen printing, Ag evaporation and

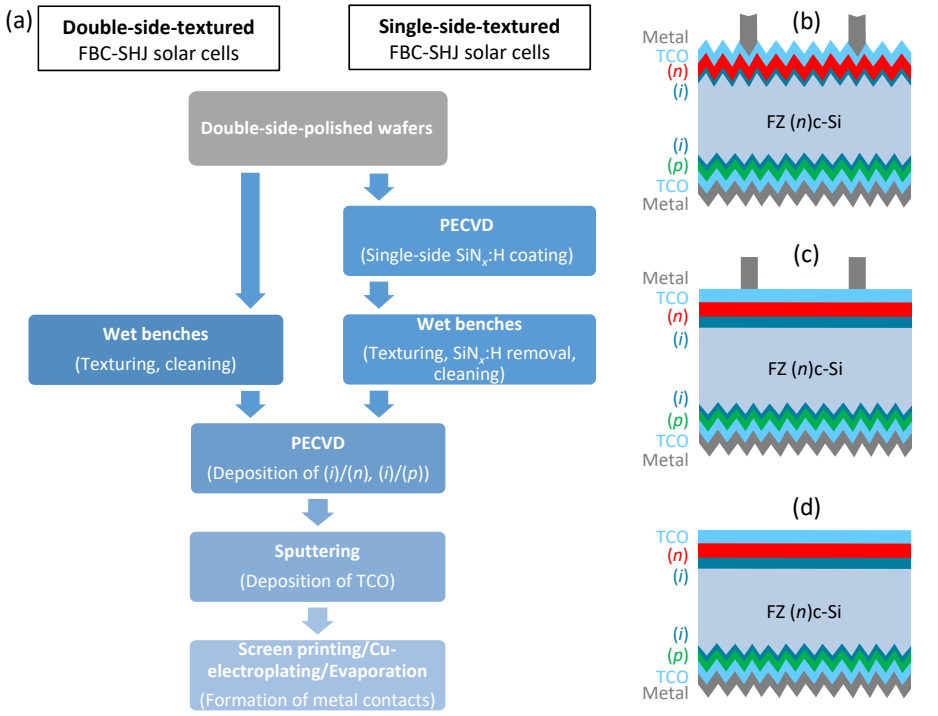

Figure 3.1: The (a) process flows and schematic sketches of (b) double-side-textured, (c) single-side-textured FBC-SHJ solar cells and (d) single-side-textured bottom sub-cells for monolithic 2T perovskite/c-Si tandem solar cells. In all sketches, *r*epresents (*i*)a-Si:H, (*n*) refers to (*n*)a-Si:H, (*n*)nc-Si:H, (*n*)nc-SiO_x:H or their possible combinations, (*p*) corresponds to (*p*)a-Si:H, (*p*)nc-Si:H, (*p*)nc-SiO_x:H or their possible combinations. In (b) – (d), the devices can be either in rear junction or front junction configuration.

Cu-electroplating. Unless otherwise stated, solar cells with screen-printed Ag contacts went through a curing step in the air at 170 °C for 40 to 45 minutes. Alternatively, cells can feature an electroplated Cu front grid and a 500-nm-thick thermally evaporated Ag rear electrode [127]. To further improve the anti-reflection effect of solar cells, a 100-nm-thick SiO_x layer was optionally deposited via e-beam evaporation on the front side of the devices. A geometrical factor of 1.7 was used for calculating the deposition durations for the textured surface based on the depositions on flat substrates. Single junction c-Si solar cells fabricated in this thesis have designated areas ranging from 4 cm^2 to 7.84 cm^2.

While to make single-side-textured (SST) FBC-SHJ solar cells (see Figure 3.1 (c)), we first deposited PECVD (Novellus Systems Inc.) grown SiN_x:H on one side of polished c-Si wafers. As SiN_x:H is comparatively etching-resilient to diluted TMAH solution, the bare c-Si side that is not covered with SiN_x:H was randomly textured. Afterwards, wafers were dipped into a buffered-HF (BHF) solution to completely remove the SiN_x:H. This

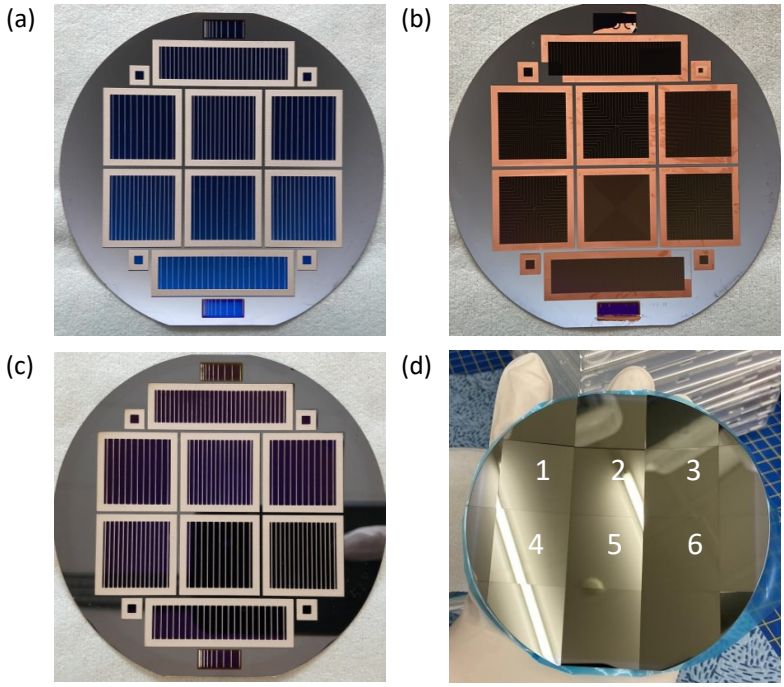

Figure 3.2: The front side of fabricated wafer samples that include (a) screen-printed double-side-textured, (b) front electroplated double-side-textured and (c) screen-printed single-side-textured FBC-SHJ solar cells, and (d) diced single-side-textured bottom sub-cells for monolithic 2T perovskite/c-Si tandem solar cells.

produced single-side-textured wafers that feature one side (100)-oriented flat surface and the other side (111)-oriented textured surface. Subsequent Si-based thin-film layer depositions, TCO sputtering and metallization were similar to that of DST FBC-SHJ solar cells.

To prepare bottom sub-cells for monolithic 2T tandem solar cells, SST solar cells were completed with a front ITO layer (around 30-nm-thick) (see Figure 3.1 (d)). Later, the wafers were diced into 2.5 cm × 2.5 cm-sized samples with Disco DAD321 (Figure 3.2) prior to deposition of perovskite top sub-cells. The fabricated monolithic 2T tandem solar cell features a designated area of 1 cm^2.

The fabricated DST, SST FBC-SHJ solar cells and SST bottom sub-cells for tandem devices are shown in Figure 3.2.

3.1.2 Main manufacturing tools for SHJ solar cells

Plasma-Enhanced Chemical Vapor Deposition

As shown in Figure 3.3, a multi-chamber Plasma-Enhanced Chemical Vapor Deposition (PECVD) cluster tool (Elettrorava S.p.A.) was used for depositing Si-based thin-film layers and applying HPT treatments. To minimize cross-contamination, the system fea-

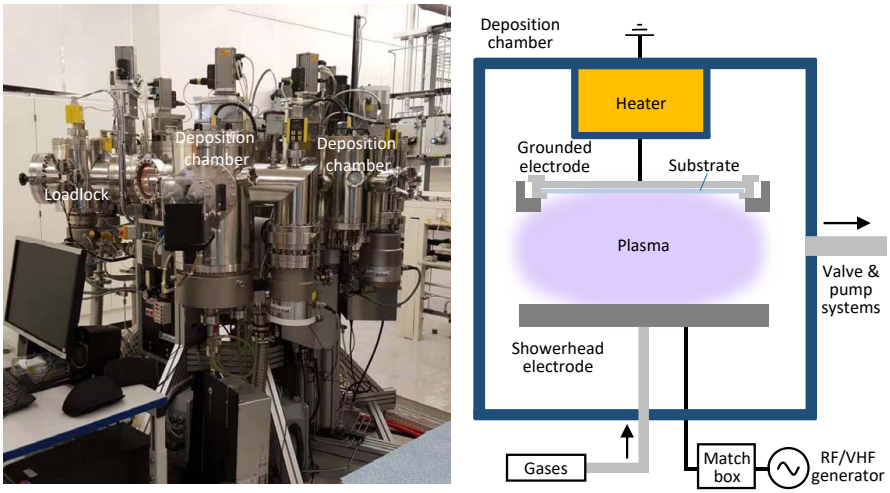

Figure 3.3: The photo of the PECVD (or so-called AMIGO) cluster tool and the schematic sketch of the deposition chamber. Note that for the deposition chamber equipped with the VHF generator, there is an additional heater beneath the bottom showerhead electrode. Photo credit: Dr. Yuan Gao. The schematic sketch is adapted from [326].

tures dedicated deposition chambers for individually depositing intrinsic, (*n*)-type and (*p*)-type materials. A schematic representation of the deposition chamber is provided in Figure 3.3. As seen in the sketch, after loading and pre-heat the sample (substrates are often heated up to 160 °C to 180 °C) in the deposition chamber, various precursor gas mixtures are supplied via the bottom showerhead electrode, which features a dimension of 12 × 12 cm^2. When both the gas mixtures and the pressure have stabilized, the RF/VHF generator supplies power to accelerate and energize electrons between two parallel capacitively coupled electrodes. Electrons with enough energy can dissociate the precursor gas molecules by collisions, forming reactive radicals, ions and other species. Eventually, radicals can diffuse to the surface of the growing film while positive ions can diffuse to the plasma sheath and be further attracted to the substrate. In this thesis, for the deposition of (*i*)a-Si:H, silane (SiH_4) or hydrogen-diluted silane (H_2 and SiH_4) was used. Doping gases such as phosphine (PH_3) or diborane (B_2H_6) were additionally added for forming (*n*)-type or (*p*)-type Si-based thin-film layers, respectively. Besides, those layers were further alloyed with oxygen by supplying carbon dioxide (CO_2) into the deposition chamber. While to obtain the optimized material properties (e.g., passivation quality, opto-electrical properties) of each layer, the deposition parameters such as power density, pressure, substrate temperature and gas compositions need to be adjusted accordingly and these parameters are listed in the following individual chapters.

Radio-frequency Magnetron Sputtering

The radio-frequency (RF) magnetron sputtering system from Polyteknic AS (see Figure 3.4) was used for depositing TCO layers. Argon (Ar), an inert gas, is used as the sputtering gas. As seen in Figure 3.4, Ar atoms that are injected into the deposition chamber can be

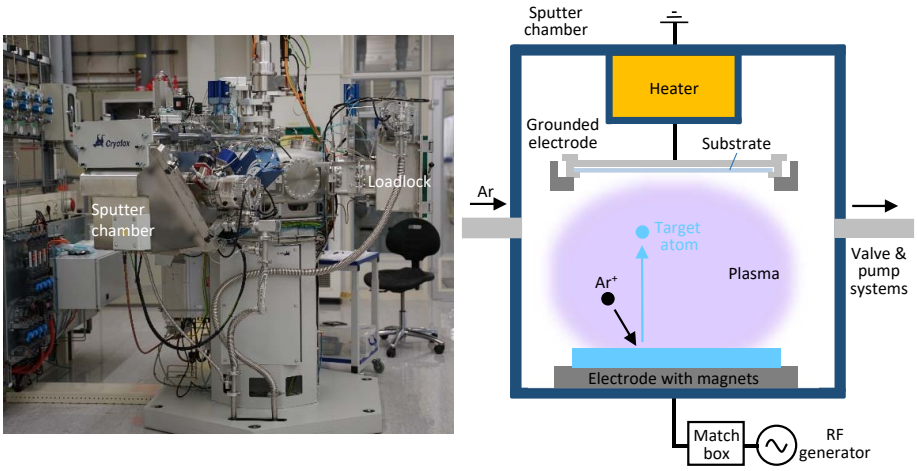

Figure 3.4: The photo of the RF magnetron sputtering system (or so-called ZORRO) and the schematic sketch of the deposition chamber. Photo credit: Dr. Yuan Gao. The schematic sketch is adapted from [326].

ionized by energetic electrons when RF power is applied. The positively charged Ar^+ ions accelerate to the target (cathode) and eject target atoms due to collisions. Those released target atoms with enough kinetic energy can eventually diffuse to the substrate (anode) and contribute to film growth. The magnets placed behind the target are to confine electrons to be close to the surface of the target, and so does the plasma. This results in an increased probability of ionizing Ar atoms, which improves the deposition rate of the sputtering process and also the quality of the deposited films. In this thesis, we used a 4-inch ITO target that contains 90 wt% In_2O_3 and 10 wt% SnO_2, and a 4-inch IWO target that consists of 95 wt% In_2O_3 and 5 wt% WO_3 [325]. The ITO films were prepared at elevated substrate temperatures of around 100 °C to 110 °C, while the IWO films were deposited at room temperature [325, 327, 328].

Metallization: Ag screen printing, Cu-electroplating and Evaporation

Screen printing which is well-established and dominant in the current PV industry is also the main metallization approach for our solar cell optimizations. To form metal contacts by screen printing, a squeegee first sweeps a viscous metallic paste over the screen surface and prints the paste on the substrate through the openings of the screen, then followed by a curing process at elevated temperatures. The screen is constructed with an interwoven thin-wire mesh that is coated with a micro-coating emulsion layer and features designated openings for patterning the metal contacts. The printed finger width is often limited to a minimum of around 20 to 30 µm [329]. In this thesis, we used low-temperature Ag paste from DuPont and the screen produced by KOENEN GmbH. More details on the screen printing setup utilized in the PVMD group can be found elsewhere [330].

Alternatively, Cu-electroplating is developed and utilized for forming ultra-fine metal fingers (width ≤ 15 µm) with low finger resistivity (typically 1.7 ± 0.1 $\mu\Omega \cdot$cm from Cu-

electroplating and 10.0 ± 5.0 μΩ · cm from Ag screen printing in our lab) [127, 331]. Besides, unlike the screen-printed Ag grid, the electroplated Cu grid appears to be void-free in the bulk and is conformal on the surface [127]. The working principle of Cu-electroplating is based on reduction-oxidation reactions. Both the wafer sample (cathode) and the sacrificing Cu sheet (anode) are immersed, usually, in a $CuSO_4$-based electrolyte. During the electroplating process, Cu is deposited on the wafer sample through the reduction reaction of Cu^{2+} ions. As Cu^{2+} ions are continuously consumed in the electrolyte, the sacrificing Cu sheet supplies Cu^{2+} ions via the oxidation reaction. In order to form desired grid patterns on the wafer, in this thesis, a full area of 100-nm-thick thermally evaporated Ag seed layer was first deposited on top of the TCO layer. Then, photolithography steps including applying photoresist, exposure and development were conducted to cover the area that is not intended to form the Cu grid with photoresist. After Cu-electroplating, the remaining photoresist and the underneath Ag seed layer were removed. Detailed descriptions of the Cu-electroplating process are available in our publications [127, 331]. Metal contacts obtained from both Ag screen printing and Cu-electroplating usually feature thicknesses of around 15 μm – 25 μm.

For cells with the electroplated Cu front grid, we thermally evaporated Ag as the seed layer (100-nm-thick) for conducting Cu-electroplating and as the rear electrode (500-nm-thick). The working principle of metal evaporation is to heat up the metallic source to above its melting point, then metal is evaporated and condensed back to the solid state on the substrate surface that features a lower temperature. For metals with low or high melting points, either thermal (resistive heating) evaporation or e-beam evaporation can be applied, respectively. For thermal evaporation, a tungsten boat that holds the metallic source is resistively heated up by applying a high current. While e-beam evaporation utilizes magnetically focused high-energy electrons to melt metals located in a water-cooled crucible. In this thesis, the Provac PRO500S system was used for metal evaporation. We used thermal evaporation for Ag and e-beam evaporation for Al deposition although Al features a relatively low melting point of 660.32 °C. This is to avoid possible alloying of Al with the tungsten boat. Last but not least, e-beam evaporation was also used for depositing a SiO_x layer (the melting point of SiO_2 is 1710 °C) for forming a double-layer anti-reflection coating (DLARC) with the TCO layer underneath.

3.2 Characterizations

3.2.1 Thin-film characterizations

For controlling the fabrication process of solar cells and understanding the device performance, the thickness, opto-electrical and microstructural properties of thin-films were characterized on dedicated samples prior to solar cell fabrication. Here, brief introductions on the techniques used for characterizing Si-based thin-films are provided. Detailed descriptions of TCO and metal characterizations are given in [332].

Optical Properties

Spectroscopic ellipsometry (SE) (M-2000DI system, J.A. Woollam Co., Inc.) was used for extracting information such as the thickness, refractive index and optical bandgap of thin-film layers deposited on either front-flat glass (Corning Eagle XG) or wafer substrates. SE is a contact-free optical measurement technique that detects the change of

the polarization state of a known polarized light when it is obliquely reflected from a sample [333]. Specifically, two wavelength-dependent values are measured, the amplitude ratio (Ψ) and the phase difference (Δ) between the p- (parallel to the plane-of-incidence) and s-polarized (perpendicular to the plane-of-incidence) light waves. The measured Ψ and Δ are defined by the ratio of the complex amplitude reflection coefficients (r_p, r_s) via [334]:

$$\rho \equiv \tan(\Psi) e^{i\Delta} \equiv \frac{r_p}{r_s} \tag{3.1}$$

where r_p and r_s are related to sample properties (e.g. complex refractive index) via Fresnel equations [333]. In most cases, an optical model is needed to fit the measured data to obtain the properties of the measured sample. The incident angle is often chosen to be close to the Brewster angle to maximize the difference between the r_p and r_s for better measurement sensitivity, and the Brewster angle is determined by the refractive indices of two adjacent materials [333]. In this thesis, for layer(s) deposited on the glass substrate, the incident angles were set to vary from 55° to 70° with 5° as the interval, while for layer(s) deposited on the c-Si substrate, the incident angles were 65°, 70° and 75°. For a-Si:H, the Cody-Lorentz dispersion model is mainly used. While for nc-Si:H-based materials, we used effective medium approximations (EMA) with Bruggeman analysis mode to describe the mixed amorphous and crystalline silicon phases of those materials [334]. A schematic sketch of the sample for SE measurements and an example of extracted optical constants (refractive index n and extinction coefficient k) are presented in Figure 3.5. The experimentally extracted optical constants of various layers were used as inputs for optical simulations.

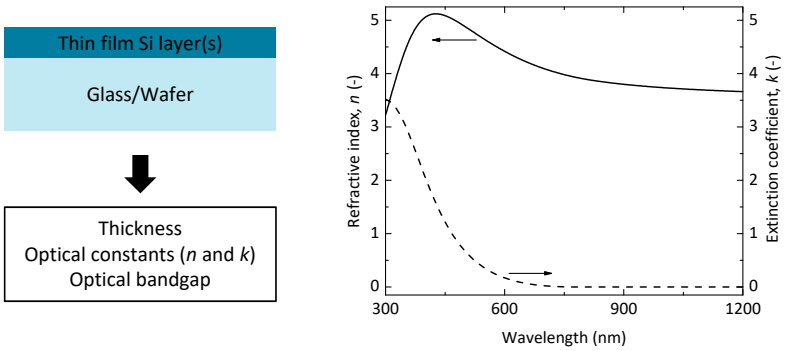

Figure 3.5: The schematic sketch of the sample for SE measurements (left) and the extracted optical constants of a typical (*i*)a-Si:H layer (right).

Alternatively, Steag ETA-Optik mini-RT was also used for extracting the optical properties of thin-film layers deposited on the glass substrate. The mini-RT setup consists of a halogen lamp, a monochromator and separate photodiodes for detecting the reflected and transmitted light. The measured wavelength-dependent reflectance (R) and transmittance (T) are fitted with the Scout software using a thin-film multi-layer model. The

O'Leary-Johnson-Lim (OJL) model was used to obtain the properties of Si-based thin-film layers, including thickness, optical constants (n and k) and bandgap (E_0) [335–337]. From both SE and mini-RT measurements, the absorption coefficient of the film can be calculated based on its extinction coefficient, which can be further used to determine the optical bandgap E_{04} of the film. The E_{04} is defined as the energy at which the absorption coefficient reaches 10^4 cm^{-1}.

Electrical Properties

Temperature-dependent dark conductivity (σ_d) measurements were conducted to extract the E_a of doped Si thin-film layers, which is insightful for understanding the selective transport of charge carriers as introduced in Section 2.3. The σ_d of a semiconductor is expressed as:

$$\sigma_d = q(n\mu_n + p\mu_p) \tag{3.2}$$

where q is the elementary charge; n and p are the density of electrons and holes under thermal equilibrium, respectively; μ_n and μ_p are the mobility of electrons and holes, respectively. It is known that both n and p are related to E_F as seen in equations 2.1 and 2.2, we can then substitute equations 2.1 and 2.2 into equation 3.2 and obtain under dark conditions ($n\mu_n \gg p\mu_p$ for (n)-type and $p\mu_p \gg n\mu_n$ for (p)-type):

$$\sigma_{d,n} = q\mu_n N_C \exp(\frac{E_F - E_C}{k_B T}) \qquad \text{for } (n)\text{-type} \tag{3.3}$$

$$\sigma_{d,p} = q\mu_p N_V \exp(\frac{E_V - E_F}{k_B T}) \qquad \text{for } (p)\text{-type} \tag{3.4}$$

From equations 3.3 and 3.4, it is apparent that σ_d is temperature-dependent. Under a certain temperature, the $\sigma_d(T)$ can be obtained by conducting dark I-V measurements:

$$\sigma_d(T) = \frac{dI}{tlV} \tag{3.5}$$

where d is the distance between electrodes, I and V are the measured current and applied voltage, respectively; t is the thickness of the deposited layer, l is the length of electrodes. By measuring the $\sigma_d(T)$ for a range of temperatures, then based on equations 3.3 and 3.4, the E_a can be obtained by:

$$\sigma_{d,n}(T) = \sigma_o \exp(\frac{E_F - E_C}{k_B T}) = \sigma_o \exp(-\frac{E_a}{k_B T}) \qquad \text{for } (n)\text{-type} \tag{3.6}$$

$$\sigma_{d,p}(T) = \sigma_o \exp(\frac{E_V - E_F}{k_B T}) = \sigma_o \exp(-\frac{E_a}{k_B T}) \qquad \text{for } (p)\text{-type} \tag{3.7}$$

where σ_o is the pre-exponential factor. Equations 3.6 and 3.7 can be rewritten as:

$$\ln(\frac{1}{\sigma_d(T)}) = E_a \frac{1}{k_B T} - \ln\sigma_o \tag{3.8}$$

A curve of $\ln(1/\sigma_d(T))$ over $1/k_B T$ can be drawn, then the slope of the fitted straight line indicates the E_a. In this thesis, samples as sketched in Figure 3.6 were prepared,

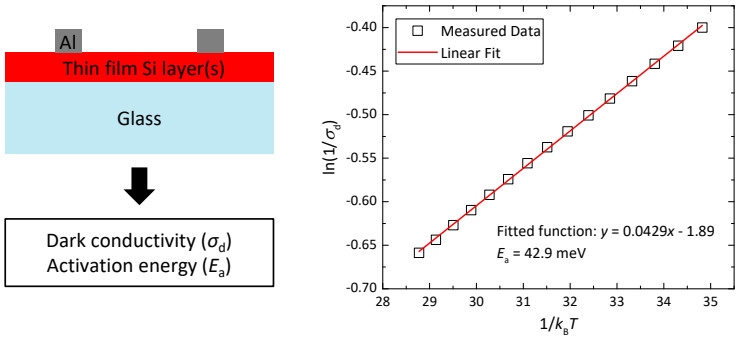

Figure 3.6: The schematic illustration of the sample structure used for temperature-dependent σ_d measurements (left) and the derivation of E_a for a typical (p)nc-Si:H layer (around 101-nm-thick) deposited on glass substrate (right). Note, doped Si thin-film layers can be deposited directly on glass substrates or on (i)a-Si:H-coated glass substrates.

where 300-nm-thick Al strips were evaporated on doped layers and were used as the contacts for the temperature-dependent I-V measurements (temperature swept from 130 °C to 60 °C). Depending on the σ_d of the doped layers, bias voltages of either 1 V, 10 V or 100 V was applied for more reliable measurements. Note, the extraction of $\sigma_d(T)$ for doped layers or (i)a-Si:H/doped layer stacks deposited on glass substrates, relied on the thickness of the doped layers, as it was anticipated that the current predominantly travels through the doped layers. It is worth noting that the derived E_a might be overestimated, or the σ_d might be underestimated, particularly in the case of very thin (e.g. below 20 nm) doped layer (stack) deposited on an (i)a-Si:H layer. This is primarily because of: (i) the band bending formed between (i)a-Si:H and doped layer (stack), leading to an overestimation of extracted E_a compared to the E_a of the bulk of the doped layer (stack); (ii) the current can pass through the (i)a-Si:H layer when the doped layer (stack) is of similar σ_d as that of (i)a-Si:H layer. As the doped layer (stack) increases in thickness, the impact from the (i)a-Si:H layers diminishes. On the other hand, in cases where the doped layer (stack) features microstructural inhomogeneity across its thickness, such as nc-Si:H-based layer (see Figure 2.10), the extracted E_a and σ_d may not accurately represent the properties of the entire layer (stack). Especially, the electrical properties of nc-Si:H-based layers in vertical directions, which are more relevant in solar cell applications, can differ from those properties derived from coplanar measurements. Nevertheless, this characterization approach still serves as a practical and valuable method for evaluating the electrical properties of doped layers, providing insights into the performance of solar cells throughout this thesis. An example plot is provided in Figure 3.6.

Microstructural Properties

Fourier transform infrared (FTIR) spectroscopy (Thermo Scientific Nicolet 5700 in the transmittance mode) was utilized for assessing the Si-H bonding configurations of (i)a-Si:H layers, which may be related to their passivation capabilities and impact the transport of charge carriers in solar cells. FTIR measures the infrared spectrum of the sample that usually features characteristic absorption peaks originating from vibrations of

bonds in the material. During the measurement, broadband IR radiation is emitted and enters the interferometer. Within the interferometer, the IR beam is directed to the beamsplitter, which splits the beam into two beams. One beam is reflected off of a fixed mirror and another one is reflected off of a movable mirror. Afterwards, the split IR beams reach back to the beamsplitter and recombine. The movement of the movable mirror causes optical path differences between the split beams, thus resulting in interference (wavelength-dependent and covers the full infrared spectrum that comes from the source) on the recombined beam. Later, this beam is further directed to the sample and reaches the detector. The obtained interferogram (time-domain) is eventually Fourier-transformed into a transmittance spectrum that is a function of the frequency (wavenumber, ω). From the FTIR measurement, the absorption coefficient ($\alpha(\omega)$) can be determined from the transmittance ($T(\omega)$) via:

$$\alpha(\omega) = -\frac{\ln(T(\omega))}{t} \tag{3.9}$$

where t is the thickness of the film. Then for a certain absorption peak, the integrated absorption or the absorption strength (I) can be obtained with [338]:

$$I = \int (\frac{\alpha(\omega)}{\omega}) \mathrm{d}\omega \tag{3.10}$$

For (i)a-Si:H, a microstructure factor (R_{SM}) that is defined for Si-H stretching modes (SM) can be extracted as [339]:

$$R_{\mathrm{SM}} = \frac{I_{\mathrm{HSM}}}{I_{\mathrm{LSM}} + I_{\mathrm{HSM}}} \tag{3.11}$$

where LSM and HSM stand for low-frequency SM (at 1980 – 2010 cm^{-1}) and high-frequency SM (at 2070 – 2100 cm^{-1}), respectively [223, 338, 340]. Further, we calculated the hydrogen content (C_{H}) of the film as the following:

$$C_{\mathrm{H}} = \frac{N_{\mathrm{H}}}{N_{\mathrm{Si}}} = \frac{I_{\mathrm{LSM}} A_{\mathrm{LSM}} + I_{\mathrm{HSM}} A_{\mathrm{HSM}}}{N_{\mathrm{Si}}} \tag{3.12}$$

where N_{H} and N_{Si} (5×10^{22} cm^{-3}) are the atomic density of H and Si atoms, respectively. A_{LSM} and A_{HSM} are proportionality constants with approximately $A_{\mathrm{LSM}} = (9.0 \pm 1.0) \times 10^{19}$ cm^{-2} and $A_{\mathrm{HSM}} = (2.2 \pm 0.2) \times 10^{20}$ cm^{-2} [338]. Similarly, C_{H} can be also extracted via absorption peak due to Si-H wagging-rocking mode (W-RM) with $A_{\text{W-RM}}$ and $I_{\text{W-RM}}$ [338]. As discussed in Chapter 7, only relative comparisons among samples are given for double-side-textured samples.

In this thesis, we used single-side-flat Siegert Czochralski (Cz) <100> c-Si wafers with thicknesses of 525 ± 20 µm and resistivities of 15 ± 5 $\Omega \cdot$cm unless otherwise stated. To gain more insights into the properties of (i)a-Si:H layers deposited with cell-relevant conditions, samples with different structures as sketched in Figure 3.7 were prepared. As for the optimization of (i)a-Si:H on the flat (100)-oriented surface, around 30-nm-thick (i)a-Si:H layers were deposited on the flat (100)-oriented surface. While for the optimization of (i)a-Si:H for double-side-textured solar cells, those FTIR wafers were textured

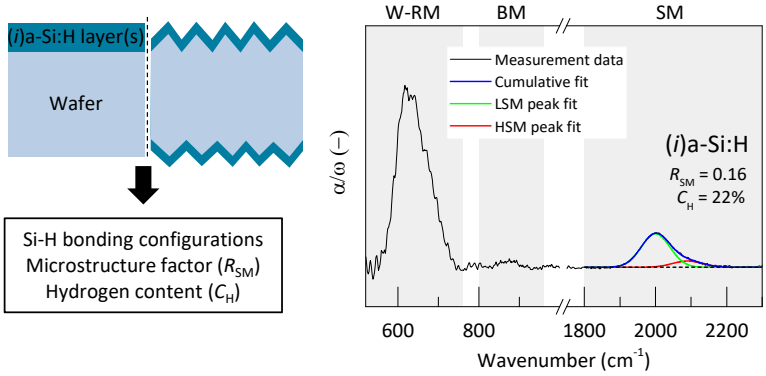

Figure 3.7: Schematic sketches of sample structures for FTIR spectroscopy measurement (left) and an example infrared spectrum of an (*i*)a-Si:H layer deposited on flat (100)-oriented surface (right). In the infrared spectrum plot, the W-RM stands for Si-H wagging-rocking modes, BM refers to Si-H polyhydrides bending modes, SM represents Si-H stretching modes. In the SM region, the green and red dashed lines represent the fitted Gaussian function for LSM and HSM, respectively. The blue solid lines are the overall fittings.

on both sides and symmetrically coated with (*i*)a-Si:H layers. For those double-side-textured samples, instead of being quantitatively analyzed as flat samples, only relative comparisons were made (discussed in Chapter 7). All samples were measured with a wavenumber range of 4000 cm^{-1} to 400 cm^{-1} and with a resolution of 2 or 4 cm^{-1}. An example infrared spectrum of an (*i*)a-Si:H layer deposited on a flat (100)-oriented surface is shown in Figure 3.7. Besides, the Si-H W-RM (at around 640 cm^{-1} [338, 341, 342]), Si-H polyhydrides bending mode (BM) (at around 880 cm^{-1} [343]) and Si-H SM modes (at around 2000 cm^{-1} and 2090 cm^{-1} [223, 338, 340]) that are most relevant for an (*i*)a-Si:H layer are also highlighted in Figure 3.7.

Raman spectroscopy (Renishaw inVia Micro-Raman Microscopy) was deployed for obtaining the crystallinity of doped Si thin-film layers, especially, the nc-Si:H-based layers. Raman spectroscopy relies on Raman scattering or inelastic scattering of the photons that results in frequency shifts of scattered photons as compared to the excitation frequency of incident photons. Depending on the energy transfer between the lattice and the scattered photon, the frequency shift can be classified as Stokes shift (or downshift, where the scattered photon loses energy and the lattice gains energy in the form of a phonon) and anti-Stokes shift (or upshift, where the scattered photon gains energy by absorbing a phonon from the lattice). During the measurement, a monochromatic laser beam is directed to and focused on the sample. In the meanwhile, reflected light and scattered light pass through filters, which ensure only frequency-shifted scattered photons are eventually fed into the detector. The Raman spectra of c-Si and a-Si:H show characteristic transverse optical (TO) peaks at near 520 cm^{-1} and 480 cm^{-1}, respectively [344, 345]. Due to the mixed phase composition of nc-Si:H-based materials, their typical spectrum consists of crystalline silicon peaks (510 cm^{-1} and 520 cm^{-1}) that are superimposed on a broad amorphous silicon peak (480 cm^{-1}). The crystalline fraction (F_C) can be extracted by [346]:

$$F_C = \frac{I_{510} + I_{520}}{I_{510} + I_{520} + I_{480}} \tag{3.13}$$

where I_x represents the integrated area of the Gaussian fitting peak centred at x cm^{-1}. More detailed discussions on the extraction of F_C from the Raman spectrum can be found elsewhere [346–348]. In this thesis, Si thin-film layers were deposited on glass substrates and a green laser (λ_{laser} = 514 nm) was used for Raman spectroscopy measurements. The penetration depths of the laser light are in the order of hundreds of nanometers for typical nc-Si:H-based layers fabricated in this thesis. An example Raman spectrum of a (*p*)nc-Si:H layer is presented in Figure 3.8.

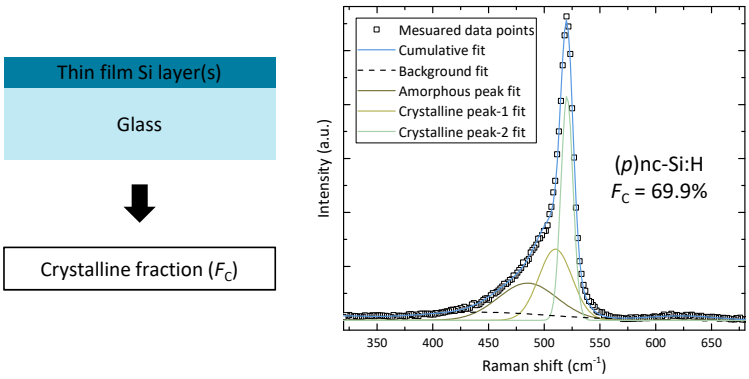

Figure 3.8: The schematic sketch of the sample structure for Raman spectroscopy measurement (left) and an example Raman spectrum of a (*p*)nc-Si:H that features an extracted crystalline fraction (F_C) of 69.9% (right). In the Raman spectrum plot, the fitting of the background, amorphous peak and two crystalline peaks are illustrated. The crystalline peak-1 and crystalline peak-2 refer to the peaks centred at around 510 cm^{-1} and 520 cm^{-1}. The background fit is the sum up of four other Gaussian distributions that are related to transverse acoustic (TA), longitudinal acoustic (LA), longitudinal optical (LO), two-phonon excitation and Si-H wagging mode of the amorphous phase [347, 349].

3.2.2 Contact stack evaluations and solar cell characterizations

Along with the fabrication process of solar cells, samples for evaluating the passivation quality and contact resistivity of contact stacks were also prepared. In this section, the techniques used for evaluating the contact stacks and the eventual solar cells are briefly introduced.

Passivation Quality Evaluation

The photoconductance lifetime tester (Sinton WCT-120) was used for measuring the passivation quality during the development of contact stacks for SHJ solar cells and monitoring the passivation quality along the fabrication of solar cells. To conduct the measurement, the test sample is placed on a temperature-controlled stage that features a built-in photodiode to measure the intensity of the light. Then a lamp located above the sample flashes light for a short period of time, which introduces photoconductance

changes in the sample due to the generation and recombination of excess charge carriers. Those changes in photoconductance of the sample are sensed by an RF coil that is inductively coupled to the wafer conductivity. Similar to equation 3.2, the photoconductivity (σ_{ph}) can be related to the excess minority carrier concentration ($\Delta n = \Delta p \gg p_0$) via:

$$\sigma_{\mathrm{ph}} = q(n_0 + \Delta n)\mu_n + q\Delta p\mu_p \tag{3.14}$$

Then, based on the continuity equation, a generalized expression of the injection level-dependent effective minority carrier lifetime (τ_{eff}) can be written as [350]:

$$\tau_{\mathrm{eff}}(\Delta p) = \frac{\Delta p(t)}{G(t) - \mathrm{d}\Delta p(t)/\mathrm{d}t} \tag{3.15}$$

where $G(t)$ is the photogeneration rate. To measure samples with short lifetimes ($\tau_{\mathrm{eff}} < 200$ µs), the quasi-steady-state-photoconductance (QSSPC) mode [351] that features a long time constant of the flash lamp is applied. In this case, $G(t) \gg \mathrm{d}\Delta p(t)/\mathrm{d}t$ and equation 3.15 can be simplified as:

$$\tau_{\mathrm{eff}}(\Delta p) = \frac{\Delta p(t)}{G(t)} \tag{3.16}$$

To measure samples with long lifetimes ($\tau_{\mathrm{eff}} > 200$ µs), transient photoconductance decay (Transient PCD) mode which sets the flash lamp to provide a short light pulse that decays rapidly is used. This results in $G(t) \ll \mathrm{d}\Delta p(t)/\mathrm{d}t$ and equation 3.15 can be approximated as:

$$\tau_{\mathrm{eff}}(\Delta p) = -\frac{\Delta p(t)}{\mathrm{d}\Delta p(t)/\mathrm{d}t} \tag{3.17}$$

The implied open-circuit voltage ($\mathrm{i}V_{\mathrm{OC}}$) can be then calculated via [351]:

$$\mathrm{i}V_{\mathrm{OC}}(\Delta p) = \frac{k_{\mathrm{B}}T}{q}\ln\left(\frac{\Delta p(n_0 + \Delta p)}{n_{\mathrm{i}}^2}\right) \tag{3.18}$$

In this thesis, the reported τ_{eff} values were obtained at an injection level ($\Delta n = \Delta p$) of 1×10^{15} cm^{-3}. The extracted $\mathrm{i}V_{\mathrm{OC}}$ at one sun corresponds to the τ_{eff} at high injection levels with a Δn or Δp usually around or above 1×10^{16} cm^{-3}. Figure 3.9 depicts the schematic sketch of the sample structure for lifetime measurements (left) and an example of an effective minority carrier lifetime curve of a double-side-textured c-Si symmetrically passivated by (*i*)a-Si:H layers.

Contact Resistivity Measurement

The dark current-voltage setup (Cascade Summit probe station CAS33 Microtech) was utilized for characterizing the contact resistivity (ρ_{c}) of the contact stacks implemented in solar cells. Figure 3.10 depicts the prepared symmetrical samples that feature contact stacks identical to those implemented in solar cells, whether it be the (*n*)- or (*p*)-contact stack. The contact stack consists of a space-charge layer inside the c-Si bulk, (*i*)a-Si:H, (*n*)- or (*p*)-layers, TCO and metal. The (*n*)-type or (*p*)-type c-Si wafer was used for evaluating (*n*)- or (*p*)-contact stack, respectively. While the measurement is taking place, the

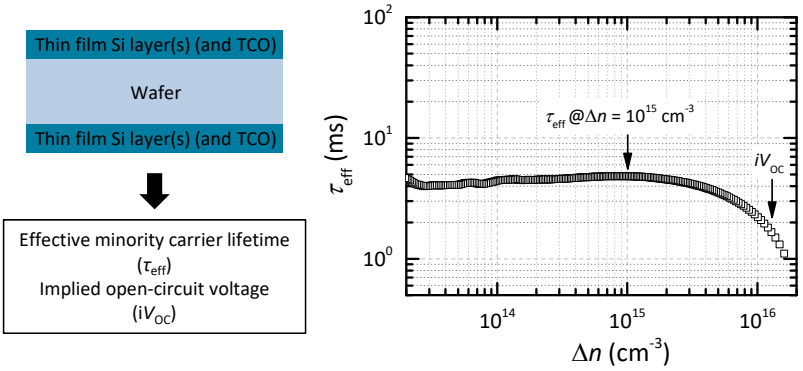

Figure 3.9: The schematic sketch of the sample structure for lifetime measurements (left) and an example of an effective minority carrier lifetime curve of a double-side-textured c-Si symmetrically passivated by (*i*)a-Si:H layers (right). Note, the wafer type, its morphology and the thin-film coating(s) on both sides can differ depending on the intended testing purposes.

test sample is contacted on both sides, and a voltage difference is applied to induce a current that passes through the test sample (I_{force}). In the meanwhile, the voltage on each side of the test sample is measured separately. Specifically, the voltage of the top surface of the sample (V_{H}) and the voltage of the sample chuck that is in contact with the rear side of the sample (V_{L}) are independently extracted without being affected by the I_{force}. Then, the total resistance of the test sample (R_{sample}) can be calculated via:

$$R_{\text{sample}} = \frac{V_{\text{H}} - V_{\text{L}}}{I_{\text{force}}} \tag{3.19}$$

In this way, the R_{sample} can be obtained with a high level of accuracy as this probing configuration minimizes possible impacts from, for instance, the sample chuck and contacting probes due to their contact resistance with the sample. Those can introduce measurement uncertainties, especially, for samples with relatively low resistance (several tens of mΩ).

With the known sample area, the R_{sample} (with a unit of mΩ) can be converted to the resistivity of the sample ($R_{\text{s,sample}}$) with a unit of m$\Omega \cdot$cm^2. Then, the total contact resistivity of samples ($R_{\text{s,contacts}}$) can be calculated with:

$$R_{\text{s,contacts}} = R_{\text{s,sample}} - R_{\text{s,bulks}} \tag{3.20}$$

where $R_{\text{s,sample}}$ is the total sample resistivity measured directly via the symmetrical sample, $R_{\text{s,bulks}}$ is the bulk resistivity contributions from c-Si and thin-film layers that form the doped contact stacks. With known $R_{\text{s,bulks}}$, we can extract the $R_{\text{s,contacts}}$ that originates from the contact interfaces. Thus, the ρ_{c} of contact stacks on one side of the sample can be obtained via:

$$\rho_{\text{c}} = \frac{R_{\text{s,contacts}}}{2} \tag{3.21}$$

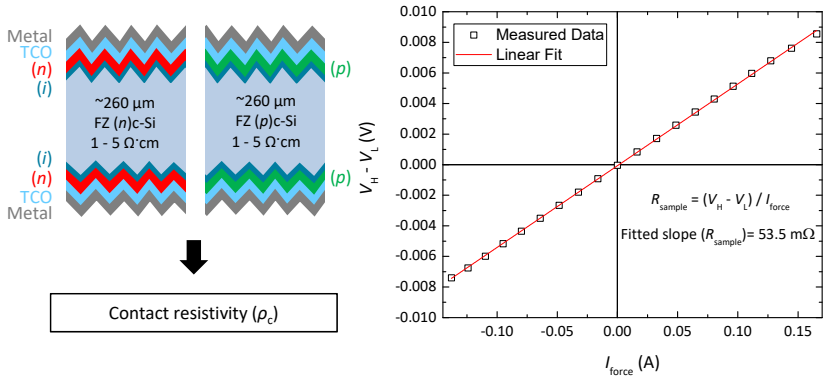

Figure 3.10: The schematic sketch of symmetrical samples used for extracting the contact resistivity (ρ_c) of contact stacks (left) and the derivation of the total resistance of a (p)-type sample (right). In the plot, the V_H represents the voltage measured on the top surface of the sample, the V_L is the voltage measured on the sample chuck that is in contact with the rear surface of the sample. I_{force} is the applied current that passes through the test sample.

where the term '2' is used by assuming the ideal symmetry of contact stacks on both sides of test samples. In our samples, the $\rho_{c,TCO/metal}$ of TCO/metal interface, typically, ITO/Ag interface is approximately 1.5 $m\Omega \cdot cm^2$ [327], which negligibly contributes to the total ρ_c of the contact stacks. Thus, the variation of extracted ρ_c reflects mainly the effectiveness of selective transport of charge carriers from c-Si to TCO [151, 201].

Illuminated Current-Voltage Evaluation

The solar simulator (AAA class Wacom WXS-90S-L2) was used to characterize the illuminated current-voltage performance of fabricated solar cells. From the measurement, external parameters, namely, short-circuit current density (J_{SC}), open-circuit voltage (V_{OC}), fill factor (FF) and power conversion efficiency (η) are extracted. The measurements were performed under standard test conditions (STC) as already introduced in Section 1.2.1. A xenon lamp and a halogen lamp are equipped in the system to simulate the AM 1.5G solar spectrum. Prior to sample measurement, calibration of the simulated spectrum is performed with reference solar cells calibrated at Fraunhofer ISE CalLab. While the solar cell is being illuminated, it undergoes a voltage sweep (typically from 1.0 to -1.0 V, and more preferably, from 0.8 to -0.2 V) and the resulting generated current is measured. A shadow mask is placed on top of the solar cell to shade the non-active area of the solar cell. The current density-voltage (J-V) curve of a 24.18%-efficient FBC-SHJ solar cell fabricated in this thesis is presented in Figure 3.11.

As illustrated in Figure 3.11, both the J_{SC} and V_{OC} are extracted from the cross points of the J-V curve and the corresponding axes. The FF represents the ratio of the power output at the maximum power point ($P_{MPP} = J_{MPP} \times V_{MPP}$) to the product of J_{SC} and V_{OC}. The η is determined as the maximum power generation over the incident irradiance (I_{in} = 1000 W/m^2 under STC).

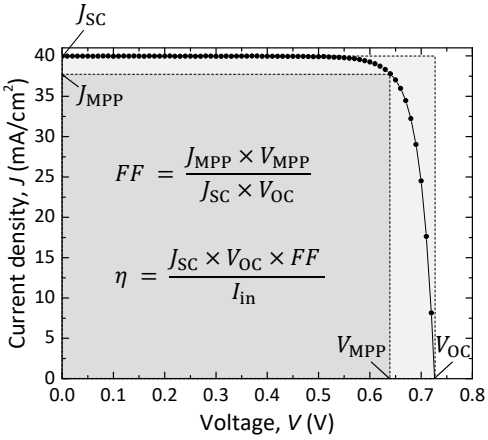

Figure 3.11: The J-V curve of a fabricated 24.18%-efficient FBC-SHJ solar cell. The inset formulas introduce the definitions of fill factor (FF) and efficiency (η). The voltage scan for the presented measurement ranged from 0.8 to -0.2 V, and data points with voltage beyond the V_{OC}, as well as those with negative voltages are not displayed in the plot.

Series Resistance Assessment

Sinton Suns-V_{OC}-150 Illumination-Voltage Tester was used to obtain the series resistance-free J-V curves of solar cells, which are valuable, especially, for extracting the series resistance of the device [52, 351, 352]. The Suns-V_{OC} measurement measures the open-circuit voltage of a solar cell as a function of the incident light intensity. The measurement of light intensity is accomplished by utilizing a calibrated reference solar cell. With the known J_{SC} value of the sample solar cell at 1-sun condition (irradiance of 1000 W/m^2) from the abovementioned illuminated I-V measurement, the pseudo current density (pJ) at certain illumination intensity (x sun) can be expressed as [353, 354]:

$$\mathrm{p}J = J_{SC}(1\ \text{sun}) - J_{SC}(x\ \text{sun}) \tag{3.22}$$

Accordingly, with various illumination intensities, a pseudo J-V (pJ-pV) curve can be plotted where pV is the measured V_{OC} at x sun. Since all the data points are noted under open-circuit voltage conditions, the measurement does not consider the loss induced by electrical transport. The effect of shunt resistance is still taken into account in the measurement. Just like that of the illuminated J-V curve, it is also possible to derive a pseudo FF (pFF) that reflects the potential achievable FF of the solar cell when excluding the impact of series resistance. In this thesis, the resistivity of solar cells ($R_{s,SunsVoc}$) is calculated via:

$$R_{s,SunsVoc} = (\mathrm{p}FF - FF)\frac{J_{SC}V_{OC}}{J_{MPP}^2} \tag{3.23}$$

On the illumination side of the solar cell, charge carriers can transport both vertically and laterally from the c-Si bulk to the metal electrode. It is possible to distinguish the resistance contributions from both directions by combining the aforementioned contact

resistivity measurements with the extracted $R_{s,SunsVoc}$ values. This aspect is further elaborated in Chapter 5.

Quantum Efficiency Measurement

An in-house-built external quantum efficiency (EQE) setup was used for evaluating the spectral response of fabricated solar cells. The EQE is the fraction of incident photons that generate electron-hole pairs, which are successfully collected, with respect to the total incident photons. In the measurement process, a xenon short arc lamp emits light that travels through the monochromator and is modulated by a chopper. The chopped monochromatic light is subsequently directed towards the sample, and the generated photocurrent is measured by converting it to voltage. The voltage is then measured using a lock-in amplifier. Mathematically, EQE(λ) is expressed as:

$$\mathrm{EQE}(\lambda) = \frac{I_{\mathrm{ph}}(\lambda)}{q\Psi_{\mathrm{ph},\lambda}} \tag{3.24}$$

where $I_{\mathrm{ph}}(\lambda)$ is the photocurrent that can be measured, $\Psi_{\mathrm{ph},\lambda}$ is the spectral photon flow incident on the solar cell. The $\Psi_{\mathrm{ph},\lambda}$ is not directly measurable but can be indirectly determined by using at least one calibrated photodiode (or reference solar cell(s)) with known EQE:

$$\Psi_{\mathrm{ph},\lambda} = \frac{I_{\mathrm{ph}}^{\mathrm{ref}}(\lambda)}{q\mathrm{EQE}^{\mathrm{ref}}(\lambda)} \tag{3.25}$$

where $I_{\mathrm{ph}}^{\mathrm{ref}}(\lambda)$ can be measured and $\mathrm{EQE}^{\mathrm{ref}}(\lambda)$ is known. After obtaining the EQE(λ) for the sample, the $J_{\mathrm{SC,EQE}}$ can be determined by:

$$J_{\mathrm{SC,EQE}} = -q\int_{300\ \mathrm{nm}}^{1200\ \mathrm{nm}} EQE(\lambda)\phi_{\mathrm{ph},\lambda}^{\mathrm{AM1.5}}\mathrm{d}\lambda \tag{3.26}$$

where $\phi_{\mathrm{ph},\lambda}^{\mathrm{AM1.5}}$ is the spectral photon flux of AM 1.5G spectrum [355] and the integration range is set from 300 nm to 1200 nm. In this thesis, the EQE was measured without the influence of the front metal grid and with a spot size of around $2\times3\ \mathrm{mm}^2$. Active-area power conversion efficiency (η_{active}) was calculated using the $J_{\mathrm{SC,EQE}}$ together with V_{OC} and *FF* obtained from *I-V* measurements. We observed that certain solar cells, which typically have low V_{OC} values as a result of insufficient selectivity of contact stacks [36], exhibit lower $J_{\mathrm{SC,EQE}}$ than J_{SC} obtained from illuminated *I-V* measurements. This observation could be related to the significant recombination of the solar cell that results in non-linearity in spectral response. This non-linearity can be more easily detected under low light intensity monochromatic illumination conditions used for EQE measurements (without bias light), despite a reasonable J_{SC} can be obtained from the *I-V* measurement with standard test conditions [356, 357].

Spectrophotometer setups (PerkinElmer Lambda 950 and 1050 systems) were used to extract the wavelength-dependent transmittance (*T*) and reflectance (*R*) of the testing layer (stack), wafer samples and, especially in this part, the reflection loss of solar cells. The Lambda spectrophotometry systems utilize light sources that are capable of emitting light covering a broad wavelength range from ultraviolet, visible, to near-infrared

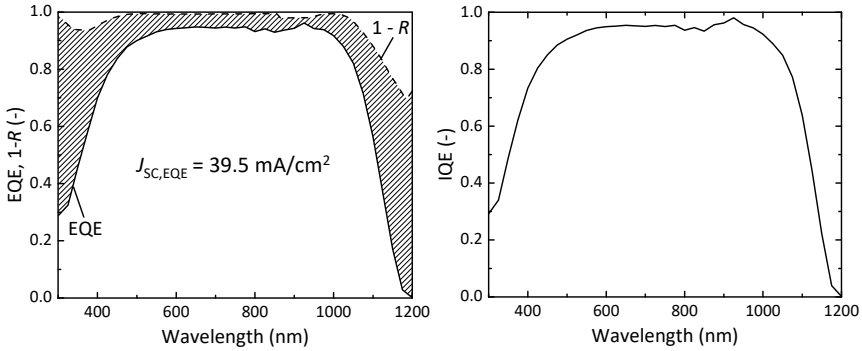

Figure 3.12: An example EQE and 1 – R of a double-side-textured FBC-SHJ solar cell (left) and the resulting IQE (right). The area with dashed lines indicates collection losses due to parasitic absorption and recombination of charge carriers.

(UV-Vis-NIR) (a deuterium arc lamp for $\lambda < 320$ nm and a tungsten-halogen lamp for λ within 300 nm and 3300 nm). The emitted light can hit diffraction gratings, which are capable of selecting certain wavelengths of light to be redirected towards the sample through a sequence of mirrors. An integrating sphere (IS) coated with a highly diffusive reflective material is installed to ensure all transmitted or reflected light can be captured by detectors after multiple internal reflections. Eventually, the measurements are compared to reference transmittance and reflectance spectra, therefore delivering results in relative terms (T and R in percentage relative to the incident light intensity).

In this thesis, the reflectance R measured with a spot size of around 3×14 mm^2 is used in combination with the measured EQE. As the EQE spectrum incorporates the losses due to reflectance, the overall reflectance of the cell is measured to determine the Internal Quantum Efficiency (IQE). The IQE represents the proportion of absorbed photons that are eventually collected as charge carriers, indicating the ability of a cell to utilize absorbed photons. In other words, the IQE can be employed to evaluate losses caused by parasitic absorption and recombination. The IQE(λ) can be obtained by using:

$$\mathrm{IQE}(\lambda) = \frac{\mathrm{EQE}(\lambda)}{1 - R(\lambda)} \tag{3.27}$$

where $R(\lambda)$ is the measured reflectance for a given wavelength λ, and $1 - R(\lambda)$ represents the effective absorptance when the rear side of the solar cell is opaque. Example EQE and 1 – R of a double-side-textured FBC-SHJ solar cell are given in Figure 3.12, and the resulting IQE of the solar cell is also provided.

3.3 Conclusions

In this chapter, the experimental process and equipment used for fabricating FBC-SHJ solar cells were introduced. Following this, the main characterization setups for assessing opto-electrical and structural properties of thin-film layers, passivation quality, contact resistivity, device external parameters and spectral response were presented to-

gether with brief introductions on their working principles.

4

Doped nc-SiO$_x$:H layers for SHJ solar cells

This chapter is based on the publication:

Y. Zhao, L. Mazzarella, P. Procel, C. Han, G. Yang, A. Weeber, M. Zeman, and O. Isabella, "Doped hydrogenated nanocrystalline silicon oxide layers for high-efficiency c-Si heterojunction solar cells," *Progress in Photovoltaics: Research and Applications*, vol. 28, no. 5, pp. 425–435, 2020.

Abstract

Hydrogenated nanocrystalline silicon oxide (nc-SiO$_x$:H) layers exhibit promising opto-electrical properties for serving as carrier-selective contacts in SHJ solar cells. However, achieving high conductivity while preserving c-Si surface passivation quality is technologically challenging for growing thin doped nc-SiO$_x$:H layers (< 20 nm) on the (*i*)a-Si:H passivating layer. In this chapter, we present the evaluation of different heterointerface engineering strategies to improve the opto-electrical properties of layer stacks founded on highly transparent nc-SiO$_x$:H layers. Using PECVD, we first investigated and demonstrated the significant adjustability of opto-electrical properties of doped nc-SiO$_x$:H layers by varying their main deposition conditions. In general, we confirmed that (*n*)-type nc-SiO$_x$:H layers offer a wider range of optical transparency for achieving lower activation energies as compared to the (*p*)-type counterparts. Afterwards, we assessed the electrical properties of these layers with the application of various heterointerface engineering techniques before and after doped layer depositions. Noticeably, we improved the dark conductivities from 0.79 S/cm to 2.03 S/cm and 0.02 S/cm to 0.07 S/cm for (*n*)- and (*p*)-layer (stack), respectively. The results suggest that the optimized interfacial treatments after (*i*)a-Si:H deposition not only promoted the nucleation of nanocrystals but also improved the c-Si surface passivation quality. Accordingly, we demonstrated *FF* improvement of 13.5%$_{\text{abs.}}$ from 65.6% to 79.1% in front/back-contacted SHJ solar cells. We achieved conversion efficiencies of 21.8% and 22.0%, for front and rear junction

configurations, respectively. The optical effectiveness of the layer stack based on (*n*)nc-SiO$_x$:H was demonstrated by an average 1.5 mA/cm^2 higher J_{SC} thus a nearly 1%$_{abs.}$ higher average cell efficiency as compared to cells with (*n*)a-Si:H.

4.1 Introduction

Silicon heterojunction (SHJ) solar cells have demonstrated excellent efficiencies that are well beyond 26% [67, 68], and therefore becoming one of the most promising photovoltaic (PV) technologies to reduce the levelized cost of electricity. The crucial ingredient to achieve such high efficiency is the remarkable high open-circuit voltage (V_{OC}), which is above 750 mV [67, 139, 358, 359]. Typically, SHJ solar cells feature layer stacks consisting of intrinsic and doped a-Si:H thin layers (< 15 nm) grown by PECVD. Those Si-based thin-film layers must feature certain properties to build efficient contacts in terms of carrier selectivity and carrier selective transport for obtaining a high fill factor (*FF*) in solar cells [150]. Such layer properties point to minimal activation energy (E_a) for both (*n*)- and (*p*)-contacts whereas a wider bandgap (E_g) is more favourable for the collection of holes ((*p*)-contact).

Despite their limited thickness, a-Si:H-based thin-films induce significant parasitic losses when placed on the sunny side of the cell [156]. Besides, doped a-Si:H layers have minimum achievable E_a values in the order of hundreds of meV due to their moderate doping efficiency [153]. The attempt to reach higher doping within a-Si:H films increases the defect density, which will deteriorate the effectiveness of the carrier collection [155]. To quench this material bottleneck and owing to their superior electrical and favorable optical properties, hydrogenated nanocrystalline silicon (nc-Si:H) layers have been proposed for carrier-selective-contacts (CSCs) in SHJ solar cells [162–164, 360]. The material consists of small nanocrystals embedded in the amorphous matrix [361] giving confirmed anisotropy properties in the growth direction [225]. Furthermore, nc-Si:H alloyed with oxygen (nc-SiO$_x$:H) allows tunable opto-electrical properties [173, 300], with the advantage of simultaneously obtaining higher E_g and lower E_a, when compared to a-Si:H. This unique feature also enables more flexibility to tailor the selective transport of charge carriers, which enhances the performance of solar cells [150]. Interestingly, with similar optical transparency, (*n*)-type nc-SiO$_x$:H layers exhibit generally higher conductivity than (*p*)-type counterparts [169, 174]. Accordingly, the use of (*p*)-type nc-SiO$_x$:H as a front emitter in SHJ cell, which demands more sensitive processing and optimizations than (*n*)-type counterpart, is rarely reported [160, 362, 363].

On the other hand, in SHJ solar cell applications, it is challenging to maintain an excellent electrical cell performance while optimizing the optical layer properties due to the substrate growth selectivity on top of the (*i*)a-Si:H layer [176]. Research and developments have been devoted to studying the interface treatment to properly grow a nanocrystalline structure [320, 321, 364–366]. In particular, hydrogen plasma treatment (HPT) is widely studied for improving the c-Si/(*i*)a-Si:H chemical interface-passivation quality [367, 368]. From Si thin-film experience, this treatment can also result in a low-temperature crystallization of a-Si [369] that might be beneficial for nanocrystal growth. Aside from HPT, oxygen-absent seed layer [365, 366] and CO_2 plasma treatments [321] are also utilized to minimize the incubation layer thickness of thin nc-Si:H layers. It is also well known that very-high-frequency (VHF) plasma may induce less ion bombard-

ment compared to radio-frequency (RF) [370] and thus, it is more efficient for reaching higher crystallinity fraction (F_C) within thin layers [314]. Therefore, it is critical to explore nucleation methods for achieving excellent bulk conductivity and nanocrystal growth of thin (< 20 nm) doped nc-SiO$_x$:H layers while maintaining excellent surface passivation quality.

In this chapter, we explore highly transparent selective transport layers for carrier collection based on nc-SiO$_x$:H for SHJ solar cells. After the section about experimental details, the remainder of this chapter is organized as follows: first, we study the tunable opto-electrical properties of doped nc-SiO$_x$:H layers by varying their PECVD deposition parameters. Afterwards, we investigate the effects of different interfacial treatments in both (*n*)-type and (*p*)-type layer stacks. Finally, we examine the impact of these interfacial treatments on the performance of front/back-contacted SHJ solar cells.

4.2 Experimental

For layer optimizations, doped nc-SiO$_x$:H layers were deposited on glass substrates with thicknesses from 40 to 100 nm. Characterization techniques for extracting thicknesses, optical properties (refractive index n @λ = 632 nm and bandgap E_0), electrical properties (E_a and dark conductivity σ_d) and microstructural properties (microstructure factor defined for Si-H stretching modes R_{SM}) of layers are introduced in Section 3.2. The PECVD deposition conditions used for layers and interfacial treatments in this chapter are presented in Table 4.1.

To investigate the effects of nucleation on the growth of doped nc-SiO$_x$:H layers, the depositions of oxygen-absent doped nc-Si:H layers, pre-HPT and/or VHF (*i*)nc-Si:H treatment were applied right after the (*i*)a-Si:H deposition. After the depositions of the doped layer (stack), post-HPT and doped a-Si:H capping layer were additionally applied (see Table 4.1). Note, the pre-HPT etches around 2 to 3 nm of the (*i*)a-Si:H. In solar cells, the indium tin oxide (ITO) layers were sputtered on both the front and rear sides of the devices with thicknesses of 75 nm and 120 nm, respectively. Cells were completed with screen-printed Ag electrodes, which were cured in an oven in the air atmosphere at a temperature of 170 °C for 45 minutes for each side. Solar cells fabricated in this study have a designated area of 7.84 cm^2 with 12.5% metal coverage or 3.92 cm^2 with 4.4% metal coverage. The active area efficiency (η_{active}) was obtained by using V_{OC} and *FF* measured under STC together with integrated $J_{SC,EQE}$ extracted from the EQE measurement on the active area of the device (see Section 3.2.2). Therefore, the influence of optical shading caused by the front metal grid is excluded for η_{active}.

4.3 Results and Discussions

4.3.1 Tunable opto-electrical properties of doped nc-SiO$_x$:H

To evaluate the optimal trade-off of opto-electrical parameters of doped nc-SiO$_x$:H for solar cell applications, we performed a series of experiments by varying the PECVD process parameters as presented in Table 4.1. The summary of measured n, σ_d, and E_0[1],

[1] In the article on which this chapter is based, the term 'E_{04}' was given whereas the correct term was supposed to be 'E_0' as described in Section 3.2.1. As a result, 'E_0' is used in this chapter instead of wherever 'E_{04}' is used in the article. This labelling issue neither changes visual or numerical elements in the article nor affects its

Table 4.1: PECVD deposition parameters for optimization of doped nc-SiO$_x$:H layers and for various interfacial treatments (doped nc-Si:H seed layers, pre-HPT, VHF (*i*)nc-Si:H treatment, post-HPT and doped a-Si:H capping layers).

PECVD parameters	(*n*)nc-SiO$_x$:H	(*p*)nc-SiO$_x$:H	(*n*)nc-Si:H	(*p*)nc-Si:H	pre-HPT	VHF (*i*)nc-Si:H	post-HPT	(*n*)a-Si:H	(*p*)a-Si:H
Frequency (MHz)	13.56	13.56	13.56	13.56	13.56	40.68	13.56	13.56	13.56
Temperature (°C)	180	180	180	180	180	180	180	180	180
Pressure (mbar)	1.1 – 4.4	1.4 – 3	2.7	2.2	2.7/2.2[a]	4	2.7	0.6	0.9
Power density (mW/cm^2)	55 – 90	55 – 90	76	90	63	69	21	28	16
SiH_4 (sccm)	1	0.8	1	0.8	-	1.2	-	40	8
H_2 (sccm)	60 – 160	110 – 210	100	170	200	120	200	-	24
CO_2 (sccm)	0 – 2.2	0 – 2.8	-	-	-	-	-	-	-
PH_3[b] (sccm)	0.7 – 3.7	-	1.2	-	-	-	-	11	-
B_2H_6[c] (sccm)	-	5 – 30	-	10	-	-	-	-	8

[a]: 2.7 mbar for (*n*)-side and 2.2 mbar for (*p*)-side;
[b]: 2% in H_2;
[c]: 200 ppm in H_2.

E_a and F_C of doped nc-SiO$_x$:H, nc-Si:H and a-SiO$_x$:H layers within the explored PECVD process window is illustrated in Figure 4.1.

As shown in Figure 4.1 (a), we first address the trade-off between the optical and electrical properties of doped nc-SiO$_x$:H layers. For (*n*)-type layers, along with the increment of *n*, the improvement of σ_d is generally observed, which indicates a lower fraction of (*n*)a-SiO$_x$:H [371] but more conductive (*n*)nc-Si:H and/or (*n*)a-Si:H phase inside the material. To be more specific, increasing the deposition pressure and decreasing deposition power result in layers featuring larger *n*, and these are also observed by Gabriel et al. who ascribe the increasing of *n* with decreased 'power to pressure ratio' to less incorporation of oxygen in the mixed-phase material [170]. Besides, changing directly the composition of precursor gases, mainly decreasing H_2 flow and CO_2 flow, results in higher *n* as well, which is observed in the literature as well [170–172, 371]. However, the nanocrystalline phase is hardly seen when depositions feature insufficient H_2 dilution (less than or equal to 60 sccm) or inappropriate pressure (less than or equal to 1.1 mbar and greater than or equal to 4.4 mbar) (see (*n*)a-SiO$_x$:H in Figure 4.1 (a)). Indeed, nucleation of nc-Si requires sufficient atomic hydrogen in the plasma, while this is not likely to happen when H_2 dilution is too low and deposition pressure is too high [172, 266, 372].

discussion and conclusions.

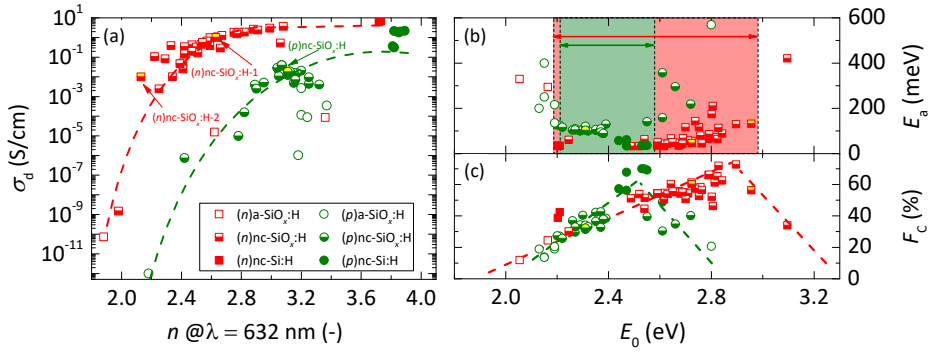

Figure 4.1: The opto-electrical properties of doped nc-SiO$_x$:H, nc-Si:H and a-SiO$_x$:H layers during the optimization process: (a) dark conductivity σ_d as a function of refractive index n; (b) activation energy E_a and (c) crystalline fraction F_C as a function of bandgap E_0. Note, half-down symbols represent nc-SiO$_x$:H layers; solid symbols indicate nc-Si:H layers without CO_2 during the depositions; open symbols suggest a-SiO$_x$:H (or amorphous phase-dominant materials), which are based on fitted F_C when it is below 25% as their nanocrystal peaks are hardly distinguishable from their Raman spectra; dashed lines in figures 1(a) and (c) are guides to the eye; colored rectangular areas in figure (b) indicate the optical window of achieving favorable E_a (< 200 meV) for solar cells application. In figures (a) – (c), doped nc-SiO$_x$:H layers that are used in fabricating solar cells are marked with yellow half-down symbols.

As for (p)-type layers, changes in deposition conditions induced the increased n of (p)-type layers may be explained similarly to that of (n)-type layers. The increased n is mainly seen by increasing deposition pressure, B_2H_6 flow and decreasing deposition power, H_2 flow and CO_2 flow. The (p)a-SiO$_x$:H shown in Figure 4.1 (a) is due to high CO_2 flow (greater than 2.8 sccm), high B_2H_6 flow (greater than 25 sccm), low H_2 flow (less than 130 sccm) or high pressure (greater than 3 mbar). The amorphization induced by the high B_2H_6 flow could be related to a similar finding reported in [168], where a monotonic decrement of F_C is observed with an increased TMB/SiH_4 ratio. Moreover, for both (n)- and (p)-type layers, highly conductive nc-Si:H layers are obtained when CO_2 is missing during the deposition.

Moreover, as shown in Figure 4.1 (b), (n)-type layers exhibit a wider optical window to achieve favoured E_a for solar cell applications as compared to (p)-type layers. Therefore, the front surface field (FSF) featuring (n)nc-SiO$_x$:H is supposed to be a better candidate and easier to apply in solar cells than (p)nc-SiO$_x$:H. Lastly, as shown in Figure 4.1 (c), the variation of extracted F_C with E_0 reflects the change of constituents of this mixed-phase material. The positive correlation between F_C and E_0 of doped nc-SiO$_x$:H is mainly due to more hydrogen and/or more oxygen incorporation into the layer [172], while the atomic hydrogen-induced nucleation effect can still compensate for the amorphization effect from oxygen. However, when oxygen incorporation exceeds a certain limit, the nanocrystal growth is compromised as discussed in the works of literature [168, 172, 298, 371].

Overall, tunable opto-electrical properties of doped nc-SiO$_x$:H layers enable the flexibility to tailor the selective transport of charge carriers for enhancing the performance of solar cells [150]. In Table 4.2, we report the optimized opto-electrical properties of

Table 4.2: Opto-electrical properties of selected doped nc-SiO$_x$:H layers for solar cells.

Layers	σ_d (S/cm)	E_a (meV)	E_0 (eV)	n @632 nm (-)	F_C (%)	Thickness (nm)
(n)nc-SiO$_x$:H-1	1.02	46.6	2.72	2.63	60.1	63.4
(n)nc-SiO$_x$:H-2	0.01	132.1	2.96	2.13	56.3	50.3
(p)nc-SiO$_x$:H	0.02	103.6	2.31	3.11	32.3	68.7

both (p)-type and (n)-type nc-SiO$_x$:H layers for subsequent solar cell applications.

4.3.2 Interfacial treatments on doped layer stacks

In this section, the variations in doped layer (stack) electrical properties (E_a and σ_d) were evaluated with different interfacial treatments, including pre-treatments and post-treatments that were applied before or after doped layer depositions, respectively. To obtain device-relevant layer (stack) properties, we coated glass substrates with 10-nm-thick (i)a-Si:H followed by depositions of (n)-type layer stack ((n)nc-SiO$_x$:H-1 + (n)nc-Si:H) or (p)-type layer stack ((p)nc-SiO$_x$:H + (p)nc-Si:H). To accelerate the nucleation of nc-SiO$_x$:H, we introduced pre-treatments including pre-HPT, the application of an oxygen-absent (n)nc-Si:H or a (p)nc-Si:H seed layer, and VHF (i)nc-Si:H treatment. Post-treatments such as doped a-Si:H capping layer applied after the growth of the layer stacks were tested. Additionally, we also applied a post-HPT after the deposition of (n)-layer stacks. Figures 4.2 (a) and (b) present the schematic illustration of interfacial treatments applied on (n)-type and (p)-type layer stack, respectively. Figures 4.2 (c) and (d) exhibit the effects of pre- and post-treatments on doped layer stacks, whereas those treatments were already optimized in terms of plasma conditions and deposition time to have better electrical properties of doped layers without causing significant detrimental impacts on the passivation quality when applied for solar cell applications. In Figure 4.2 (c), the combined treatment-1 represents the pre-HPT + (n)nc-Si:H seed + (n)-type layer stack + post-HPT + (n)a-Si:H, while combined treatments-2 represents: pre-HPT + VHF (i)nc-Si:H treatment + (n)-type layer stack + post-HPT + (n)a-Si:H. The distinction between these two combined treatments lies in the application of either (n)nc-Si:H seed or VHF (i)nc-Si:H treatment before the deposition of (n)-layer stacks.

As seen in Figure 4.2 (c), considering (n)-type layer stack without any treatment indicated as the reference, layers exposed to single pre-treatment and post-treatment exhibit decrements of E_a. Especially, for the single treatments, the use of (n)a-Si:H capping layer plays the most significant role in reducing E_a from 53.5 meV to 36.5 meV and doubling σ_d from 0.79 S/cm to 1.57 S/cm. Such an effect strongly suggests that (n)a-Si:H allows a better interface contact with metal than (n)nc-Si:H counterpart. Note that (n)a-Si:H we used in this experiment was previously optimized with an E_a of 206 meV and a σ_d of 0.02 S/cm. Thus, this observation might also suggest potentially easier surface oxidation of (n)nc-Si:H compared to (n)a-Si:H upon exposure to air. Faster nucleation is seen by applying pre-HPT, oxygen-absent (n)nc-Si:H and VHF (i)nc-Si:H treatment, which increase σ_d as compared to the reference sample. However, it is worth noting that the layer stack after the 20-minutes post-HPT treatment exhibits slightly reduced lateral σ_d than the reference sample. Since the lateral σ_d is measured by probing contacts which are

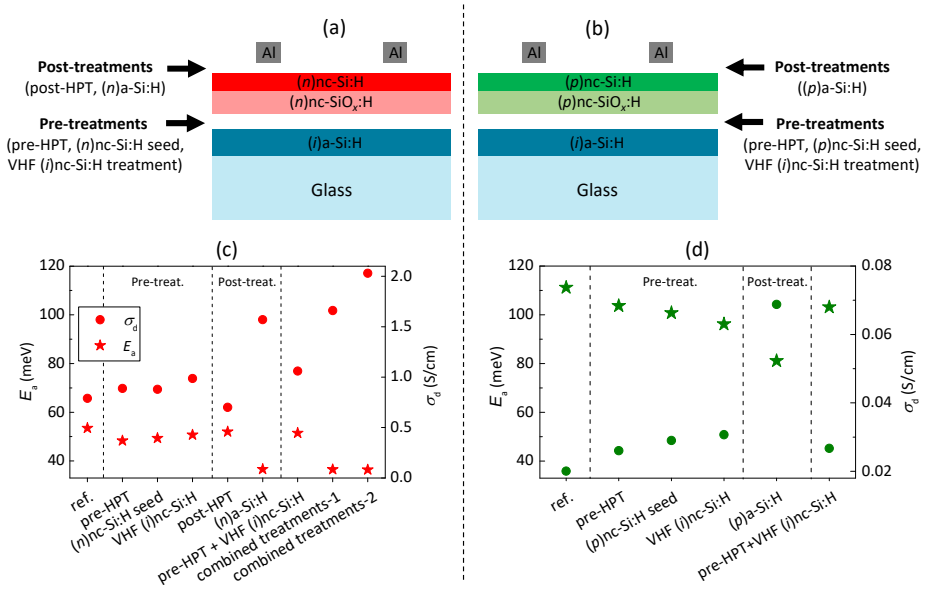

Figure 4.2: Schematic illustrations of pre- and post-treatments applied on (a) (*n*)-type layer stack (approx. 76 (*n*)nc-SiO$_x$:H-1 + 4 nm (*n*)nc-Si:H) and (b) (*p*)-type layer stack (approx. 74 nm (*p*)nc-SiO$_x$:H + 8 nm (*p*)nc-Si:H), respectively. Measured electrical properties (E_a and σ_d) of (c) (*n*)-type and (b) (*p*)-type layer stacks with different pre- or post-treatments. For pre-treatments, both the pre-HPT and VHF (*i*)nc-Si:H treatment have a duration of 2 minutes. The thicknesses of oxygen-absent seed layers are around 3 nm for (*n*)nc-Si:H and 4 nm for (*p*)nc-Si:H. For post-treatments, the doped a-Si:H capping layer has a thickness of 2 nm. The treatment time of post-HPT after the deposition of (*n*)-type layer stack is 20 minutes.

formed on the surface of the layer, the reduction of lateral σ_d indicates that the surface of the layer stack is less laterally conductive after post-HPT. We speculate that surface amorphization (a few nanometers) is induced by this low-power post-HPT leading to a less conductive amorphous film. Nevertheless, we could not detect such shallow-surface F_C changes as compared to the thick bulk layer. This is due to the Raman Spectroscopy used in this study, which features a penetration depth in the range of hundred nanometers. HPT-induced amorphization of nc-Si:H is reported [373], for which a layer with initial F_C over 20% (with the existence of grain boundaries) experienced a decrease of F_C after HPT, resulting from migrating H atoms that minimize lattice strain energy. As reported elsewhere [374], the formation of a few nanometers disordered surface layer on (*p*)-type CZ-Si after HPT was confirmed by cross-sectional transmission electron microscopy (TEM). In any case, by means of SE, we observed no etching of the (*n*)-type layer stack after the post-HPT. By combining the applied pre- and post-treatments, we were able to improve further the σ_d of the (*n*)-type layer stacks from 0.79 S/cm to 2.03 S/cm as compared to the reference sample.

For (*p*)-type layer stack, we noted positive effects in applying pre-treatments in terms of lower E_a and higher σ_d. Among pre-treatments, the most obvious enhancement of E_a (from 111.2 meV to 96.4 meV) and σ_d (from 0.02 S/cm to 0.03 S/cm) is seen when apply-

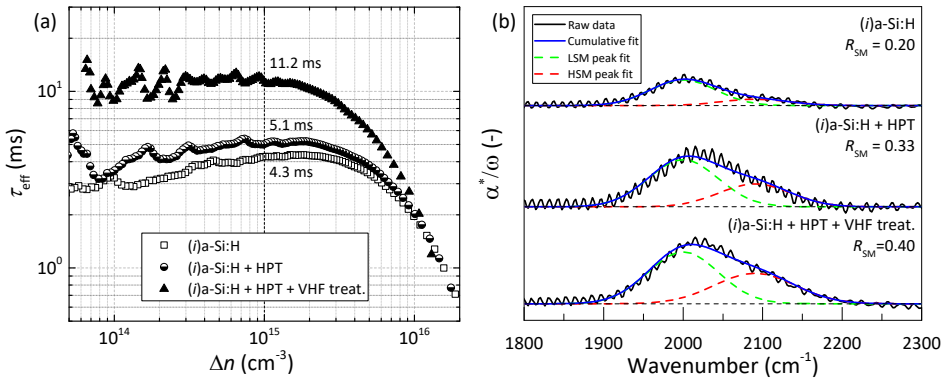

Figure 4.3: (a) Injection level-dependent minority carrier lifetime (τ_{eff}) curves and (b) infrared spectra measured for symmetrical samples with (*i*)a-Si:H, (*i*)a-Si:H with additional pre-HPT and (*i*)a-Si:H with additional pre-HPT and VHF (*i*)nc-Si:H treatment. Note that in figure (b), the background subtraction and the resulting fitting range, as used in the article on which the chapter is based, have been improved by consistently utilising the procedure applied in Chapter 7. These improvements do not affect the conclusions drawn in the article.

ing VHF (*i*)nc-Si:H treatment. The VHF plasma conditions used in this study are acting mainly as surface treatment, since no change in thickness was detected by SE, even after 6 minutes of deposition. Similar to that of (*n*)-type layer stack, the σ_{d} was boosted to 0.07 S/cm and E_{a} was reduced to 81.1 meV by adding a (*p*)a-Si:H capping layer on (*p*)-type layer stack. Moreover, we also observed improved electrical properties by combining the pre-HPT and VHF (*i*)nc-Si:H treatment as compared to the reference sample, while the combined treatments do not outperform samples with the corresponding single treatments.

To further understand the effects of pre-HPT and VHF (*i*)nc-Si:H treatment on the thin (*i*)a-Si:H layer, we evaluated the passivation quality and the layer's microstructure. To this purpose, we prepared double-side textured symmetrical samples with 10-nm-thick (*i*)a-Si:H layers on each side with the abovementioned treatments. We monitored the effective lifetime (τ_{eff}) of those symmetrical samples and measured the structural change in those layers with Fourier-transform infrared spectroscopy (FTIR). Figure 4.3 (a) depicts the injection level dependent τ_{eff} and the infrared spectra related to the (*i*)a-Si:H without treatment, with pre-HPT, and with pre-HPT + VHF (*i*)nc-Si:H treatment. Note, the deposition conditions of pre-HPT for the (*n*)-side, as listed in Table 4.1, were used as the representative HPT for those symmetrical samples.

As shown in Figure 4.3 (a), the reference sample without treatment demonstrated a τ_{eff} slightly over 4 ms (at the injection level Δn of 1×10^{15} cm^{-3}), while we noticed improved passivation quality (τ_{eff} above 5 ms) when pre-HPT was implemented after the deposition of (*i*)a-Si:H. Interestingly, applying pre-HPT + VHF (*i*)nc-Si:H treatment, we observed the most significant τ_{eff} enhancement resulting in a τ_{eff} beyond 11 ms.

To investigate possible reasons for these enhancements in passivation quality, we report in Figure 4.3 (b) the corresponding infrared spectra of these symmetrical passivation samples, which reveal the changes in hydrogen content and microstructure of

(*i*)a-Si:H layer. As seen in Figure 4.3 (b), the absorption peak can be de-convoluted into two Gaussian distributions, which are related to the low stretching mode (LSM) and high stretching mode (HSM) of Si-H bonds. It has been demonstrated that the LSM is attributed to monohydrides in small volume deficiencies [343, 375], whereas HSM is assigned to mainly the monohydrides and some polyhydrides at internal surfaces of larger volume deficiencies like nano-sized voids [338, 343, 375]. As a result of the different Si-H bonding nature of LSM and HSM, a higher fraction of HSM, thus a higher R_{SM} (defined previously in section 3.2.1) indicates a less compact (underdense) or void-rich film.

As shown in Figure 4.3 (b), we observed overall increased absorption strength after applying either only HPT or combined treatments (HPT + VHF (*i*)nc-Si:H treatment) on (*i*)a-Si:H layer. These observations imply increased hydrogen content inside the (*i*)a-Si:H layer [367], which can enhance its passivation capability. Besides, the R_{SM} was also increased when either only HPT or combined treatments were applied, thus suggesting the reduced compactness of the (*i*)a-Si:H layer after those treatments. In other words, the microstructure of (*i*)a-Si:H gets closer to the amorphous-to-crystalline transition region, which can foster more effectively the nucleation of doped nc-Si:H-based layers [308]. Besides, HPT can induce high compressive stress within the amorphous silicon network, which has been reported to be crucial for the nucleation of nanocrystals from the amorphous phase [376]. The elevation in compressive stress caused by HPT can be ascribed to several factors, including (i) the incorporation of hydrogen into the strained Si-Si bonds, (ii) the hydrogen-hydrogen repulsive force, and (iii) the presence of trapped H_2 molecules in the a-Si:H [376]. These factors are closely associated with our HPT or combined treatments treated (*i*)a-Si:H layers, which exhibited significant hydrogen incorporation and possibly trapped H_2 molecules within formed vacancies (see Figure 4.3 (b)). Despite the existence of vacancies can reduce the compressive stress in the a-Si:H [377], our HPT and combined treatment may allow more presence of H_2 molecules inside these potentially formed vacancies as suggested by the substantial increase of absorption strength of the HSM. Therefore, these treatments might also initiate the nucleation based on intrinsic stress accumulated within the film. These effects on the nucleation of nanocrystals are expected to be more noticeable when those doped layers have thinner thicknesses.

To sum up, the investigated pre-treatments applied for both (*n*)-type and (*p*)-type layer stacks can enhance the electrical properties of test samples. In the meanwhile, the combination of pre-HPT and VHF (*i*)nc-Si:H treatment was found to significantly improve the c-Si/(*i*)a-Si:H interface passivation quality. As for post-treatments, boosts of σ_d are observed when doped a-Si:H capping layers are applied on the corresponding doped layer stacks. In the following, we investigated the effects of the aforementioned interfacial treatments on the performance of solar cells.

4.3.3 Solar cells

Front/back-contacted SHJ solar cells were fabricated featuring the (*n*)-type and (*p*)-type layer stacks discussed in Figure 4.2. In order to evaluate both optically and electrically the aforementioned interfacial treatments on the solar cell level, we located the layer stacks under study on the front of the device. Therefore, we analyzed various (*n*)-type ((*p*)-type) layer stacks in rear (front) junction devices. The schematic illustrations of

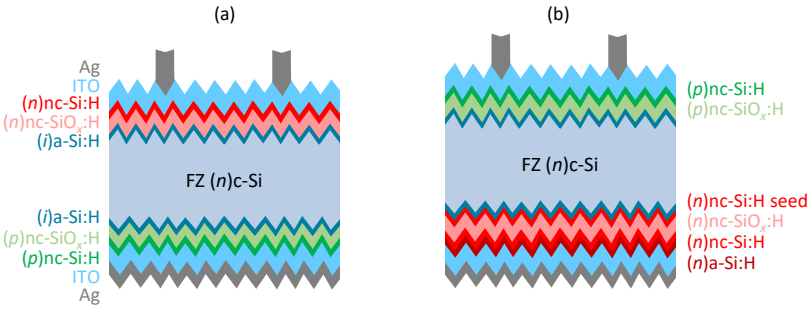

Figure 4.4: Schematic sketches of reference cells for investigating effects of interfacial treatments applied on (a) (*i*)a-Si:H/(*n*)-type layer stack (8 nm (*i*)a-Si:H + 12 nm (*n*)nc-SiO$_x$:H-1 + 3 nm (*n*)nc-Si:H) and (b) (*i*)a-Si:H/(*p*)-type layer stack (8 nm (*i*)a-Si:H + 10 nm (*p*)nc-SiO$_x$:H + 10 nm (*p*)nc-Si:H). In (a), the rear side (*i*)a-Si:H/(*p*)-type layer stack remains unchanged as 8 nm (*i*)a-Si:H + 10 nm (*p*)nc-SiO$_x$:H + 10 nm (*p*)nc-Si:H. In (b), the rear side (*i*)a-Si:H/(*n*)-type layer stack is fixed as 8 nm (*i*)a-Si:H + pre-HPT + 2 nm (*n*)nc-Si:H seed + 8 nm (*n*)nc-SiO$_x$:H-1 + 3 nm (*n*)nc-Si:H + post-HPT + 2 nm (*n*)a-Si:H.

reference solar cells are shown in Figure 4.4. Besides the various interfacial treatments herein analyzed, the layer stacks under study closely follow the sort of potentially optimized contact stack for achieving efficient transport of charge carriers across heterointerfaces in SHJ cells [150]. In a nutshell, such an optimal layer stack comprises (i) an optimized (*i*)a-Si:H to achieve excellent surface passivation, (ii) a high bandgap silicon-alloy layer with a low E_a (e.g. nc-SiO$_x$:H) to induce strong band banding at c-Si/(*i*)a-Si:H interface and (iii) a layer with low E_a (e.g. oxygen-absent nc-Si:H) to enable efficient charge exchange with the TCO.

During the evaluation of (*n*)-type layer stacks, the rear side (*p*)-type layer stack was kept constant as 8 nm (*i*)a-Si:H + 10 nm (*p*)nc-SiO$_x$:H + 10 nm (*p*)nc-Si:H, with reference (*n*)-type layer stack as 8 nm (*i*)a-Si:H + 12 nm (*n*)nc-SiO$_x$:H-1 + 3 nm (*n*)nc-Si:H (see Figure 4.4 (a)). The external parameters of corresponding solar cells are presented in Figure 4.5.

As seen in Figure 4.5 (a), the reference cell showed a *FF* of 65.6%, a V_{OC} of 723 mV, a $J_{SC,EQE}$ of 38.5 mA/cm^2 and a η_{active} of 18.3%. When pre-HPT was applied, we measured improved EQE response, which is related to bandgap widening inside (*i*)a-Si:H with H incorporation that improves the short wavelength response [368]. However, the cell with only pre-HPT exhibited a comparable V_{OC} but a drastic *FF* drop of over 10%$_{abs.}$ as compared to the reference cell. Such an effect could be ascribed to unexpected changes in contact properties of (*n*)nc-Si:H/ITO interface, even though further investigation is necessary for understanding this observation. While *FF* drop was induced by pre-HPT, it was fully recovered and even improved when we additionally applied a post-HPT or with an extra (*n*)a-Si:H capping layer. Among these solutions, (*n*)a-Si:H was more beneficial with a *FF* gain of 6.3%$_{abs.}$ as compared to the reference cell. Such an effect is consistent with results discussed in Section 4.3.2, where the (*n*)a-Si:H capping layer delivered lower E_a and higher σ_d values when (*n*)a-Si:H is in contact with the metal. Both observations might be related to the possible easier surface oxidation of (*n*)nc-Si:H than (*n*)a-Si:H.

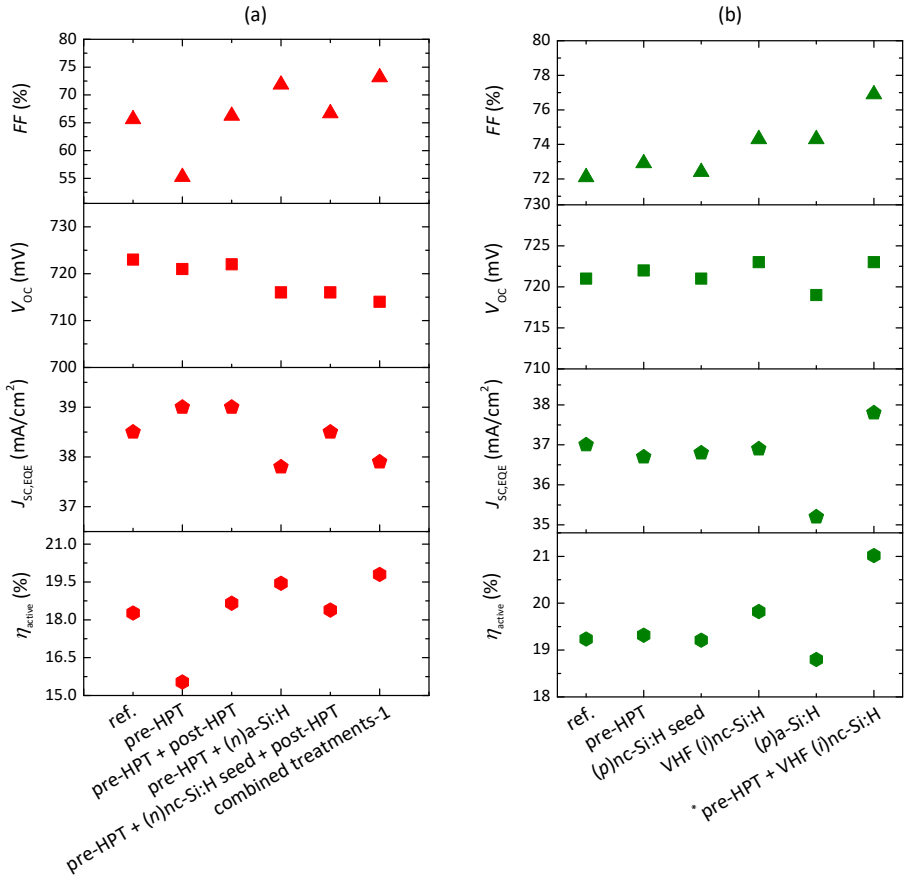

Figure 4.5: The *J*-*V* parameters of solar cells with different interfacial treatments applied (a) on (*n*)-type layer stack in rear junction configuration and (b) on (*p*)-type layer stack in front junction configuration as described in Figure 4.4. In (a), combined treatments-1 represents pre-HPT + 2 nm (*n*)nc-Si:H seed + (*n*)-type layer stack + post-HPT + 2 nm (*n*)a-Si:H. In (b), the cell with *pre-HPT + VHF (*i*)nc-Si:H features more optimized thicknesses of (*i*)a-Si:H on both sides and (*n*)nc-SiO$_x$:H on the rear side. Each data point represents one solar cell.

Moreover, in solar cells, (*n*)-type layer stack is in contact with sputtered ITO instead of metal. Thus, the gain of *FF* by applying (*n*)a-Si:H capping layer may also result from different mechanisms as compared to the sample shown in Figure 4.2 (c). Nevertheless, a study of the (*n*)-type layer/ITO interface using X-ray photoelectron spectroscopy depth profiling measurements showed that (*n*)a-Si:H forms a better interface with sputtered ITO as compared to (*n*)nc-Si:H [378]. This is due to (i) a lack of oxygen segregation, (ii) much less oxidized Si atoms near the interface region and (iii) less ITO diffusion into (*n*)a-Si:H layer, while the formation of highly oxidized interface and ITO in-diffusion happened when (*n*)nc-Si:H was applied [378]. Besides, the formation of a-SiO$_x$:H(In) in ITO/(*n*)-Si interface during sputtering of ITO, which builds a potential barrier (i.e.

blocking the transport of electrons), was also reported [379]. Those studies may explain the gain of *FF* by applying the (*n*)a-Si:H capping layer before ITO sputtering. Similarly, the possible shallow surface amorphization of layer stack result from the post-HPT as discussed in Section 4.3.2 may explain the improved *FF* of the solar cell, because amorphous layers relax the sharp potential change at TCO hetero-interfaces thus improving energy band alignment [380]. Nevertheless, the highly absorptive (*n*)a-Si:H induced an overall degradation of the $J_{SC,EQE}$ to below 38 mA/cm^2. Moreover, the insertion of 2-nm-thick (*n*)nc-Si:H seed layer in combination with pre- and post-HPT provides a tiny *FF* improvement (0.4%$_{abs.}$) but with a passivation degradation of 6 mV as compared to the cell with only pre- and post-HPT. This little gain of *FF* may be ascribed to the faster nucleation induced by the oxygen-absent (*n*)nc-Si:H seed layer [365, 366], while the drop of V_{OC} is due to the rather aggressive deposition of (*n*)nc-Si:H directly on (*i*)a-Si:H layer. Eventually, a solar cell with combined treatments-1, namely, pre-HPT + 2 nm (*n*)nc-Si:H seed + (*n*)-type layer stack + post-HPT + 2 nm (*n*)a-Si:H, exhibits a 7.6%$_{abs.}$ of *FF* improvement relative to the reference cell.

Similarly, we investigate the effect of different treatments for (*p*)-type layer stack in front junction solar cells as shown in Figure 4.4 (b). The reference (*i*)a-Si:H/(*p*)-type layer stack consists of 8 nm (*i*)a-Si:H + 10 nm (*p*)nc-SiO$_x$:H + 10 nm (*p*)nc-Si:H. We kept the optimized strategy of (*n*)-type layer stack (combined treatments-1) as discussed in Figure 4.5 (a) for all cells unless otherwise stated.

As illustrated in Figure 4.5 (b), compared to the reference cell, different single pre-treatments, namely, pre-HPT, (*p*)nc-Si:H seed layer and the VHF (*i*)nc-Si:H treatment improved the *FF* without deteriorating V_{OC}, which remains above 720 mV. It is worth noting that both VHF (*i*)nc-Si:H treatment and (*p*)a-Si:H capping layer were demonstrated to be effective single treatments for improving the *FF* of 2.2%$_{abs}$. from 72.1% to 74.3%. The *FF* enhancement corresponds to observed σ_d and E_a enhancements as reported in Figure 4.2 (b). However, (*p*)a-Si:H, which is highly parasitically absorptive, degraded the $J_{SC,EQE}$ from 37.0 mA/cm^2 to 35.2 mA/cm^2. Therefore, there was no gain in η_{active} by applying the (*p*)a-Si:H capping layer. Lastly, we combined pre-HPT and VHF (*i*)nc-Si:H treatment. Together with further thicknesses optimizations of layer stacks, we were able to obtain a cell with overall improved V_{OC} from 721 mV to 723 mV, $J_{SC,EQE}$ from 37.0 mA/cm^2 to 37.8 mA/cm^2, *FF* from 72.1% to 76.9% and η_{active} from 19.2% to 21.0% as compared to the reference sample. The gain of performance is expected, as discussed in Figure 4.3 (b), since (*i*)a-Si:H layer after the combined treatments, tends to promote nucleation of nanocrystals while providing excellent passivation quality to c-Si/(*i*)a-Si:H interface.

In return, as inspired by the optimized combined pre-HPT and VHF (*i*)nc-Si:H treatment for (*p*)-type layer stack, these treatments were also applied for (*n*)-type layer stack in solar cells as shown in Figure 4.4 (a). Indeed, as known from Figure 4.2 (a), by replacing (*n*)nc-Si:H seed layer (combined treatments-1) with VHF (*i*)nc-Si:H treatment (combined treatments-2), the σ_d of (*n*)-type layer stack was further improved. However, the passivation quality of solar cells before TCO was hardly preserved with direct application of (*n*)nc-SiO$_x$:H-1 layer after the pre-HPT and VHF (*i*)nc-Si:H treatment. Instead, the use of (*n*)nc-SiO$_x$:H-2 exhibited a better-preserved passivation quality when it was combined with pre-HPT+VHF (*i*)nc-Si:H treatments and even with thinner (*i*)a-Si:H layer beneath. Together with more advantageous optical properties of (*n*)nc-SiO$_x$:H-2,

Table 4.3: The illuminated *J-V* characterizations and pseudo *FF* of the best solar cells.

Cell	Cell area (cm^2)	Metal Coverage (%)	Junction position[a]	V_{OC} (mV)	J_{SC} (mA/cm^2)	*FF* (%)	η (%)	p*FF* (%)
#1	7.84	12.5	Front	718	32.9	77.9	18.4	81.0
#2			Rear	714	34.0	75.3	18.3	81.5
#3	3.92	4.4	Front	714	38.6	79.1	21.8	83.6
#4			Rear	712	39.3	78.6	22.0	83.9

[a]: Front or rear junction solar cells used either (*n*)nc-SiO_x:H-1 or (*n*)nc-SiO_x:H-2 layer, respectively.

the combination of combined treatments-2 with (*n*)nc-SiO_x:H-2 offers simultaneously better passivation and transparency, which are beneficial when they are placed on the illuminated side of solar cells. Therefore, we used combined treatment-2 with (*n*)nc-SiO_x:H-2 for further optimizing rear junction cells, together with the optimized (*p*)-type layer stacks featuring pre-HPT and VHF (*i*)nc-Si:H treatment as shown in Figure 4.5 (b). On the other hand, mainly due to the relaxed optical limitations when layer stack is applied on the rear side of solar cells, the combined treatment-1 with (*n*)nc-SiO_x:H-1 were implemented for front junction solar cells.

The *J-V* parameters of the best front and rear junction solar cells featuring a cell area of 7.84 cm^2 are listed in Table 4.3 (cells #1 and #2). The corresponding design of the front metal grid features a metal coverage of 12.5%, which limited the measured J_{SC} to a maximal 34.0 mA/cm^2. Alternatively, we redesigned the front metal grid, which allows a lower metal coverage of 4.4%. This new design was implemented with cells that have a designated area of 3.92 cm^2. By implementing the new cell design together with fine-tuning the thicknesses of layers stacks and the interfacial treatments, more performant solar cells were obtained (see Table 4.3, cells #3 and #4). Especially, the optimizations of (*p*)-layer stacks, including the thickness combinations of the (*p*)nc-SiO_x:H and (*p*)nc-Si:H from 10 nm + 10 nm (cells #1 and #2) to 4 nm + 12 nm (cells #3 and #4), are further elaborated in Chapter 5.

Thanks to the highly transparent (*n*)nc-SiO_x:H-2 layer, at least 0.7 mA/cm^2 higher J_{SC} values were obtained for rear junction cells as compared to front junction cells in both '7.84 cm^2' and '3.92 cm^2' cell designs. Nevertheless, the higher *FF* values achieved in front junction configuration yield eventually similar η for both junction configurations. Note that these cells in Table 4.3 do not have a double-layer anti-reflection coating on the front to demonstrate more clearly the transparency of our optimized (*n*)-type layer stack. Finally, cells with both front and rear junction structures achieved η of around 22.0%.

Furthermore, to clarify the advantage of using (*n*)nc-SiO_x:H layer stack over (*n*)a-Si:H layer, the *J-V* parameters and EQE curves of rear junction solar cells with either combined 8 nm (*n*)nc-SiO_x:H-2 + 3 nm (*n*)nc-Si:H + 2 nm (*n*)a-Si:H layer stack or only 6 nm (*n*)a-Si:H are compared in Table 4.4 and Figure 4.6, respectively. Note, in Table 4.4, all cells feature 8 nm (*i*)a-Si:H + pre-HPT + VHF (*i*)nc-Si:H treatment before the deposition of (*n*)-type layers.

As presented in Table 4.4, solar cells with (*n*)nc-SiO_x:H layer stack exhibited an av-

Table 4.4: The illuminated *J-V* parameters of rear-junction solar cells using different front (*n*)-type layer (stack). Results are averaged from three similar solar cells.

(*n*)-type layer (stack)	Cell area (cm^2)	Metal Coverage (%)	Junction position	V_{OC} (mV)	J_{SC} (mA/cm^2)	*FF* (%)	η (%)
(*n*)nc-SiO$_x$:H layer stack[a]	3.92	4.4	Rear	713.3 ± 1.2	38.9 ± 0.5	79.0 ± 0.3	21.9 ± 0.2
(*n*)a-Si:H[b]				712.0 ± 1.0	37.4 ± 0.3	79.4 ± 0.2	21.1 ± 0.2

[a]: 8 nm (*i*)a-Si:H + pre-HPT + VHF (*i*)nc-Si:H treatment + 8 nm (*n*)nc-SiO$_x$:H-2 + 3 nm (*n*)nc-Si:H + post-HPT + 2 nm (*n*)a-Si:H ((*n*)nc-SiO$_x$:H-2 with combined treatments-2);

[b]: 8 nm (*i*)a-Si:H + pre-HPT + VHF (*i*)nc-Si:H treatment + 6 nm (*n*)a-Si:H.

erage efficiency gain of 0.8%$_{abs.}$ as compared to the (*n*)a-Si:H counterparts, primarily thanks to an average gain of 1.5 mA/cm^2 in their J_{SC}. Specifically, Figure 4.6 further reveals that the use of (*n*)nc-SiO$_x$:H layer stack led to a significantly enhanced EQE response from 300 nm to 650 nm and a slightly improved infrared response (from 1000 nm to 1200 nm).

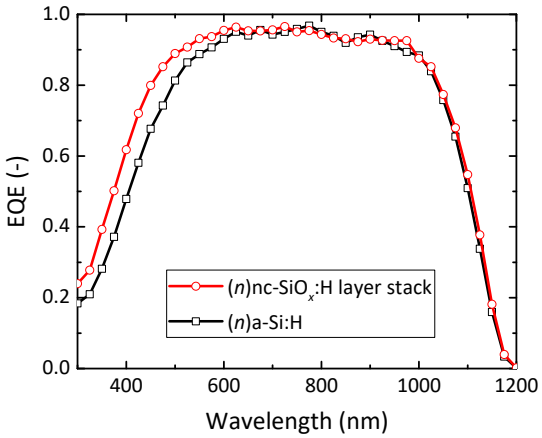

Figure 4.6: The EQE curves of rear junction cells with only 6 nm (*n*)a-Si:H layer and 8 nm (*n*)nc-SiO$_x$:H-2 + 3 nm (*n*)nc-Si:H + 2 nm (*n*)a-Si:H layer stack.

Even though transport mechanisms have been unveiled for achieving ultimate *FF* in SHJ cells [150], the pre-conditioning for achieving optimum growth of layers, less resistive interfaces and other experimental steps, such as pre- and post-treatments as well as back-end metallization, heavily impact the road towards more efficient transport of charge carriers. The notable difference between p*FF* and *FF* as seen in Table 4.3 indicates further optimization efforts are required to minimize the transport resistivity of charge carriers. In this respect, a measurement of the contact resistance between doped layer stacks and TCO layers would provide more insights. Therefore, Chapter 5 further details the design and optimization of hole collectors based on extracted contact resistivities of doped contact stacks.

Last but not least, additional optimizations of TCO and front metal grid are required for improving further the cell efficiency. It is expected that solar cells with mainly doped nc-SiO$_x$:H and nc-Si:H layer stacks, combined with (i) thinner wafers, (ii) lower metallization fraction and (iii) high-mobility TCOs, such as hydrogenated fluorine-doped indium oxide [327], will enable efficiency well beyond 23% even without double-layer anti-reflective coating. Moreover, we also expect that doped nc-Si:H-based layers deposited under VHF will deliver better layer properties and cell performances than layers deposited under RF.

4.4 Conclusions

In this chapter, we developed transparent carrier-selective transport layers mainly based on nc-SiO$_x$:H alongside interfacial treatments to improve carrier collection in SHJ solar cells.

Doped nc-SiO$_x$:H layers featuring state-of-the-art opto-electrical properties were achieved, and the selected layers were integrated into FBC-SHJ solar cells. We observed improved electrical properties (E_a and σ_d) of test structures after pre-treatments (pre-HPT, oxygen-absent nc-Si:H seed layer and VHF (*i*)nc-Si:H treatment) and also excellent passivation on c-Si/(*i*)a-Si:H interface with an τ_{eff} over 11 ms when combined pre-HPT and VHF (*i*)nc-Si:H treatments were applied. The post-treatments, especially 2 nm of (*n*)a-Si:H and (*p*)a-Si:H capping layer applied on (*n*)-type and (*p*)-type layer stacks, respectively, exhibited significant improvements on σ_d from 0.79 S/cm to 2.03 S/cm for (*n*)-type layer stacks and from 0.02 S/cm to 0.07 S/cm for (*p*)-type layer stacks. Eventually, we implemented various interfacial treatments into front/back-contacted SHJ solar cells giving a guideline for nanocrystalline film development. We monitored the *FF* and V_{OC} to evaluate the effects of different treatments, which affect the nucleation of doped layers and/or their interface with ITO. Combining optimized interfacial treatments on the layer stacks, we improved the *FF* from 65.6% in a rear junction cell to 77.9% in a front junction cell with a cell area of 7.84 cm^2. Furthermore, cells with an area of 3.92 cm^2 featuring further reduced metal coverage demonstrated improvements of *FF* from 77.9% to 79.1% and 75.3% to 78.6%, thus enhancements of η from 18.4% to 21.8% and 18.3% to 22.0% for front and rear junction solar cells, respectively, with the perspective of further improvements by optimizing the front metal grid, bulk thickness and using more transparent TCO.

5

Design and optimization of hole collectors based on nc-SiO$_x$:H for SHJ solar cells

This chapter is based on the publication:

Y. Zhao, P. Procel, C. Han, L. Mazzarella, G. Yang, A. Weeber, M. Zeman, and O. Isabella, "Design and optimization of hole collectors based on nc-SiO$_x$:H for high-efficiency silicon heterojunction solar cells," *Solar Energy Materials and Solar Cells*, vol. 219, p. 110779, 2021. [1]

Abstract

Low activation energy (E_a) and wide bandgap (E_g) are favored for (p)-contacts to achieve effective hole collection in silicon heterojunction (SHJ) solar cells. In this work, we studied PECVD (p)-type hydrogenated nanocrystalline silicon oxide, (p)nc-SiO$_x$:H, combined with (p)nc-Si:H as (p)-contact in front/back-contacted SHJ solar cells. We first evaluated the effect of hydrogen plasma treatments applied at the (i)a-Si:H/(p)-contact interface on the thickness-dependent E_a of (p)-contacts. Notably, when the (p)nc-Si:H layer is thinner than 20 nm, the E_a of (p)-contacts was decreased by applying the combined hydrogen plasma treatment and very-high-frequency (i)nc-Si:H treatment. Such combined interface treatments also significantly reduced the contact resistivity of the (p)-contact stacks ($\rho_{c,p}$), resulting in an improvement of 6.1%$_{abs.}$ in *FF* of the completed solar cells. Thinning down the (i)a-Si:H passivating layer to 5 nm leads to a low $\rho_{c,p}$ (144 m$\Omega \cdot$cm^2) for (p)-contact stacks. Interestingly, we observed an increment of *FF* from 72.9% to 78.3% by using (p)nc-SiO$_x$:H layers featuring larger differences between their optical gap (E_{04}) and E_a, which tend to enhance the built-in potential at the c-Si/(i)a-Si:H interface. Furthermore, we observed clear impacts on $\rho_{c,p}$, V_{OC}, and *FF*

[1] This paper was invited for publication in the special issue 'SiliconPV 2020' of Solar Energy Materials and Solar Cells, Proceedings of the 10th International Conference on Silicon Photovoltaics.

by optimizing the thicknesses of (*p*)-contacts that influence their E_a. In front junction solar cells, the vertical and lateral transport of holes towards the front metal electrode is affected by $\rho_{c,p}$ of (*p*)-contact stacks. This observation is also supported by TCAD simulations which revealed different components of lateral contributions. Lastly, we obtained both front junction and rear junction solar cells with certified *FF* well-above 80% and the best efficiency of 22.47%.

5.1 Introduction

Front/back-contacted silicon heterojunction (FBC-SHJ) solar cells with carrier-selective passivating contacts based on hydrogenated amorphous silicon (a-Si:H) achieved conversion efficiency well-above 25% [129]. However, the application of (*p*)a-Si:H for hole collection is challenging because of its high parasitic absorption [156] and moderate doping efficiency [152–154]. The latter imposes constraints on the energy alignment for charge carrier transport from c-Si bulk to the indium tin oxide (ITO) transparent conductive oxide (TCO), thus limiting the device fill factor (*FF*) and open-circuit voltage (V_{OC}) [150, 151, 155, 214, 381, 382]. A theoretical study performed by our group [150] suggests that an efficient (*p*)-contact prefers a wide bandgap (E_g) and a low activation energy (E_a) for improving the junction built-in voltage (V_{bi}), thus improving the selectivity for holes. Specifically, we assume a heterostructure that consists of a (*n*)c-Si substrate and a (*p*)-type layer. For simplicity, we neglect the (*i*)-type layer in between the (*n*)c-Si and the (*p*)-type layer. Under thermal equilibrium, the band bending at (*n*)c-Si/(*p*)-type layer interface is indicated by the V_{bi} and it is defined as [150]:

$$V_{bi} = \phi_p - \phi_n \tag{5.1}$$

and

$$\phi_p = \chi_{e,p} + E_{g,p} - E_{a,p} \tag{5.2}$$

with ϕ_p the work function of the (*p*)-type layer, ϕ_n the work function for the (*n*)c-Si substrate, $\chi_{e,p}$ the electron affinity of the (*p*)-type layer, $E_{g,p}$ and $E_{a,p}$ the bandgap and activation energy of the (*p*)-type layer, respectively. By substituting equation 5.2 into equation 5.1, we obtain:

$$V_{bi} = \chi_{e,p} + E_{g,p} - E_{a,p} - \phi_n \tag{5.3}$$

Since ϕ_n is fixed for the (*n*)c-Si and the $\chi_{e,p}$ is assumed constant for silicon thin-film layers [383], to maximize the V_{bi} (and also c-Si band bending), a maximal $E_{g,p} - E_{a,p}$ is preferred. That is, the requirement for a low $E_{a,p}$ (*p*)-type layer is relaxed if the layer also features a higher $E_{g,p}$ [150].

As already discussed in Chapter 4, hydrogenated nanocrystalline silicon oxide (nc-SiO$_x$:H), featuring tunable and superior opto-electrical properties over standard a-Si:H, has been proposed as carrier-selective passivating contact and implemented in SHJ solar cells [160, 173–175, 300, 362, 363, 384–392]. Specifically, E_a and E_g of nc-SiO$_x$:H can be so finely tuned that efficient selective transport of charge carriers can be achieved. To further improve the selective transport of holes, (*p*)nc-SiO$_x$:H and (*p*)nc-Si:H can be combined in a (*p*)-contact stack [150]. Indeed, aside from their optical advantages over the

standard doped a-Si:H layers [164, 175], the bi-layer (*p*)-contact minimizes the transport losses by (i) improving the hole accumulation at c-Si/(*i*)a-Si:H interface with a wide E_g (*p*)nc-SiO$_x$:H, and (ii) enhancing the charge exchange from (*p*)-contact to ITO and also the band bending near the c-Si/(*i*)a-Si:H interface with a low E_a (*p*)nc-Si:H layer. Due to the substrate-dependent and thickness-dependent growth characteristics of (*p*)nc-SiO$_x$:H [176], prompt nucleation of nanocrystals [175] is required for its implementation into SHJ solar cells featuring an (*i*)a-Si:H passivation layer, thus achieving a low E_a (*p*)-contact close to the c-Si/(*i*)a-Si:H interface.

To provide more insights about the transport mechanisms of charge carriers, efforts have been devoted to investigating the origins of solar cell series resistance (R_{series}), revealing contributions from the bulk of the component materials and their discontinuous interfaces due to different E_g of adjacent materials [216, 393–395]. Among those contributions, doped contact stacks are interesting due to their major contributions to the total device R_{series} [212, 217, 396–398] in terms of contact resistivity (ρ_c). Experimental [201] and theoretical studies [151] reveal close correlations between ρ_c and external parameters (*FF* and V_{OC}) of solar cells, where ρ_c can be tuned by adjusting the properties of the doped layer (E_a and E_g) and the TCO layer (carrier concentration, N_{TCO}). In other words, manipulation of those electrical properties in bi-layer hole collectors based on (*p*)nc-SiO$_x$:H and (*p*)nc-Si:H determines the alignment of energy states and thus the effectiveness of the charge carrier transport. The transport mechanisms of charge carriers are discussed in detail in Section 2.3.

In this chapter, we first investigated the thickness-dependent E_a of the bi-layer charge carrier collectors based on (*p*)nc-SiO$_x$:H and (*p*)nc-Si:H as a function of interfacial treatments [175]. Afterwards, we assessed the $\rho_{c,p}$ of (*p*)-contact stacks under varying contacting conditions. Accordingly, we evaluated the effect of $\rho_{c,p}$ on the V_{OC} and *FF* of FBC-SHJ solar cells. To infer the hole transport losses, we decomposed the R_{series} of solar cells in vertical and lateral contributions and we conducted advanced device simulations to understand the lateral collection mechanism of holes in various front junction cell configurations.

5.2 Methodology

We present in Table 5.1 the PECVD deposition conditions of (*p*)-contact investigated in this study. We determined the optical bandgap (E_{04}) of the thin-film layers with SCOUT software [335, 336]. In solar cells, 75 nm and 150 nm indium tin oxide (ITO) were deposited on the front and rear sides, respectively. Solar cells studied in this chapter feature a designated cell area of 3.92 m^2.

TCAD Sentaurus from Synopsys Inc. was used for numerical simulations with experimentally measured geometry, E_a, and E_{04} as input parameters [399]. More details about models and parameters can be found in previous studies [150, 151, 201]. In this chapter, we used (*i*)a-Si:H, (*p*)nc-SiO$_x$:H, (*p*)nc-Si:H, ITO, Ag electrodes as shown in Figure 5.1 for the collection of holes. These layers induce band bending inside the c-Si, which is referred to as the space-charge layer inside the (*n*)c-Si bulk in this study. Therefore, we define the (*p*)-contact stack that consists of a space-charge layer inside the (*n*)c-Si bulk, (*i*)a-Si:H, (*p*)nc-SiO$_x$:H, (*p*)nc-Si:H, ITO, and Ag. A schematic sketch of the band diagram of (*p*)-contact stack (till ITO) is given in Figure 5.1 [150].

Table 5.1: PECVD parameters for optimization of (*p*)nc-SiO$_x$:H, (*p*)nc-Si:H, HPT, VHF (*i*)nc-Si:H treatment.

PECVD parameters	(*p*)nc-SiO$_x$:H	(*p*)nc-Si:H	HPT	VHF (*i*)nc-Si:H
Frequency (MHz)	13.56	13.56	13.56	40.68
Temperature (°C)	180	180	180	180
Pressure (mbar)	1.4 – 3	2.2	2.2	4
Power density (mW/cm^2)	76	90	63	69
SiH_4 (sccm)	0.8	0.8	-	1.2
H_2 (sccm)	170	170	200	120
CO_2 (sccm)	1.4	0	-	-
B_2H_6[a] (sccm)	10	10	-	-
Deposition rate[b] (nm/s)	0.018 – 0.036	0.047	-	~0 [c]
Duration (s)	-	-	120	120

[a]: 200 ppm in H_2;
[b]: The deposition rate refers to layers deposited on the flat glass substrates;
[c]: The deposition is hardly detectable by SE measurement after 6 minutes of deposition.

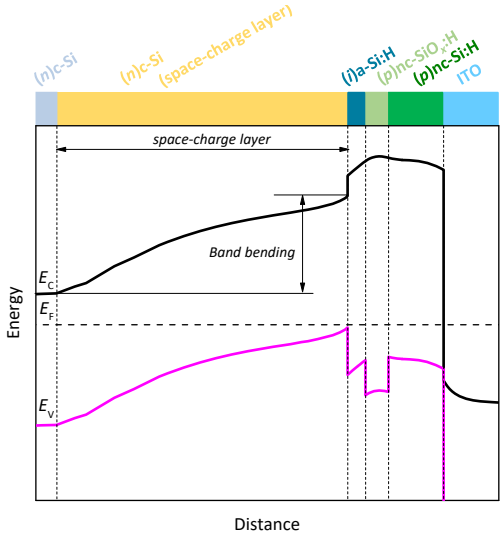

Figure 5.1: The band diagram under the dark thermal equilibrium condition (diagram) of the proposed (*p*)-contact stack for SHJ solar cells with the bi-layer (*p*)-contact. In general, the (*p*)-contact stack consists of a space-charge layer inside the (*n*)c-Si bulk, (*i*)a-Si:H, (*p*)nc-SiO$_x$:H, (*p*)nc-Si:H, ITO, and Ag (not shown here). Figure adapted from [150].

5.3 Results and Discussions

5.3.1 Activation energy of the (*p*)-layer stack

The bi-layer (*p*)-contacts, consisting of a (*p*)nc-SiO$_x$:H (10 nm) and a (*p*)nc-Si:H (varied thickness), were deposited on glass substrates coated with an (*i*)a-Si:H (10 nm). This test structure aims for taking into account the substrate-dependent growth of nc-SiO$_x$:H thin-films, which is relevant in SHJ solar cells [176]. We assessed the E_a and σ_d of the (*p*)-contact with schematic structures given in Figure 5.2. To accelerate the nucleation of the (*p*)nc-SiO$_x$:H, we additionally applied a combined interface treatment including hydrogen plasma treatment (HPT) and very-high-frequency (VHF) (*i*)nc-Si:H treatment (thereafter, simply denoted as HPTs) before the (*p*)-contact deposition, as is proposed in Chapter 4 [175]. The thickness-dependent E_a and σ_d of (*p*)-contacts with and without interface treatment are illustrated in Figure 5.2.

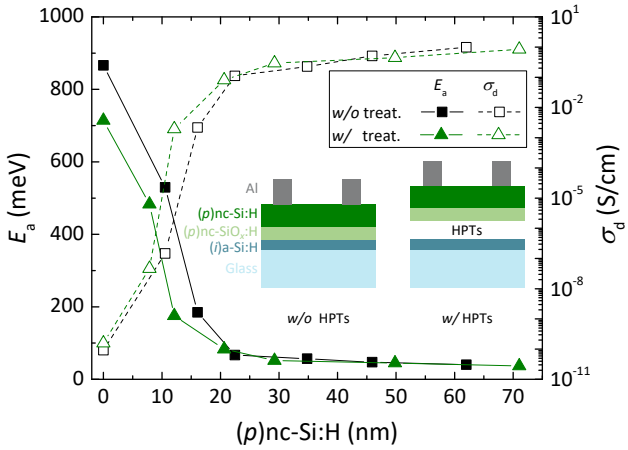

Figure 5.2: The influence of interfacial HPT + VHF treatment (HPTs) on E_a and σ_d of bi-layer (*p*)-contact consisting of a 10-nm-thick (*p*)nc-SiO$_x$:H and a (*p*)nc-Si:H with varied thickness. The insets illustrate the schematic structures for assessing E_a and σ_d of the bi-layer (*p*)-contacts.

As depicted in Figure 5.2, similar to what has been reported by Roca i Cabarrocas et al, [176], E_a decreased and σ_d increased in both types of (*p*)-contacts (*w*/*o* and *w*/ HPTs) with increasing (*p*)nc-Si:H thickness. Both E_a and σ_d tend to gradual saturation for (*p*)nc-Si:H thicknesses above around 20 nm (see Figure 5.2). Besides this general trend, we also observed that the HPTs induced improvements in the electrical properties of (*p*)-contacts, especially, when (*p*)nc-Si:H is thinner than 20 nm. In other words, the HPTs promote the formation of slightly more conductive layers with lower E_a values and thus potentially a better performing (*p*)-contact for SHJ solar cell applications. Therefore, the HPTs were chosen to enhance the selective transport of holes [150], because it may lead to reduced resistive losses and therefore higher *FF*s in completed solar cells.

5.3.2 Contact resistivity of the contact stacks

As shown in Figure 5.3 (b), symmetrical samples were prepared with doped contact stacks that originate from solar cells, as schematically sketched in Figure 5.3 (a), to extract the ρ_c of dope contact stacks [396]. The method of obtaining the ρ_c is described in detail in Section 3.2.2. With this, we first studied the effects of the HPTs and the thickness of (*i*)a-Si:H layer on the $\rho_{c,p}$ of the (*p*)-contact stacks. Then, we assessed the effects of (*p*)nc-SiO$_x$:H layers that featured different E_{04} and E_a. Lastly, we investigated the $\rho_{c,p}$ by varying the thickness combinations in the bi-layer (*p*)-contact.

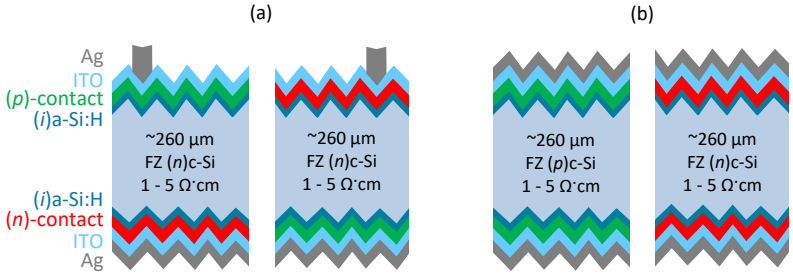

Figure 5.3: Schematic sketches of (a) the front junction (left) and rear junction (right) solar cells studied in this chapter, and (b) symmetrical samples for extracting the ρ_c of (*p*)-type (left) and (*n*)-type (right) contact stacks. The (*n*)-contact represents either (*n*)a-Si:H or the optimized (*n*)nc-SiO$_x$:H-based layer stack as discussed in Chapter 4 [175], where the (*p*)-contact refers to the (*p*)nc-SiO$_x$:H + (*p*)nc-Si:H layer stack. In (b), we used either (*p*)- or (*n*)-type c-Si bulk for studying the (*p*)- or (*n*)-contact stacks, respectively.

Effect of the HPTs and (*i*)a-Si:H layer thickness on contact resistivity

To investigate the effect of the HPTs and the thickness of (*i*)a-Si:H layer on $\rho_{c,p}$ of the (*p*)-contact stacks, we fabricated symmetrical samples, following the structure depicted in Figure 5.3 (b), with (*p*)-contact consisting of a 4-nm-thick (*p*)nc-SiO$_x$:H and a 16-nm-thick (*p*)nc-Si:H layer. We evaluated carrier transport and passivation quality in terms of $\rho_{c,p}$ of (*p*)-contact stacks and iV_{OC} of the symmetrical samples before ITO sputtering, as shown in Figure 5.4.

Looking at the samples with a 7-nm-thick (*i*)a-Si:H (see Figure 5.4), it is noticeable that the HPTs significantly reduced the average $\rho_{c,p}$ from 1221 m$\Omega\cdot$cm^2 down to 325 m$\Omega\cdot$cm^2. As the $\rho_{c,ITO/Ag}$ of ITO/Ag interface is around 1.5 m$\Omega\cdot$cm^2 [327], its contribution is negligible to the total $\rho_{c,p}$ of the contact stack. The reduced $\rho_{c,p}$ then reflects the improvement of contacts from c-Si to ITO, which indicates that the HPTs enabled enhanced selectivity for the transport of holes. This beneficial effect on $\rho_{c,p}$ is consistent with the reduced E_a of the (*p*)-contact [150] as is shown in Figure 5.2. Furthermore, the HPTs boosted the passivation quality of the (*p*)-type wafer, resulting in an iV_{OC} improvement of 18 mV which is similar to what was reported previously for the (*n*)-type wafer after applying the optimized HPTs [175]. By further thinning the (*i*)a-Si:H layer thickness from 7 nm to 5 nm, the $\rho_{c,p}$ was cut down to 144 m$\Omega\cdot$cm^2, which is lower than the majority of reported values in literature featuring either (*p*)a-Si:H or (*p*)nc-Si:H as (*p*)-contact [164, 201, 217, 396–398, 400]. Nevertheless, it is not our intention to pass any unfair argument on the goodness of (*p*)nc-SiO$_x$:H-based (*p*)-contact with respect to the (*p*)a-Si:H

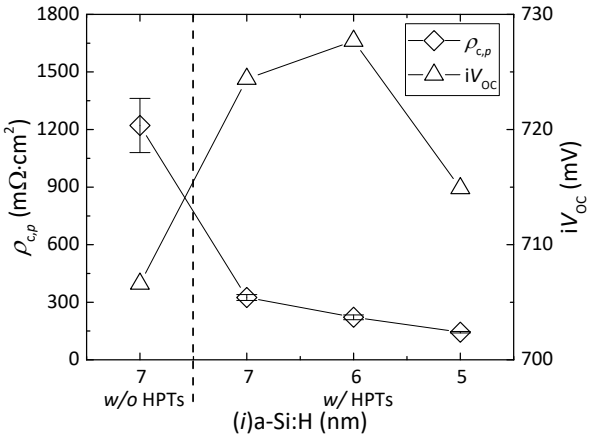

Figure 5.4: The contact resistivity $\rho_{c,p}$ and iV_{OC} of (*p*)-contact stacks without and with HPT + VHF (*i*)nc-Si:H interface treatment (or simply denoted as HPTs), and depending on the (*i*)a-Si:H layer thickness. The passivation quality of the symmetrical test samples was measured before ITO sputtering. The results present averaged $\rho_{c,p}$ from two symmetrical samples and the error bars represent the standard deviations.

contact with the context provided. Specifically, $\rho_{c,p}$ was reduced more than twice by reducing the thickness of the (*i*)a-Si:H layer by only 2 nm. This layer is directly beneath the (*p*)-contact and applying a thinner layer does hardly impact the passivation quality. This observation on the reduction of $\rho_{c,p}$ with a thinner (*i*)a-Si:H is in line with the trends that have been reported by Leilaeioun et al. with a (*p*)a-Si:H layer [397]. Indeed as reported by others [400–402], a thinner (*i*)a-Si:H may improve the carrier collections through increased carrier tunneling probability. Within this series, a 6-nm-thick (*i*)a-Si:H layer delivered the highest iV_{OC} of 728 mV and a relatively low $\rho_{c,p}$ of 222 m$\Omega \cdot$cm^2. Thus we implemented this (*i*)a-Si:H layer thickness together with the HPTs in the samples that will be discussed in the following sections.

Effect of opto-electrical properties of (*p*)nc-SiO$_x$:H on contact resistivity

To maximize the $V_{bi,p}$ at the c-Si/(*i*)a-Si:H interface and, thus, the hole accumulation at the c-Si/(*i*)a-Si:H interface [150], we applied (*p*)nc-SiO$_x$:H with a varying difference between E_{04} and E_a by adjusting the deposition pressure as given in Table 5.1, where E_{04} is considered as an indication of the layer's mobility gap (E_g) [232]. Here, we compared symmetrical test samples, which featured a 4-nm-thick (*p*)nc-SiO$_x$:H deposited after the optimized HPTs and coated with a 12-nm-thick (*p*)nc-Si:H layer. To extract the E_a and E_{04} of the three different (*p*)nc-SiO$_x$:H layers, slightly different from the structure shown in Figure 5.2, we deposited 20-nm-thick (*p*)nc-SiO$_x$:H layers on glass substrates without the (*i*)a-Si:H coating. The measured E_a and E_{04} of (*p*)nc-SiO$_x$:H layers are given in Table 5.2 and indicated as Type-*a*, Type-*b*, and Type-*c*. Then, we evaluated the iV_{OC} of symmetrical samples before ITO sputtering and $\rho_{c,p}$ of (*p*)-contact stacks endowed with (*p*)nc-SiO$_x$:H layers featuring various $E_{04} - E_a$ values. The results are shown in Figure 5.5.

Table 5.2: The opto-electrical properties of three types of (p)nc-SiO$_x$:H layers prepared with different deposition pressure.

(p)nc-SiO$_x$:H	Deposition pressure (mbar)	E_{04} (eV)	E_a (meV)	$E_{04} - E_a$ (eV)
Type-a	3.0	2.19	320	1.870
Type-b	2.2	2.36	353	2.007
Type-c	1.4	2.51	424	2.086

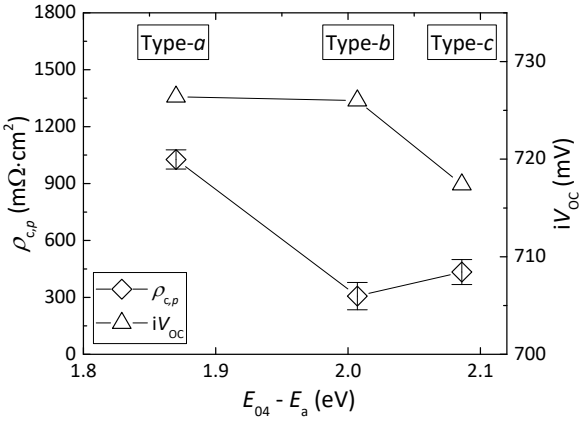

Figure 5.5: The contact resistivity $\rho_{c,p}$ and iV_{OC} of (p)-contact stacks with (p)nc-SiO$_x$:H layers featuring various $E_{04} - E_a$. The passivation quality of the symmetrical test samples was measured before ITO sputtering. The results present averaged $\rho_{c,p}$ from two symmetrical samples and the error bars represent the standard deviations.

As illustrated in Figure 5.5, by widening the $E_{04} - E_a$ difference from Type-a to Type-b (from 1.870 eV to 2.007 eV), $\rho_{c,p}$ of the (p)-contact stacks significantly drops. Its value was reduced from 1027 m$\Omega \cdot$cm^2 to 307 m$\Omega \cdot$cm^2. We ascribe the reduction of $\rho_{c,p}$ by using Type-b (p)nc-SiO$_x$:H layer to the improved $V_{bi,p}$, which indicates an enhanced band bending at the c-Si/(i)a-Si:H interface and therefore an increased hole accumulation [150]. By using Type-c (p)nc-SiO$_x$:H layer, which features much higher E_a and $E_{04} - E_a$ as compared to that of Type-a (p)nc-SiO$_x$:H layer, the $\rho_{c,p}$ of the contact stacks was also significantly reduced. A degradation in iV_{OC} was observed for the sample with Type-c (p)nc-SiO$_x$:H as compared to samples with Type-a and Type-b (p)nc-SiO$_x$:H. We ascribe this to the loss in chemical passivation of (i)a-Si:H, which is sensitive to the varied plasma conditions for realizing the opto-electrical properties of Type-c (p)nc-SiO$_x$:H. Therefore, considering both passivation quality and electrical behavior, Type-b (p)nc-SiO$_x$:H is preferred for solar cell fabrication.

Effect of thickness combinations of the bi-layer (p)-contact on contact resistivity

Aside from building up a sufficient $V_{bi,p}$ at the c-Si/(i)a-Si:H interface, a low E_a (p)-contact is critical for achieving an effective transport of holes from the (p)-contact to the ITO. As known from the thickness-dependent E_a of (p)-contact discussed in Section

5.3.1, we tuned the E_a of the (p)-contact via varying the thickness combinations between (p)nc-SiO$_x$:H and (p)nc-Si:H. In Figure 5.6, we present their influence on $\rho_{c,p}$ of the symmetrical test samples.

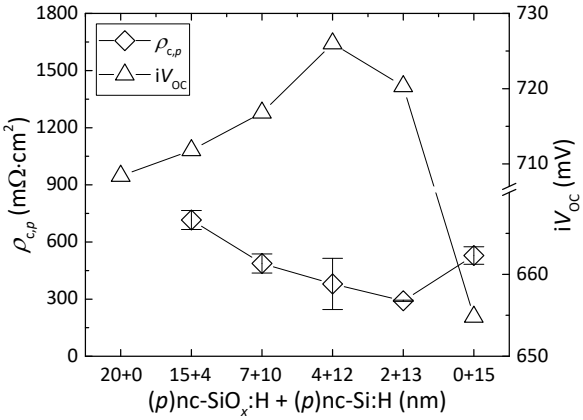

Figure 5.6: The contact resistivity $\rho_{c,p}$ and iV_{OC} of (p)-contact stacks with varying (p)nc-SiO$_x$:H and (p)nc-Si:H layer thicknesses. The passivation quality of the symmetrical test samples was measured before ITO sputtering. The results present averaged $\rho_{c,p}$ from two symmetrical samples and the error bars represent the standard deviations.

As can be seen in Figure 5.6, the average $\rho_{c,p}$ decreased to a minimum of 291 mΩ·cm^2 with increasing thickness fraction of (p)nc-Si:H. The $\rho_{c,p}$ reduction can be explained by the thickness-dependent E_a of the (p)-contact as shown in Figure 5.2. Indeed, by lowering the E_a, not only the band bending at the c-Si/(i)a-Si:H interface enhances, but also the potential barrier for holes decreases [150]. Both effects can contribute to the more efficient transport of holes from c-Si to ITO. Besides, this also explains the enhanced iV_{OC} up to 726 mV by increasing the (p)nc-Si:H thickness. It is worth noting that in the absence of (p)nc-Si:H (20 + 0 nm) beneath the ITO layer, we observed a diode behavior of the symmetrical test sample. We ascribe this to an excessively large transport barrier at the (p)-contact/ITO interface possibly due to a parasitic junction in our 20-nm-thick (p)nc-SiO$_x$:H. Further, the complete removal of the (p)nc-SiO$_x$:H (0 + 15 nm) resulted in an iV_{OC} of only 655 mV, which indicates a very defective c-Si/(i)a-Si:H interface. In return, this defective interface might also negatively affect the $\rho_{c,p}$ of the contact stacks. Therefore, the best thickness combination in terms of both iV_{OC} and $\rho_{c,p}$ was found for the stack with 4 nm (p)nc-SiO$_x$:H + 12 nm (p)nc-Si:H. The presence of a 4 nm thick (p)nc-SiO$_x$:H layer not only guarantees an excellent passivation quality but also enhances the band bending at c-Si/(i)a-Si:H interface.

To sum up, we found that the application of the HPTs together with a thinner (i)a-Si:H layer is crucial to minimize the carrier transport losses ($\rho_{c,p}$) in the (p)-contact stacks. We also observed (p)nc-SiO$_x$:H with a larger $E_{04} - E_a$ difference is critical for a significant reduction of $\rho_{c,p}$. Lastly, a bi-layer (p)-contact with a thicker (p)nc-Si:H tends to deliver a lower $\rho_{c,p}$.

5.3.3 Solar cells

The studies about $\rho_{c,p}$ of (p)-contact stacks reveal various possible approaches to reduce the $\rho_{c,p}$ by improving the selectivity and minimizing the transport losses of holes. Accordingly, these approaches were further evaluated in both front and rear junction SHJ solar cells, as sketched in Figure 5.3 (a), to analyze their influence on the resistivity and performance of solar cells. To this purpose, we first extracted the solar cell's p*FF* via Suns-V_{OC} measurement and then used the p*FF* to evaluate the solar cell's $R_{s,SunsVoc}$ (with a unit of m$\Omega \cdot$cm^2) (see Section 3.2.2) [52, 351, 352]. In the subsequent sections, the key performance metrics (V_{OC}, *FF*, p*FF* and $R_{s,SunsVoc}$) of solar cells are presented and discussed as the trend in efficiency of these solar cells is primarily influenced by the *FF* of these devices.

Effect of the HPTs and (*i*)a-Si:H layer thickness on solar cell performance

We fabricated front junction solar cells that feature an (n)a-Si:H as (n)-contact at the rear side, while optionally applying the HPTs and varying (i)a-Si:H layer thickness before the deposition of the front (p)-contact stack (4 nm (p)nc-SiO$_x$:H + 16 nm (p)nc-Si:H). The key performance metrics of solar cells are depicted in Figure 5.7.

As shown in Figure 5.7, the HPTs boosted the average *FF* from 70.9% to 77.0% corresponding to a halved $R_{s,SunsVoc}$ from 2920 m$\Omega \cdot$cm^2 to 1440 m$\Omega \cdot$cm^2. This reduction in $R_{s,SunsVoc}$ is expected from the previous contact resistivity study discussed in Figure 5.4, where we observed a more-than-twice reduction in the $\rho_{c,p}$ of the (p)-contact stacks by applying the HPTs. By reducing the thickness of the (i)a-Si:H layer beneath the (p)-contact from 7 to 5 nm, we observed a 2.3%$_{abs.}$ *FF* gain without significant loss in V_{OC}. Accordingly, the average $R_{s,SunsVoc}$ reduced from 1440 m$\Omega \cdot$cm^2 to 930 m$\Omega \cdot$cm^2. Therefore, (i)a-Si:H with a thickness of around 5 to 6 nm is promising to improve the device *FF* while preserving V_{OC}.

Effect of opto-electrical properties of (p)nc-SiO$_x$:H on cell performances

In Figure 5.8, we present the effect of (p)nc-SiO$_x$:H layers featuring various $E_{04}-E_a$ values on *J*-*V* parameters of rear junction FBC-SHJ solar cells ((p)-contact located on the rear side). These results highlight the effect of $E_{04} - E_a$ on the vertical collections of holes. The thickness of the (i)a-Si:H layer under the (p)-contact is 6 nm. The front side of the solar cells features an (n)a-Si:H layer as (n)-contact.

As shown in Figure 5.8, we observed a slight decrease of V_{OC} from 720 to 717 mV but an improvement in *FF* from 72.9% to 78.3% with increasing $E_{04} - E_a$. Correspondingly, the extracted average $R_{s,SunsVoc}$ was halved from 2002 m$\Omega \cdot$cm^2 down to 972 m$\Omega \cdot$cm^2. Since the (p)-contact stacks are placed at the rear side of the solar cells, we can conclude the gain in *FF* mainly comes from the reduced vertical resistance contribution, which originates from decreased $\rho_{c,p}$ of the (p)-contact stacks as discussed in Figure 5.5.

Effect of thickness combinations of the bi-layer (p)-contact on cell performance

To evaluate the influence of the (p)-contact including the different thickness combinations, we compared V_{OC} and *FF* of FBC-SHJ solar cells with different layer stacks as mentioned in Figure 5.6. The *J*-*V* parameters of both front and rear junction configurations are presented in Figures 5.9 and 5.10, respectively.

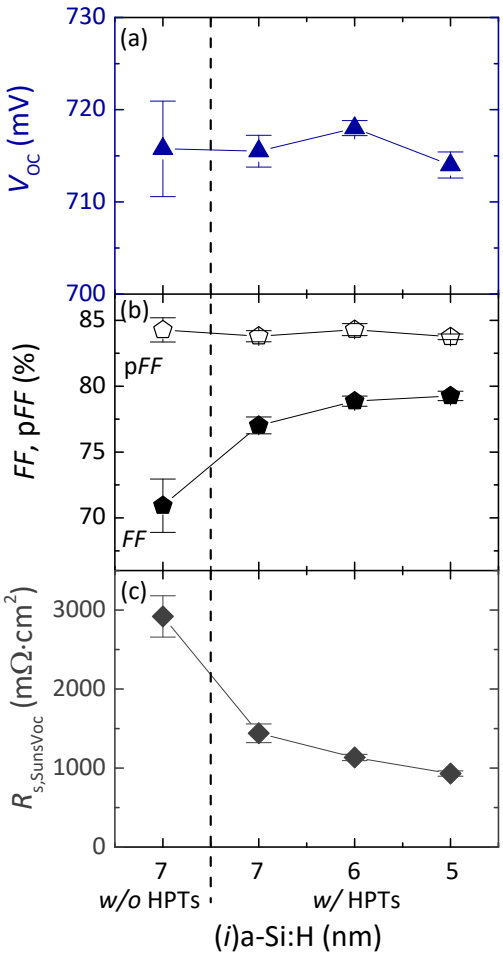

Figure 5.7: Front junction FBC-SHJ solar cells processed without and with HPT + VHF (*i*)nc-Si:H interface treatment (or simply denoted as HPTs) with varying thicknesses of (*i*)a-Si:H beneath the (*p*)-contact (4 nm (*p*)nc-SiO$_x$:H + 16 nm (*p*)nc-Si:H): (a) V_{OC}; (b) *FF* and p*FF*; (c) $R_{s,SunsVoc}$. Solar cells feature a nominal 3.2% front metal coverage. The results present averaged parameters from four solar cells (the sample with 5 nm (*i*)a-Si:H represents the results of two cells). The error bars represent the standard deviations.

In the series of front junction cells as shown in Figure 5.9, (*n*)-contact based on (*n*)nc-SiO$_x$:H as previously optimized in Chapter 4 was applied on the rear side [175]. We observed that V_{OC} and *FF* change simultaneously with increasing the thickness fraction of (*p*)nc-Si:H. As compared to cells with only 20 nm (*p*)nc-SiO$_x$:H as (*p*)-contact, solar cells with (*p*)nc-Si:H layers exhibited significant *FF* improvements, revealing the crucial role of a low E_a layer that is in contact with the ITO and additionally enhancing the band bending at the c-Si/(*i*)a-Si:H interface [175]. Indeed, *FF* was increased by more than 8.5%$_{abs.}$ to up to 79.5% by applying the '4 + 12 nm' (*p*)-contact combination. Accordingly,

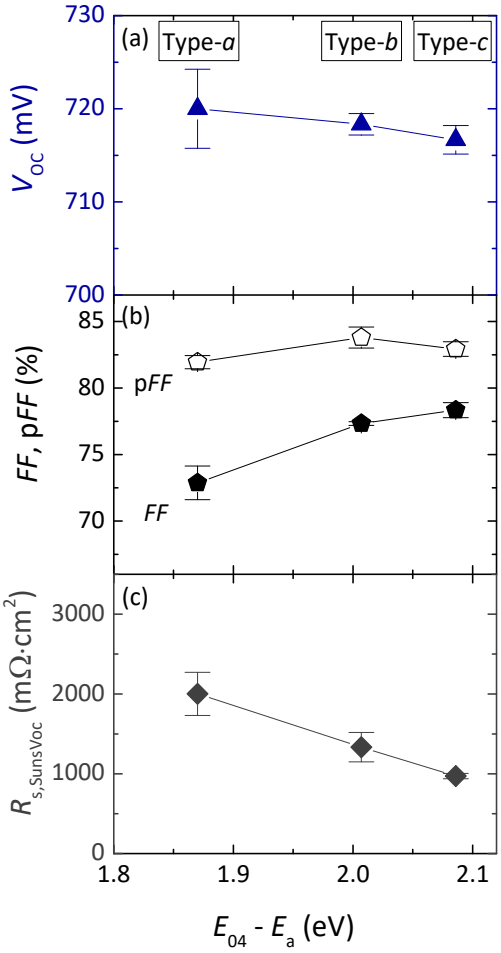

Figure 5.8: Rear junction FBC-SHJ solar cells with (*p*)nc-SiO$_x$:H featuring varying $E_{04} - E_a$ in the (*p*)-contact (4 nm (*p*)nc-SiO$_x$:H + 16 nm (*p*)nc-Si:H): (a) V_{OC}; (b) *FF* and p*FF*; (c) $R_{s,SunsVoc}$. Solar cells feature a nominal 4.4% front metal coverage. The results represent averaged parameters from three solar cells (the sample with Type-*a* (*p*)nc-SiO$_x$:H represents the results of two cells). The error bars represent the standard deviations.

the average $R_{s,SunsVoc}$ was also reduced from 2310 m$\Omega \cdot$cm^2 down to 950 m$\Omega \cdot$cm^2 for all cells with a (*p*)-contact consisting of both (*p*)nc-SiO$_x$:H and (*p*)nc-Si:H. In the meanwhile, the V_{OC} was also improved from 692 mV to 714 mV when using the optimized '4 + 12 nm' (*p*)-contact combination. Due to the aggressive deposition conditions of our (*p*)nc-Si:H, at least 4 nm of (*p*)nc-SiO$_x$:H was again proven to be necessary to preserve the device passivation quality, which also affects the *FF*. Moreover, for cells with only 15 nm of (*p*)nc-Si:H, we also observed an increased average $R_{s,SunsVoc}$ when the cell was poorly passivated.

Lastly, (*p*)-contacts with a fixed 4-nm thick (*p*)nc-SiO$_x$:H and with a varying thickness

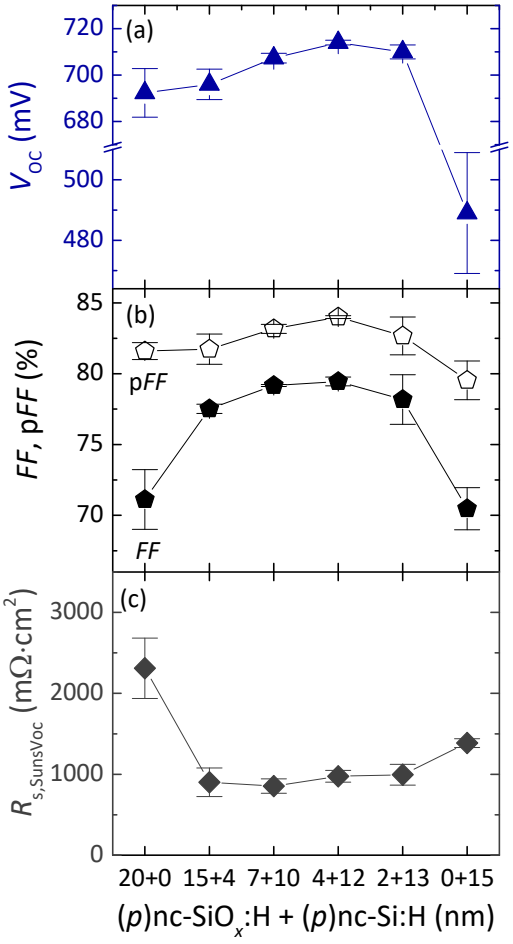

Figure 5.9: Front junction FBC-SHJ solar cells with varying thicknesses of (*p*)-contact ((*p*)nc-SiO$_x$:H + (*p*)nc-Si:H): (a) V_{OC}; (b) *FF* and p*FF*; (c) $R_{s,SunsVoc}$. Solar cells feature a nominal 4.4% front metal coverage. The results represent averaged parameters from three solar cells. The error bars represent the standard deviations.

of (*p*)nc-Si:H were applied to rear junction FBC-SHJ solar cells. The corresponding *J*-*V* parameters are reported in Figure 5.10. The front side of the solar cells has an (*n*)a-Si:H layer as the (*n*)-contact.

As illustrated in Figure 5.10, we noticed a general increment of average V_{OC} and *FF* by increasing the (*p*)nc-Si:H layer thickness. The gains in V_{OC} and *FF* are expected because of the reduced E_a of the (*p*)-contact, supported by the thickness-dependent E_a of (*p*)-contact that is already shown in Figure 5.2. Besides, the absolute gain in *FF* was more pronounced when increasing the (*p*)nc-Si:H layer thickness from 4 nm to 8 nm. We ascribe this to the initial sharp reduction of E_a of the (*p*)-contact when (*p*)nc-Si:H is thinner than 10 nm (see Figure 5.2). Further increasing the thickness of the (*p*)nc-Si:H layer

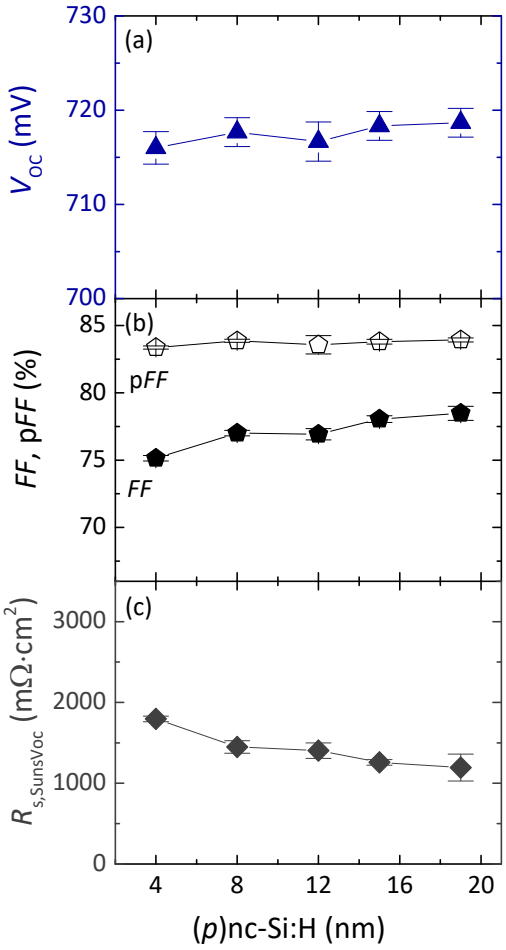

Figure 5.10: Rear junction FBC-SHJ solar cells with (*p*)-contacts featuring a fixed 4-nm thick (*p*)nc-SiO$_x$:H but varying (*p*)nc-Si:H layer thicknesses: (a) V_{OC}; (b) *FF* and p*FF*; (c) $R_{s,SunsVoc}$. Solar cells feature a nominal 4.4% metal coverage. The results represent averaged parameters from three solar cells. The error bars represent the standard deviations.

resulted in the gradual saturation of the *FF* at around 78.5%. This was also reflected in the evolution of the $R_{s,SunsVoc}$ of solar cells, where the average $R_{s,SunsVoc}$ tended to reach a minimum of 1200 m$\Omega \cdot$cm^2 with the increasing (*p*)nc-Si:H layer thickness.

5.3.4 Resistivity contributions of solar cells: $R_{s,lateral}$ vs $R_{s,vertical}$

In front junction solar cells with a (*n*)-type c-Si wafer, (*p*)-contact stacks involve not only vertical but also lateral collections of holes. This stimulates our interest in distinguishing the resistance contributions from both directions. To this end, we decomposed the $R_{s,SunsVoc}$ of the abovementioned front junction FBC-SHJ cells with the assistance of the

symmetrical test samples as shown in Figure 5.3 (b). With the obtained $R_{s,SunsVoc}$, we can derive the lateral $R_{s,lateral}$ that originates from the front side of the solar cells via:

$$R_{s,lateral} = R_{s,SunsVoc} - R_{s,vertical} \tag{5.4}$$

where:

$$R_{s,vertical} = (R_{s,symmetrical,p} + R_{s,symmetrical,n})/2 \tag{5.5}$$

the $R_{s,symmetrical,p}$ and $R_{s,symmetrical,n}$ correspond to resistivity contributions measured from symmetrical samples with the (p)-contact stacks and the (n)-contact stacks, respectively. The $R_{s,symmetrical,p}$ and $R_{s,symmetrical,n}$ are divided by 2 to obtain vertical resistivity contribution from one side of the contact stack as that in solar cells, which are denoted as $R_{s,vertical,p}$ and $R_{s,vertical,n}$. Therefore, aside from the symmetrical (p)-contact stacks samples that were already made, we also fabricated symmetrical samples with (n)-contact stacks, which have the same structures as the rear (n)-contact stacks in the corresponding solar cells. As front junction solar cells were studied, we consider here only the vertical transport of electrons through the rear (n)-contact stacks.

The $R_{s,SunsVoc}$ breakdown of solar cells with different layers and treatments is illustrated in Figure 5.11.

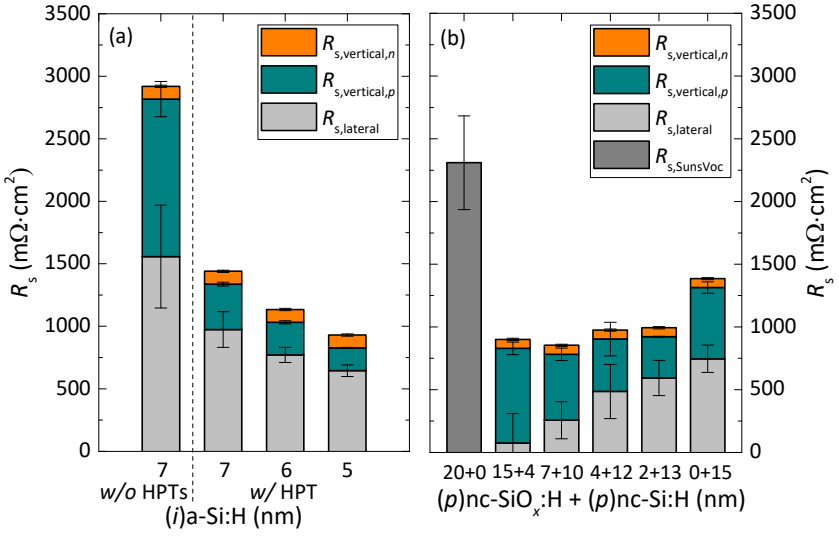

Figure 5.11: The $R_{s,SunsVoc}$ decompositions of front junction FBC-SHJ solar cells with $R_{s,vertical}$ and $R_{s,lateral}$: (a) the effect of the HPTs and (i)a-Si:H layer thickness; (b) the effect of thickness combinations of the bi-layer (p)-contact. $R_{s,vertical}$ is distinguished between (n)-type contact stacks $R_{s,vertical,n}$ and (p)-type contact stacks $R_{s,vertical,p}$. The error bars represent the standard deviations.

As it can be seen from the analysis of $R_{s,SunsVoc}$ in Figures 5.11 (a) and (b), the variations in $\rho_{c,p}$ of the (p)-contact stacks (see Section 5.3.2) change not only directly the $R_{s,vertical,p}$ but also the distribution of the $R_{s,lateral}$. In Figure 5.11 (a), the (n)a-Si:H based (n)-contact stacks account for an $R_{s,vertical,n}$ of 102 mΩ·cm^2 ($\rho_{c,n}$ of 63 mΩ·cm^2), which

is less resistive than (*p*)-contact stacks. After applying the HPTs, we observed a significant reduction in $R_{\mathrm{s,vertical},p}$ as a result of the decrement of $\rho_{\mathrm{c},p}$ of the (*p*)-contact stacks. In the meanwhile, we also recognized a lower contribution from $R_{\mathrm{s,lateral}}$. The reduction of $R_{\mathrm{s,lateral}}$ may result from both stronger band bending and better collection of holes from (*p*)-contact to the ITO layer. Moreover, thinning down the (*i*)a-Si:H beneath the (*p*)-contact also follows the trends but with rather comparable reductions of both $R_{\mathrm{s,vertical},p}$ and $R_{\mathrm{s,lateral}}$. In fact, (*p*)-contact stacks with thinner (*i*)a-Si:H layer features lower vertical resistance, which promotes lateral transport through ITO, thus a lower $R_{\mathrm{s,lateral}}$ as well.

In Figure 5.11 (b), the contribution of the (*n*)-contact stack based on (*n*)nc-SiO$_x$:H to the $R_{\mathrm{s,vertical},n}$ accounted for 71 m$\Omega\cdot$cm^2 ($\rho_{\mathrm{c},n}$ of 33 m$\Omega\cdot$cm^2). Differently, by varying thickness combinations of the (*p*)-contact, we observed a trade-off between $R_{\mathrm{s,vertical},p}$ and $R_{\mathrm{s,lateral}}$. Due to the observed diode behavior of the symmetrical sample (see Figure 5.6) with only (*p*)nc-SiO$_x$:H ('20 + 0 nm' (*p*)-contact), we present only its device $R_{\mathrm{s,SunsVoc}}$, which is the most resistive within the series. Along with the increased thickness fraction of (*p*)nc-Si:H layer, we noticed the gradual lowering of $R_{\mathrm{s,vertical}}$ because of the reduced $\rho_{\mathrm{c},p}$ of the (*p*)-contact stacks (see Figure 5.6). However, the increased contribution from $R_{\mathrm{s,lateral}}$ compensated the reduced $R_{\mathrm{s,vertical}}$, thus maintaining the $R_{\mathrm{s,SunsVoc}}$ of solar cells nearly constant. We ascribe this to competing effects between the ones on carrier collections due to thinner (*p*)nc-SiO$_x$:H and thicker (*p*)nc-Si:H. It is worth noting that a thicker (*p*)nc-SiO$_x$:H or (*p*)nc-Si:H tends to enhance the band bending inside (*n*)c-Si as a result of thickness-dependent E_{a} of (*p*)-contact, thus reducing $\rho_{\mathrm{c},p}$ and promoting the lateral transport inside ITO for both cases. Therefore, on the one hand, a thinner (*p*)nc-SiO$_x$:H is less likely to induce an efficient space-charge layer (band bending) inside the (*n*)c-Si bulk as compared to its thicker counterpart. Thus, a thinner (*p*)nc-SiO$_x$:H layer may require more support for the lateral transport of holes from the space-charge layer inside the (*n*)c-Si bulk. On the other hand, a thicker (*p*)nc-Si:H is capable of reducing the E_{a} of the (*p*)-contact and thus the $\rho_{\mathrm{c},p}$ and for this reason, a more efficient lateral transport of holes inside the ITO is expected. As it can be seen from Figure 5.11 (b), the increased $R_{\mathrm{s,lateral}}$ with thinner (*p*)nc-SiO$_x$:H and thicker (*p*)nc-Si:H indicates that more holes transport laterally through the (*n*)c-Si bulk. Therefore, there is a more dominating effect of the (*p*)nc-SiO$_x$:H layer thickness on the lateral transport distribution of holes. Besides, similar $R_{\mathrm{s,SunsVoc}}$ values with different vertical and lateral components also reveal that $R_{\mathrm{s,SunsVoc}}$ was limited by lateral transport in the device ascribed to ITO mobility and front Ag grid pitch size. Lastly, the cell that has only (*p*)nc-Si:H presents both increased $R_{\mathrm{s,vertical}}$ and $R_{\mathrm{s,lateral}}$ that result from increased $\rho_{\mathrm{c},p}$ and deteriorated Voc.

To gain a better understanding of the role of the $R_{\mathrm{s,lateral}}$ as observed in Figure 5.11 (b), we performed TCAD simulations to analyze front junction FBC-SHJ solar cells featuring varied thickness combinations of the bi-layer (*p*)-contact. We evaluated the charge per second that moves laterally in each layer on the front sides of solar cells under maximum power point (MPP) conditions. Since the lateral current flow through the (*p*)-contact is negligible as compared to the one of the c-Si bulk and the ITO layer, we present here only the results of the c-Si bulk and ITO layer. The values are normalized for all samples and are shown in Figure 5.12 (a). Note, the component that is missing in Figure 5.12 (a) to reach 100% for each thickness combination indicates non-collected (recombined) carriers as compared to the optimal sample featuring '4 +

12 nm' (*p*)-contact.

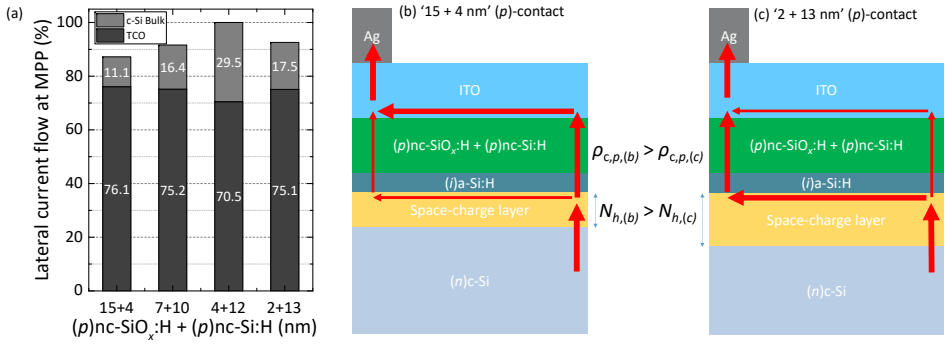

Figure 5.12: The (a) simulations and (b), (c) schematic sketches of simulated lateral current flow distributions within the c-Si bulk and ITO layer in front junction FBC-SHJ solar cells with varying thickness combinations of the bi-layer (*p*)-contact. Note, the component that is missing in (a) to reach 100% for each thickness combination indicates non-collected (recombined) carriers as compared to the optimal sample featuring '4 + 12 nm' (*p*)-contact. The $\rho_{c,p,(b)}$ and $\rho_{c,p,(c)}$ represent the contact resistivity of the contact stacks featuring '15 + 4 nm' and '2 + 13 nm' (*p*)-contact, respectively. $N_{h,(b)}$ and $N_{h,(c)}$ refer to the hole concentration in the space-charge layer of (*n*)c-Si for cells featuring '15 + 4 nm' and '2 + 13 nm' (*p*)-contact, respectively.

As noticeable in Figure 5.12 (a), the lateral current flow at MPP increased with a thicker (*p*)nc-Si:H (or a thinner (*p*)nc-SiO$_x$:H). By lowering the $\rho_{c,p}$ of the (*p*)-contact stacks, the probability of holes to be transported from the c-Si to the ITO increases. Interestingly, with increasing the thickness of the (*p*)nc-Si:H layer (or decreasing the thickness of the (*p*)nc-SiO$_x$:H layer), we observed varied c-Si bulk contributions. Not only the absolute current that is laterally transported through the c-Si bulk increased but also its relative fraction increased. This is evident, especially, by comparing samples with '15 + 4 nm' and '4 + 12 nm' (*p*)-contacts. As expected, these increased c-Si bulk contributions elucidate the higher $R_{s,lateral}$ as observed in Figure 5.11 (b). Besides, the schematic sketches of lateral current flows in the simulated solar cells are shown in Figures 5.12 (b) and (c). In fact, from the simulations, the hole concentration (N_h) in the space-charge layer differs by implementing (*p*)-contacts with different thickness combinations. Specifically, the N_h in the space charge layer is around 10^{17} cm^{-3} for the cell with '15 + 4 nm' (*p*)-contact, which is nearly one order of magnitude higher than that of the cell with '2 + 13 nm' (*p*)-contact. This varied N_h in the space-charge layer is reflected in the form of varied space-charge layer thickness as shown in Figures 5.12 (b) and (c). Although the cell with '15 + 4 nm' (*p*)-contact features a higher $\rho_{c,p}$ as compared to that of the cell with '2 + 13 nm', a stronger band bending induced by the thicker (*p*)nc-SiO$_x$:H promotes the carrier lateral collection through ITO, and vice versa.

With the knowledge of solar cells' performances and during this study further careful processing of the FBC-SHJ solar cells, we present in Figures 5.13 (a) and (b) the independently certified *I*-*V* characteristics of the best front and rear junction FBC-SHJ solar cells, respectively. The corresponding $R_{s,SunsVoc}$ decompositions of solar cells are also presented in Figure 5.13. For the front junction solar cell, we used (*n*)a-Si:H as (*n*)-contact and we implemented the optimized 6 nm (*i*)a-Si:H and '4 + 12 nm' (*p*)-contact

together with the HPTs at the front side. While for the rear junction solar cell, instead of '4 + 12 nm' (*p*)-contact, we applied '4 + 16 nm' due to less strict optical limitations when the (*p*)-contact is located at the rear side of the solar cell. With these, we have achieved *FF* of 80.9% and 80.4% for front and rear junction configurations, respectively. Moreover, thanks to the more transparent (*n*)-contacts based on (*n*)nc-SiO$_x$:H placed on the sunny side [175], we achieved an efficiency as high as 22.47% in the rear junction configuration. Lastly, as seen from the decompositions of solar cells' $R_{s,SunsVoc}$, the higher $R_{s,lateral}$ for this rear junction cell indicates that more electrons transport laterally through the (*n*)c-Si bulk as compared to the fraction transporting through the ITO. This corresponds to similar observations as previously reported by Bivour, et al. [198].

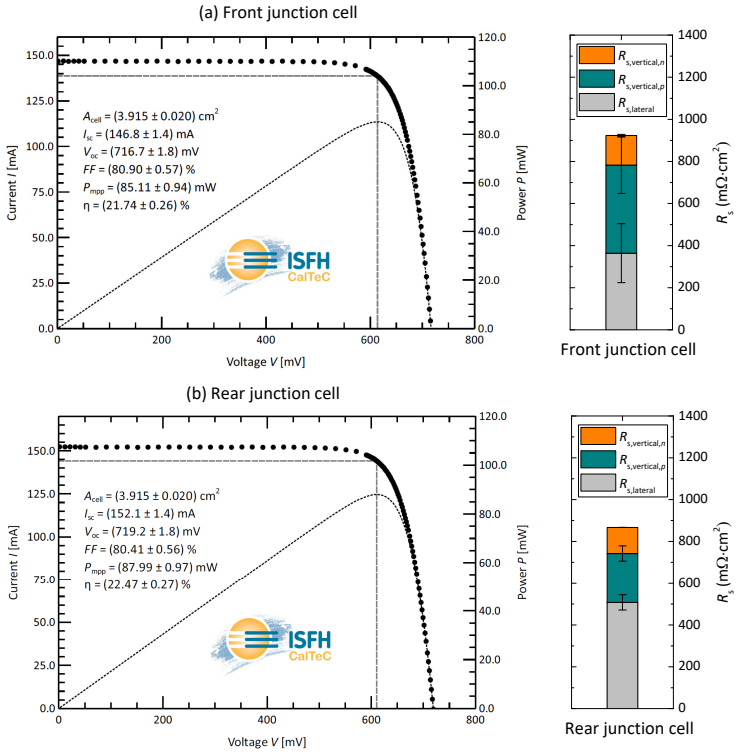

Figure 5.13: The independently certified *I*-*V* characteristics and device parameters of the best (a) front junction and (b) rear junction FBC-SHJ solar cells. The corresponding decompositions of solar cells' $R_{s,SunsVoc}$ are also presented. The *I*-*V* characteristics certifications were performed at ISFH CalTeC (Germany).

5.4 Conclusions

In this chapter, we investigated and optimized hole collectors – or (*p*)-contact stacks – based on bi-layers of (*p*)nc-SiO$_x$:H and (*p*)nc-Si:H, which are integrated into high-efficiency SHJ solar cells.

We determined the thickness-dependent E_a of the bi-layer (*p*)-contact, for which the

thicker the (*p*)nc-Si:H the lower the E_a of the (*p*)-contact. Meanwhile, we demonstrated the necessity of our optimized HPTs interfacial treatment, which significantly improved the electrical properties of the bi-layer (*p*)-contact, especially when the (*p*)nc-Si:H is thinner than 20 nm. Accordingly, the HPTs also induced significant $\rho_{c,p}$ reduction of the (*p*)-contact stacks. Besides, a thinner (*i*)a-Si:H layer was proved to minimize transport losses for holes and we report a (*p*)-contact stack featuring a low contact resistivity ($\rho_{c,p}$ of 144 m$\Omega\cdot$cm^2) when (*i*)a-Si:H is 5 nm. Interestingly, (*p*)nc-SiO$_x$:H layers featuring a larger $E_{04} - E_a$ were found to be beneficial for reducing the $\rho_{c,p}$. Moreover, by varying the thickness combinations in the (*p*)nc-SiO$_x$:H and (*p*)nc-Si:H stacks, we were able to prove the critical roles of both (*p*)nc-SiO$_x$:H and (*p*)nc-Si:H. In particular, (*p*)nc-SiO$_x$:H preserves the passivation quality and enables sufficient band bending at c-Si/(*i*)a-Si:H interface, while (*p*)nc-Si:H enhances the transport of holes to ITO and the band bending as well.

Subsequently, we observed that the *FF* evolution of solar cells was closely correlated to their $R_{s,SunsVoc}$ and to the $\rho_{c,p}$ of (*p*)-contact stacks. It is worth noting that in front junction FBC-SHJ solar cells, the $\rho_{c,p}$ of (*p*)-contact stacks was found to affect the distribution of vertical and lateral transport of holes. The application of the HPTs and a thinner (*i*)a-Si:H layer reduced both vertical and lateral resistance losses at the same time. Differently, we noticed a trade-off between vertical and lateral resistance when we varied the thickness combinations of the (*p*)-contact. The latter finding was supported by TCAD simulation, from which we observed increased contributions from the space-charge layer inside the (*n*)c-Si bulk when a thinner (*p*)nc-SiO$_x$:H and a thicker (*p*)nc-Si:H were applied. Our best cells were certified to feature *FF* well-above 80% for both front and rear configurations, and an efficiency of 22.47% was achieved for a rear junction solar cell.

6

Ultra-thin electron collector based on nc-Si:H for SHJ solar cells

This chapter is based on the publication:

Y. Zhao, L. Mazzarella, P. Procel, C. Han, F. D. Tichelaar, G. Yang, A. Weeber, M. Zeman, and O. Isabella, "Ultra-thin electron collectors based on nc-Si:H for high-efficiency silicon heterojunction solar cells," *Progress in Photovoltaics: research and applications*, vol. 30, no. 8, pp. 809–822, 2022. [1]

Abstract

Low parasitic absorption and high conductivity enable (*n*)-type hydrogenated nanocrystalline silicon ((*n*)nc-Si:H), eventually alloyed with oxygen ((*n*)nc-SiO$_x$:H), to be deployed as the window layer in high-efficiency silicon heterojunction (SHJ) solar cells. Besides the appropriate opto-electrical properties of these nanocrystalline films, a reduction of their thickness is sought for minimizing parasitic absorption losses. Many strategies proposed so far revealed practical limits of the minimum (*n*)-layer thickness that we address and overcome in this manuscript. We demonstrated the successful application of an ultra-thin layer of only 3-nm-thick based on (*n*)nc-Si:H PECVD plasma growth conditions without the use of additional contact or buffer layers. For simplicity, we still name this ultra-thin layer as (*n*)nc-Si:H and the solar cell endowed with it delivered a certified efficiency η of 22.20%. This cell showed a 0.61 mA/cm^2 overall J_{SC} gain over the (*n*)a-Si:H counterpart mainly owing to the higher transparency of (*n*)nc-Si:H, while maintaining comparable V_{OC} > 714 mV and *FF* > 80%. Our optimized (*n*)nc-Si:H layer yields low absorption losses that are commonly measured for (*n*)nc-SiO$_x$:H films. In this way,

[1] This paper was invited for publication in the special issue 'EU PVSEC' (2022) of *Progress in Photovoltaics: Research and Applications*.

we are able to avoid the detrimental effect that oxygen incorporation has on the electrical parameters of these functional layers. Further, by applying a MgF_2/ITO double-layer anti-reflection coating, the cell with 3-nm-thick (*n*)nc-Si:H exhibited a $J_{SC,EQE}$ up to 40.0 mA/cm^2. By means of EDX elemental mapping, we additionally identified the (*n*)nc-Si:H/ITO interface is critical for electron transport due to unexpected oxidation. To avoid this interfacial oxidation, insertion of a 2-nm-thick (*n*)a-Si:H on the 3-nm-thick (*n*)nc-Si:H contributed to *FF* gains of 1.4%$_{abs.}$ (*FF* increased from 78.6% to 80.0%), and showing further room for improvement.

6.1 Introduction

Front/back-contacted silicon heterojunction (FBC-SHJ) solar cells with passivating contacts based on hydrogenated amorphous silicon (a-Si:H) have demonstrated conversion efficiency (η) well above 25% [129]. To reduce the parasitic absorption at the illuminated side, doped a-Si:H is often substituted by doped hydrogenated nanocrystalline silicon (nc-Si:H) and/or its oxygen alloy (nc-SiO$_x$:H) that concurrently enable better transparency and higher conductivity [132, 160, 173–175, 300, 360, 403]. These advantageous opto-electrical properties of nc-Si:H-based thin-films mainly originate from their mixed-phase compositions, which consist of nanocrystals embedded in the amorphous matrix [361, 404].

However, nc-Si:H-based thin-films feature thickness- and substrate-dependent growth characteristics [176, 405]. Therefore, efforts have been devoted to minimizing the thickness of the initial amorphous incubation layer regardless of the influence from the substrate. Methods, such as applying a CO_2 plasma treatment [320, 321], employing an oxygen-absent doped/non-doped seed layer and/or a contact layer [164, 175, 321, 365, 366, 386, 406], using a very-high-frequency (VHF) plasma [163, 314], utilizing a phosphorous treatment [388], and implementing a hydrogen plasma treatment [364] or a low-temperature crystallization by hydrogen plasma [369, 407] were reported. Such approaches can accelerate the nucleation of nanocrystals, thus enabling doped layers with low activation energies (E_a). And those low values of E_a are critical for achieving effective carrier-selective transport through nc-Si:H-based carrier-selective passivating contacts (CSPCs) in SHJ solar cells, which feature (*i*)a-Si:H passivating layers [150]. Besides, prompt nucleations also provide the possibility to minimize the total thicknesses of the nc-Si:H-based CSPCs which results in a lower parasitic absorption while maintaining advantageous electrical properties, especially, when they are located on the illuminated side of the solar cells. As reported, for rear junction SHJ solar cells that feature a (*n*)nc-Si:H-based window layer, the thickness of this (*n*)nc-Si:H layer should generally be at least around 10 nm to achieve a decent *FF* of above 77% [163, 164]. For a (*n*)nc-SiO$_x$:H-based contact, a minimum of approximately 8-nm-thick (*n*)-type nc-SiO$_x$:H in addition to a nc-Si:H layer stack, which acts as a seed and/or contact layer, is needed to form effective electron CSPCs for ensuring excellent electrical cell performance including preserving the surface passivation quality [386, 387]. Attempts for further reducing the thicknesses of nc-Si:H-based (*n*)-contact have so far resulted in losses of both *FF* and V_{OC} of the solar cells [164, 387, 408]. Despite this limited thickness, the typical rather slow deposition rates of nc-Si-based thin-films as compared to a-Si:H [175] also impose challenges for their industrial feasibility. Therefore, the development

of a thin (*n*)-contact that preserves the electrical performance of solar cells is of great interest for reducing parasitic absorption by lowering material consumption and enabling higher industrial throughputs.

In this study, we aim at minimizing the parasitic absorption of the (*n*)-type window layers while keeping excellent electrical performances. We investigated and compared the opto-electrical properties of (*n*)a-Si:H, (*n*)nc-SiO_x:H, and (*n*)nc-Si:H layers and their performances (as thin as 2 nm) in rear junction FBC-SHJ solar cells. By means of our optimized hydrogen plasma treatment (HPT) and very-high-frequency (VHF) (*i*)nc-Si:H treatment (hereafter denoted as HPTs), we demonstrated the successful application of an ultra-thin layer of only 3-nm-thick based on (*n*)nc-Si:H PECVD plasma growth conditions without the use of additional contact or buffer layers that delivered a certified conversion efficiency (η) of 22.20%. Furthermore, to understand the interfacial properties of thin (*n*)-layers and their effect on the solar cell output parameters, we performed high-resolution transmission electron microscopy (HRTEM) measurements and energy dispersive X-Ray (EDX) elemental mapping analyses on completed solar cells.

6.2 Experimental details

In this study, the PECVD deposition conditions that were adjusted to obtain various (*n*)-type layers, namely, (*n*)a-Si:H, (*n*)nc-Si:H and (*n*)nc-SiO_x:H, are listed in Table 6.1. More descriptions of the PECVD deposition conditions of (*p*)-contact can be found in Table 5.1 [312]. Specifically, to characterize the opto-electrical properties of different (*n*)-type layers, two sample configurations were used as schematically illustrated in Figure 6.1 (a). As seen in Figure 6.1 (a), for the first configuration, (*n*)-type layers with a thickness of approximately 20 nm were directly deposited on glass substrates. For the second configuration and to simulate the actual structure in solar cells that feature (*i*)a-Si:H passivating layers, 5 to 20-nm-thick (*n*)-type layers were deposited on 10-nm-thick (*i*)a-Si:H coated glass substrates. Spectroscopic ellipsometry (SE) was used to measure the thicknesses of deposited layers and to extract the refractive index (*n*), the extinction coefficient (*k*) and the optical bandgap (E_{04}). Raman spectroscopy (equipped with a green laser, λ_{laser} = 514 nm) was used to characterize the microstructures of (*n*)-type thin-films with sample structures as shown in Figure 6.1 (a). The schematic sketches of fabricated FBC-SHJ solar cells with various (*n*)-layers as the (*n*)-contacts are illustrated in Figure 6.1 (b).

Along with the fabrication process of solar cells, the implied V_{OC} (iV_{OC}) of solar cell precursors were measured before and after the ITO sputtering. For HRTEM and EDX analysis of fabricated solar cells, an FEI cubed Cs-corrected Titan was used, operating at 300 kV. EDX maps were obtained using the 4-detector ChemiSTEM of Thermo Fisher. Ray-tracing GenPro4 optical simulations [409] with inputs from SE-characterized *n* and *k* of Si thin-films and ITO were performed for our fabricated SHJ solar cells.

6.3 Results and Discussions

6.3.1 Opto-electrical properties and Raman spectra of (*n*)a-Si:H, (*n*)nc-SiO_x:H and (*n*)nc-Si:H

The opto-electrical properties of optimized (*n*)a-Si:H, (*n*)nc-SiO_x:H and (*n*)nc-Si:H are shown and compared in Figure 6.2 and Table 6.2.

Table 6.1: PECVD parameters for optimized of (*n*)nc-SiO$_x$:H, (*n*)nc-Si:H, HPT, VHF (*i*)nc-Si:H treatments.

PECVD parameters	(*n*)a-Si:H	(*n*)nc-Si:H	(*n*)nc-SiO$_x$:H-1	(*n*)nc-SiO$_x$:H-2	HPT	VHF (*i*)nc-Si:H
Frequency (MHz)	13.56	13.56	13.56	13.56	13.56	40.68
Temperature (°C)	180	180	180	180	180	180
Pressure (mbar)	0.6	2.7	2.7	1.5	2.7	4
Power density (mW/cm^2)	28	76	76	76	63	69
SiH_4 (sccm)	40	1	1	1	-	1.2
H_2 (sccm)	-	100	100	100	200	120
CO_2 (sccm)	-	-	1.6	1.6	-	-
PH_3[a] (sccm)	11	1.2	1.2	1.2	-	-
Duration (s)	-	-	-	-	120	120

[a]: 2% in H_2;

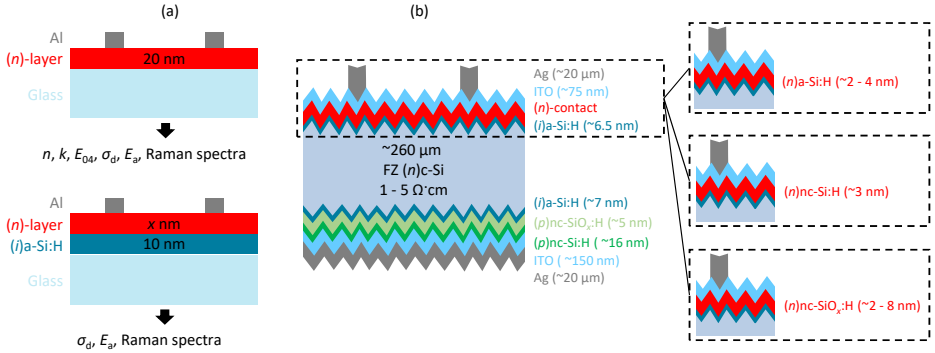

Figure 6.1: Schematic sketches of (a) sample structures to extract n, k, E_{04}, σ_d, E_a and Raman spectra of (*n*)-type layer; and (b) rear junction FBC-SHJ solar cells with different (*n*)-layers stacks studied, namely, (*n*)a-Si:H, (*n*)nc-Si:H and (*n*)nc-SiO$_x$:H.

Electrically, as illustrated in Figure 6.2, around 20-nm-thick (*n*)nc-Si:H that was deposited on a glass substrate showed the highest σ_d of 1.07 S/cm and the lowest E_a of 52.6 meV. This is due to its higher crystalline fraction thus enabling higher doping efficiency as revealed later with Raman spectroscopy measurement. However, the σ_d drops to 3.5×10^{-4} S/cm and the E_a increases to 304.4 meV when (*n*)nc-Si:H was deposited on an (*i*)a-Si:H coated glass substrate. Similarly, substrate-dependent σ_d and E_a were ob-

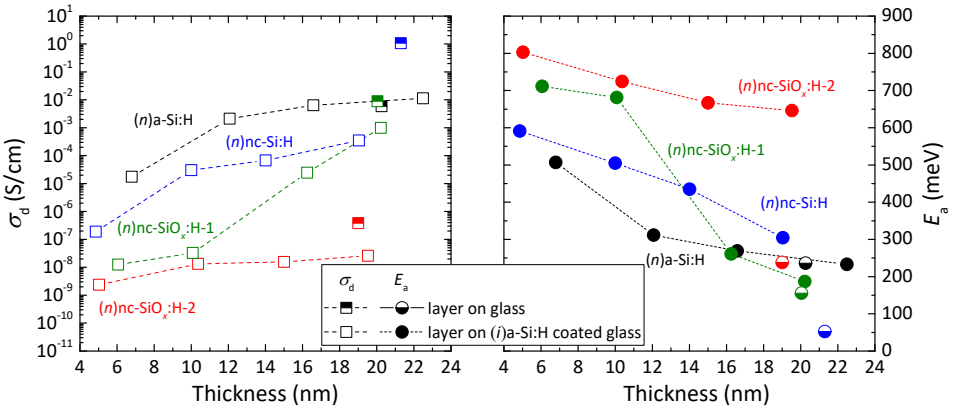

Figure 6.2: The σ_d (left) and E_a (right) of (*n*)nc-SiO$_x$:H, (*n*)nc-Si:H and (*n*)a-Si:H layers as function of the layer thickness and of the different substrates.

Table 6.2: Opto-electrical properties of optimized (*n*)a-Si:H, (*n*)nc-SiO$_x$:H and (*n*)nc-Si:H

Layers	Deposition rate[a] (nm/s)	n @ λ = 632 nm (-)	E_{04} @ ~20 nm (eV)	σ_d @ ~20 nm (S/cm)	σ_d[b] @ ~20 nm (S/cm)	σ_d[b] @ ~5 nm (S/cm)
(*n*)a-Si:H	0.101	4.16	1.86	5.9×10^{-3}	1.1×10^{-2}	1.8×10^{-5}
(*n*)nc-SiO$_x$:H-1	0.023	2.60	2.26	8.9×10^{-3}	9.9×10^{-4}	1.3×10^{-8}
(*n*)nc-SiO$_x$:H-2	0.031	2.08	2.60	3.8×10^{-7}	2.6×10^{-8}	2.4×10^{-9}
(*n*)nc-Si:H	0.027	3.25	1.95	1.07	3.5×10^{-4}	1.9×10^{-7}

[a]: Deposition rates were calculated based on the measured thicknesses of deposited layers and their deposition time;
[b]: Layers were deposited on 10-nm-thick (*i*)a-Si:H coated glasses.

served for both (*n*)nc-SiO$_x$:H films. This substrate-dependent growth characteristic is known for nc-Si:H-based thin-films [176, 321, 405, 410]. Ultimately, by thinning all layers down to around 5 nm, which is close to the thickness of (*n*)-contact in solar cells, (*n*)a-Si:H resulted to be the most conductive, followed by (*n*)nc-Si:H, (*n*)nc-SiO$_x$:H-1, and (*n*)nc-SiO$_x$:H-2. As will be discussed later in this section, the higher σ_d and generally lower E_a of (*n*)a-Si:H could be attributed to its deposition conditions and its distinctive doping properties, which differ from the amorphous incubation phase of nc-Si:H-based films. Moreover, we observed thickness-dependent σ_d and E_a not only for (*n*)nc-SiO$_x$:H and (*n*)nc-Si:H layers, but also for (*n*)a-Si:H layers. That is, a thicker layer exhibits a higher σ_d and a lower E_a. Apart from the known evolution of nanocrystals that results in improved electrical properties for nc-Si:H-based layers [176], the effects due to the underlying (*i*)a-Si:H layer, as discussed in Section 3.2.1, can also play a role for observed thickness-dependent E_a and σ_d of both nc-Si:H-based layers and (*n*)a-Si:H layers. It is unlikely that the thickness-dependent E_a and σ_d of (*n*)a-Si:H layers can be ascribed to the non-coalesced films during their initial stage of layer growth [411], which results in reduced material densities and thus may negatively affect their electrical properties.

Nevertheless, thickness-dependent electrical properties were also reported previously for (*n*)a-Si:H thicker than around 100 nm [412–414], and those were ascribed to the existence of a resistive space-charge layer at the substrate-film interface or a resistive surface layer, which becomes more dominant when the layer gets thinner.

As listed in Table 6.2, (*n*)a-Si:H, which features the highest n and the lowest E_{04} is optically the least favorable among these various (*n*)-layers. It will be better to make (*n*)nc-Si:H and (*n*)nc-SiO$_x$:H-1 layers, while (*n*)nc-SiO$_x$:H-2 features the lowest n of 2.08 and the largest E_{04} of 2.60 eV. The larger E_{04} of nc-Si:H as compared to (*n*)a-Si:H could be ascribed to the formation of small Si nanocrystals embedded in (*n*)a-Si:H matrix, where the quantum size effect of nanocrystals [415], higher H-incorporation into the amorphous matrix due to the H-rich deposition condition [368] or higher void fraction [411] may play a role. Despite the aforementioned possible explanations for (*n*)nc-Si:H, the incorporation of oxygen into the amorphous matrix further widens the E_{04} of both (*n*)nc-SiO$_x$:H layers [416]. In particular, a relatively higher fraction of oxygen incorporation could account for the higher E_{04} of (*n*)nc-SiO$_x$:H-2 as compared to (*n*)nc-SiO$_x$:H-1. The n and k of various (*n*)-type thin-films as a function of wavelength are provided in Appendix A, Figure A.1.

To further correlate the opto-electrical properties of various (*n*)-type thin-films to their microstructural properties, we measured Raman spectra of various (*n*)-type thin-films deposited on top of bare glasses and the ones on 10-nm-thick (*i*)a-Si:H coated glasses. The results are reported in Figure 6.3.

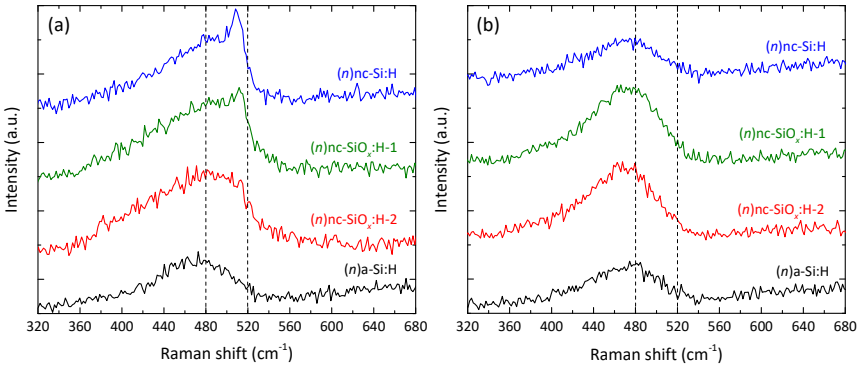

Figure 6.3: Raman spectra of various (*n*)-type thin-films that were deposited on top of the (a) glass substrate, and (b) 10-nm (*i*)a-Si:H coated glass substrate. Dashed vertical lines indicate the Raman shift of 480 cm^{-1} and 520 cm^{-1}. Schematic sketches of sample structures are shown in Figure 6.1 (a). The thicknesses of deposited (*n*)-type thin-films are around 20 nm.

As illustrated in Figure 6.3 (a), where layers were deposited directly on glass substrates, both nc-Si:H and (*n*)nc-SiO$_x$:H-1 exhibited distinguishable peaks near 520 cm^{-1}, which is characteristic of crystalline Si [344]. This evidences the existence of Si nanocrystals in the films, although those crystalline Si peaks slightly downshifted to around 510 cm^{-1}, which is an indication of rather small-size Si nanocrystals in our deposited 20-nm-thick films [417–419] and/or the tensile strain effect of Si nanocrystals [420]. It is

worth noting that these crystalline Si peaks were also superimposed on a broad amorphous Si peak centered at 480 cm^{-1} [345], which suggests the coexistence of amorphous and nanocrystal phases in those films. Nevertheless, the existence of Si nanocrystals in (*n*)nc-Si:H and (*n*)nc-SiO_x:H-1 enabled better doping efficiencies than amorphous Si [152, 153, 421, 422], explaining their relative higher σ_d and lower E_a as reported in Figure 6.2. However, (*n*)nc-SiO_x:H-1 exhibited a slightly lower σ_d as compared to (*n*)nc-Si:H due to oxygen incorporation, which results in a weakened doping efficiency [423]. On the other hand, the (*n*)nc-SiO_x:H-2 layer revealed a relatively lower fraction of Si nanocrystals, which could be ascribed to the excessive oxygen incorporation, suppressing the growth of nanocrystals [168, 172, 298, 371]. This observation also explains the highest E_{04} and the lowest σ_d obtained for (*n*)nc-SiO_x:H-2. As expected, only a broad amorphous Si peak was observed for (*n*)a-Si:H.

When equivalent-thick 20 nm (*n*)-type thin-films were deposited on (*i*)a-Si:H coated glasses, all layers appeared to be nearly fully amorphous as shown in Figure 6.3 (b). This is probably due to the green laser used for measuring their Raman spectra, whose penetration depth is in the range of hundreds of nanometers for our nc-Si:H-based layers. Thus the non-negligible signals from the 10-nm-thick (*i*)a-Si:H coatings may overwhelm the signals from those tiny crystals [315]. Nevertheless, those nc-Si:H-based layers were amorphous-phase-dominant as nanocrystals were yet to be well-developed to promote higher σ_d or lower E_a than that of the standard (*n*)a-Si:H (see Figure 6.2 and Table 6.2). This is because the initial amorphous incubation phase of nc-Si:H-based layer might feature different doping efficiency from that of the standard (*n*)a-Si:H. As known from the secondary-ion-mass spectroscopy studies for thin (*p*)nc-Si:H (< 10 nm) and standard (*p*)a-Si:H by Umishio H, et al. [315], we attribute our observations of higher σ_d and generally lower E_a for the (*n*)a-Si:H than nc-Si:H-based layers to the following reasons: (i) the nearly ten times higher flow of doping gas (PH_3) for (*n*)a-Si:H that can contribute to a higher phosphorous content in (*n*)a-Si:H (see Table 6.1), (ii) the probably higher phosphorous incorporation efficiency under the deposition conditions of (*n*)a-Si:H, and (iii), a lesser significant dopant inactivation induced by the hydrogen passivation in (*n*)a-Si:H than in those nc-Si:H-based layers [296, 424, 425].

As for thickness-dependent σ_d and E_a, for all nc-Si:H-based films, we suspect that the trends should be still related to the nucleation and growth of nanocrystals despite having observed broad amorphous peaks in Raman spectra obtained by the green laser. This assumption is reasonable as for (*n*)nc-Si:H and (*n*)nc-SiO_x:H-1 thicker than 15 nm there were steeper slopes of variations of σ_d and E_a than that of the standard (*n*)a-Si:H (see Figure 6.2). This suggests an improved doping efficiency with higher fractions of nanocrystals when layers get thicker. Especially, (*n*)nc-SiO_x:H-1 layers thicker than 15 nm had already demonstrated a lower E_a than that of the standard (*n*)a-Si:H (see Figure 6.2 (b)). To further reveal the nanocrystalline fractions in those layers, an ultraviolet laser should be implemented [315].

6.3.2 Solar cells – Various (*n*)-type window layers ≤ 8 nm

Based on the opto-electrical and microstructural properties of various (*n*)-type thin-films as shown in Section 6.3.1, we fabricated rear junction FBC-SHJ solar cells as sketched in Figure 6.1 (b). Before the depositions of (*n*)-contacts, we also applied pre-

viously optimized HPTs [175], which were found to have negligible effects on the σ_d for all (*n*)-type layers with thicknesses around 5 nm (See Appendix A, Figure A.2). In this section, we compare the performance of solar cells featuring various single-layer (*n*)-contacts (i.e. without additional contact or buffer layers) with different thicknesses. Based on previous optimizations, the 3-nm-thick (*n*)nc-Si:H was chosen as it is the minimum thickness that can already deliver good V_{OC} and *FF* (see Appendix A, Figure A.3). The *J*-*V* parameters of solar cells are given in Figure 6.4.

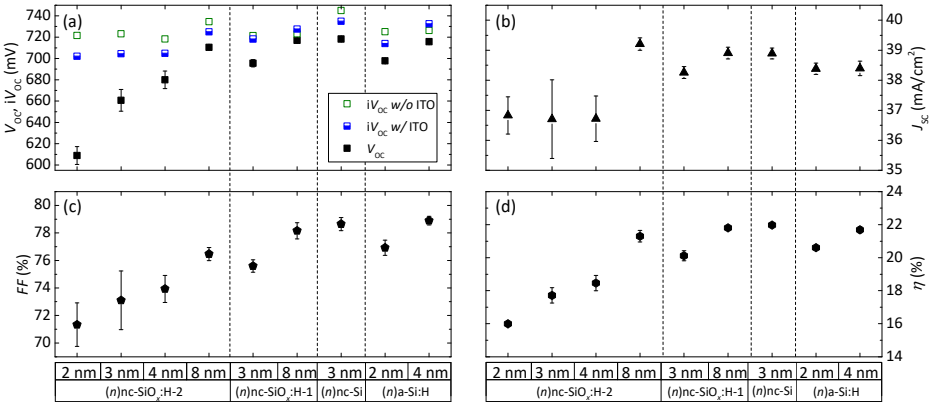

Figure 6.4: The *J*-*V* characteristics of rear junction FBC-SHJ solar cells with various (*n*)-type contacts: (a) iV_{OC} and V_{OC}, (b) J_{SC}, (c) *FF*, and (d) η. The results represent averaged parameters of four solar cells (3.92 cm^2) and the error bars represent the standard deviations.

First, as shown in Figure 6.4 (a), we discuss the effect of the ITO sputtering on the passivation quality of solar cells with different window layers, which are reflected by the iV_{OC} with and without the ITO. Within the thickness range investigated, we observed iV_{OC} drops of around 10 - 19 mV for all cell precursors with less conductive (and high E_a) (*n*)nc-SiO$_x$:H-2 after ITO sputtering. In comparison, the use of 3 nm and 8 nm (*n*)nc-SiO$_x$:H-1 showed much lower iV_{OC} degradations and even improved iV_{OC}, respectively. We ascribe this to the thickness-dependent σ_d and E_a (see Figure 6.2), and the stronger capability of more conductive (and a lower E_a) (*n*)nc-SiO$_x$:H-1 to preserve the field-effect passivation after the ITO sputtering as compared to (*n*)nc-SiO$_x$:H-2. Moreover, we observed a nearly 10 mV iV_{OC} degradation for cell precursors with 3-nm-thick (*n*)nc-Si:H. Notwithstanding this 3-nm-thick (*n*)nc-Si:H might have higher σ_d and lower E_a than that of 8-nm-thick (*n*)nc-SiO$_x$:H-1 as expected from Figure 6.2, this degradation could be attributed to the too-thin thickness and seemingly porous or less dense structure of this (*n*)nc-Si:H that makes it less robust to sputtering damages as will be discussed later in Section 6.3.3. Despite the comparisons among different (*n*)-contacts, samples with the same type but a thicker (*n*)-contact showed better passivation resilience against the ITO sputtering as compared to the thinner counterparts.

Besides, we observed significant degradations from iV_{OC} to V_{OC} after cell metallizations with both (*n*)nc-SiO$_x$:H layers thinner than 5 nm as seen in Figure 6.4 (a). For instance, although cells with 2 nm to 4 nm (*n*)nc-SiO$_x$:H-2 exhibited comparable iV_{OC} of

around 705 mV before metallization (with ITO), the loss from iV_{OC} to V_{OC} increased for cells with the thinner (*n*)nc-SiO$_x$:H-2. We linked those larger losses to the insufficient selectivity and increased recombinations, which seem to be related to the thickness-dependent σ_d and E_a of (*n*)-contacts as shown in Figure 6.2 [150]. Nevertheless, cells with 8-nm-thick (*n*)nc-SiO$_x$:H-2 showed the minimum iV_{OC} to V_{OC} drops among the (*n*)nc-SiO$_x$:H-2 thickness series. Similar observations were found for cells with (*n*)nc-SiO$_x$:H-1 and (*n*)a-Si:H where a thicker (*n*)-contact accounts for lesser iV_{OC} to V_{OC} degradations. Similar trends were also found before by H. Wernerus, et al. for both (*n*)nc-Si:H and (*n*)a-Si:H in rear junction SHJ solar cells [411]. Therefore, around 8 nm of (*n*)nc-SiO$_x$:H single-layer is at least required for preserving the passivation quality while being capable of effective electron collections [386, 387]. Despite the iV_{OC} losses after ITO and metallization for cells with the 3-nm-thick (*n*)nc-Si:H, mainly thanks to the initial high iV_{OC} of 745 mV achieved before ITO sputtering, the completed solar cells can still exhibit a good V_{OC} of around 719 mV. This high iV_{OC} could be attributed to beneficial hydrogen incorporations during the deposition of (*n*)nc-Si:H layers [165, 315].

Then as illustrated in Figures 6.4 (b) and (c), cells with both 8-nm-thick (*n*)nc-SiO$_x$:H exhibited recovered J_{SC} [408] and higher *FF* [150, 387, 391] values as compared to their thinner counterparts. These variations can again be related to the thickness-dependent σ_d and E_a trends as seen in Figure 6.2. Specifically, the recovered J_{SC} values resulted from the reduced recombinations and the improved selective transport of electrons, which were also suggested by their improved V_{OC} values (See also Appendix A, Figure A.4). For well-passivated solar cells (V_{OC} > 710 mV), the *J-V* characteristics of solar cells corresponded well to the optical properties of (*n*)-layers and electrical properties of around 5-nm-thick layers as summarized in Table 6.2. In other words, (*n*)-layer with a higher σ_d (lower E_a) or a larger E_{04} tends to deliver a higher *FF* [150] or J_{SC} in the solar cell, respectively. Thus, cells with (*n*)a-Si:H demonstrate the highest average *FF* of 78.9% while cells with 8-nm-thick (*n*)nc-SiO$_x$:H-2 exhibit the highest average J_{SC} of 39.2 mA/cm^2. However, both of their η were slightly limited by the non-optimal tradeoff between the optical and electrical properties of their (*n*)-contacts. Interestingly, solar cells with only 3-nm-thick (*n*)nc-Si:H featured not only a favored average J_{SC} of 38.9 mA/cm^2 but also a decent average *FF* of 78.6% and a V_{OC} of 719 mV, thus the highest average η of 22.0% was achieved.

Note that this 3-nm-thick (*n*)nc-Si:H (*n*)-contact is expected to feature a high E_a value of around 590 meV (see Figure 6.2) and yet, the corresponding solar cells delivered decent *FF*s above 78.6% (see Figure 6.4). Notwithstanding the limited active doping, in such a thin Si layer, the electrons are able to tunnel directly from (*n*)c-Si to TCO, making the transport of electrons less sensitive to the condition of (*n*)-contact/TCO heterointerface after processing. Therefore, electrons can be collected effectively as long as the passivation quality is well-preserved. In the case of thicker layers, a similar transport path also happens if the nc-Si:H-based (*n*)-contacts feature well-developed nanocrystals [151] and with special processing conditions at (*n*)-contact/TCO interface [175]. However, the parasitic absorption of thick (*n*)-contacts will limit the efficiency of solar cells. Nevertheless, (*n*)-contact with a low E_a still benefits the effective collection of electrons [150]. Thus, a combination of thinner (*n*)-contacts exhibiting low E_a is promising to boost the conversion efficiency of solar cells.

The EQE, 1 - R spectra and IQE spectra of cells with 8-nm-thick (n)nc-SiO$_x$:H (both types), 3-nm-thick (n)nc-Si:H and 4-nm-thick (n)a-Si:H are plotted in Figure 6.5.

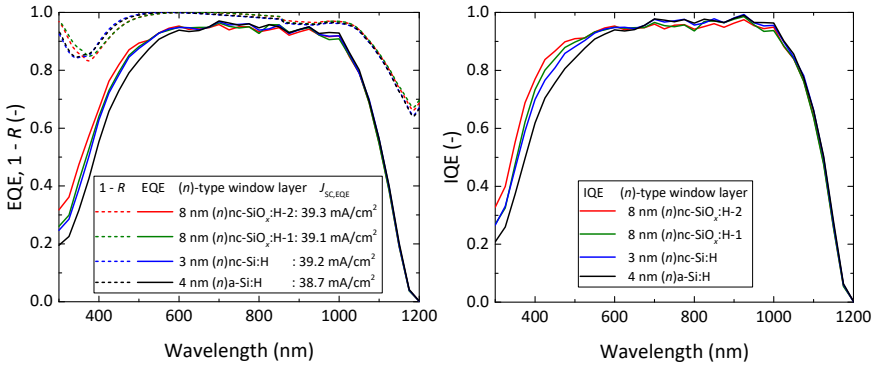

Figure 6.5: The (a) EQE, 1 - R spectra, and (b) IQE spectra of rear junction FBC-SHJ cells with various (n)-contacts.

As shown in Figure 6.5 (a), the differences among various EQE spectra were mainly found in the wavelength range from 300 nm to 600 nm. In this wavelength range, compared to the cell with (n)a-Si:H, the (n)nc-SiO$_x$:H-2 cell exhibits a $J_{SC,EQE}$ gain of 0.8 mA/cm^2, while both (n)nc-SiO$_x$:H-1 and (n)nc-Si:H counterparts show $J_{SC,EQE}$ improvements of around 0.6 mA/cm^2. These EQE differences once more correspond well to the reported optical properties of the (n)-layers as given in Table 6.2. Specifically, the derived IQE spectra in Figure 6.5 (b) further reveal the dominant role of parasitic absorptions of various (n)-type window layers on these EQE differences [173]. This finding was also confirmed by performing optical simulations of our solar cells (See Appendix A, Figure A.5). Although the cell with 8-nm-thick (n)nc-SiO$_x$:H-2 showed the highest integrated $J_{SC,EQE}$ of 39.3 mA/cm^2, the device with 3-nm-thick (n)nc-Si:H delivered a comparable $J_{SC,EQE}$ of 39.2 mA/cm^2 thanks to the ultra-thin thickness of the (n)-contact. Those results suggest that this 3-nm-thick (n)nc-Si:H is an optically promising window layer for FBC-SHJ solar cells.

6.3.3 Solar cells – HRTEM and EDX elemental mapping

We further conducted HRTEM with EDX elemental mapping to investigate: (i) the thickness of (n)-type layers deposited; (ii) the microstructural characteristics of various (n)-type films deposited in solar cells; (iii) the appearance of (n)c-Si/(i)a-Si:H and (n)-contact/ITO interfaces. The HRTEM images resulting from the front side interfaces of solar cells with 4-nm-thick (n)a-Si:H and 3-nm-thick (n)nc-Si:H are provided in Figure 6.6.

As illustrated in Figures 6.6 (a) and (b), together with recognizing around 6.5-nm-thick (i)a-Si:H layer (See Appendix A, Figure A.6), we confirmed that the deposited thicknesses of (n)-contacts in the devices are close to the designated thicknesses, which were approximately 4 nm and 3 nm for (n)a-Si:H and (n)nc-Si:H, respectively. Besides, both (n)-contacts exhibited nearly fully amorphous microstructures. Although the (n)nc-Si:H

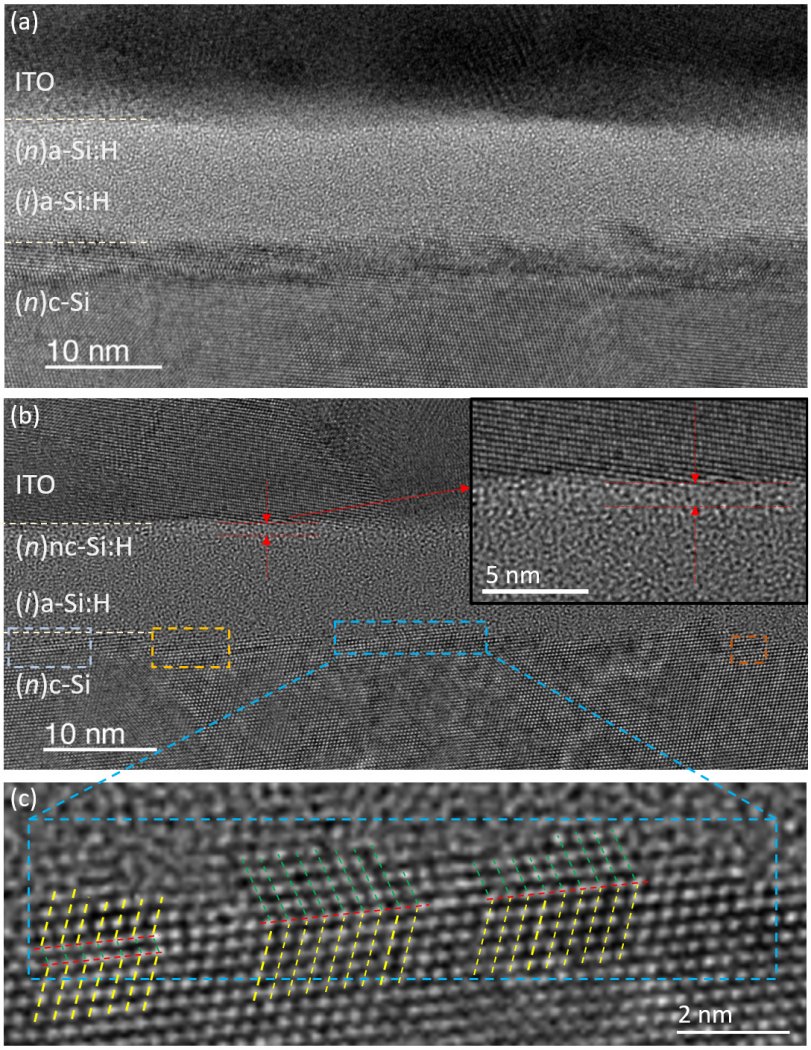

Figure 6.6: HRTEM cross-sectional images of FBC-SHJ solar cell's (*n*)-contact structures featuring (a) ~4-nm-thick (*n*)a-Si:H, and (b) ~3-nm-thick (*n*)nc-Si:H viewed from <110> orientation. The white dashed lines are guides to the eyes for distinguishing (*n*)c-Si/(*i*)a-Si:H and (*n*)-contact/ITO interfaces. In Figure (b), the red dashed lines and arrows highlight the 1 to 2 nm sub-layer that is rougher than the (*i*)a-Si:H + (*n*)nc-Si:H bulk. The inset of Figure (b) is the magnified region of the red dashed lines and arrows. The dashed colored rectangular areas include possible Si atoms double stacking faults and tiny twinned crystals with the c-Si wafer substrate. Figure (c) exhibits the magnified dashed blue rectangle in Figure (b). In Figure (c), the dashed yellow lines represent the consistent Si atoms stacking with the c-Si wafer, and the green dashed lines represent the Si atoms stackings with different orientations from the c-Si wafer.

layer appeared amorphous, 1 to 3 nm crystalline seeds embedded in otherwise amorphous material cannot be excluded in the relatively thick TEM foil of about 20 nm. Typically, the amorphous incubation phase is around 2 to 3-nm-thick when the layer is deposited on (*i*)a-Si:H [426]. As the (*n*)nc-Si:H layer used in this study was only around 3 nm, it was difficult to observe any nanocrystalline phase in this 3-nm-thick (*n*)nc-Si:H layer. As the incubation phase is also part of the formation of (*n*)nc-Si:H layer, we still consider this 3-nm-thick layer to be (*n*)nc-Si:H or based on (*n*)nc-Si:H PECVD plasma growth conditions. Further advanced characterizations could help us to identify the eventual existence of nanocrystals in such a thin layer. For simplicity, we still name this 3-nm-thick layer as (*n*)nc-Si:H unless otherwise stated. Nevertheless, this (*n*)nc-Si:H layer exhibited different characteristics from the standard (*n*)a-Si:H. For the solar cell with (*n*)nc-Si:H, we observed a 1 to 2-nm-thick sub-layer that was rougher than that of the (*i*)a-Si:H + (*n*)nc-Si:H bulk. This sub-layer can be attributed to the formation of oxygen-rich (*n*)nc-Si:H/ITO interface as elaborated later in Figures 6.7 (a) and (b) with EDX results. Besides, it is also worth noting that for the cell with 3-nm-thick (*n*)nc-Si:H, on some occasions Si atoms double stacking faults and tiny twinned crystals on top of the c-Si substrate could be seen as shown in Figure 6.6 (c). A comprehensive study with similar observations was recently reported [427]. The formation of those crystals at c-Si/(*i*)a-Si:H interface could be induced by the highly hydrogen-diluted plasma and the lack of oxygen during the deposition [266, 371, 428]. For these reasons, unlike (*n*)nc-Si:H, we hardly observed those crystalline structures at c-Si/(*i*)a-Si:H interface for both cells with (*n*)a-Si:H and (*n*)nc-SiO_x:H-2 (See Appendix A, Figure A.6).

As shown in the oxygen (O) maps of Figures 6.7 (a) and (b), we observed more oxygen presence in/near the P-rich region of the 3-nm-thick (*n*)nc-Si:H as compared to the (*n*)a-Si:H counterparts. Further, from the Si map, we also identified a reduced Si atomic fraction of deposited (*n*)nc-Si:H close to ITO, while (*n*)a-Si:H remains a similar atomic percentage of Si as compared to that of the (*i*)a-Si:H beneath. Similar observations of reduced Si atomic fraction and prominent O incorporation were also found for (*n*)nc-SiO_x:H-2 (See Appendix A, Figure A.6). Therefore, both O and Si maps of the cell with (*n*)nc-Si:H indicate significant amounts of oxygen incorporations into the deposited (*n*)nc-Si:H. The more numerous oxygen incorporations can be ascribed to the possibly more porous or less dense phase of (*n*)nc-Si:H as it was close to the intermediate highly porous amorphous-to-crystalline transition phase [308]. This finding suggests a possible less resistive (*n*)a-Si:H/ITO interface as compared to (*n*)nc-Si:H/ITO interface, which may additionally explain the slightly higher *FF* observed for cells with (*n*)a-Si:H aside from the fact that our 4-nm-thick (*n*)a-Si:H was more conductive than 3-nm-thick (*n*)nc-Si:H (see Figure 6.4). Similar observations were also reported by S. Sheng, et al., who conducted X-ray photoelectron spectroscopy (XPS) depth profiling measurements on (*n*)-type layer/ITO interface for amorphous silicon solar cells [378]. The (*n*)a-Si:H/ITO interface exhibited advantageous characteristics as compared to that of (*n*)μc-Si:H, such as lack of oxygen segregation, less oxidized Si thin-films around the interface region, and less ITO in-diffusion. While as seen in our EDX results, indium (In) was well constrained within ITO for all (*n*)-contacts investigated. Lastly, due to the very tiny atomic fractions and large scatterings of phosphorus (P) content in all samples, we cannot justify if there is any statistical difference in P content from those EDX results

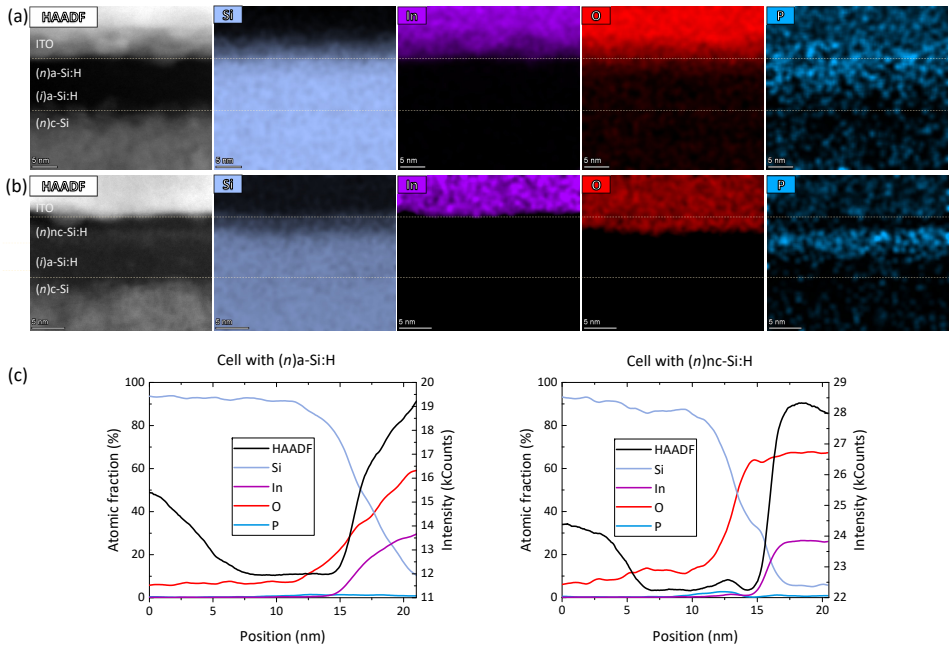

Figure 6.7: The scanning TEM (STEM) high-angle annular dark-field (HAADF) images combined with chemical compositional mapping measured by EDX of solar cells with (a) ~4-nm-thick (*n*)a-Si:H, and (b) ~3-nm-thick (*n*)nc-Si:H (*n*)-contacts. The white dashed lines are guides to the eyes for distinguishing (*n*)c-Si/(*i*)a-Si:H and (*n*)-contact/ITO interfaces. Note, the phosphorus (P) signal detected outside P-rich zones is an artifact, just as the oxygen (O) signal in the c-Si substrate. Figure (c) presents the (relative) atomic fractions (intensity) of different elements (HAADF) for EDX mapping results that are shown in Figures (a) and (b). The '0-nm' position lies inside the (*n*)c-Si wafer and it is close to the (*n*)c-Si/(*i*)a-Si:H interface.

between the two samples, though a near-zero P content in the oxygen-rich (*n*)nc-Si:H layer can be concluded from the EDX results. Further investigations are needed for a more complete comparison between the (active) doping concentrations in the various thin (*n*)-contacts.

6.3.4 Solar cells – Effects of interfacial treatments

To mitigate the possible resistive interface of (*n*)nc-Si:H with ITO as observed in Figure 6.7, we deposited a 2-nm-thick (*n*)a-Si:H capping layer on top of the 3-nm-thick (*n*)nc-Si:H. This extra (*n*)a-Si:H aims at improving mainly the transport of electrons through (*n*)a-Si:H/ITO interface. Besides, the effects of HPTs, which were already applied for solar cells with 3-nm-thick (*n*)nc-Si:H (*n*)-contact in Figure 6.4, are also investigated in this section. The *J*-*V* parameters of solar cells are shown in Figure 6.8.

As presented in Figure 6.8, the HPTs significantly improved iV_{OC} of cells before ITO sputtering from 734 mV to 745 mV. Aside from an 11 mV gain of V_{OC}, we also observed a slightly increased J_{SC} and a nearly 3%$_{abs.}$ *FF* improvement by applying the HPTs. These improvements are related to more hydrogen incorporation induced by the treatments,

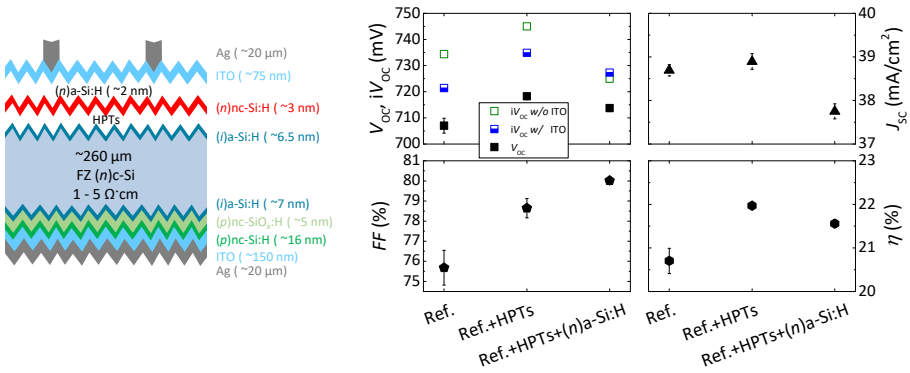

Figure 6.8: The schematic sketches and external parameters of rear junction FBC-SHJ cells featuring 3-nm-thick (*n*)nc-Si:H as the (*n*)-type contact as function of HPTs and (*n*)a-Si:H capping layer interfacial treatments. Solar cells without any treatment are denoted as the reference (Ref.). The results represent averaged parameters with four solar cells (3.92 cm^2) and the error bars represent the standard deviations.

which improve the passivation quality and increase the bandgap of (*i*)a-Si:H layers [368]. Nevertheless, the additional 2 nm of (*n*)a-Si:H capping layer further improved the *FF* to 80%, which could partially be attributed to a better (*n*)a-Si:H/ITO interface as expected from the EDX results and also a more conductive layer stack as the (*n*)-contact as discussed in Section 6.3.1. Although we observed a slightly lower iV_{OC} already before ITO deposition when (*n*)a-Si:H capping layer was applied, the sample preserved its passivation quality after ITO sputtering, unlike passivation degradations observed for other (*n*)nc-Si:H single-layer counterparts. Nevertheless, mainly due to extra parasitic absorption that was induced by this additional (*n*)a-Si:H layer, solar cells exhibited 0.4%$_{abs.}$ lower efficiency as compared to the cells with only the HPTs. Overall, 3-nm-thick (*n*)nc-Si:H with the optimized HPTs is appealing to be used as the window layer mainly thanks to the high J_{SC} and the promising *FF* of the solar cells.

6.3.5 Solar cells – Certified *I-V* and the double-layer anti-reflection coating

The best cell with 3-nm-thick (*n*)nc-Si:H and the reference cell with 4-nm-thick (*n*)a-Si:H were chosen to be independently certified at ISFH CalTec (Hamelin, Germany). Both cells featured the same layer stacks and fabrication process except for the layers used as the (*n*)-contact. The measured *I-V* parameters are shown in Figure 6.9. The cell with 3-nm-thick (*n*)nc-Si:H exhibited a certified η of 22.20%, which is 0.44%$_{abs.}$ higher than that of (*n*)a-Si:H counterparts mainly due to the highly transparent thin (*n*)nc-Si:H window layer. As reported previously [163, 164], for doped layers thicker than ~9 nm, J_{SC} gains were observed for cells with doped nc-Si:H rather than for cells with a-Si:H with comparable thicknesses. Here, we exploited further the more optical advantageous (*n*)nc-Si:H over the (*n*)a-Si:H at an ultra-thin thickness level (~3 to 4 nm). Comprehensive studies including fine-tuning of our processes are needed to draw more detailed conclusions. It is worth noting that our screen-printed Ag front fingers feature a designated width

of ~70 µm, which leaves still plenty of room for improving further the J_{SC} of the solar cells. Nevertheless, our 3-nm-thin (*n*)nc-Si:H enabling cell efficiency above 22% is thinner than the state-of-art minimum required thickness for (*n*)nc-Si:H or (*n*)nc-SiO$_x$:H-based (*n*)-contacts for high-efficiency SHJ solar cells [163, 164, 386, 387], thus allowing lower material consumptions and potentials for higher industrial throughputs.

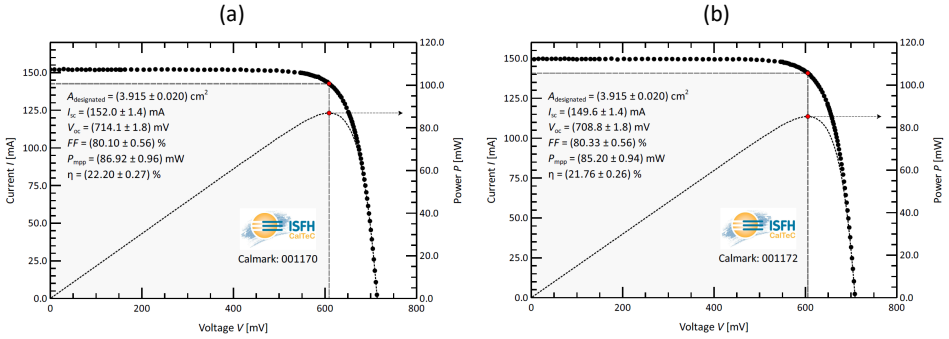

Figure 6.9: The independently certified *I-V* characteristics and device parameters of the best rear junction FBC-SHJ solar cells featuring (a) 3-nm-thick (*n*)nc-Si:H and (b) 4-nm-thick (*n*)a-Si:H contact. Both cells feature the same layer stacks and fabrication process except for the (*n*)-contact. The certifications were performed at ISFH CalTeC (Hamelin, Germany).

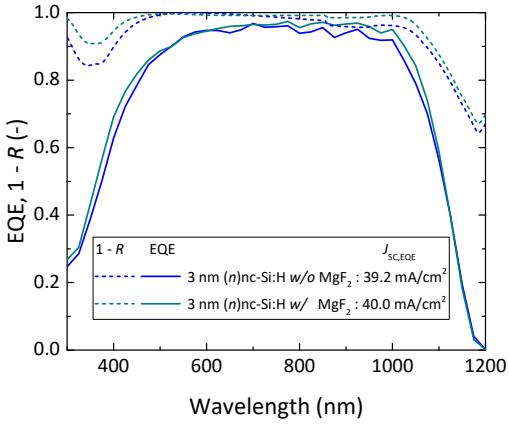

Figure 6.10: The EQE and 1 - *R* spectra of rear junction FBC-SHJ cell featuring 3-nm-thick (*n*)nc-Si:H with and without MgF_2 for forming the double-layer anti-reflection coating with ITO.

To further explore the potential of the optimized stack, we applied an additional 100-nm-thick MgF_2 layer on top of the ITO to form the double-layer anti-reflection coating (DLARC) [325, 429]. We demonstrated a $J_{SC,EQE}$ up to 40.0 mA/cm^2 for the cell with 3-nm-thick (*n*)nc-Si:H as shown in Figure 6.10. This $J_{SC,EQE}$ gain brings the active area cell efficiency η_{active} to 22.88%, which originates from the better anti-reflection effects in-

duced by the DLARC. Thus, we observed 0.2 mA/cm^2 and 0.6 mA/cm^2 $J_{SC,EQE}$ improvements in the wavelength ranges below and above 600 nm, respectively, by applying the MgF_2 layer. Further improvements to achieve cell η over 23% in the short-term are (i) a more transparent TCO, such as IFO:H [327], (ii) a lower front metal coverage via finer-line screen printing or copper-electroplating [430] and (iii) a better passivation quality by applying a bi-layer (*i*)a-Si:H layer stack [427, 431].

6.4 Conclusions

In this chapter, aiming at minimizing the parasitic absorptions induced by (*n*)-type window layers, we studied opto-electrical properties of (*n*)a-Si:H, two types of (*n*)nc-SiO_x:H, and (*n*)nc-Si:H layers and implement them (as thin as 2 nm) into rear junction FBC-SHJ solar cells.

We first investigated and compared various (*n*)-type layers both optically and electrically, where (*n*)a-Si:H was the least optical favorable then followed by (*n*)nc-Si:H and two (*n*)nc-SiO_x:H layers. However, due to the observed thickness- and substrate-dependent electrical properties, nc-Si:H-based layers exhibited lower σ_d and generally higher E_a values than that of (*n*)a-Si:H when they were deposited on (*i*)a-Si:H coated glasses with thicknesses below 20 nm. Then, those layers were integrated into rear junction FBC-SHJ solar cells. We noticed a strong correlation between (*n*)-contacts properties and passivation qualities of cells after ITO sputtering. That is, a thicker and a more conductive (*n*)-contact tended to exhibit a higher passivation resilience to ITO sputtering and a smaller gap from iV_{OC} to V_{OC} thanks to the improved selectivity. Besides, we also found that (*n*)-layer with a higher E_{04} or a larger σ_d (lower E_a) delivered a higher J_{SC} or a higher *FF* in well-passivated solar cells (V_{OC} > 710 mV), respectively.

Subsequently from HRTEM and EDX analysis, a higher oxygen presence near (*n*)nc-Si:H/ITO interface was revealed as compared to the (*n*)a-Si:H counterpart, which suggests a less resistive (*n*)a-Si:H/ITO interface and thus contributing to slightly higher *FF*s observed in solar cells. Eventually, we demonstrated the successful application of an ultra-thin layer of only 3-nm-thick based on (*n*)nc-Si:H PECVD plasma growth conditions together with the optimized HPTs that delivered a certified η of 22.20%. This cell showed 0.61 mA/cm^2 J_{SC} gain over the (*n*)a-Si:H counterpart owing to the higher transparency of (*n*)nc-Si:H, while maintaining comparable V_{OC} > 714 mV and *FF* > 80%. Further, the cell with 3-nm-thick (*n*)nc-Si:H featuring MgF_2/ITO DLARC exhibited a $J_{SC,EQE}$ of 40.0 mA/cm^2 and achieved an active area cell efficiency η_{active} of 22.88%.

7

Effects of (*i*)a-Si:H deposition temperature on high-efficiency SHJ solar cells

This chapter is based on the publication:

Y. Zhao, P. Procel, A. Smets, L. Mazzarella, C. Han, G. Yang, L. Cao, Z. Yao, A. Weeber, M. Zeman, and O. Isabella, "Effects of (*i*)a-Si:H deposition temperature on high-efficiency silicon heterojunction solar cells," *Progress in Photovoltaics: research and applications*, 2022. [1]

Abstract

Excellent surface passivation induced by (*i*)a-Si:H is critical to achieve high-efficiency silicon heterojunction (SHJ) solar cells. This is key for conventional single-junction solar cell applications but also for bottom-cell applications in tandem devices. In this study, we investigated the effects of (*i*)a-Si:H deposition temperature on passivation quality and SHJ solar cell performance. At the lower end of temperatures ranging from 140 °C to 200 °C, it was observed with Fourier-transform infrared spectroscopy (FTIR) that (*i*)a-Si:H films were less dense, thus hindering their surface passivation capabilities. However, with the additional hydrogen plasma treatments (HPTs), those (*i*)a-Si:H layers deposited at lower temperatures exhibited significant improvements and better passivation qualities than their counterparts deposited at higher temperatures. On the other hand, even though we observed the highest V_{OC}s for cells with (*i*)a-Si:H deposited at the lowest temperature (140 °C), the related *FF*s were poorer as compared to their higher temperature counterparts. The optimum trade-off between V_{OC} and *FF* for the SHJ cells was found with temperatures ranging from 160 °C to 180 °C, which delivered independently certified efficiencies of 23.71%. With further improved (*p*)-layers that enabled a

[1] This paper was invited for publication in the special issue 'EU PVSEC' of *Progress in Photovoltaics: Research and Applications*.

FF of 83.3%, an efficiency of 24.18% was achieved. Thus, our study reveals two critical requirements for optimizing the (*i*)a-Si:H layers in high-efficiency SHJ solar cells: (i) excellent surface passivation quality to reduce losses induced by interface recombination and simultaneously (ii) less-defective (*i*)a-Si:H bulk to not disrupt the charge carrier collection.

7.1 Introduction

Front/back-contacted silicon heterojunction (FBC-SHJ) solar cells have achieved remarkable efficiencies well above 26% [67]. Application of SHJ cells in tandem devices resulted in record two-terminal (2T) perovskite-silicon tandem efficiencies beyond 30% [109]. One of the crucial ingredients that enable such high efficiencies is the excellent open-circuit voltage (V_{OC}) above 750 mV of SHJ cells, which is mainly provided by a few nanometer thick hydrogenated intrinsic amorphous silicon ((*i*)a-Si:H) film. Therefore, careful optimization of the (*i*)a-Si:H deposition conditions is essential to enable high-efficiency SHJ solar cells and their application in tandem solar cells. In general, optimized (*i*)a-Si:H should be deposited with a high bulk quality while suppressing the detrimental epitaxial growth at the c-Si/(*i*)a-Si:H interface [432]. Approaches have been proposed to enhance the surface passivation qualities of (*i*)a-Si:H layer, such as using hydrogen-diluted SiH_4 [433–436], pre- or post-hydrogen plasma treatment (HPT) [175, 368, 437–442], (*i*)a-Si:H bi-layer or multi-layer stacks [131, 132, 427, 431, 436, 443–446] and post-annealing [432, 447, 448]. Subsequent overlaying of doped layers and transparent conductive oxide (TCO) layers on the (*i*)a-Si:H layers also impose challenges on preserving their passivation qualities of the c-Si surface [155, 449].

Apart from the necessity of having excellent passivation induced by (*i*)a-Si:H, SHJ solar cells should also feature efficient charge carrier transport from c-Si bulk to the TCO. Notwithstanding the importance of tuning the electrical properties of doped layers and TCO layers for achieving efficient selective transport of charge carriers [150], different bulk qualities of (*i*)a-Si:H may also differently impact the charge carrier collection [431, 450, 451]. Interestingly, either (*i*)a-Si:H mono-layers or bi-layers that feature an underdense (*i*)a-Si:H layer close to c-Si surface showed better passivation qualities as compared to their dense counterparts. On the other hand, those underdense films may also cause increased series resistance of solar cells [431, 450, 451]. Therefore, the revealed trade-off between passivation and carrier collection with respect to (*i*)a-Si:H requires attentive optimization efforts.

Aiming at further understanding and exploring the potential of the excellent passivation induced by (*i*)a-Si:H, in this study, we analyzed in detail the optical and microstructural properties of (*i*)a-Si:H layers deposited under various temperatures between 140 °C and 200 °C, and applied them to SHJ solar cells. Besides, the effects of our optimized HPT and very-high-frequency treatment (hereafter simplified as HPTs) [175] on (*i*)a-Si:H passivation quality were also studied. We addressed the microstructural evolution of (*i*)a-Si:H layers under various conditions via Fourier-transform infrared (FTIR) spectroscopy measurements. Accordingly, those microstructural properties of (*i*)a-Si:H layers provided possible explanations for their passivation capabilities and their impacts on solar cells.

Table 7.1: PECVD deposition parameters of different (*i*)a-Si:H layers, HPT and VHF treatment.

PECVD parameters	(*i*)a-Si:H-1	(*i*)a-Si:H-2	HPT	VHF treatment
SiH_4 (sccm)	40	10	0	1.2
H_2 (sccm)	0	30	200	120
Pressure (mbar)	0.7	1.4	2.7/2.2 (for (*n*)/(*p*)-side)	4.0
Power density (mW/cm^2)	20.8	20.8	62.5	90.3
Temperature (°C)	140 – 200	140 – 200	180	180
Frequency (MHz)	13.56	13.56	13.56	40.68
Duration (s)	-	-	120	120

7.2 Experimental details

In this chapter, various (*i*)a-Si:H layers as listed in Table 7.1 were obtained by adjusting their deposition conditions. Additionally, we also applied the previously optimized HPTs on (*i*)a-Si:H layers. The main deposition parameters are provided in Table 7.1 [175]. The detailed deposition conditions of doped layers can be found in Chapters 5 and 6 [167, 312]. Different glass and (*n*)-type c-Si samples, as schematically illustrated in Figure 7.1, were prepared to evaluate the effects of the deposition temperature and HPTs on (*i*)a-Si:H layers and their further applications in SHJ solar cells. The abbreviations, stack descriptions and temperatures for layers and HPTs investigated in this study are given in Table 7.2. Specifically, spectroscopic ellipsometry (SE) was used to extract the optical bandgap (E_{04}) and refractive index (n at the wavelength of 632 nm) of (*i*)a-Si:H layers deposited on glass substrates. Note, the deposition conditions of HPT for the (*p*)-side, as listed in Table 7.1, were used as the representative HPT for both FTIR and symmetrical (*i*)a-Si:H passivation samples. The HPTs etch around 2 nm of the (*i*)a-Si:H bi-layer on each side of the c-Si wafer.

For solar cell fabrication, room-temperature sputtered tungsten-doped indium oxide (IWO) layers were deposited with thicknesses of 50 nm and 150 nm on the front and rear sides, respectively [325]. Solar cells were fabricated either with screen-printed (SP) Ag contacts on both sides or alternatively, with our optimized room-temperature copper-electroplating metallization approach to form the front metal grid while using 500-nm-thick thermally evaporated Ag for forming the rear contact [127]. To further improve the anti-reflection effect of the completed solar cells, a 100-nm-thick SiO_x was optionally deposited on the front side of the devices [325, 429]. Solar cells fabricated in this chapter have a designated area of 3.92 cm^2. The independently certified *I-V* parameters were obtained from the CalTeC of the Institute for Solar Energy Research Hamelin (ISFH), Germany.

Based on FTIR measurements, we extracted the microstructure factor (R_{SM}) that is

defined for Si-H stretching modes (SM) of (*i*)a-Si:H layers as described in Chapter 3.2.1. Note, in this case, the $\alpha^*(\omega)$ that represents the effective absorption coefficient at ω was used. The $\alpha^*(\omega)$ is proportional to -ln($T(\omega)$)/t if $\alpha^*(\omega)\,t \ll 1$. The $T(\omega)$ is the transmittance obtained from the FTIR measurements, and t is the effective thickness of the film, which counts for films deposited on both sides. Typically, FTIR analyses are performed on films deposited on flat c-Si substrates, however, in this work, the textured c-Si substrates as integrated in the SHJ solar cell devices are used. For simplicity, the effective film thickness on each side is assumed to be 1.7 times of film thickness that is perpendicular to the pyramid facet. Note, in reality, the effective film thickness is larger than this assumption due to effects induced by the use of textured samples, such as reduced reflection thus resulting in enhanced light incorporation and prolonged optical path. Nevertheless, the relative comparisons among samples are still valid with this assumption.

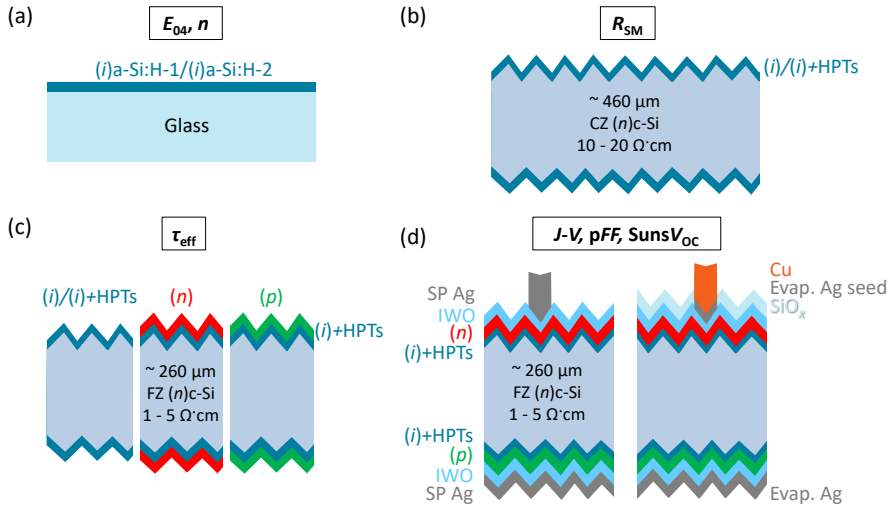

Figure 7.1: Schematic sketches of sample structures for (a) extracting E_{04} and n, (b) FTIR measurements, (c) obtaining τ_{eff}, and (d) rear junction FBC-SHJ solar cells fabricated in this study. In part (d), SP stands for screen-printed and Evap. is the abbreviation of the 'evaporated'.

7.3 Results and Discussions

7.3.1 Temperature effects on optical properties of (*i*)a-Si:H mono-layers

To understand the effects of (*i*)a-Si:H deposition temperature on their optical properties, we deposited the two types of (*i*)a-Si:H (~20 nm) described in Table 7.1 on glass substrates (see Figure 7.1 (a)). Figure 7.2 presents the extracted E_{04} and n at the wavelength of 632 nm of (*i*)a-Si:H layers via SE.

As shown in Figure 7.2, for the temperature range investigated (140 °C to 200 °C), we observed monotonic decrements of the E_{04} and increments of the n with higher deposition temperatures for both (*i*)a-Si:H layers. A higher E_{04} often indicates a higher hy-

Table 7.2: Abbreviations, stack descriptions and deposition temperatures for layers and HPTs forming the SHJ solar cells.

Abbreviations	Descriptions	Temperature (°C)
(*i*)	1 nm (*i*)a-Si:H-1 + 7 or 8 nm (*i*)a-Si:H-2[a]	140 - 200
HPTs	HPT + VHF treatment	180
(*n*)	3 nm (*n*)nc-Si:H[b] + 2 nm (*n*)a-Si:H	180
(*p*)	5 nm (*p*)nc-SiO$_x$:H[b] + 16 nm (*p*)nc-Si:H	180

[a]: 7 nm and 8 nm (*i*)a-Si:H-2 for (*n*)- and (*p*)-layers, respectively;
[b]: With such thin thicknesses, both the 3 nm (*n*)nc-Si:H [167] and 5 nm (*p*)nc-SiO$_x$:H are amorphous-phase dominant (see Figure B.1) and yet to develop well-defined nanocrystals.

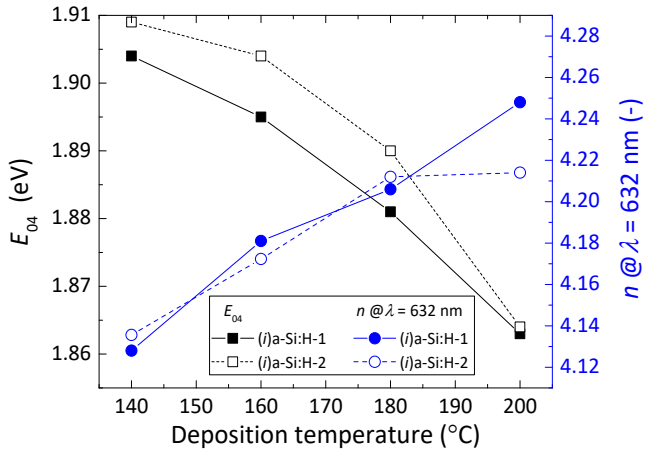

Figure 7.2: The E_{04} and n of (*i*)a-Si:H layers deposited at variable temperatures.

drogen content in the (*i*)a-Si:H layer [202]; that is, both (*i*)a-Si:H layers deposited under lower temperatures were likely to be more hydrogen-rich than the higher temperature counterparts. Besides, we ascribe the lower n of (*i*)a-Si:H deposited under lower temperatures to the relatively lower film densities. Those observations agree well with previous studies [435, 446]. Therefore, based on both E_{04} and n, the films seem to become denser but they incorporate less hydrogen by increasing the deposition temperature of the (*i*)a-Si:H layers.

7.3.2 Temperature and HPTs effects on (*i*)a-Si:H layers' microstructural properties

To prevent possible epitaxial growth of the highly hydrogen-diluted (*i*)a-Si:H-2 when deposited directly on c-Si, we followed the bi-layer approach that improved the passivation quality and efficiency of our SHJ solar cells (see Appendix B, Table B.2). The bi-layer consists of a 1-nm-thick (*i*)a-Si:H-1 layer without additional hydrogen-dilution [452] that acts as a buffer for the subsequent deposition of the highly hydrogen-diluted (*i*)a-Si:H-2

layer. To gain more insights into the (*i*)a-Si:H layers with cell-relevant growth conditions, it is worth noting that we used double-side-textured substrates with the same (*i*)a-Si:H thicknesses as used in solar cells for FTIR measurements. The microstructure and hydrogen-bonding configuration of bi-layer stacks deposited under various temperatures were assessed by FTIR on dedicated samples as sketched in Figure 7.1 (b). Besides, we also evaluated the effects of HPTs on the microstructural properties of the bi-layer stacks. The infrared spectra of different (*i*)a-Si:H bi-layers are presented in Figure 7.3. The infrared spectra of single (*i*)a-Si:H layers deposited at 160 °C were given in Appendix B, Figure B.3.

As seen in Figure 7.3 (a), detailed information from the peaks around the wavenumber of 2000 cm^{-1}, 880 cm^{-1} and 640 cm^{-1} can be extracted to characterize our (*i*)a-Si:H bi-layers. Firstly, the peak around 2000 cm^{-1} can be typically deconvoluted into two Gaussian distributions for a-Si:H, which are related to the Si-H low-frequency SM (LSM) and high-frequency SM (HSM) as visible in Figure 7.3 (a). It has been demonstrated that the LSM is attributed to monohydrides in small volume deficiencies [343, 375], whereas HSM is assigned to mainly the monohydrides and some polyhydrides at internal surfaces of larger volume deficiencies like nano-sized voids [338, 343, 375]. As a result of the different Si-H bonding nature of LSM and HSM, a higher fraction of HSM, thus a higher R_{SM} (defined previously in Section 3.2) indicates a less compact or void-rich film. For simplicity, as for (*i*)a-Si:H bi-layers without HPTs, peaks centered at 2000 cm^{-1} and 2090 cm^{-1} are assigned to LSM and HSM, respectively.

As seen around the SM region in Figure 7.3 (a), for (*i*)a-Si:H bi-layers without HPTs, instead of the I_{LSM} that only slightly vary with deposition temperatures, we observed more significant monotonic decrements of I_{HSM} with increasing deposition temperatures. As a result, (*i*)a-Si:H bi-layers deposited at lower temperatures featured larger R_{SM} values as compared to the higher temperature counterparts. In other words, (*i*)a-Si:H bi-layers were more void-rich as they contain silicon hydrides at internal void surfaces when deposited at lower temperatures, which could result in higher hydrogen content in the films as well. This finding is in good agreement with the optical properties we reported in Figure 7.2 as well as with previous studies [435, 446, 453–455]. Moreover, at the wavenumber of around 880 cm^{-1}, which reflects the bending modes (BM) of polyhydrides [343], we observed peaks with gradually decreased absorption strength for layers with higher deposition temperatures. This also suggests the relatively higher fractions of polyhydrides for films deposited under lower temperatures.

Similar to (*i*)a-Si:H bi-layers without HPTs, the R_{SM} for the (*i*)a-Si:H bi-layers with HPTs was also higher for films deposited at lower temperatures, although the R_{SM} differences between different temperatures were less prominent (see Figure 7.3 (a)). The overall increased R_{SM} indicates that hydrogen-incorporation through our HPTs reconfigures the Si-H bonding configurations and favors the formation of the HSM components in the (*i*)a-Si:H bi-layers. The formation of polyhydrides that contribute to the HSM after HPTs is also reflected in the observed peaks that represent polyhydrides BM as presented in Figure 7.3 (a). It is worth noting that we applied a slight shift of frequency from 2000 cm^{-1} to 2010 cm^{-1} for the LSM to obtain better fittings to the raw data. This shift of frequency is a result of the reduced electrical screening of the Si-H dipole vibrations by a less dense dielectric and additionally indicates the formation of more porous films af-

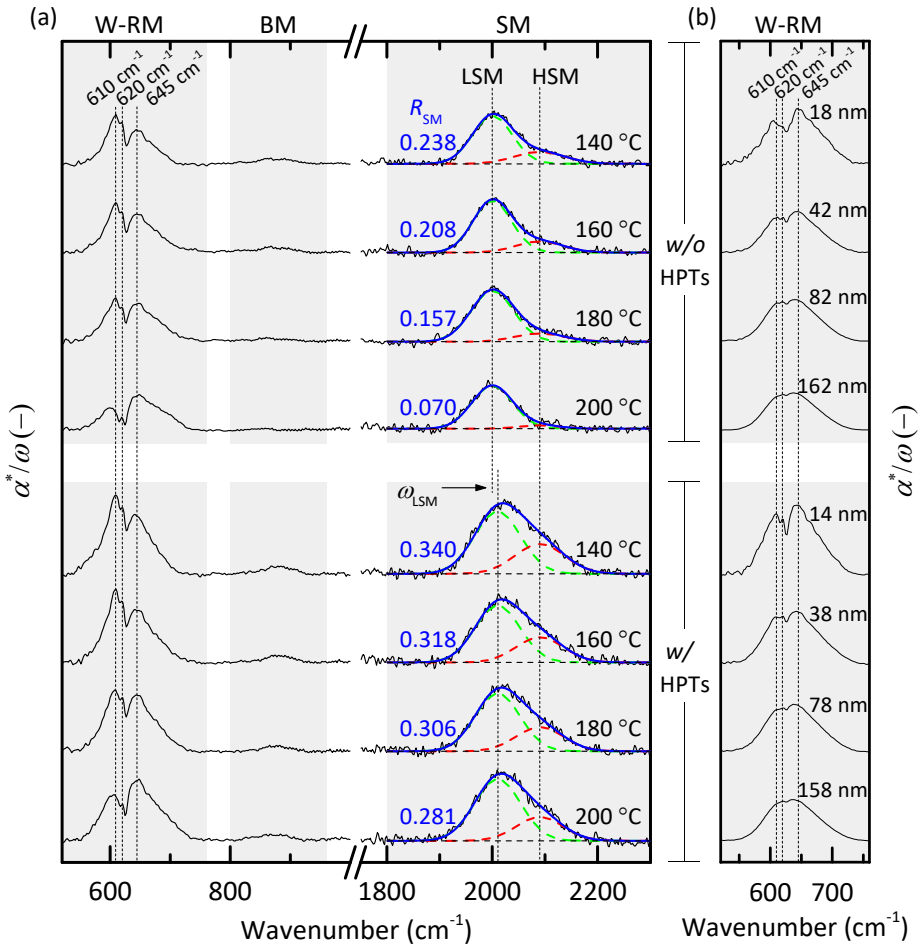

Figure 7.3: The infrared spectra of (*i*)a-Si:H bi-layers deposited (a) at various temperatures with (*w*/) or without (*w*/*o*) HPTs; (b) with various thicknesses *w*/ or *w*/*o* HPTs. For part (a), the thickness of deposited layers, which is perpendicular to the pyramid facet, before and after HPTs is in total 18 nm and 14 nm on both sides of the substrate, respectively. For part (b), these (*i*)a-Si:H bi-layers consist of a 1-nm-thick (*i*)a-Si:H-1 layer with a (*i*)a-Si:H-2 layer featuring varied thickness, the deposition temperature was fixed at 160 °C and the indicated thickness numbers are total thickness on both sides of the wafer. These thicknesses were estimated based on the deposition rates calculated from flat samples. In both parts, W-RM stands for Si-H wagging-rocking modes, BM refers to Si-H polyhydrides bending modes, SM represents Si-H stretching modes. In the SM region, the green and red dashed lines represent the fitted Gaussian function for LSM and HSM, respectively. The blue solid lines are the overall fittings. Note that the series of samples in Figure 7.3 (a) were processed in different batches as compared to Figure 7.3 (b).

ter HPTs as discussed in the previous work [224]. Besides, we also noticed the overall improved absorption strength of the SM as compared to films without HPTs [175]. This could be correlated to the following causes: (i) the HPTs incorporate significant amounts

of additional hydrogen into the films [224]; (ii) as the (*i*)a-Si:H bi-layers after HPTs are thinner, hydrogen-rich 'interface' or 'surface' layers will be more dominant (HSM) in reference to the 'bulk' component (LSM) [309], and therefore featuring relatively higher volume deficiencies. Thus, the average dielectric constant will be lower and, as a consequence, the proportionality constant of the dipole oscillation is lower as well [456]. For a given hydrogen content, this lower proportionality constant will eventually result in enhanced absorption signals for layers with HPTs. Nevertheless, the latter cannot be the main contribution to the overall enhanced absorption signals, and HPTs indeed resulted in significant additional hydrogen-incorporation into the (*i*)a-Si:H bi-layers. Overall, it is not straightforward to calculate absolute hydrogen concentration based on the proportionality constants provided in literature [338] because these 'constants' may vary with layers' thicknesses for very thin films, and with the textured morphology of our FTIR samples, which enables the prolonged optical path of infrared light inside the (*i*)a-Si:H bi-layers as compared to typically used flat samples.

With respect to the Si-H wagging-rocking mode (W-RM), commonly one absorption peak centered at the wavenumber of 640 cm^{-1} is observed [338, 341, 342, 457]. Instead, it should be noticed that we observed at least three distinguishable peaks at around 610 cm^{-1}, 620 cm^{-1} and 645 cm^{-1} (see Figure 7.3 (a)). Although similar observations were reported in the literature for a-Si:H, only two peaks around 590 and 635 cm^{-1} were identified [340, 458]. To the best of our knowledge, here we report for the first time at least three distinctive peaks around the W-RM for (*i*)a-Si:H. To further investigate the possible origin of this unexpected multi-peak characteristic, we carried out experiments with variable (*i*)a-Si:H bi-layer thickness as shown in Figure 7.3 (b). These (*i*)a-Si:H bi-layers consist of a 1-nm-thick (*i*)a-Si:H-1 layer with a (*i*)a-Si:H-2 layer featuring varied thicknesses. Interestingly, with a thicker bi-layer, we noticed a progressively decreased absorption strength of the peak at around 610 cm^{-1} (see Figure 7.3 (b)). In the meanwhile, the signature of peaks at around 610 cm^{-1} and 620 cm^{-1} became less distinguishable for thicker layers as they started to merge with the third absorption peak centered at around 645 cm^{-1}. This thickness-dependent characteristic suggests that the peak at around 610 cm^{-1} may be attributed to well-defined silicon-hydride wagging mode(s) that is(are) specific to the 'surface' or 'interface' nature between the (*i*)a-Si:H and c-Si surface, while peaks at around 645 cm^{-1} (also 620 cm^{-1}) may be ascribed to the 'bulk' component as proposed in [309] (detailed discussions can be found in Appendix B, Figure B.4). Unlike that of SM, due to the insufficiently distinctive assignments of absorption peaks around W-RM [340, 341, 343, 459], it is not possible for us to deconvolute the observed W-RM absorption peaks. Still, several attempts for deconvoluting W-RM have been reported previously for investigating the phase transition from a-Si:H to μc-Si:H, in which a similar vibrational origin for peaks at 620 cm^{-1} and 2100 cm^{-1} was proposed [460, 461].

Nevertheless, for (*i*)a-Si:H bi-layers without HPTs as shown in Figure 7.3 (a), we noticed that the absorption strength of mainly the peak at the wavenumber of 610 cm^{-1} decreases with increasing deposition temperatures, while the absorption strength of peaks at 620 cm^{-1} and 645 cm^{-1} seemingly only slightly varied. That is, (*i*)a-Si:H bi-layers deposited at higher temperatures featured reduced 'surface' or 'interface' components, thus resulting in a higher fraction of 'bulk' components according to our speculations based on samples with varied thicknesses. It is known that the 'surface' and 'interface'

parts of the (*i*)a-Si:H are more void- and hydrogen-rich as compared to the 'bulk' counterpart mainly due to their higher fraction of polyhydrides [262, 309–311]. Thus the variations of absorption strength around the W-RM may reflect a denser film with higher deposition temperatures. This finding agrees well with the observed lower R_{SM} with higher deposition temperatures as seen from the SM (see Figure 7.3 (a)). Furthermore, for (*i*)a-Si:H bi-layers with HPTs, the same temperature-dependent trend was found. Similarly, we also observed systematically enhanced absorption strength of peaks after HPTs, which can be attributed to the same reasons as proposed for the SM. Overall, especially for layers with HPTs, those absorption peaks around W-RM seem to be more sensitive to varied deposition temperatures as compared to those around the SM. Thus, those peaks around W-RM might be capable of revealing more details about the changes in microstructure and Si-H bonding configurations in the film or the interface between c-Si and the film (see also the discussion in Appendix B, Figure B.4). To understand more about these absorption peaks around the W-RM, more distinct assignations of specific Si-H vibrational modes around those wavenumbers would provide more insights.

To summarize, for layers with and without HPTs, a lower deposition temperature tends to result in more void-rich and hydrogen-rich (*i*)a-Si:H layers. The HPTs significantly incorporate additional hydrogen into the films and increase the large volume deficiencies of the films, and consequently, resulting in more hydrogenated surfaces in the (*i*)a-Si:H layers.

7.3.3 Temperature effects on passivation quality for SHJ solar cells

We investigated the effects of (*i*)a-Si:H deposition temperature on the passivation qualities of the (*i*)a-Si:H layers and the effects of the additional HPTs on symmetrically coated c-Si wafers (see the schematic sketch in Figure 7.1 (c)). Further, the passivation qualities of the (*i*)a-Si:H layers coated with doped contacts were also investigated. The τ_{eff} values of symmetrical samples are plotted in Figure 7.4 (a).

As seen in Figure 7.4 (a), for passivation samples with only (*i*)a-Si:H bi-layer (open symbols), higher deposition temperatures of (*i*)a-Si:H bi-layers resulted in better passivation qualities. This could be attributed to the denser or less-defective (*i*)a-Si:H bi-layers deposited at higher temperatures as confirmed by our FTIR measurements (see Figure 7.3 (a)) [454]. However, when additional HPTs were applied, the trend is reversed. For (*i*)a-Si:H bi-layer deposited under 140 °C (160 °C) and treated with HPTs, the τ_{eff} was boosted from 1.4 ms (4.2 ms) to 11.7 ms (12.3 ms), while the passivation qualities with the additional HPTs showed fewer improvements and even degraded τ_{eff} for (*i*)a-Si:H bi-layers deposited with temperatures above 160 °C. As known from the FTIR results shown in Figure 7.3 (a), the HPTs increase both the porosity and the hydrogen concentration of the (*i*)a-Si:H bi-layer. In the meanwhile, HPTs could also create defects near the c-Si/(*i*)a-Si:H interface [428]. We ascribe the observed better passivation qualities with (*i*)a-Si:H bi-layer deposited under lower temperature conditions to: (i) their initial highly porous microstructure, which is beneficial for more effectively preventing the possible detrimental epitaxial growth induced by highly hydrogen-diluted (*i*)a-Si:H-2; (ii) protecting near-surface c-Si bulk from defect formations induced by hydrogen radicals within HPTs [446]; (iii) their higher concentrations of polyhydrides, which could be beneficial for further passivating the c-Si dangling bonds as they can act as hydrogen-reservoir for hydro-

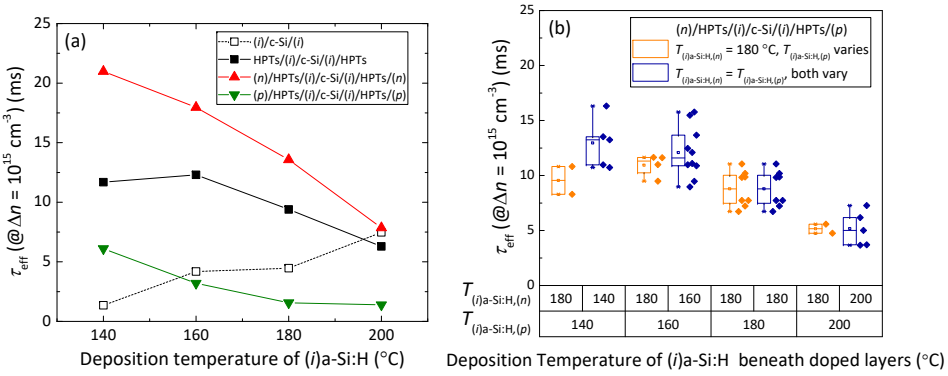

Figure 7.4: The τ_{eff} values of (a) symmetrical samples for individually checking passivation of different (*i*)a-Si:H layers under various deposition temperatures and with doped layers, and (b) solar cell precursors ((*n*)/HPTs/(*i*)/c-Si/(*i*)/HPTs/(*p*)) with various deposition temperatures of (*i*)a-Si:H bi-layers. In part (a), lines are guides to the eye. In part (b), $T_{(i)\text{a-Si:H},(n)}$ and $T_{(i)\text{a-Si:H},(p)}$ represent the deposition temperature of (*i*)a-Si:H bi-layers beneath the (*n*)- and (*p*)-layers, respectively. The deposition temperatures of doped layers and HPTs were kept constant at 180 °C as listed in Table 7.2. In part (b), for the samples that feature $T_{(i)\text{a-Si:H},(n)} = T_{(i)\text{a-Si:H},(p)} = 180$ °C, the box plot is duplicated for easier comparison in different temperature series.

genations during the thermal processes [309]; and (iv) their more void-rich or defect-rich films that could promote easier hydrogen diffusion to the c-Si/(*i*)a-Si:H interface [462–464]. Please note that in this context, more porous (*i*)a-Si:H layers deposited at lower temperatures without the HPTs tend to disrupt the ordered arrangement needed for epitaxial growth. In contrast, porous (*i*)a-Si:H layers obtained after HPTs can potentially facilitate the nucleation of nanocrystals. The main difference lies in the reduced compressive stress in films deposited at lower temperatures without HPTs, whereas HPTs can increase the compressive stress that is critical for the nucleation of nanocrystals (discussed also in Figure 4.3 (b)) [376]. This higher compressive stress in HPTs-treated (*i*)a-Si:H layers can be attributed to significant hydrogen incorporation into strained Si-Si bonds and the increase in voids filled with trapped H_2 molecules [376]. Moreover, it has been also reported that the compressive stress is primarily determined by hydrogen incorporation rather than the pre-existing hydrogen content within the film [376].

Lastly, with doped layers, we observed similar trends to that of the bi-layer with HPTs. We found overall improved passivation qualities when (*n*)-layers were applied, mainly thanks to improved field-effect passivation and enhanced chemical passivation. Particularly, the latter can be attributed to the beneficial hydrogen incorporation during the deposition of (*n*)nc-Si:H, which was deposited with highly hydrogen-diluted plasma conditions [165, 167, 315]. It is worth noting that a τ_{eff} of nearly 21.0 ms was achieved with the (*i*)a-Si:H bi-layer deposited at 140 °C and coated with (*n*)-layers. Notwithstanding, we observed non-negligible degradations of τ_{eff} after the depositions of the (*p*)-layers that may require further passivation optimizations. Nevertheless, those degraded τ_{eff} values could be also ascribed to defect formation in (*i*)a-Si:H layer as a result of Fermi level shift due to the overlaying (*p*)-layer stack [155, 465–467] and the over-annealing of the firstly

deposited (*i*)/(*p*) stack during the deposition of the second (*i*)/(*p*) stack on the other side of the wafer [155, 465].

Subsequently, solar cell precursors ((*n*)/HPTs/(*i*)/c-Si/(*i*)/HPTs/(*p*)) following the findings in Figure 7.4 (a) were fabricated. The deposition temperatures of (*i*)a-Si:H bi-layers underneath either only the (*p*)-layers or both doped layers were varied. The description of solar cell precursors and their τ_{eff} values are presented in Figure 7.4 (b). As expected, cells before TCO sputtering that feature (*i*)a-Si:H bi-layer with lower deposition temperatures exhibited better passivation qualities for both temperature series as shown in Figure 7.4 (b). Especially, a high τ_{eff} of 16.3 ms was achieved with the (*i*)a-Si:H bi-layer deposition temperature fixed at 140 °C for both doped layers. This good passivation is promising to achieve high-efficiency SHJ solar cells.

7.3.4 Temperature effects on *J*-*V* parameters of solar cells

As (*i*)a-Si:H not only passivates the c-Si surface but should also contribute to the transport of charge carriers, different bulk qualities of (*i*)a-Si:H may impact the charge carrier collection differently. To this end, we fabricated FBC-SHJ solar cells with screen-printed Ag contacts (sketched in Figure 7.1 (d)) to evaluate the effects of (*i*)a-Si:H deposition temperature on *J*-*V* parameters of solar cells. The results are summarized in Figure 7.5. Note that the effects of HPTs on solar cells were discussed in previous chapters (Chapters 4 to 6) when optimizing either (*n*)- or (*p*)-type nc-Si:H-based contact stack with (*i*)a-Si:H deposited at 180 °C [167, 175, 312]. In those studies, we found that solar cell performances were improved after applying the HPTs mainly due to the hydrogen-rich and porous (*i*)a-Si:H layers formed after the HPTs (see Figure 7.3), where the hydrogen can largely suppress the surface recombination (see Figure 7.4 (a)). Besides, the nucleation of overlaying doped nc-Si:H layers could also be promoted resulting in an enhancement of the selective transport of charge carriers [151, 266, 271, 308].

For solar cells with a fixed (*i*)a-Si:H deposition temperature underneath the (*n*)-layers ($T_{(i)\text{a-Si:H},(n)}$) (see Figure 7.5), we observed higher average V_{OC} values for cells with lower (*i*)a-Si:H deposition temperatures as expected from the trends discussed in Figure 7.4. However, the *FF* values of cells with (*i*)a-Si:H deposited at 140 °C beneath (*p*)-layers ($T_{(i)\text{a-Si:H},(p)}$ = 140 °C) were averagely lower than those obtained for (*i*)a-Si:H deposited at higher temperatures. We ascribe this fact mainly to the more porous or defect-rich (*i*)a-Si:H bi-layer deposited at 140 °C as elucidated in Figure 7.3 (a). Besides, the rather wide distribution of *FF* for cells with $T_{(i)\text{a-Si:H},(p)}$ = 140 °C could be attributed to the less microstructurally homogeneous films under such deposition conditions. The observation of these lower *FF* values is also supported by literature, where more defect-rich (*i*)a-Si:H deposited under lower temperature also increased the device series resistance [446] (see also Appendix B, Figure B.5). Besides, it is also discussed in the literature that void-rich (*i*)a-Si:H layers resulted in increased contact resistivity as those layers may feature unfavorable energetic position of defect states, the possible lower effective contact area on the c-Si surface, and likely the stronger effects on weakening the band bending induced by doped layers [451]. While solar cells with slightly less-defective (*i*)a-Si:H that was deposited at 160 °C exhibited significantly improved *FF* to above 80% as compared to those with 140 °C. Further, by increasing the deposition temperatures up to 200 °C, solar cells showed saturated or slightly lower *FF*s, which are mainly due to

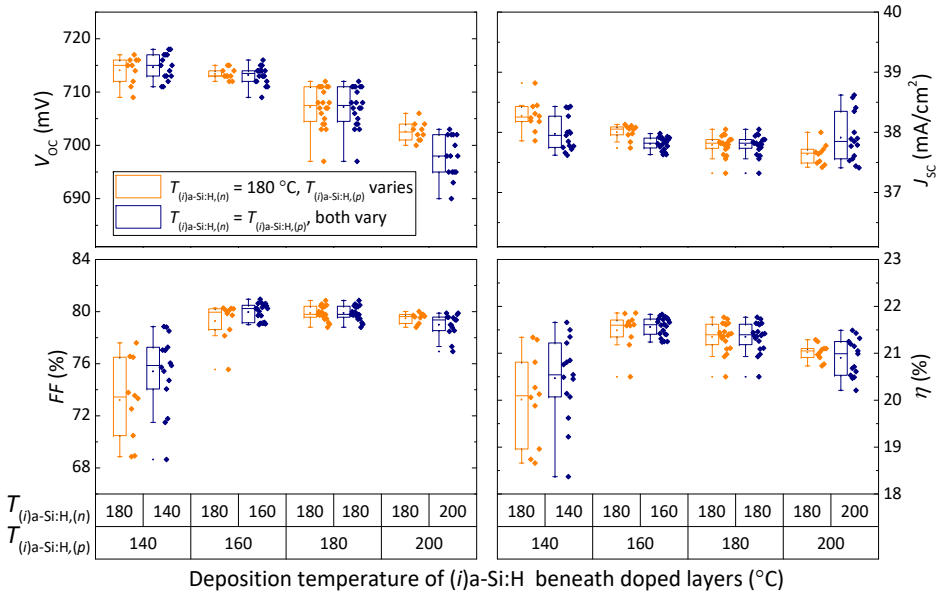

Figure 7.5: The *J*-*V* parameters of FBC-SHJ solar cells prepared under various deposition temperatures of (*i*)a-Si:H bi-layers. Solar cells feature both sides screen-printed Ag contacts. Note, $T_{(i)a\text{-}Si:H,(n)}$ and $T_{(i)a\text{-}Si:H,(p)}$ represent the deposition temperature of (*i*)a-Si:H bi-layers beneath (*n*)- and (*p*)-layers, respectively. The deposition temperatures of doped layers and HPTs were kept constant at 180 °C as listed in Table 7.2. For the samples that feature $T_{(i)a\text{-}Si:H,(n)}$ = $T_{(i)a\text{-}Si:H,(p)}$ = 180 °C, the box plot is duplicated for easier comparison in different temperature series.

7

the increased surface recombination as indicated by their lower V_{OC} values [129, 450]. Therefore, a trade-off between the passivation and carrier collection is revealed for varied $T_{(i)a\text{-}Si:H,(p)}$. Minor effects of (*i*)a-Si:H deposition temperature on J_{SC} were found (see also Appendix B, Figure B.5).

Interestingly, by comparing solar cells with fixed $T_{(i)a\text{-}Si:H,(p)}$, higher $T_{(i)a\text{-}Si:H,(n)}$ seemed to result in slightly lower *FF* values despite having denser (*i*)a-Si:H bi-layers (see Figure 7.3 (a)). This suggests that higher deposition temperatures are not favorable for the passivation and transport of charge carriers, thus resulting in lower V_{OC} and *FF* than samples with (*i*)a-Si:H deposited at lower temperatures. This observation is also well-aligned with our previous study where nearly 3%$_{abs.}$ *FF* gain was reported by applying the HPTs before the deposition of (*n*)-layers, which improved mainly the V_{OC} of solar cells [167]. Therefore, as expected, for efficient collection of charge carriers, it is crucial to have (*i*)a-Si:H layers fostering the passivation quality. Nevertheless, (*p*)-contact is particularly more sensitive to the bulk quality of (*i*)a-Si:H layers than (*n*)-contact [450, 451]. This observation could be correlated to the different dominant transport mechanisms for collecting electrons (thermionic emission) and holes (tunnelling) as also discussed in [151, 451]. Overall, in this study, solar cells with (*i*)a-Si:H deposited at 160 °C exhibited the best efficiencies among all other investigated temperature counterparts owing to

their better trade-off between the passivation qualities and the collection of charge carriers.

To exclude any temperature anneal effects during the screen printing (Ag paste curing at 170 °C for 40 minutes), we alternatively applied our optimized room-temperature Cu-electroplating metallization approach [127] for cells with (*i*)a-Si:H deposited under various temperatures and with an additional 100-nm-thick SiO_x capping the front IWO to form a double-layer anti-reflection coating [200, 325, 429]. As provided in Appendix B, Figure B.5, the *J*-*V* parameters of those cells that feature front electroplated Cu electrodes and rear thermally evaporated Ag contacts exhibited similar trends as shown in Figure 7.5. Noticeably, likely due to the 'gentler' process of our optimized copper-plating process [127], the optimum trade-off between V_{OC} and *FF* was found for the temperature range from 160 °C to 180 °C. For both $T_{(i)\text{a-Si:H}}$ of 160 °C to 180 °C, the best cells exhibited an independently certified conversion efficiency of 23.71% (see Table 7.3 and Figure B.6). Based on those results, we improved further the thickness combinations of (*p*)-layers of SHJ cells with (*i*)a-Si:H layers deposited at 160 °C, which exhibited a high *FF* of 83.3%, a V_{OC} of 726.0 mV, a J_{SC} of 39.97 mA/cm^2, and an efficiency of 24.18% (see Table 7.3 and Figure B.7).

Table 7.3: The external parameters of the best FBC-SHJ solar cells in this study. Those cells feature electroplated Cu front electrodes and SiO_x/IWO double-layer anti-reflection coating.

$T_{(i)\text{a-Si:H}}$ (°C)	V_{OC} (mV)	J_{SC} (mA/cm^2)	*FF* (%)	η (%)	Certified/in-house measurements
160	724.5	39.81	82.2	23.71	ISFH CalTeC
180	722.1	39.71	82.7	23.71	ISFH CalTeC
160[a]	726.0	39.97	83.3	24.18	In-house

[a]: This cell featured improved thickness combinations of the (*p*)-layers that consist of 5 nm (*p*)nc-SiO_x:H + 30 nm (*p*)nc-Si:H.

7.4 Conclusions

In this chapter, we studied the effect of (*i*)a-Si:H deposition temperature on the passivation quality and solar cell performance. Within the investigated temperature range from 140 °C to 200 °C, we observed better passivation quality of (*i*)a-Si:H layers deposited under higher temperatures possibly due to their denser film as confirmed by SE and FTIR measurements. Interestingly, porous or less dense films deposited at lower temperatures exhibited significantly improved and better passivation qualities with additionally applied HPTs, which favor the formation of porous and hydrogen-rich films. Besides, we also noticed distinctive absorption peaks around Si-H W-RM in the infrared spectra, which seemingly reveal microstructural properties of thin-film (*i*)a-Si:H layers that are still unclear, for which further investigations on the vibrational origins of those peaks are still required.

At the device level, even though we observed the highest V_{OC} values for cells with (*i*)a-Si:H deposited at the lowest temperature (140 °C), the related *FF* values were poorer as compared to their higher temperature counterparts. The optimal trade-off between V_{OC} and *FF* was found for SHJ solar cells fabricated with (*i*)a-Si:H layers deposited from

160 °C to 180 °C, which exhibited independently certified efficiencies of 23.71%. Further optimized (*p*)-layers enabled an even higher *FF* of 83.3% and an efficiency of 24.18% for the cell with (*i*)a-Si:H deposited at 160 °C. As the deposition temperature of (*i*)a-Si:H and associated materials properties affect solar cells performance, we showed that high-performance devices should meet critical requirements in optimizing the (*i*)a-Si:H that are not only limited to an excellent surface passivation quality to reduce losses induced by interface recombination. Furthermore, (*i*)a-Si:H films should feature less-defective bulk to not disrupt the collection of charge carriers. Particularly, (*p*)-contact is more sensitive to the bulk quality of (*i*)a-Si:H layers than (*n*)-contact. We demonstrate that carefully optimizing (*i*)a-Si:H layers that fulfill both requirements can contribute to higher SHJ solar cell efficiencies.

8

SHJ bottom-cells for perovskite/c-Si tandem solar cells

This chapter is based on:

Y. Zhao[1], K. Datta, N. Phung, A. E. A. Bracesco, V. Zardetto, G. Paggiaro, H. Liu, M. Fardousi, R. Santbergen, P. Procel Moya, C. Han, G. Yang, J. Wang, D. Zhang, B. T. van Gorkom, T. P. A. van der Pol, M. Verhage, M. M. Wienk, W. M. M. Kessels, A. Weeber, M. Zeman, L. Mazzarella, M. Creatore, R. A. J. Janssen, and O. Isabella, "Optical simulation-aided design and engineering of monolithic perovskite/silicon tandem solar cells," *ACS Applied Energy Materials*, vol. 6, no. 10, pp. 5217–5229, 2023.

Y. Zhao, P. Procel, A. Smets, L. Mazzarella, C. Han, G. Yang, L. Cao, Z. Yao, D. Zhang, V. Zardetto, M. Najafi, M. Creatore, R. Janssen, S. Veenstra, G. Coletti, A. Weeber, M. Zeman, and O. Isabella, "Effects of (*i*)a-Si:H deposition temperature on high-efficiency silicon heterojunction solar cells for four-terminal tandem solar cells", *2022 8th World Conference on Photovoltaic Energy Conversion (WCPEC)*, Milan, Italy, oral presentation, 2022. [2]

Abstract

Perovskite/c-Si tandem solar cells have attracted enormous research attention and have achieved efficiencies well above 30% for both two-terminal (2T) and four-terminal (4T) configurations. In this chapter, we present the development and integration of SHJ bottom sub-cells for 2T and 4T perovskite/c-Si tandem solar cells and highlight optical simulations to assist the implementation of light-management techniques. For front-flat and rear-textured 2T tandem devices, we first engineered (*i*)a-Si:H passivating layers for (100)-oriented flat c-Si surfaces and combined them with various (*n*)a-Si:H, (*n*)nc-Si:H, and (*n*)nc-SiO_x:H interfacial layers for SHJ bottom sub-cells. In a symmetrical configuration, a long minority-carrier lifetime of 16.9 ms was achieved when combining (*i*)a-

[1] co-first author with K. Datta

[2] This work received the 'Student Award'.

Si:H bi-layers with (*n*)nc-Si:H (extracted at an injection level of 10^{15} cm^{-3}). Together with photostable mixed-halide perovskite top sub-cells, we demonstrated front-side-flat tandem solar cells with efficiencies above 23% (a maximum of 25.1%) using all three types of (*n*)-layers. Observations from experimentally prepared devices and optical simulations indicate that both (*n*)nc-SiO_x:H and (*n*)nc-Si:H are promising for application in high-efficiency tandem solar cells. This is possible thanks to minimized reflection at the interfaces between the perovskite and SHJ sub-cells by optimized interference effects, demonstrating the applicability of such light management techniques to various tandem structures. Moreover, by combining our optimized double-side-textured front/back-contacted SHJ solar cell with a certified semitransparent perovskite top sub-cell, we demonstrated a 4T tandem solar cell with an efficiency of 30.1%.

8.1 Introduction

The rapid development of tandem solar cell technology combining perovskite and crystalline silicon (c-Si) sub-cells in various configurations, namely, two-terminal (2T), three-terminal (3T) and four-terminal (4T), has led to significant increases in device performance in recent years. For instance, compared to the first reported 2T perovskite/c-Si tandem solar cell exhibiting a power conversion efficiency (η) of approximately 14% in 2015, material and device optimization strategies to minimize optical losses and maximize energetic yield have increased η to well above 33% till April of 2023 [109, 117, 468–471]. Besides, monolithic 3T tandem solar cells and mechanically stacked 4T tandem solar cells have also achieved remarkable record efficiencies of 29.56% and 30.79% back in 2022 [110, 111]. The adjustable optical bandgap (E_g), high absorptivity, and high defect tolerance observed in perovskite semiconductors make them ideal candidates as the top sub-cell in such tandem devices. Typically, a wide-bandgap (WBG) perovskite top sub-cell, usually prepared using mixed-halide (iodide-bromide) compositions, is used to allow better utilization of the high energy photons of the solar spectrum and enable a balanced light absorption in the two sub-cells [472]. Moreover, mainly thanks to the high open-circuit voltage (V_{OC}) and good near-infrared (NIR) response [194, 359], SHJ solar cells are among the most promising PV technologies that can be used as the bottom sub-cell in tandem devices [469].

High-efficiency tandem solar cells must feature high V_{OC} that results from minimal non-radiative recombination losses in both sub-cells. The key to obtaining a high V_{OC} in the SHJ bottom sub-cell mainly comes from excellent surface passivation of the c-Si facilitated by (*i*)a-Si:H [51]. For 2T tandem solar cells, the device design must account for processing challenges. Specifically in this study, this is related to the development of the conformally-coated solution-processed perovskite top sub-cells using SHJ bottom sub-cells as the substrates. As a result, bottom sub-cells with front-flat and rear-textured surfaces, i.e. single-side-textured (SST), were here chosen as a compromise between processing considerations of the perovskite top sub-cells and light absorption in the SHJ bottom sub-cells. In this thesis, single-side-textured <100> c-Si wafers were prepared with a (100)-oriented flat front surface and a (111)-oriented textured rear surface. As passivation optimizations and contact stack development for the (111)-oriented textured surface have been addressed in Chapters 4 to 7, efforts are still required to develop contact stacks that ensure excellent surface passivation and efficient charge carrier col-

lection on (100)-oriented flat surfaces.

Furthermore, in a 2T tandem device, balanced absorption of incident visible (vis) and NIR photons, which guarantee current-matching conditions between the series-connected sub-cells, is critical to achieve a high short-circuit current density (J_{SC}) output of the tandem solar cell. Barring that, the sub-cell generating the lowest current limits the overall output of the tandem device. As a result, light management guided by advanced optical simulations to minimize parasitic absorption and reflection losses is of great importance for tandem device design [93, 117, 473–475]. Especially, the reflection loss, due to suboptimal refractive index matching at intermediate interfaces between the top and bottom sub-cells, should be minimized to enhance light coupling into the bottom sub-cell. As for 4T tandem applications, due to the ease of processing restrictions and the absence of a need for current matching, double-side-textured (DST) front/back-contacted (FBC) SHJ solar cells, which have been developed and optimized in this thesis, can be directly combined with semitransparent perovskite top sub-cells forming 4T tandem devices.

In this chapter, we present the development of high-efficiency 2T and 4T tandem solar cells assisted by optical simulations, focusing on the tandem application-oriented optimization of SHJ bottom sub-cells. Firstly, the experimental development of SST SHJ bottom sub-cells and their integration in 2T tandem solar cells supported by optical simulations are highlighted. Then, aiming at achieving efficient light management of tandem devices, the optical potential of various types of (*n*)-layers utilized in SHJ bottom sub-cells are evaluated. Furthermore, an optimized DST FBC-SHJ solar cell is combined with a certified semitransparent perovskite top sub-cell, forming a high-efficiency 4T tandem solar cell.

8.2 Experimental details

The deposition parameters, thicknesses and duration for optimized (*i*)a-Si:H layers and hydrogen-plasma treatment (HPT) can be found in Table 8.1. For (*i*)a-Si:H layers, two deposition methods, i.e. without added H_2 ((*i*)-1) and with added H_2 ((*i*)-2) to the SiH_4, were used. Various (*n*)-layers, namely, (*n*)a-Si:H, (*n*)nc-Si:H and (*n*)nc-SiO_x:H were implemented into single-junction SHJ and tandem applications. The deposition parameters of these (*n*)-layers can be found in Table 6.1. The (*n*)nc-SiO_x:H-1 was chosen as the (*n*)nc-SiO_x:H layer investigated in this chapter. Deposition conditions of (*p*)-layers can be found in Table 5.1 instead. A geometrical factor of 1.7 was used for calculating the deposition durations for the textured surface. For passivation optimizations, the thicknesses of symmetrically deposited (*i*)a-Si:H layers were kept constant at around 10 nm on each side. Details on the preparation and characterization of single-junction perovskite solar cells and top sub-cells for tandem devices can be found in our previous publication [476].

For the characterization of the 2T tandem solar cells, current density versus voltage (*J*-*V*) measurements were done using a tungsten-halogen lamp filtered by a UV filter (Schott GG385) and a daylight filter (Hoya LB120) with the intensity adjusted to 100 mW/cm^2. A shadow mask of 1 cm^2 was used for measuring the 2T tandem solar cells. During the *J*-*V* measurement, the solar cells were operated between + 2.0 V and – 0.5 V at a scan rate of 0.25 V/s by a Keithley 2400 source meter. For external quantum effi-

ciency (EQE) measurements, a modulated monochromatic probe light (Philips focusline 50 W) was used to illuminate the solar cells through an aperture (1 mm radius). The response was recorded and converted to EQE using a calibrated silicon reference cell. To measure the EQE of the individual sub-cells of the 2T tandem devices, bias lights with a wavelength of 530 nm or 940 nm were used for saturating perovskite and silicon cells, respectively, together with a forward voltage bias close to the V_{OC} of the corresponding single-junction cell. For the characterization of 4T tandem solar cells with area-mismatched sub-cells, we followed the measurement procedure as described in the literature [477, 478]. The *J-V* parameters of the FBC-SHJ solar cell under standard test conditions (STC) and under perovskite-filtered conditions were characterized with the Neonsee solar simulator. The EQE of the FBC-SHJ solar cell was measured with a setup from Rera Solutions B.V. [479]. Genpro4 [409], which combines ray-tracing and wave-optics, was used for optical simulations of the perovskite/SHJ tandem solar cells. Spectroscopic ellipsometry (SE) was utilized to extract the complex refractive index of layers used in tandem devices for optical simulations. The optical constants of Ag and c-Si are taken from literature [480, 481].

Table 8.1: PECVD deposition parameters of optimized (*i*)a-Si:H layers and the HPT.

PECVD parameters	(*i*)-1	(*i*)-2	HPT
$f[H_2]/f[SiH_4]$ (sccm/sccm)	0/40	30/10	200/0
Pressure (mbar)	0.7	1.4	2.2
Power density (mW/cm^2)	20.8	20.8	41.7
Temperature (°C)	160	160	160
Thickness (nm)	10/5[a]	5	-
Duration (s)	-	-	20

[a]: 10 nm and 5 nm (*i*)-1 layers were used for mono- and bi-layer passivation strategies, respectively.

8.3 Results and Discussions

8.3.1 Development and integration of SHJ bottom sub-cells for 2T tandem solar cells

8.3.1.1 Passivation optimization of (100)-oriented flat c-Si surface

As explained in detail in Section 2.4.4, the passivation optimization of (100)-oriented flat c-Si surface is challenging. Especially when a highly hydrogen-diluted (*i*)a-Si:H is used, such surface is known to be more prone to detrimental epitaxial growth of (*i*)a-Si:H as compared to the (111)-oriented surface [303–307]. Therefore, we developed and optimized the surface passivation of the (100)-oriented flat c-Si surface. In addition to op-

timizations of mono-(*i*)a-Si:H layer via tuning process conditions of plasma-enhanced chemical vapor deposition (PECVD) (namely, hydrogen dilution, pressure, power, substrate temperature), approaches such as bi-layers and hydrogen plasma treatment (HPT) were also studied [367, 368, 427, 431, 445, 482, 483]. The effective lifetime (τ_{eff}) of symmetrically passivated c-Si wafers featuring double-side-flat (100)-oriented surfaces with different (*i*)a-Si:H passivation approaches and different (*n*)-layers, namely, (*n*)a-Si:H, (*n*)nc-Si:H and (*n*)nc-SiO$_x$:H are presented in Figure 8.1 (a). Besides, the infrared spectra of different (*i*)a-Si:H films, which were obtained via Fourier-transform infrared (FTIR) spectroscopy measurement, are shown in Figure 8.1 (b).

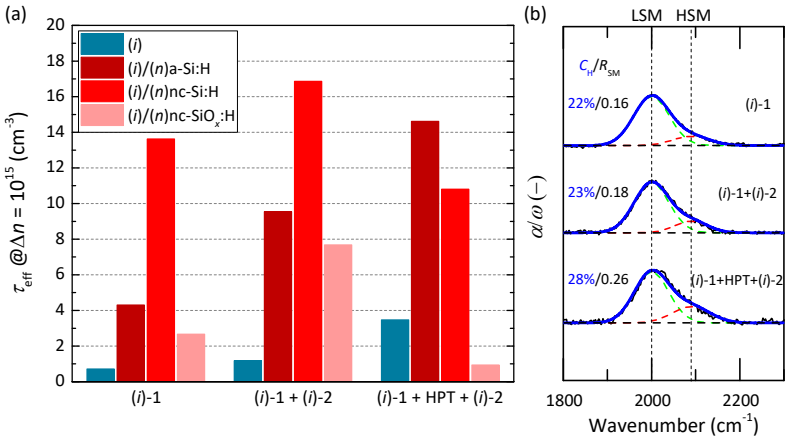

Figure 8.1: The (a) effective lifetime (τ_{eff}) of symmetrically passivated c-Si wafers featuring double-side-flat (100)-oriented surfaces with different (*i*)a-Si:H passivation approaches (around 10 nm (*i*)-1, 5 nm (*i*)-1 + 5 nm (*i*)-2, 5 nm (*i*)-1 + HPT + 5nm (*i*)-2) and different (*n*)-layers (5 nm (*n*)a-Si:H, 20 nm (*n*)nc-Si:H, 60 nm (*n*)nc-SiO$_x$:H). (b) Infrared spectra of various (*i*)a-Si:H layers (around 30-nm-thick). In part (a), the τ_{eff} values were obtained for an injection level (Δn) of 10^{15} cm^{-3}. In part (b), C_{H} stands for the hydrogen content and R_{SM} represents the microstructure factor as defined from Si-H stretching mode (SM). The green and red dashed lines are the fitted Gaussian function for low-frequency SM (LSM) and high-frequency SM (HSM), respectively. The blue solid lines are the overall fittings.

As seen in Figure 8.1 (a), for samples with only (*i*)-layer, the τ_{eff} was increased from 0.7 ms for (*i*)-1 to 1.2 ms for a (*i*)-1 + (*i*)-2 bi-layer. Furthermore, by applying an optimized HPT at the interface between (*i*)-1 and (*i*)-2, the τ_{eff} was further enhanced to 3.5 ms. Infrared spectra, as illustrated in Figure 8.1 (b), indicate a higher absorption strength of the high-frequency stretching mode (HSM) when using a bi-layer and/or the additional HPT. It is well-established that the low-frequency stretching mode (LSM) is assigned to monohydrides in small volume deficiencies [343, 375], while HSM is mainly attributed to monohydrides and some polyhydrides at internal surfaces of larger volume deficiencies [338, 343, 375]. As a result, higher hydrogen contents (C_{H}) in the bi-layer ((*i*)-1 + (*i*)-2) and the bi-layer with HPT ((*i*)-1 + HPT + (*i*)-2) are calculated (see Figure 8.1 (b)). The increased absorption strength of HSM, and thus a higher microstructure factor (R_{SM}), indicates the film is less dense and more hydrogen-rich when we apply the bi-layer, which further increases when implementing the additional HPT.

The passivation was further improved when (*n*)-type layers were subsequently deposited on the (*i*)-layer (Figure 8.1 (a)). When a (*n*)a-Si:H was stacked on (*i*)-layer, noticeable τ_{eff} improvements were observed for all (*i*)-layer types. Following the τ_{eff} trend of (*i*)-layer only samples, we also found the optimized passivation quality and the highest absolute τ_{eff} improvement (τ_{eff} increased from 3.5 ms to 14.6 ms) when bi-layer with HPT was applied for (*n*)a-Si:H. This τ_{eff} improvement could be explained by their highest concentrations of HSM components for the bi-layer with HPT (see Figure 8.1 (b)), which can further passivate the c-Si surface dangling bonds by acting as a hydrogen-reservoir for hydrogenations during thermal processes [309]. However, when using (*n*)nc-Si:H and (*n*)nc-SiO_x:H, the bi-layer approach without the additional HPT yielded the highest τ_{eff} values of 16.9 ms and τ_{eff} of 7.7 ms, respectively. This is due to the fact that (*n*)nc-Si:H and (*n*)nc-SiO_x:H require higher hydrogen dilution during their depositions as compared to (*n*)a-Si:H [266]. As a result, the excessively incorporated hydrogen may induce additional defects near the c-Si surface [428], thus hindering the passivation quality. Similar to trends observed for nc-Si:H-based (*n*)-layers, bi-layer without the additional HPT also delivered the optimized passivation quality for nc-Si:H-based (*p*)-layer ((*p*)nc-SiO_x:H + (*p*)nc-Si:H) (see Appendix C, Figure C.1).

To summarize, although the bi-layer without the additional HPT did not exhibit the best passivation quality with only (*i*)a-Si:H layers, it relaxes the optimization efforts for further stacking on top, especially, doped nc-Si:H-based layers that are deposited with highly hydrogen-diluted plasma conditions.

8.3.1.2 Single-junction SST FBC-SHJ solar cells

Further, we applied different (*n*)-type layers combined with the (*i*)a-Si:H bi-layer ((*i*)-1 + (*i*)-2) to fabricate single-junction SST rear junction solar cells as sketched in Figure 8.2. On the textured rear side of solar cells, we applied the optimized contact stacks based on (*p*)nc-SiO_x:H and (*p*)nc-Si:H for hole collection as developed in Chapter 5 [312]. The representative *J*-*V* characteristics of these solar cells are depicted in Figure 8.2.

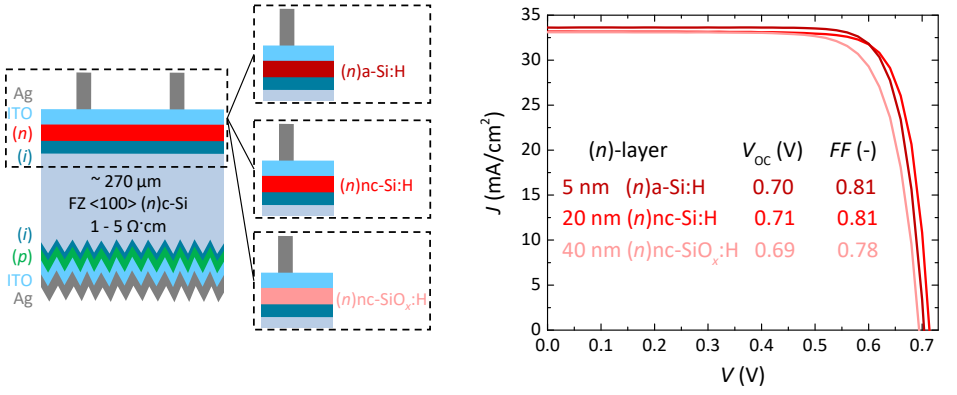

Figure 8.2: The schematic sketches of single-junction single-side-textured (SST) rear junction SHJ solar cells with various front (*n*)-layers (left) and their typical *J*-*V* curves (right). The (*p*)-layer on the rear side consists of 5 nm (*p*)nc-SiO_x:H + 16 nm (*p*)nc-Si:H (see Chapter 5 or [312]).

As seen in Figure 8.2, both 5 nm (*n*)a-Si:H and 20 nm (*n*)nc-Si:H (*n*)-contacts delivered V_{OC} values above 0.70 V and a *FF* of 0.81. Solar cells with (*n*)nc-SiO_x:H exhibited slightly lower V_{OC} (0.69 V) and *FF* (0.78) than their oxygen-absent counterparts. The τ_{eff}, implied V_{OC} (iV_{OC}) and implied fill factor (i*FF*) of these solar cells before metallization are provided in Table C.1 (Appendix C). By comparing these parameters with *J*-*V* parameters of finished solar cells, we noticed drops from iV_{OC} to V_{OC} and i*FF* to *FF*. We attribute these drops, at least in part, to our lab-standard non-optimized screen printing process [127], which degraded the passivation quality of solar cells. Additionally, these drops may be also due to insufficient selectivity of electron and/or hole contact stacks used in solar cells [36]. The EQE spectra of solar cells with various (*n*)-layers are presented in Figure C.2 (Appendix C). Besides, the EQE spectra and *J*-*V* parameters of single-junction cells using different (*n*)nc-SiO_x:H thicknesses are also provided in Figures C.2 and C.3 (Appendix C). Despite cells with (*n*)nc-SiO_x:H single layers being less performant than cells with (*n*)a-Si:H and (*n*)nc-Si:H, in tandem devices, the (*n*)nc-SiO_x:H can present optical advantages by improving light coupling into the bottom sub-cell [474]. This aspect will be further elaborated in Section 8.3.1.5.

8.3.1.3 Light management of 2T tandem solar cells

With the aim of realizing 2T tandem solar cells with a high V_{OC}, apart from the necessity of ensuring excellent surface passivation quality of SHJ bottom sub-cells, non-radiative recombination losses of perovskite top sub-cells should be also minimized. Therefore, a photostable mixed-halide wide-bandgap perovskite absorber with a nominal composition of $K_{0.05}Cs_{0.05}(FA_{0.75}MA_{0.25})_{0.90}Pb(I_{0.75}Br_{0.25})_3$ and a E_g of 1.69 eV was first developed. Moreover, choline chloride was used to passivate the perovskite/C_{60} interface reducing the energetic losses at this interface [476]. The detailed development of perovskite top sub-cells, including optimizations of perovskite composition, selection of efficient hole- and electron-transport layers and application of surface passivation treatment, is presented in our publication [476]. Further information on the integration of established perovskite top sub-cells on the optimized SHJ bottom sub-cells can be also found in our publication [476]. Eventually, monolithic 2T tandem solar cells with an active area of 1 cm^2 were prepared.

Optimized light management in perovskite/SHJ tandem solar cells is important for achieving high current densities at current-matching conditions. Therefore, using the GenPro4 simulation tool [409], we performed optical simulation studies based on our practical tandem devices to further guide the experimental work. The schematic structure of the monolithic perovskite/c-Si tandem solar cell with (*n*)a-Si:H as a representative is illustrated in Figure 8.3 (a). Considering one electron-hole pair generated by each absorbed photon, negligible recombination, and only the active area (without front metal electrodes), the simulated implied photocurrent density (J_{imp}) of sub-cells, tandem cell, and the reflected fraction in the wavelength range from 300 nm to 1200 nm are shown in Figures 8.3 (b) - (e).

By identifying the minima in implied reflected photocurrent density and the maxima in implied photocurrent density contributions of the sub-cells, optimum thicknesses of MgF_2 and SnO_x layers were found. The highest implied photocurrent density in the perovskite top sub-cell (Figure 8.3 (b)) was found at a MgF_2 thickness of around 100 nm whereas for the SHJ bottom sub-cell (Figure 8.3 (c)), that optimal thickness was between

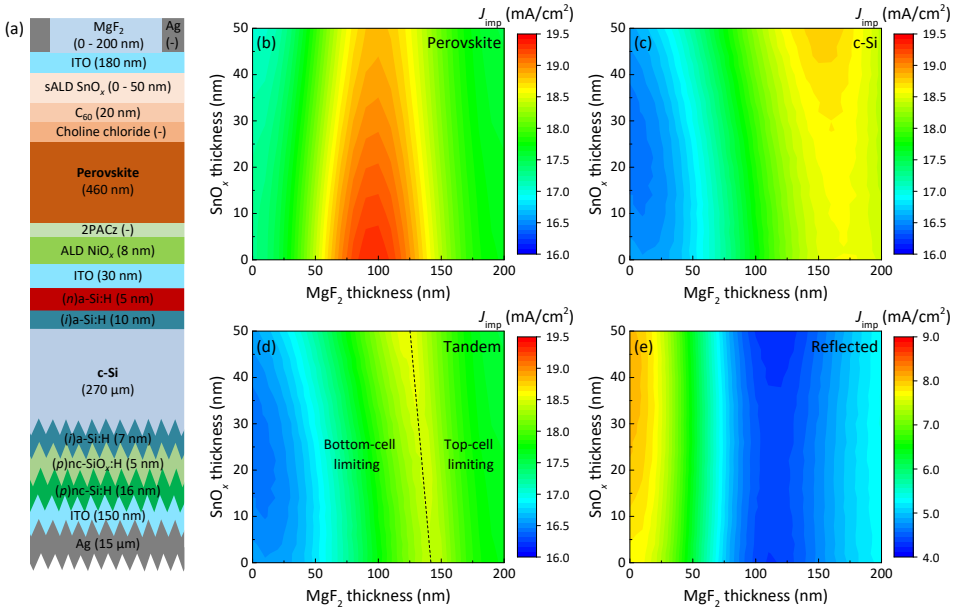

Figure 8.3: Optical simulations of perovskite/SHJ tandem devices. (a) Schematic sketch of perovskite/SHJ solar cell used for simulations. Implied photocurrent density in (b) perovskite top sub-cell, (c) silicon bottom sub-cell, (d) tandem cell, and (e) implied reflected photocurrent density. In (a), sALD stands for spatial atomic layer deposition. The dashed line in panel (d) is a guide to the eye for distinguishing between configurations that are limited either by the bottom sub-cell or the top sub-cell.

160 nm and 180 nm. The J_{imp} of the tandem device (Figure 8.3 (d)) was determined by the current-limiting sub-cell, which is related to both the reflection losses (Figure 8.3 (e)) and the absorption characteristics of both sub-cells. With the presented tandem structure, it was found that the maximum implied tandem current density (approximately 18.6 mA/cm^2) requires a MgF_2 layer with a thickness of approximately 120 to 160 nm, whereas the thickness of SnO_x is of minor consequence.

Figure 8.4 further shows the simulated absorptance in different layers of the stack as a function of layer thicknesses (MgF_2, SnO_x and C_{60}). Two sets of values for MgF_2, SnO_x and C_{60} thicknesses were considered (0, 45, 20 nm and 120, 20, 15 nm, respectively) to illustrate their influence on the reflection, parasitic absorption and absorptance in sub-cells.

As seen in Figure 8.4 (b), the absence of an anti-reflection coating (without MgF_2) leads to significant reflection losses in the 400 – 500 nm wavelength range, decreasing absorption in the perovskite top sub-cell. The reflection loss also leads to a minimum absorption in the c-Si bottom sub-cell in the wavelength range of 800 – 900 nm. Besides, noticeable parasitic absorption in the C_{60} layer (for wavelength below 600 nm, see Figure 8.4 (a)) further decreases absorption in the perovskite sub-cell [484]. By decreasing the thicknesses of C_{60} and SnO_x (Figures 8.4 (c) and (d)), and introducing the anti-reflection coating, reflection losses are minimized by an equivalent of 3.6 mA/cm^2, thus resulting

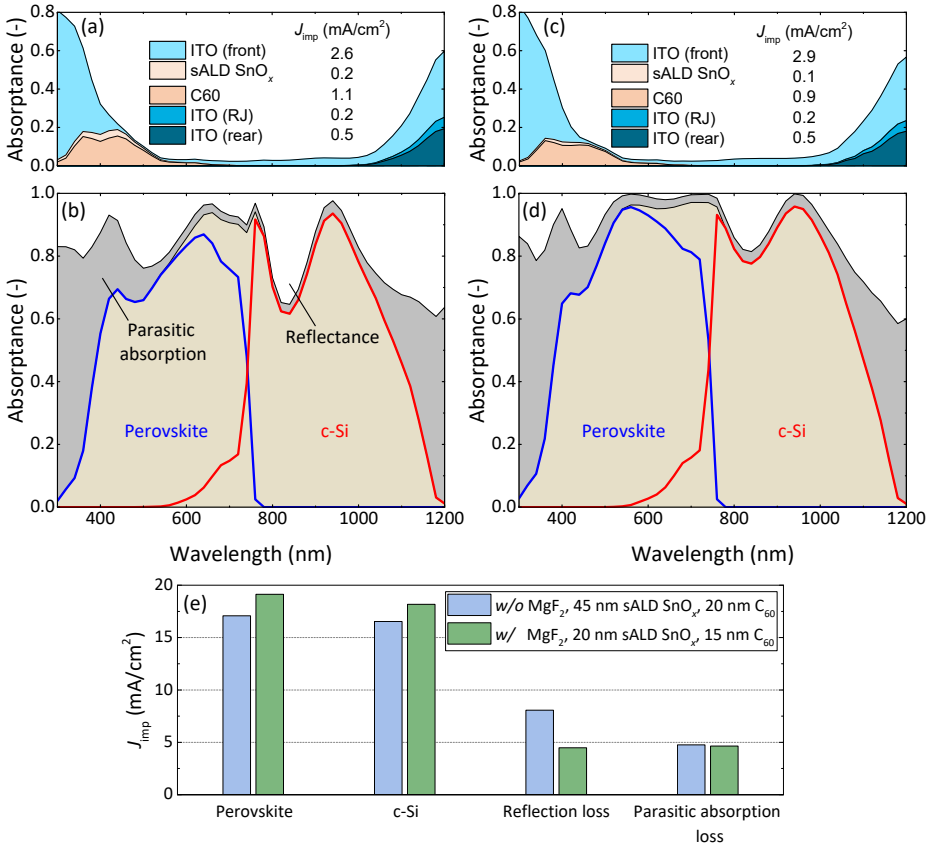

Figure 8.4: The simulated absorptance spectra of the cells (a, b) without MgF_2 and thick (20 nm) C_{60} layer, and (c,d) with MgF_2 (120 nm) and thin (15 nm) C_{60} layer. The SnO_x thickness is 45 nm (20 nm) before (after) the optimizations, respectively. In figures (a) and (c), ITO (RJ) represents the ITO recombination junction. In figures (b) and (d), the light-brownish area represents the sum of the absorptance of the perovskite and silicon sub-cells. Figure (e) presents the integrated J_{imp} for both sub-cells, reflection, and parasitic absorption losses before and after optimizations.

in improved spectral response of both perovskite and c-Si absorbers (see Figure 8.4 (e)).

The light management strategies as suggested by these simulation results were employed to enhance the performance of fabricated tandem solar cells. Our experimental observations on the EQE spectra of fabricated tandem solar cells corroborated the effectiveness of these strategies through optimization of the anti-reflection effect and reducing the parasitic absorption losses [476]. For instance, Figure C.4 (Appendix C) further compares experimentally determined EQE spectra to simulated absorptance spectra and finds good agreement between the behavior of devices using different MgF_2 and C_{60} layer thicknesses.

8.3.1.4 2T tandem solar cells with SHJ sub-cells featuring various (*n*)-type layers

Our preliminary fabricated tandem solar cells indicated that the perovskite top sub-cell was the current limiting factor. Therefore, in order to enhance the J_{SC} of the perovskite top sub-cell, the bromide content in the perovskite was reduced from 25% to 21% resulting in a decrease in E_g from 1.69 eV to 1.67 eV [476]. Table 8.2 and Figure 8.5 show the *J-V* characteristics of tandem solar cells using different (*n*)-type layers. As seen in Figure 8.5, the (*n*)-type layers predominantly influenced optical interference in the NIR region that affects $J_{SC,silicon}$. For instance, using a 20-nm-thick (*n*)nc-Si:H layer led to a current-matched tandem solar cell at a J_{SC} of 18.2 mA/cm^2. On the other hand, using a 5-nm-thick (*n*)a-Si:H or 40-nm-thick (*n*)nc-SiO$_x$:H layer caused a slightly higher absorption in the bottom sub-cell whereas the top sub-cell response remained largely unchanged, leading to top sub-cell-limited tandem devices.

In all cases, a high V_{OC} of 1.81 V can be measured, representing low V_{OC} losses (30 - 50 mV) upon integration compared to the sums of the V_{OC} of perovskite and SHJ single-junction devices. A proportion of the V_{OC} loss resulted from reduced light incidence on the SHJ sub-cell while additional interfacial losses at the recombination junction can also lower the V_{OC}. Finally, on account of a higher *FF* (78%), the cell based on the (*n*)a-Si:H layer yields a tandem efficiency of 25.1% compared to cells based on (*n*)nc-Si:H (23.4%) or (*n*)nc-SiO$_x$:H (23.2%), representing a 6.0%$_{abs.}$ gain from the single-junction efficiency of the SHJ solar cell and a 6.8%$_{abs.}$ gain from that of the perovskite solar cell. The *J-V* curve and EQE spectrum of this 25.1% tandem solar cell is presented in Figure C.5 (Appendix C). This tandem cell was further combined with a flow electrochemical cell forming a light-driven water splitting system. Under 1-sun equivalent light intensity, the system exhibited stable operation through three simulated day-night cycles and achieved a solar-to-hydrogen efficiency of exceeding 21%, which was among the most efficient water splitting systems to date [485].

Table 8.2: Photovoltaic performance of single-junction perovskite and SHJ solar cells and monolithic tandem devices.

Solar cell type	V_{OC} (V)	J_{SC} (mA/cm^2)	*FF* (-)	η (%)	η gain[a] (*vs* SHJ) (%$_{abs.}$)	η gain[b] (*vs* perovskite) (%$_{abs.}$)
Single-junction solar cells						
Perovskite	1.15	20.2	0.79	18.3	-	-
SHJ (*n*)a-Si:H	0.70	33.6	0.81	19.1	-	-
SHJ (*n*)nc-Si:H	0.71	33.2	0.81	19.1	-	-
SHJ (*n*)nc-SiO$_x$:H	0.69	33.1	0.78	17.8	-	-
Tandem solar cells						
(*n*)a-Si:H	1.81	18.1	0.75	24.6	5.5	6.3
(*n*)nc-Si:H	1.81	18.2	0.71	23.4	4.3	5.1
(*n*)nc-SiO$_x$:H	1.81	18.3	0.70	23.2	5.4	4.9
(*n*)a-Si:H (best cell)	1.80	17.9	0.78	25.1	6.0	6.8

[a] and [b] indicate the absolute gain in power conversion efficiency in tandem solar cells compared to the power conversion efficiencies of corresponding SHJ and perovskite single-junction solar cells respectively.

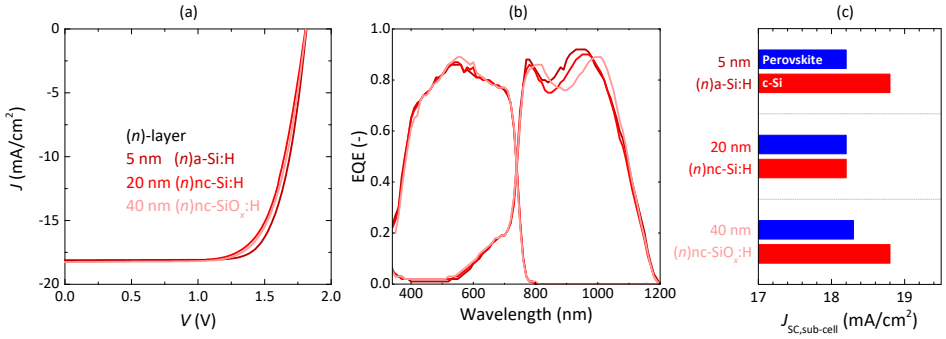

Figure 8.5: Photovoltaic performance of optimized tandem solar cells. (a) J-V curves and (b) EQE spectra of monolithic tandems prepared using different (n)-type layers (5 nm (n)a-Si:H, 20 nm (n)nc-Si:H, and 40 nm (n)nc-SiO$_x$:H). (c) J_{SC} contributions of sub-cells extracted from EQE spectra in figure (b).

8.3.1.5 Discussions and Outlooks

To further explore the potential of using different (n)-layers in tandem solar cells, we identified optimum (n)-layer thicknesses through optical simulations. To better understand the origin of reflection losses in simulated tandem solar cells, we decomposed the total front reflection into three components: reflections at the front of the perovskite top sub-cell (R_1), in between the perovskite top sub-cell and SHJ bottom sub-cell (R_2), and at the rear side of the SHJ bottom sub-cell (R_3) [475]. The refractive indices of different (n)-layers can be found in Figure C.6 (Appendix C). Prior to these simulations, we checked the optical simulation models by comparing the simulated absorption with measured EQE curves reported in Figure 8.5 (b), which show good correspondence between the simulation and measured data (see Appendix C, Figure C.7).

Figure 8.6 shows the J_{imp} in sub-cells and tracks the reflected light as a function of (n)-layer thickness. In all cases, R_1 and R_3 are nearly constant across all configurations using different (n)-layer thicknesses whereas R_2 is strongly influenced by the (n)-layer. The optimum thickness of (n)a-Si:H is 5 nm (Figure 8.6 (b)). A further increase of the (n)a-Si:H thickness resulted in increased internal reflections between the top and bottom sub-cells (R_2), which reduces the amount of light being coupled into the SHJ bottom sub-cell, widening the current-mismatch between sub-cells. In contrast, the R_2 was minimized when the thicknesses of (n)nc-Si:H (Figure 8.6 (c)) and (n)nc-SiO$_x$:H (Figure 8.6 (d)) were optimized to 95 nm and 115 nm, respectively. Especially in this case, with (n)nc-SiO$_x$:H, we minimized R_2 to below 0.1 mA/cm^2. Electrically, as demonstrated in Figure C.3, single junction SHJ solar cells using a thick (around 110-nm-thick) (n)nc-SiO$_x$:H layer still exhibited an average FF approaching 79%, demonstrating its potential for the high-efficiency tandem solar cell [117, 474]. Similarly, we expect (n)nc-Si:H layer to be a promising candidate for high-efficiency tandem devices [486]. The observed beneficial effects upon thickness optimization of (n)nc-SiO$_x$:H and (n)nc-Si:H can be attributed to their better refractive index matching in the tandem solar cell than (n)a-Si:H (Appendix C, Figure C.6).

Taking the case of (n)nc-Si:H as an example, Figures 8.7 (a) and (b) show the simulated absorptance spectra of tandem solar cells with 20 nm and 95 nm (n)nc-Si:H in-

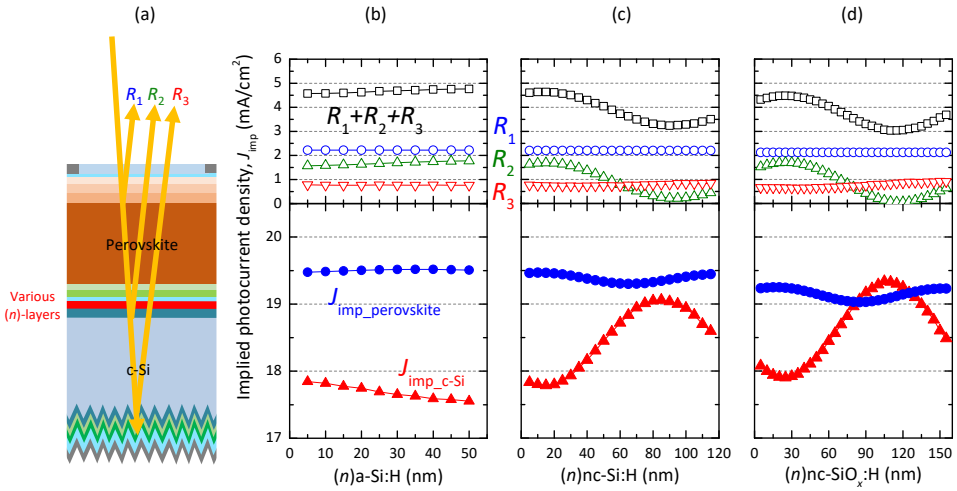

Figure 8.6: Light management in monolithic tandem solar cells. (a) Schematic sketch of the perovskite/SHJ tandem solar cell for optical simulations, and (b – d) implied photocurrent density of the perovskite top sub-cell, SHJ bottom sub-cell and reflected light as a function of (*n*)-layer thickness and types of (*n*)-layer.

terlayers, respectively. The parasitic absorption induced by (*n*)nc-Si:H was increased from around 0 mA/cm^2 to 0.3 mA/cm^2 (highlighted red regions in Figures 8.7 (a) and (b)) when the thickness of (*n*)nc-Si:H was increased from 20 nm to 95 nm. Nevertheless, Figures 8.7 (a) and (b) reveal that the reflection loss in the 800 nm to 900 nm wavelength range, which is primarily caused by the intermediate interfaces, was significantly suppressed. This decrease in reflection loss, as also seen in Figure 8.6 (c) where R_2 was reduced from 1.7 to 0.2 mA/cm^2, was substantial enough to outweigh the additional parasitic absorption loss. Therefore, the implied photocurrent density of the c-Si bottom sub-cell increased from 17.8 mA/cm^2 to 19.0 mA/cm^2 (see Figure 8.7 (c)). The absorptance in other layers remained nearly unaffected. The observation of reduced R_2 at intermediate interfaces can be explained by the optimized interference effect, which can be affected by the wavelength-dependent refractive indices (e.g. different types of (*n*)-layers), and thicknesses of layers used in the device. As a proven first-order approximation [474], the advantageous implementation of (*n*)nc-Si:H and (*n*)nc-SiO$_x$:H, as seen in Figures 8.6 (c) and (d), can be attributed to their proper refractive indices that lie between those of perovskite and c-Si absorbers within the 800 nm to 1200 nm wavelength range. In contrast, the refractive indices of (*n*)a-Si:H do not exhibit such a favorable match (Appendix C, Figure C.6). Additionally, by adjusting the optical thickness, which is the product of the refractive index and the film thickness, destructive interference can be achieved, leading to increased light transmittance to the bottom sub-cell.

Optimizing interference effects, especially due to intermediate interfaces, as a route to light management in tandem devices can therefore be a general strategy to optimize device design for maximizing matched tandem current density. For example, in a monolithic tandem device design that employs (*n*)nc-Si:H/(*p*)nc-Si:H or (*n*)nc-SiO$_x$:H/(*p*)nc-SiO$_x$:H as the recombination junction instead of ITO, we were also able to apply this

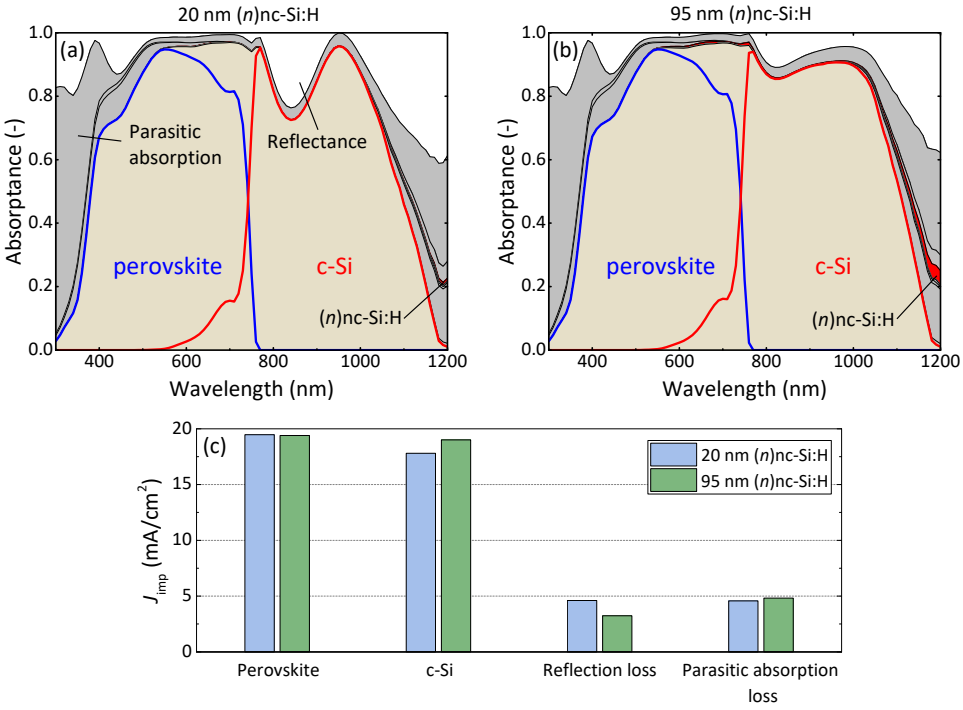

Figure 8.7: Simulated absorptance spectra of tandem solar cells using (*n*)nc-Si:H interlayers with a thickness of (a) 20 nm or (b) 95 nm. Figure (c) presents the integrated J_{imp} for both sub-cells, reflection, and parasitic absorption losses before and after optimizations. In Figures (a) and (b), the light-brownish area represents the sum of the absorptance of the perovskite and silicon sub-cells. The red areas represent parasitic absorption induced by the (*n*)nc-Si:H layer.

technique to optimize the interference effect at intermediate interfaces, thus minimizing reflection losses from these interfaces (R_2) [487]. Similarly, the strategy used here for SST tandem solar cells can also be applied to optimize DST (typical pyramidal texture) tandem devices, as demonstrated in Figure C.7 (Appendix C). However, the benefits of using (*n*)nc-Si:H or (*n*)nc-SiO$_x$:H over (*n*)a-Si:H were found to be less significant in DST devices, as textured surfaces already result in decreased reflection losses.

Furthermore, the V_{OC} of tandem devices was restricted by the V_{OC} of the perovskite sub-cell, due to non-radiative recombination in wide-bandgap compositions and interfaces [488–492]. These losses can be further minimized by, for instance, optimizing the perovskite composition and adding additives for reducing bulk defects [493, 494], applying charge carrier transport layers with better energetic alignment and better hole extraction [495–499], implementing surface passivation treatment (such as choline chloride applied in this study) [488, 500, 501] and improving electron-selective contact layers [502, 503]. The V_{OC} of the bottom SHJ cell can be also further enhanced by improving the passivation quality and selectivity of contact stacks. Besides, due to the non-optimized screen-printing process, the V_{OC} of all SHJ single-junction and tandem solar cells are

expected to be improved if a thermally evaporated Ag rear contact is used [313].

Finally, beyond light management techniques suited to standard test conditions, with the view of evaluating the energy output under real-world conditions, energy yield analysis is important for developing tandem solar cells as it can guide other device optimization strategies (e.g. perovskite bandgap, bi-faciality) [93, 469, 504].

8.3.2 High-efficiency 4T tandem solar cells

Apart from deploying SST FBC-SHJ bottom sub-cells for monolithic 2T tandem applications, we also fabricated 4T tandem solar cells by combining DST FBC-SHJ solar cells developed in previous chapters with semi-transparent perovskite top sub-cells.

A representative 24.2%-efficient DST FBC-SHJ solar cell, as schematically sketched in Figure 7.1 (d), was chosen for integration into the 4T tandem solar cell. The selected cell showcased notable features, such as a double-layer anti-reflection coating (DLARC) and an electroplated-Cu front grid. Indeed, as demonstrated in Figure 8.8 (a), thanks to the use of the DLARC, this cell exhibited an excellent EQE response in the (near-)infrared wavelength range that is crucial for the tandem application [167, 313, 325]. Besides, this cell also featured low shading losses enabled by photolithography patterned fine-line Cu grid, which accounts for only 1.58% metal coverage [127]. Overall, the combination of the DLARC and the low shading losses in the optimized solar cell holds great promise for realizing high-efficiency 4T tandem devices.

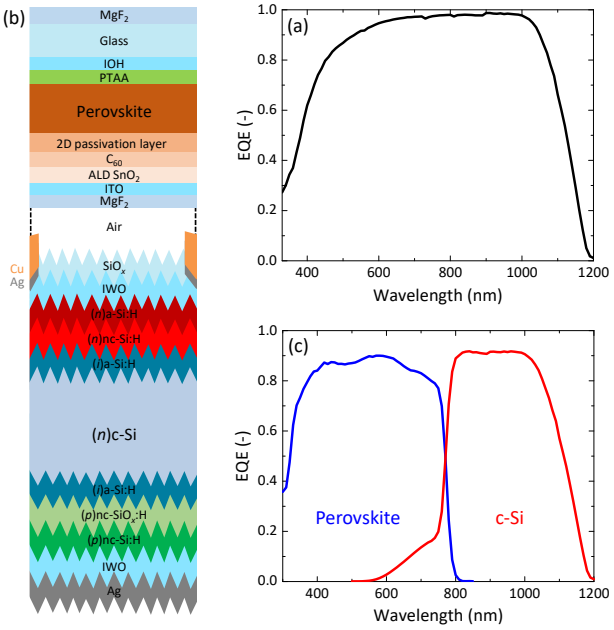

Figure 8.8: The (a) EQE spectrum of optimized single-junction double-side-textured FBC-SHJ solar cells for 4T tandem solar cells, (b) the schematic sketch of the 4T perovskite/SHJ tandem solar cell and (c) the EQE spectra (active area) of the 4T perovskite/SHJ tandem solar cell. An air gap serves as the optical coupling layer.

To form the 4T tandem solar cell, a semi-transparent perovskite top sub-cell with an absorber E_g of 1.6 eV and a nominal composition of $Cs_{1-x-y}MA_xFA_yPb(I_{1-z}Br_z)_3$ was utilized. The resulting 4T tandem solar cell is schematically sketched in Figure 8.8 (b). The *J-V* parameters and the EQE spectra (active area) of the 4T tandem solar cell are provided in Table 8.3 and Figure 8.8 (c), respectively. As presented in Table 8.3, the semi-transparent perovskite top sub-cell was independently certified at European Solar Test Installation (ESTI ISPRA), which exhibited an efficiency of 19.7%. The FBC-SHJ solar cell was characterized with an efficiency of 24.2% under standard test conditions. After being filtered by the perovskite top sub-cell, the bottom sub-cell delivered an efficiency of 10.4%. As a result, we obtained a 4T tandem solar cell with an efficiency of 30.1% [505].

Table 8.3: *J-V* parameters of the semi-transparent perovskite top sub-cell, SHJ bottom sub-cell and the 4T tandem device.

Cell type	Description	V_{OC} (mV)	J_{SC} (mA/cm^2)	*FF* (%)	η (%)
Perovskite[a]	Top cell	1139	22.0	78.6	19.7
SHJ[b]	Single junction	729	40.0	83.0	24.2
	Filtered bottom cell	711	17.8	82.0	10.4
4T Tandem					30.1

[a]: Certified at ESTI ISPRA @ STC, the cell area is 0.0901 cm^2;
[b]: Measured in-house, the cell area is 3.92 cm^2.

In order to gain more insights into the light management of the 4T tandem solar cell, we further calibrated our optical simulation model based on the measured EQE spectra. As presented in Figure C.8 (Appendix C), we achieved a rather good agreement between the measured EQE spectra and the simulated absorptance of the 4T tandem solar cell. It is worth noting that in the 4T tandem solar cell as sketched in Figure 8.8 (b), a MgF_2 layer was deposited at the rear side of the semi-transparent top sub-cell to enhance the light transmittance to the bottom sub-cell [479]. The thickness of this additional MgF_2 layer was optimized when considering an air gap between the sub-cells [479]. Besides, as known from our optical simulation studies (see Appendix C, Figure C.9) [506], in case of an air gap, the desired thickness of SiO_x on top of the SHJ bottom sub-cell is similar to its optimum thickness range for reducing reflection to air in single junction SHJ solar cells. Therefore, the use of optimized DLARC in our optimized FBC-SHJ solar cell also contributed to the current generation in the bottom sub-cell. Nevertheless, with the view of fabricating 4T tandem modules, practical encapsulants, such as polyolefine (n = 1.49 @λ = 800 nm), are essential for electrically separating both sub-cells, providing good resistance of the cell to moisture, UV exposure, and other environmental conditions. With such encapsulants as the optical coupling layer in 4T tandem devices, both sub-cells require re-optimization to maximize the light in-coupling to the bottom sub-cell [506].

8.4 Conclusions

In this chapter, we presented the development and integration of SHJ bottom sub-cells for 2T and 4T perovskite/c-Si tandem solar cells and highlighted light-management techniques assisted by optical simulation.

We first developed SST FBC-SHJ solar cells with various (*n*)-layers, namely, (*n*)a-Si:H, (*n*)nc-Si:H, and (*n*)nc-SiO_x:H, and combined them with perovskite top sub-cells forming monolithic 2T tandem solar cells. Different (*i*)a-Si:H passivation strategies were first developed for (100)-oriented flat c-Si surface and subsequently integrated with said (*n*)-layers. Interestingly, the bi-layer with HPT that exhibited the best (*i*)a-Si:H passivation quality showed degraded minority carrier lifetime when implemented with highly hydrogen-diluted nc-Si:H-based layers. Instead, the bi-layer without HPT enabled a high minority carrier lifetime of 16.9 ms when combined with (*n*)nc-Si:H in a symmetrical configuration.

Furthermore, based on optical simulations, the anti-reflection coating and interfacial layers in 2T tandem solar cells were optimized to minimize parasitic absorption and reflection losses in order to increase the J_{SC} of tandem solar cells and decrease the current mismatching. As a result, 2T tandem solar cells with efficiencies above 23% (a maximum of 25.1%) were achieved with all three types of (*n*)-layers with good current matching. The potential of various (*n*)-layers for optimized light management of tandem solar cells was further explored via optical simulations. The use of around 95-nm-thick (*n*)nc-Si:H and 115-nm-thick (*n*)nc-SiO_x:H enables reflection reductions of 1.35 mA/cm^2 and 1.51 mA/cm^2, respectively, as compared to 5 nm (*n*)a-Si:H at the intermediate interfaces between the perovskite and c-Si bottom sub-cells, thus allowing better light coupling into the bottom c-Si solar cells. This marks both (*n*)nc-Si:H and (*n*)nc-SiO_x:H as promising candidates for achieving high-efficiency tandem solar cells. The reduced reflection loss was achieved by minimizing reflection originating from intermediate interfaces between the sub-cells through the optimization of interference effects. This technique can be adapted to different tandem designs to realize optimal light management in tandem devices.

Passing to 4T tandem configuration, by combining our optimized DST FBC-SHJ solar cell with an independently certified semi-transparent perovskite top sub-cell and with an air gap, we demonstrated a 30.1%-efficient 4T perovskite/SHJ tandem solar cell. Our optimized design of FBC-SHJ solar cell allows effective light coupling into the bottom sub-cell in 4T tandem solar cells. This is made possible thanks to the minimized shading losses enabled by the electroplated Cu grid and minimized reflection losses due to the use of optimum DLARC. The beneficial effect of employing the DLARC was further supported by optical simulations.

9

Conclusions and outlook

This chapter is partially based on:

Y. Zhao, P. Procel, C. Han, L. Cao, G. Yang, E. Özkol, A. Alcañiz, K. Kovačević, G. Limodio, R. Santbergen, A. Smets, A. Weeber, M. Zeman, L. Mazzarella and O. Isabella, "Strategies for realizing high-efficiency silicon heterojunction solar cells", *Solar Energy Materials and Solar Cells*, vol. 258, p. 112413, 2023. [1]

9.1 Conclusions

This thesis describes the understanding and advancement of high-efficiency front/back-contacted silicon heterojunction (FBC-SHJ) solar cells featuring doped nc-Si:H-based carrier-selective passivating contacts as single-junction devices, as well as their applications as bottom sub-cells in two-terminal (2T) and four-terminal (4T) tandem devices with perovskite top sub-cells. Throughout this work, with the assistance of advanced opto-electrical simulations, we explored the development of materials, optimization of contact stacks and their eventual integration in completed solar cells resulting in high-efficiency single-junction and tandem solar cells.

This thesis starts with emphasizing the significance of (photovoltaic) PV solar cell technology for energy transition and highlighting both the promising potentials and technical challenges of SHJ solar cell technology, which served as the motivation for this work. It proceeds with explaining the basic principles underlying the physics of the SHJ solar cells in **Chapter 2** and presenting experimental details in **Chapter 3**. Then, in **Chapter 4**, we developed transparent doped nc-SiO_x:H layers alongside various interfacial engineering techniques for their less-resistive integration into FBC-SHJ solar cells. Subsequently, we designed and optimized hole and electron collectors featuring nc-Si:H-based layers as shown in **Chapter 5** and **Chapter 6**, respectively. Afterwards, the effects of (*i*)a-Si:H deposition temperature on the performance of SHJ solar cells were investigated in **Chapter 7**. Lastly, optical simulation-aided design and development of

[1] This paper was invited for publication in the special issue 'SiliconPV 2023' of Solar Energy Materials and Solar Cells, Proceedings of the 13th International Conference on Silicon Photovoltaics.

SHJ bottom sub-cells for high-efficiency 2T and 4T perovskite/c-Si tandem solar cells are presented in **Chapter 8**. The main conclusions reached in this study are summarized below.

To begin with, the opto-electrical properties of doped nc-SiO$_x$:H layers can be effectively tuned by varying their deposition conditions. The remarkable flexibility in tuning opto-electrical properties of doped nc-SiO$_x$:H layers enables one to improve the selective transport of charge carriers, thereby influencing the *J*-*V* output of solar cells. According to the material database built in this thesis for doped nc-SiO$_x$:H layers, we observed that (*n*)-type nc-SiO$_x$:H layers offer a broader optical transparency range for achieving desirable low activation energy (E_a) values as compared to the (*p*)-type counterparts. This suggests that the optimization of (*n*)-type nc-SiO$_x$:H-based window layers for high-efficiency FBC-SHJ solar cells requires less stringent effort. The optical effectiveness of the layer stack based on (*n*)nc-SiO$_x$:H was demonstrated by an average 1.5 mA/cm^2 higher J_{SC}, thus a nearly 1%$_{abs.}$ higher average cell efficiency as compared to the (*n*)a-Si:H counterparts in rear junction solar cells.

Furthermore, heterointerfaces engineering allows for efficient incorporations of nc-SiO$_x$:H-based contact stacks into high-efficiency SHJ solar cells. Different heterointerface engineering techniques were investigated to promote fast nucleation of nanocrystals in doped nc-Si:H-based layers and to establish less resistive doped-Si/TCO interfaces. These techniques include the utilization of oxygen-absent nc-Si:H seed layers, hydrogen plasma treatments (HPTs), doped a-Si:H capping layers, post-HPT and their various combinations. Beneficial effects were found on the electrical properties of layers (stack) and the *FF* of corresponding solar cells by applying these techniques. With the optimized interfacial treatments developed for (*n*)-type and (*p*)-type contact stacks, we demonstrated a *FF* improvement of 12.3%$_{abs.}$ from 65.6% to 77.9% in FBC-SHJ solar cells.

Thirdly, optimized (*p*)-contact stacks featuring (*p*)nc-SiO$_x$:H and (*p*)nc-Si:H enable efficient selective transport of holes. Particularly, with both theoretical understanding of the transport mechanism of holes and our experimental observations, (*p*)nc-SiO$_x$:H plays a crucial role in maintaining the passivation quality and enabling sufficient band bending at c-Si/(*i*)a-Si:H interface, while the addition of (*p*)nc-Si:H minimizes the transport losses of holes from (*p*)-layer to ITO and enhances the band bending as well. The contact resistivities of (*p*)-type contact stacks can be reduced by several means, including using a thinner (*i*)a-Si:H layer, employing a (*p*)nc-SiO$_x$:H with a larger difference between the E_{04} and E_a, finding an appropriate thickness combination of (*p*)nc-SiO$_x$:H and (*p*)nc-Si:H, and applying the optimized HPTs. As a result of improved selective transport of holes, the optimized (*p*)-type contact stacks exhibited significant contact resistivity ($\rho_{c,p}$) reductions (a minimum $\rho_{c,p}$ of 144 m$\Omega \cdot$cm^2) and contributed to achieving certified *FF* values well above 80% for both front and rear junction solar cells. Moreover, the corroborative experimental and simulation findings indicate that the variation in contact resistivities of the (*p*)-type contact stack can impact the distribution of vertical and lateral transport of holes on the illuminated side of solar cells.

In addition, a 3-nm-thick (*n*)nc-Si:H-based layer combined with the optimized HPTs can be used as an efficient electron collector. We experimentally assessed a minimum thickness of approximately 8 nm is essential for a single (*n*)nc-SiO$_x$:H layer to

maintain the passivation quality and be effective for electron transport, while the minimum thickness required for (*n*)nc-Si:H and (*n*)a-Si:H can be as thin as 3 to 4 nm. This difference is related to their expected dissimilar capability of incorporating active doping in such thin thicknesses (< 10 nm), where (*n*)a-Si:H appeared to be the most conductive, then followed by (*n*)nc-Si:H and (*n*)nc-SiO_x:H layers when they were deposited on (*i*)a-Si:H layers. Despite the high E_a of this thin (*n*)nc-Si:H layer, the solar cell endowed with this (*n*)-contact delivered a certified efficiency of 22.2% and a *FF* of 80.1%, and showed a 0.61 mA/cm^2 J_{SC} gain over the (*n*)a-Si:H counterpart mainly owing to the higher transparency of (*n*)nc-Si:H. Besides, thanks to its ultra-thin thickness, this optimized (*n*)nc-Si:H layer yielded low absorption losses similar to those commonly measured for (*n*)nc-SiO_x:H films. Nevertheless, by stacking a 2-nm-thick (*n*)a-Si:H on top of this thin (*n*)nc-Si:H, we observed further improved *FF* of solar cells. The addition of this (*n*)a-Si:H capping layer can (i) lower the E_a of the (*n*)-contact, (ii) preserve the passivation quality after TCO sputtering, and (iii) prevent surface oxidation of (*n*)nc-Si:H possibly induced by the TCO sputtering, which was identified from EDX elemental mapping analysis.

Following that, an optimized (*i*)a-Si:H layer (stack) should ensure simultaneously an excellent surface passivation quality and a high bulk quality itself. Our observations indicate that (*i*)a-Si:H layers became hydrogen-rich and less dense when deposited at lower temperatures or combined with the HPTs. In particular, (*i*)a-Si:H bi-layers deposited at lower temperatures generally exhibited lower effective minority carrier lifetime (τ_{eff}) as compared to those deposited at higher temperatures. However, after applying the HPTs, significant τ_{eff} improvements and better passivation qualities were observed for (*i*)a-Si:H bi-layers deposited at lower temperatures. At the solar cell level, even though higher V_{OC} values were obtained when the (*i*)a-Si:H bi-layer was deposited at a lower deposition temperature (140 °C), the related *FF* values were poorer as compared to higher temperature counterparts (160 °C to 180 °C). The higher V_{OC} and lower *FF* of solar cells with (*i*)a-Si:H bi-layer deposited at 140 °C is comprehended by the hydrogen-rich and underdense film obtained with a lower deposition temperature (140 °C). A deposition temperature of 200 °C led to increased recombination which degraded both the V_{OC} and *FF* of solar cells. The observed trade-off between V_{OC} and *FF* reveals critical requirements for optimizing (*i*)a-Si:H for high-efficiency SHJ solar cells: (i) excellent surface passivation quality to reduce losses induced by interface recombination and simultaneously (ii) a high bulk quality to not disrupt the charge carrier collections. Particularly, (*p*)-contact is more sensitive to the bulk quality of (*i*)a-Si:H layers than (*n*)-contact. Eventually, by choosing the rather optimum deposition temperature (160 °C), together with the Cu-electroplating metallization and the double-layer anti-reflection coating (DLARC), the resulting solar cell exhibited an efficiency of 24.18% and a *FF* of 83.3%.

Last but not least, effective light management assisted by optical simulations is critical for achieving high-efficiency 2T and 4T tandem solar cells. For realizing 2T tandem solar cells with solution-processed perovskite top sub-cells, we developed front-flat and rear-textured (or single-side-textured) FBC-SHJ solar cells by focusing on the optimization of (*i*)a-Si:H layer together with various doped layers on (100)-oriented flat c-Si surface, as it is more prone to detrimental epitaxial growth as compared to the (111)-oriented counterparts. To minimize the reflection losses of 2T tandem solar cells with

front-flat surfaces and to reduce the current mismatch between the sub-cells, optical simulations were utilized for guiding the development of high-efficiency 2T tandem solar cells. Efficiencies from 23% to 25% (a maximum of 25.1%) were demonstrated for 2T tandem solar cells with SHJ bottom sub-cells featuring various (*n*)-layers, namely, (*n*)a-Si:H, (*n*)nc-Si:H and (*n*)nc-SiO$_x$:H. Moreover, findings from experimentally prepared devices and optical simulations mark both (*n*)nc-Si:H and (*n*)nc-SiO$_x$:H as promising candidates for realizing high-efficiency 2T tandem solar cells. Their capability to minimize intermediate reflections between the perovskite and c-Si absorbers through optimization of the interference effects highlights the applicability of such light management techniques to various tandem designs. Lastly, through the combination of our optimized double-side-textured (DST) FBC-SHJ solar cell, an independently certified semi-transparent perovskite top sub-cell, and an air gap between the sub-cells, a 30.1%-efficient 4T tandem solar cell was demonstrated. The DST FBC-SHJ solar cell featured an excellent (near-)infrared response thanks to the use of DLARC which reduces reflection losses to the air. As is known from our optical simulations, for 4T tandem devices with an air gap, this DLARC as optimized for the single-junction application can also enhance the current generation in the bottom sub-cell. Further with practical encapsulants as the optical coupling layer in 4T tandem solar cells and modules, both sub-cells require re-optimization to maximize the light in-coupling to the bottom sub-cell.

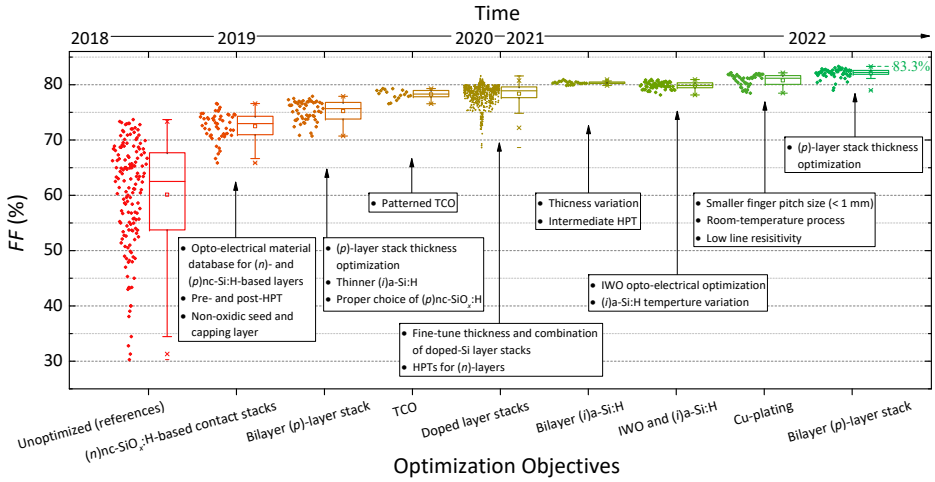

Figure 9.1: The review of *FF* development for FBC-SHJ solar cells with nc-Si:H-based contact stacks throughout this thesis. The review includes detailed optimization objectives and approximate periods of different development steps. The data points in the plot represent the *FF* of individual solar cells.

To sum up, as a result of the abovementioned main conclusions, which serve as design strategies for achieving efficient selective transport and collection of charge carriers for high-efficiency SHJ solar cells, we present in Figure 9.1 the review of *FF* development for FBC-SHJ solar cells that employ nc-Si:H-based contact stacks throughout this thesis work. Initially, due to the limited insights on charge carrier transport and the insufficient control over crucial processing steps and materials, we observed a rather large spread of

FF for cells with unoptimized nc-Si-based contact stacks. Thanks to the rigorous device simulations performed in our group, we gained a better comprehension of the transport mechanisms of charge carriers [150, 151]. The simulations also revealed key accessible material parameters that can be utilized to efficiently develop and optimize the contact stacks [150, 151]. Specifically, with different optimization objectives as depicted in Figure 9.1, we progressively improved in a few years the maximum achievable *FF* and constrained the distribution of the obtained *FF*. In this contribution, we present the best attained *FF* value of 83.3%, which can be further enhanced with the continuous process and material optimizations on the passivation, the effectiveness of the contact stack and the metallizations. Those aspects will be discussed together with light management of FBC-SHJ solar cells in the following section on outlook.

9.2 Outlook

This section discusses further research topics that can contribute to the efficiency advancement of FBC-SHJ solar cells based on nc-Si:H-based contact stacks. These aspects should be integrated with developments made on In-free and Ag-free SHJ solar cells, aiming towards more sustainable mass production of SHJ solar cells as also introduced in Chapter 1[149].

9.2.1 Balancing the light management and electrical performance of FBC-SHJ solar cells

Optimized light management, including minimized losses from parasitic absorption, reflection and metal shading, is essential for achieving high-efficiency solar cells [156]. In this thesis, the parasitic absorption loss was reduced by applying at the front side our developed (*n*)-type nc-Si-based layer stacks, as they are more transparent than using single-layer (*n*)a-Si:H or Si-based (*p*)-layers [167, 175]. Moreover, the use of high-mobility IWO TCO film also lowered the parasitic absorption as compared to our standardly used ITO layers [325]. To suppress the reflection loss of the solar cells, a SiO_x layer with an optimum thickness was added to form a DLARC with the adjacent TCO layer [325, 429], which allows maximum light coupling into the solar cells. Furthermore, to decrease shading losses while maintaining a low finger resistivity, metal electrodes with a high aspect ratio are required. Such metal electrodes were realized by implementing the optimized Cu-electroplating metallization approach [127, 331]. A small metal coverage of around 1.6% was realized with the electroplated ultra-fine Cu grid (width $\leq$ 15 µm), which is much less as compared to our lab-standard screen-printed Ag grid (around 3.25%). The best FBC-SHJ solar cell fabricated in this thesis (24.18%-efficient with *J*-*V* parameters given in Table 7.3), as schematically sketched in Figure 7.1 (d), incorporated all light management techniques as mentioned above. With a perspective to enhance further the light-harvesting of our FBC-SHJ solar cells, the optical simulation model GenPro4 was employed for understanding the optical constraints of the current device design [409]. In Figure 9.2, we present the schematic sketch of the simulation structure of the fabricated 24.18%-efficient FBC-SHJ solar cell, its measured EQE spectrum (active area) and the simulated absorptance spectra with GenPro4.

As illustrated in Figure 9.2, the overall good correspondence between the measured

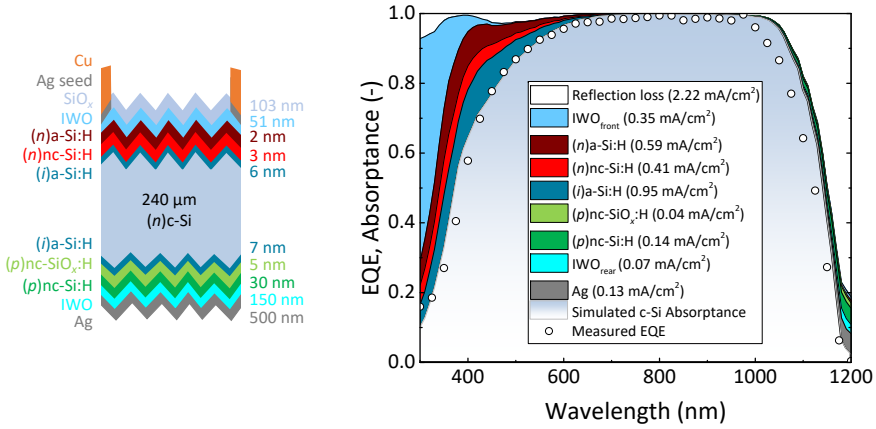

Figure 9.2: The schematic sketch of the simulation structure of the fabricated 24.18%-efficient SHJ solar cell (left), and its EQE spectrum (active area) and simulated absorptance spectra (right). The mismatch between the EQE spectrum and the simulated absorptance spectra can be attributed to (i) the non-ideal collection efficiency of charge carriers in EQE measurement while the simulation considers only optical effects, (ii) underestimated absorption of TCO in the near-infrared range due to limited sensitivity of the reflective-type SE used for extracting the extinction coefficient [334], (iii) possible non-negligible plasmonic absorption of rear Ag is not considered in the simulation [194].

EQE spectrum and simulated absorptance of the c-Si absorber provides insights into the optical losses of the device, which can guide further improvements in device light management. For instance, we compare here our results obtained from optical simulation with the optical loss analysis reported for the top-tier 26.74%-efficient bifacial FBC-SHJ solar cell [67]. The simulation of our best cell indicated rather comparable total reflection losses and parasitic absorption losses induced by TCO layers. While in our case, the front (*n*)-layer stack that consists of 3-nm-thick (*n*)nc-Si:H and 2-nm-thick (*n*)a-Si:H exhibit an absorption loss of around 1.00 mA/cm^2, which is 0.79 mA/cm^2 higher than that of the 26.74%-efficient solar cell. Moreover, our (*i*)a-Si:H bi-layer also appears to be more absorptive with a contribution of 0.95 mA/cm^2, while the (*i*)a-Si:H layer from the 26.74%-efficient solar cell only accounts for 0.34 mA/cm^2. These comparisons address the various aspects that can further enhance the light management of FBC-SHJ solar cells. **While it is important to note that the effectiveness of light management in eventually improving the efficiency of solar cells relies on its optical advantages outweighing any potential compromises to the electrical performance of solar cells.** Take monofacial rear junction solar cells with an (*n*)-contact on the illuminated side as an example, several potential pathways to eventually attain a J_{SC} over 41 mA/cm^2 while ensuring favorable V_{OC} and *FF* are discussed as follows:

- **A thinner and more transparent (*i*)a-Si:H layer (stack) on the illumination side while maintaining excellent passivation and transport quality.** As discussed throughout the whole thesis, the (*i*)a-Si:H passivating layer (stack) should guarantee excellent surface passivation, which becomes challenging if the thickness

of the (*i*)a-Si:H layer is too thin [507]. This aspect is particularly addressed in Chapter 5 during the (*i*)a-Si:H thickness optimization of the (*p*)-contact, where we found a minimum thickness of around 6 nm for the overall optimum performance of solar cells. Similarly, we also investigated the minimum thickness of (*i*)a-Si:H underneath the (*n*)-contact using either (*n*)nc-Si:H or (*n*)a-Si:H. The results are presented in Figure D.1 (Appendix D), where we noticed (*i*)a-Si:H thickness can be reduced from around 6 nm to as thin as 4 nm for cells with (*n*)a-Si:H without compromising the *FF* and V_{OC}. In the meanwhile, cells also exhibited expected higher J_{SC} values with thinner (*i*)a-Si:H layers. The *J*-*V* parameters of optimized solar cells featuring 4 nm (*i*)a-Si:H and 4 nm (*n*)a-Si:H are presented in Table D.1 (Appendix D). Whereas similar reductions of (*i*)a-Si:H thickness underneath (*n*)nc-Si:H resulted in cells with degraded V_{OC} and J_{SC}. These different trends can be ascribed to the distinct deposition conditions for (*n*)nc-Si:H and (*n*)a-Si:H (see Table 6.1), which impact differently on the interfacial properties of the c-Si absorber (see Figure 6.6). Overall, this observation suggests that the (*i*)a-Si:H thickness reduction can be enabled by minimizing the deposition damage induced by the depositions of the (*n*)-contact. This is possible by adjusting the PECVD deposition conditions, for example, using higher plasma excitation frequency to deposit doped layers [315, 508, 509].

Nevertheless, if we adhere to the current deposition conditions for (*n*)a-Si:H and (*n*)nc-Si:H layers, and according to results shown in Figure D.1 (Appendix D), the thickness of (*i*)a-Si:H layer can be as thin as 4 nm (instead of 6 nm) by depositing a thin (*n*)a-Si:H buffer layer before the deposition of the (*n*)nc-Si:H-based layer. In this case, the optical benefit of using a thinner (*i*)a-Si:H is expected to be rather minor due to the use of the additional (*n*)a-Si:H buffer layer. However, as inspired by results from Chapter 7, the insertion of this thin (*n*)a-Si:H is expected to enhance the V_{OC} and *FF* of the devices thanks to (i) the overall more conductive (*n*)-contact close to the (*n*)c-Si/(*i*)a-Si:H interface that enhances the band bending, and (ii) also improved carrier transport from (*n*)-contact to the TCO layer. In other words, thanks to the improved electrical properties of the (*n*)-contact, it also enables possible optical response improvement by using a thinner (*n*)-contact. The eventual efficiency improvement relies on the careful balancing of the optical and electrical performance of solar cells.

Moreover, (*i*)a-Si:H alloys, such as (*i*)a-SiO_x:H, can be also promising for reducing parasitic absorption losses and providing excellent surface passivation [389, 510–513]. While special attention should be given to not hinder the transport of charge carriers, especially, the holes when using these alloys [511, 513]. Last but not least, in the 26.81%-efficient SHJ solar cell, an oxygen-terminated surface formed by using HF/H_2O_2 solution was implemented for preventing epitaxial growth [67]. Overall, by employing a multi-layer approach that incorporates (*i*)a-Si:H layers with various microstructural properties and/or their alloys, along with optimized plasma treatment (e.g. HPTs developed in this study), it becomes possible to simultaneously achieve both excellent surface passivation and a less resistive transport of charge carriers [67, 132, 427, 431, 445]. This, in turn, could facilitate the use of a more transparent and a thinner (*i*)a-Si:H layer stack.

- **A more transparent (*n*)nc-SiO$_x$:H-based layer stack while enabling efficient selective transport of electrons from c-Si to TCO layer.** The optical advantages of (*n*)nc-SiO$_x$:H have been demonstrated in Table 6.2 and Figure 6.4, where the (*n*)nc-SiO$_x$:H layers featuring higher E_{04} also contributed to higher J_{SC} values as compared to cells with oxygen-absent (*n*)nc-Si:H or (*n*)a-Si:H. However, the maximum attainable *FF* of solar cells with various single (*n*)-layers is well-correlated to the E_a of these (*n*)-layers. As a result, these oxygen-absent (*n*)-contacts enabled better *FF* values than (*n*)nc-SiO$_x$:H layers. To utilize the superior optical transparency of (*n*)nc-SiO$_x$:H while maintaining decent *FF*, solar cells with 8 nm (*n*)nc-SiO$_x$:H-1 (see Table 6.2) + 3 nm (*n*)nc-Si:H as the (*n*)-contact were fabricated. These cells featured the same processing conditions as the 24.18%-efficient solar cell except for the choice of the (*n*)-contact. The *J*-*V* parameters are presented in Table D.1 (Appendix D). As seen in Table D.1, by using 8 nm (*n*)nc-SiO$_x$:H-1 + 3 nm (*n*)nc-Si:H as the (*n*)-contact, cells only achieved an average *FF* of 77.61%. By adding 1 nm of (*n*)a-Si:H capping layer on top of this (*n*)-contact, the average *FF* was boosted to 82.06% although the corresponding J_{SC} was reduced by 0.4 mA/cm^2. These cells with 8 nm (*n*)nc-SiO$_x$:H-1 + 3 nm (*n*)nc-Si:H + 1 nm (*n*)a-Si:H exhibited a higher average J_{SC} of 40.39 mA/cm^2 but 0.7%$_{abs.}$ lower *FF* as compared to the cells with 3 nm (*n*)nc-Si:H + 2 nm (*n*)a-Si:H. Consequently, comparable average efficiencies of around 24% were achieved for both types of (*n*)-contacts.

  As this 1-nm-thick (*n*)a-Si:H appears to be critical for ensuring a less resistive interface between (*n*)-contact/TCO, further thinning down the (*n*)nc-Si:H layer from 3 nm to 1 nm was expected to further reduce the parasitic absorption without significantly compromising the *FF*. As seen in Table D.1, by reducing the (*n*)nc-Si:H from 3 nm to 1 nm, we indeed observed an improved J_{SC} of 0.28 mA/cm^2 but this comes with a degraded *FF* of 0.61%$_{abs.}$ due to the weakened E_a of the (*n*)-contact. Eventually, a slightly lower average efficiency of 23.90% was obtained.

  Overall, according to the abovementioned results with cell efficiencies of around 24%, the use of (*n*)nc-SiO$_x$:H can indeed enhance the J_{SC} of solar cells, while careful optimization is essential to ensure a less resistive transport from c-Si to the TCO. The observed trade-off between the optical transparency and transport quality of (*n*)-contact points to optimum combinations of different (*n*)-layers and fine-tuning their thicknesses for eventually realizing superior efficiency of solar cells. A thinner thickness of nc-Si:H-based layer stack with optimum opto-electrical properties can be facilitated by fine-tuning the PECVD deposition conditions as showcased in Chapter 4, and promisingly, by exploiting prompt nucleation of nanocrystals enabled by higher excitation frequency of plasma [163, 314, 315] along with more optimized interfacial engineering techniques.

- **Other light management techniques.** As seen in Figure 9.2, the rear bi-layer (*p*)-contact (5 nm (*p*)nc-SiO$_x$:H + 30 nm (*p*)nc-Si:H) accounts for a parasitic absorption loss of 0.18 mA/cm^2. This loss can be reduced by enabling desired electrical properties of (*p*)-contact within a limited thickness [315]. Moreover, further optimized high-mobility TCO layers (e.g. cerium-doped indium oxide [67, 514]), which feature broadband transparency and a minimum carrier concentration of around

10^{20} cm^{-3}, should be developed. These TCO layers can minimize the parasitic absorption losses, especially the free carrier absorption loss [515–517], and enable efficient transport of charge carriers [151]. Besides, a dielectric layer with a metal electrode on the rear side forming an efficient back reflector (e.g. SiO_2/Ag [518]) can also enhance the infrared response of the solar cell [194, 518–520]. The significance of these light management techniques, which improve the infrared response of solar cells, becomes more pronounced when thinner wafers are employed. The use of thinner wafers, which is enabled by the low processing temperature of SHJ solar cells [125], is advantageous for not only achieving V_{OC} above 750 mV as a result of reduced bulk recombination if the surface recombination is adequately suppressed [67, 521], but also reducing the material cost of manufacturing. Eventually, a front metal grid with minimized metal coverage, while maintaining an optimum pitch size, can further improve the J_{SC} of solar cells without any negative impacts on the *FF*. To accomplish this, it is necessary to form an ultra-fine metal grid, such as that achieved through Cu-electroplating [200, 430].

To sum up, as an outlook to achieve higher efficiencies above 26% for FBC-SHJ solar cells, both solid theoretical understandings and exceptional experimental practices should collaborate effectively. Thanks to the clear pathways elucidated by the fundamental understanding of the transport mechanisms of charge carriers in SHJ solar cells [150, 151], the methodologies and ideas presented in this thesis [522], along with the outlook described earlier, exhibit significant resemblances with those reported by Lin, et al. in achieving the record 26.81%-efficient FBC-SHJ solar cells [67]. The key difference lies in the realization of composing layer stacks with excellent opto-electrical properties and minimized interface resistive losses, achieved through, for example, process optimizations and the utilization of optimum deposition techniques and equipment. Moreover, post-treatments applied on completed solar cells such as light-soaking and/or electric bias are also promising to enhance further the performance of SHJ solar cells [67, 523–526].

9.2.2 'Beyond' standard FBC-SHJ architectures

The aforementioned results and discussions show our lab-scale research experience in processing and optimizing low-thermal budget FBC-SHJ solar cells. With a similar approach, the industry reported recently a record conversion efficiency of 26.81% for single-junction c-Si devices using SHJ solar cell technology, which achieved almost its maximal potential [67]. This excellent result indicates that SHJ solar cell technology is ready to explore alternative device architectures to simplify the process while being highly performant. In this context, we propose here novel solar cell structures and point out their corresponding advantages and potential drawbacks or limitations. To do so, we utilized TCAD simulations tools [399], which were consistently coupled with GenPro4 [409], to simulate different solar cell architectures under one sun illumination accounting for the same c-Si parametrization (i.e. 2 $\Omega \cdot$ cm, 100-µm-thick) as the optimized reference baseline SHJ solar cell. All cells have a front pitch size of 800 µm, a metal figure width of 16 µm, and a 2% front metallization coverage. Figure 9.3 shows the schematic sketches of the proposed device configurations with reference stacks of layers. Note that for the sake of simplicity, we report the structure with better light management between

front or rear junction (FJ or RJ) schemes considering realistic choices of thin-film layers. As a result, we evaluated architectures featuring dopant-free, TCO-selective and buried junctions with FJ structures, whereas the reference baseline SHJ solar cells and devices with localized contacts were assessed with RJ configurations. Table 9.1 summarizes the simulated external parameters of the various device structures.

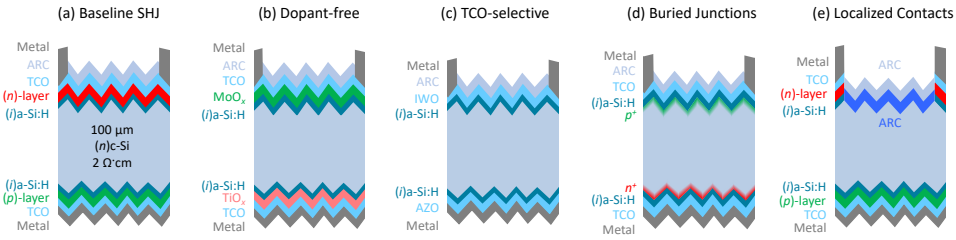

Figure 9.3: Schematic sketches of various SHJ-based device architectures with reference stacks of layers, namely, baseline SHJ solar cells, dopant-free SHJ solar cells, TCO-selective SHJ solar cells [527], SHJ solar cells with buried junctions [528] and SHJ solar cells with localized contacts [529].

Table 9.1: Simulated external parameters of various SHJ-based device architectures.

	J_{SC} (mA/cm^2)	V_{OC} (V)	FF (-)	η (%)
Baseline SHJ	40.99	0.753	0.869	26.82
Dopant-free	41.13	0.753	0.870	26.96
TCO-selective	41.19	0.753	0.863	26.76
Buried Junction	41.33	0.741	0.852	26.12
Localized Contacts	42.34	0.753	0.865	27.60

As seen in Table 9.1, for the reference baseline SHJ device (see Figure 9.3 (a)), we simulated an efficiency of 26.82% with a V_{OC} of 0.753 V, a FF of 0.869 and a J_{SC} of 40.99 mA/cm^2. Note that we considered (n)-layer on the front as such a functional layer is typically less absorptive than a functional (p)-layer [175]. Further, SHJ solar cells with dopant-free passivating contacts are a viable alternative to substitute rather parasitically absorptive doped Si-based thin-film layers when placed on the illumination side. With this device configuration as shown in Figure 9.3 (b), we performed simulations based on our optimized ultra-thin MoO_x layer on the front side [86], which led to an increment in J_{SC} to 41.13 mA/cm^2. As a result, the calculated performance of the dopant-free structure is 0.14%$_{abs.}$ higher than the simulated baseline SHJ solar cells.

Moreover, aiming at having more transparent contacts and simpler processes, we propose a solar cell structure in which front and rear TCOs act as hole transport layer (HTL) or electron transport layer (ETL) layers, without doped or dopant-free layers (see Figure 9.3 (c)) [527]. As expected, the external parameters depend on the opto-electrical properties of the TCO, in particular the one acting as the HTL. In this regard, promising TCO candidates are those that can induce an electrical field within the bulk of the c-Si absorber due to their relatively high work function. For instance, IWO is one such

candidate [325]. Similarly, Al-doped zinc oxide (AZO) exhibits the properties of being a promising candidate as the ETL [380]. As a result, for TCO-selective devices, we calculated 41.19 mA/cm^2, 0.753 V, 0.863 and 26.76% as J_{SC}, V_{OC}, *FF* and conversion efficiency, respectively. Such parameters are similar to those calculated for the baseline SHJ structure. Nevertheless, the main advantage of such solar cells stands in the fact that fewer layers are used, besides the eventual practical challenges, such as realising a thin (*i*)a-Si:H layer (stack) being resilient against subsequent TCO processing. Moreover, the use of less damaging TCO deposition techniques, such as pulsed-laser deposition [530] and reactive plasma deposition [531, 532], is expected to also contribute to the experimental optimizations of TCO-selective SHJ solar cells.

Taking the TCO-selective structure as a reference but to allow more flexibility in choosing TCO materials, we propose to combine this approach with a c-Si wafer that has previously been boron- and/or phosphorus-diffused (see Figure 9.3 (d)). The purpose of this doping profile is to enable a built-in internal electrical field inside the bulk fulfilling the junction condition similar to the in-diffusion of cells with poly-Si-based carrier-selective passivating contacts [533–535]. With this structure, we were able to select rather transparent TCOs on both sides that lead to a simulated J_{SC} of 41.33 mA/cm^2, which is 0.2 mA/cm^2 higher than the dopant-free option. Despite the optical gain, we observed a V_{OC} drop of 0.12 V and a *FF* reduction of 1.7%$_{abs.}$ as compared to the baseline SHJ solar cells, due to the increased intrinsic recombination in the highly doped regions. Accordingly, the calculated conversion efficiency is 26.12% for SHJ solar cells with buried junctions.

Alternatively, we evaluated a solar cell structure with the same contact stack as the baseline SHJ devices, but the front contact layers, namely, (*i*)a-Si:H, (*n*)-layer and TCO are localized beneath the front metal contact as depicted in Figure 9.3 (e). With this structure, we obtained a 1.35 mA/cm^2 increase in J_{SC} which results in 0.78%$_{abs.}$ efficiency gain with respect to the baseline SHJ solar cells, leading to a conversion efficiency of 27.6%. The experimental development of this solar cell architecture might require the fabrication of proof-of-concept intermediate structures such as cells with localized TCO, or devices with localized TCO and doped layers. It is worth noting, besides all these proposed architectures as shown in Figure 9.3 can be adapted to be bifacial, they can be also modified to be used as bottom sub-cells for tandem applications, for example, with perovskite top sub-cells.

The work presented in this thesis showcases various possible configurations (single-side-textured or double-side-textured, rear junction or front junction) of standard SHJ bottom sub-cells, which can be combined with either *p-i-n* or *n-i-p* perovskite top sub-cells in 2T and 4T tandem configurations [476, 483]. For 2T tandem applications, bottom sub-cells with doped layer/TCO or TCO-free recombination junctions (not included in this thesis), utilizing doped nc-Si:H-based layers, demonstrated the capability to minimise reflection losses from intermediate interfaces between perovskite and SHJ sub-cells. This characteristic allows for great flexibility in tuning the light absorption in sub-cells. Additionally, for 4T tandem applications, the optical redesign that is required when going from the 30.1%-efficient 4T lab cell to modules, considering both mono- and bifacial applications with a practical encapsulant, has also been explored (not included in this thesis) [505, 506].

To further enhance the efficiency of perovskite/c-Si tandem solar cells, several crucial aspects need to be addressed. Firstly, achieving optimum light management of the tandem devices, assisted by optical simulations, is essential for maximizing the current generation in tandem solar cells. This involves, for instance, optimizing the thicknesses of composing layers and also the E_g of the perovskite absorber. Secondly, the infrared response and electrical performance of the bottom sub-cells should be further improved. Thirdly, a lossless integration of sub-cells. Last but not least, it is of great importance to minimize the charge carrier losses arising from recombination in the perovskite top-cells, especially, at charge carrier collection interfaces of the perovskite [470, 471, 495, 536].

A

Electron collectors based on nc-Si:H for SHJ solar cells

This chapter is based on the Supporting Information of the following publication:

Y. Zhao, L. Mazzarella, P. Procel, C. Han, F. D. Tichelaar, G. Yang, A. Weeber, M. Zeman, and O. Isabella, "Ultra-thin electron collectors based on nc-Si:H for high-efficiency silicon heterojunction solar cells," *Progress in Photovoltaics: research and applications*, vol. 30, no. 8, pp. 809–822, 2022.

A.1 Optical properties of various (*n*)-type thin-films

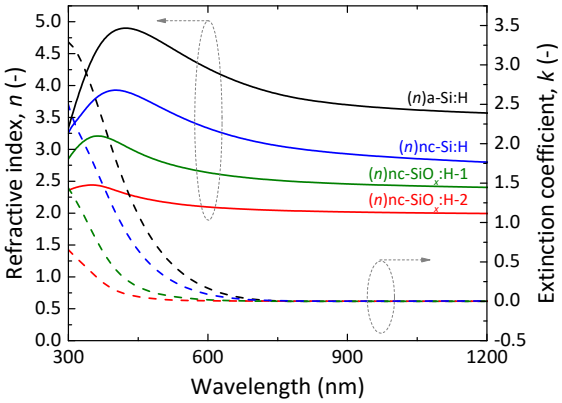

Figure A.1: The n and k of (*n*)nc-SiO$_x$:H, (*n*)nc-Si:H and (*n*)a-Si:H layers as a function of wavelength. Approximately 20-nm-thick layers were deposited directly on glass substrates and characterized.

A

A.2 Effects of the HPTs on the σ_d and E_a of various (*n*)-type layers with thicknesses around 5 nm

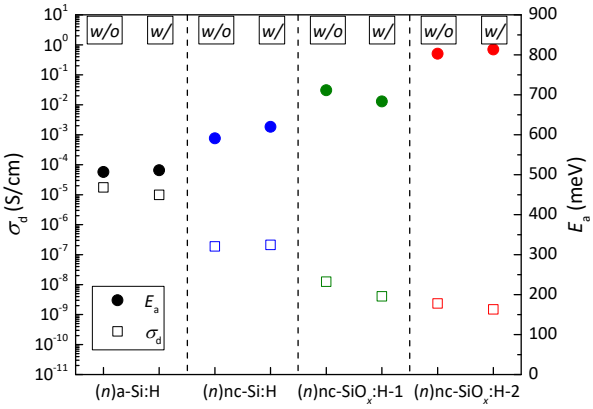

Figure A.2: The σ_d and E_a of (*n*)a-Si:H, (*n*)nc-Si:H and (*n*)nc-SiO$_x$:H layers without and with the HPTs. Around 5-nm-thick (*n*)-type layers were deposited on 10-nm-thick (*i*)a-Si:H coated glass substrates. The HPTs were applied before the depositions of (*n*)-type layers.

As shown in Figure A.2, we observed negligible variations of σ_d and E_a of various (*n*)-type layers (~5-nm-thick) without and with the HPTs. This is because for such thin nc-Si:H-based layers, the effect of possible faster nucleation is not yet observable. According to previous studies [386, 426], the incubation phase for (*n*)nc-Si:H and (*n*)nc-SiO$_x$:H is typically around 2 to 3-nm-thick when they are deposited on (*i*)a-Si:H. Thus, in our nc-Si:H-based films with thicknesses around 5 nm, the nanocrystals are likely to be very small sized and in relatively small fraction compared to the amorphous matrix. In other words, the size and number of these nanocrystals are insufficient to form the percolation path in nc-Si:H [537]. As we obtained σ_d and E_a by performing lateral conductance measurement, it is therefore difficult to observe any significant lateral conductance differences induced by the HPT + VHF (*i*)nc-Si:H treatment for very thin nc-Si:H-based layers. Moreover, as discussed in Section 3.2.1, the influence of the underlying (*i*)a-Si:H can also affect the derived σ_d and E_a of these thin (*n*)-layers. It is also worth noting that the σ_d and E_a of such thin layers are sensitive to their thicknesses, which can vary slightly due to PECVD batch-to-batch variations. Overall, the comparisons among various (*n*)-type layers with combined treatments still suggest that (*n*)a-Si:H is the most conductive film, then followed by (*n*)nc-Si:H, (*n*)nc-SiO$_x$:H-1, and (*n*)nc-SiO$_x$:H-2 for the thickness level of around 5 nm.

A.3 Thickness optimizations of thin (*n*)nc-Si:H

We conducted thickness optimizations of thin (*n*)nc-Si:H (2 to 4 nm) in rear junction solar cells as sketched in Figure A.3. The cells feature the same HPTs as other solar cells presented in Figure 6.4. While the rear side featured a non-optimized mainly in terms of the 8.5-nm-thick (*i*)a-Si:H layer beneath the (*p*)-contact, which was around 1.5 nm thicker than that of cells presented in Figure 6.4 (~7 nm). The *J*-*V* characteristics of cells

with varied (*n*)nc-Si:H thicknesses are presented in Figure A.3 (averaged results and the standard deviation of four solar cells).

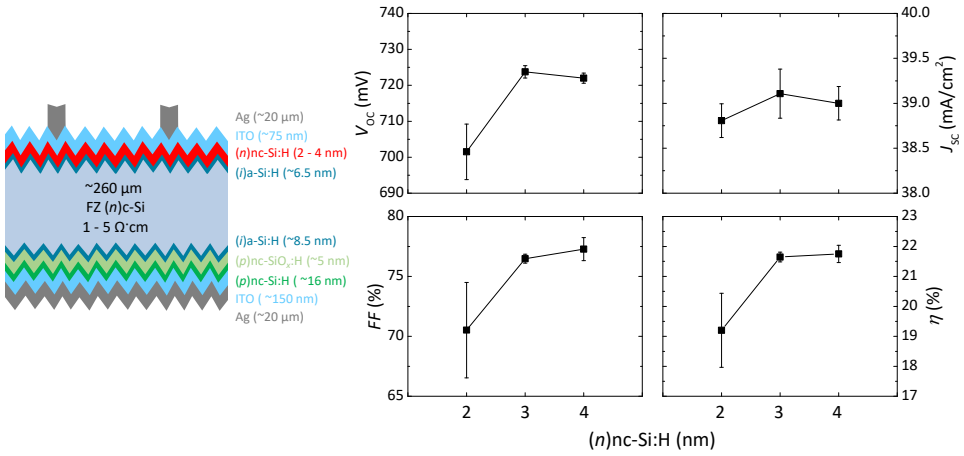

Figure A.3: The *J*-*V* characteristics of rear junction FBC-SHJ solar cells with varied thicknesses of (*n*)nc-Si:H. The results represent averaged parameters of four solar cells (designated area: 3.92 cm^2) and the error bars represent the standard deviations.

As seen in Figure A.3, solar cells with 2-nm-thick (*n*)nc-Si:H showed significantly lower average V_{OC} and *FF* than cells endowed with 3-nm and 4-nm-thick counterparts. This observation indicates that 2-nm-thick (*n*)nc-Si:H is too thin to preserve the passivation quality from subsequent processes. While cells with 3-nm and 4-nm-thick (*n*)nc-Si:H showed overall improved *J*-*V* parameters as compared to cells with 2-nm-thick (*n*)nc-Si:H. As our attention is on minimizing the (*n*)nc-Si:H thickness while keeping good electrical performance of solar cells, we chose the 3-nm-thick (*n*)nc-Si:H which delivered not only the highest J_{SC} but also good V_{OC} and *FF*. Due to a ~1.5 nm thicker (*i*)a-Si:H layer on the (*p*)-contact side as compared to that of cells presented in Figure 6.4, this batch of devices showed slightly higher V_{OC} but lower *FF* [312] as compared to the results in Figure 6.4.

A.4 Bilayer (*n*)nc-Si:H + (*n*)a-Si:H contact layer for (*n*)nc-SiO$_x$:H-2

From the results presented in Figure 6.4, we can state that too thin (2 to 4 nm) (*n*)nc-SiO$_x$:H-2 layer alone is not capable of preserving the passivation quality (iV_{OC} and V_{OC}), whereas the increased recombination negatively affects also the J_{SC} and *FF* of solar cells. To improve the selectivity of thin (*n*)nc-SiO$_x$:H-2 and preserve the passivation, we deposited an additional bilayer contact layer consisting of (*n*)nc-Si:H and (*n*)a-Si:H (~5 nm in total) on top of (*n*)nc-SiO$_x$:H-2. The *J*-*V* parameters of solar cells without and with the bilayer contact layer are presented in Figure A.4.

As presented in Figure A.4, by applying the contact layer, cells with 2-nm-thick and 4-nm-thick (*n*)nc-SiO$_x$:H-2 layer exhibited overall improved external *J*-*V* parameters. As both (*n*)nc-Si:H and (*n*)a-Si:H are much more conductive than the (*n*)nc-SiO$_x$:H-2 layer,

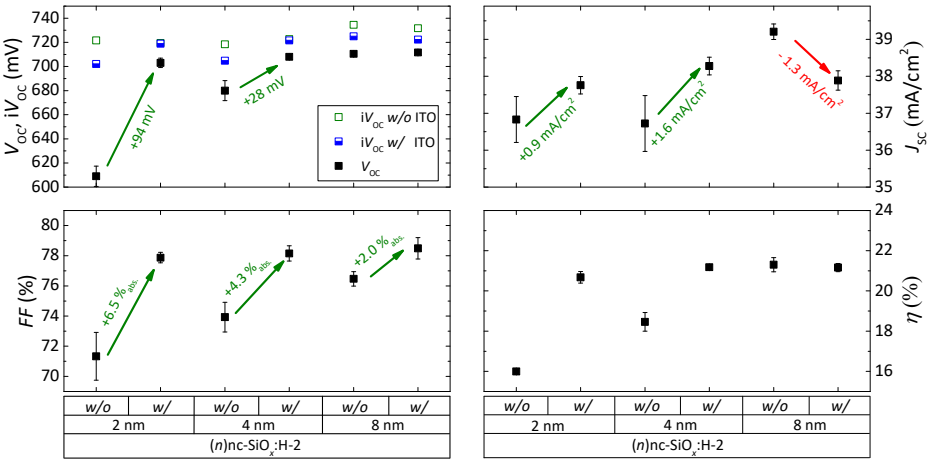

Figure A.4: The *J*-*V* characteristics of rear junction FBC-SHJ solar cells without and with the contact layer on (*n*)nc-SiO$_x$:H-2. The results represent averaged parameters of four solar cells (designated area: 3.92 cm^2) and the error bars represent the standard deviations.

as seen in Table 6.2 and Figure 6.2, the improvement in those *J*-*V* parameters can be explained by better passivation and enhanced electron collections when this bilayer contact layer stack was applied. Especially, the improved J_{SC} values indicate the enhanced electron collections overcompensated the absorption losses brought by the additional contact layer. Interestingly, the contact layer can still improve the *FF* (with 2%$_{abs.}$) of cells with 8-nm-thick (*n*)nc-SiO$_x$:H-2. Nevertheless, the parasitic absorption induced by the contact layer resulted in an average J_{SC} drop of 1.3 mA/cm^2 for cells with 8-nm-thick (*n*)nc-SiO$_x$:H-2, thus the contact layer did not contribute to an eventual higher average η.

A.5 Optical simulations of FBC-SHJ solar cells with various (*n*)-contacts

To understand the distributions of optical losses in our FBC-SHJ solar cells, we performed optical simulations using GenPro4 [409].

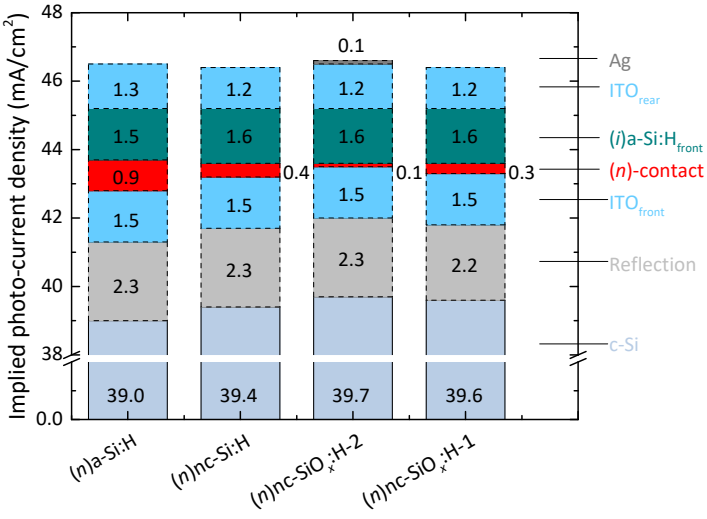

Figure A.5: Optical Simulations of rear junction FBC-SHJ solar cells with various (*n*)-contacts by GenPro4. Specifically, the provided *n* and *k* data of various (*n*)-type layers in Figure A.1 were used as inputs for the simulations.

As shown in Figure A.5, the implied photo-current density differences among c-Si substrates of solar cells are mainly caused by the different optical losses resulting from the various (*n*)-contacts. As expected, (*n*)a-Si:H showed the highest optical loss of 0.9 mA/cm^2 while (*n*)nc-SiO$_x$:H-2 presented the least parasitic absorption loss of 0.1 mA/cm^2. Nevertheless, using a more transparent TCO layer, depositing a thinner (*i*)a-Si:H layer, and applying optimized anti-reflection coatings would further enhance the optical absorption in c-Si absorbers.

A.6 HRTEM with EDX mapping for cell with 8 nm (*n*)nc-SiO$_x$:H-2

We also performed HRTEM with EDX elemental mapping for the FBC-SHJ solar cell with around 8-nm-thick (*n*)nc-SiO$_x$:H-2 and the results are given in Figure A.6.

As seen in Figure A.6 (a), we observed an abrupt (*n*)c-Si/(*i*)a-Si:H interface. Besides, the (*n*)nc-SiO$_x$:H-2 exhibited a rather amorphous structure, which is rougher as compared to the bottom (*i*)a-Si:H part. This can be further explained by EDX Si and O maps in Figure A.6 (b). From the Si and O maps, we identified the (*i*)a-Si:H and (*n*)nc-SiO$_x$:H-2, that is, the (*n*)nc-SiO$_x$:H-2 exhibited a lesser atomic percentage of Si and a significantly higher amount of O incorporation than that of (*i*)a-Si:H. Note that the O signal in both (*n*)c-Si wafer and (*i*)a-Si:H layer could be mainly caused by the surface oxidation of the TEM foil. Together with other EDX maps presented in Figure A.6 (b), we estimated that the thickness of the (*i*)a-Si:H layer was around 6.5 nm, which falls within our expectations. Note, the thickness of total (*i*)a-Si:H + (*n*)nc-SiO$_x$:H-2 was around 15 nm ± 2 nm as

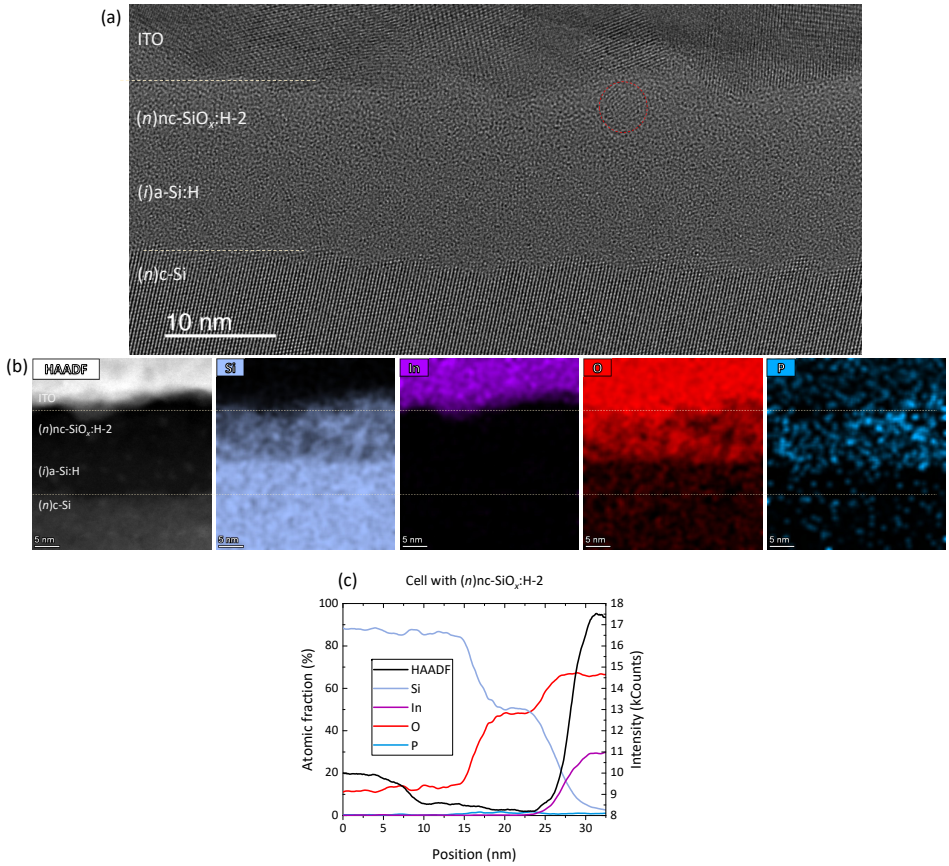

Figure A.6: FBC-SHJ solar cell's (*n*)-contact structure featuring ~8-nm-thick (*n*)nc-SiO$_x$:H-2: (a) HRTEM cross-sectional image viewed from <110> orientation, (b) the scanning TEM (STEM) high-angle annular dark-field (HAADF) images combined with chemical compositional mapping measured by EDX, and (c) (relative) atomic fractions (intensity) of different elements (HAADF) for EDX mapping results. The white dashed lines are guides to the eyes for distinguishing (*n*)c-Si/(*i*)a-Si:H and (*n*)nc-SiO$_x$:H-2/ITO interfaces. Note, the P signal detected outside P-rich zones is an artifact, just as the O signal in the c-Si substrate. The red dashed circle in figure (a) indicates the formation of Si nanocrystals. The lattice spacing of this crystal is (3.12 ± 0.05) Å, consistent with the 111 lattice spacing of 3.13 Å of Si. The '0 nm' position lies inside the (*n*)c-Si wafer and it is close to the (*n*)c-Si/(*i*)a-Si:H interface.

shown in Figure A.6 (c), while the variations were caused by the surface roughness of the substrate and the deposited Si thin-film layers. Therefore, the deposited (*n*)nc-SiO$_x$:H-2 layer had a thickness of around 8.5 ± 2 nm that is also close to its designated thickness.

B

SHJ solar cells with (*i*)a-Si:H bi-layers deposited at various temperatures

This chapter is based on the Supporting Information of the following publication:

Y. Zhao, P. Procel, A. Smets, L. Mazzarella, C. Han, G. Yang, L. Cao, Z. Yao, A. Weeber, M. Zeman, and O. Isabella, "Effects of (*i*)a-Si:H deposition temperature on high-efficiency silicon heterojunction solar cells," *Progress in Photovoltaics: research and applications*, 2022.

B.1 UV Raman spectra of (*p*)nc-SiO$_x$:H layers on (*i*)a-Si:H-coated textured c-Si wafers

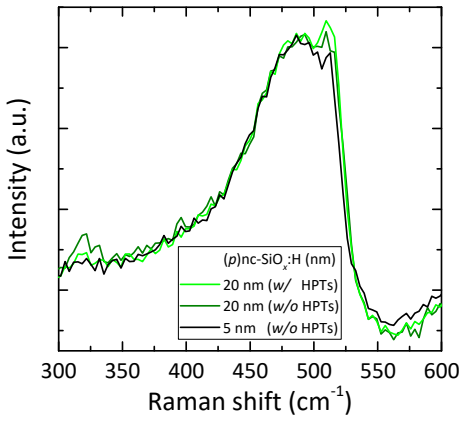

Figure B.1: The UV Raman spectra of samples that consist of textured c-Si/(*i*)a-Si:H-2 (8 nm)/(*p*)nc-SiO$_x$:H (varied thickness) with optionally applied HPTs. The wavelength of the laser is 325 nm.

B

B.2 The effects of (*i*)a-Si:H bi-layers on *J*-*V* parameters of solar cells

To investigate the effects of using a bi-layer (*i*)a-Si:H layer in SHJ solar cells, we deposited firstly 1-nm-thick (*i*)a-Si:H-1 layer without additional hydrogen-dilution that acts as a buffer for the subsequent deposition of the high-hydrogen-diluted (*i*)a-Si:H-2 layer. We compared here the *J*-*V* parameters of cells with single (*i*)a-Si:H-2 layers to cells with bi-layer approaches. FBC-SHJ solar cells as sketched in Figure B.2 were fabricated. The abbreviations and stack descriptions are listed in Table B.1. The deposition temperature of all layers and HPTs presented in Table B.1 is 180 °C. Solar cell *J*-*V* parameters are listed in Table B.2. The results represent averaged parameters of five solar cells and the error bars represent the standard deviations.

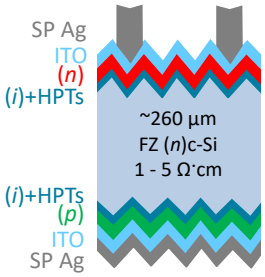

Figure B.2: The schematic sketch of SHJ solar cells featuring different (*i*)a-Si:H layers and/or their combinations.

Table B.1: Abbreviations and stack descriptions for layers forming SHJ solar cells.

Abbreviations	Descriptions
(*i*)-2	8 or 9 nm (*i*)a-Si:H-2[a]
(*i*)-1 + (*i*)-2	1 nm (*i*)a-Si:H-1 + 7 or 8 nm (*i*)a-Si:H-2[b]
HPTs	HPT + VHF treatment
(*n*)	3 nm (*n*)nc-Si:H + 1 nm (*n*)a-Si:H
(*p*)	5 nm (*p*)nc-SiO$_x$:H + 16 nm (*p*)nc-Si:H

[a]: 8 nm and 9 nm (*i*)a-Si:H-2 for (*n*)- and (*p*)-layers, respectively.
[b]: 7 nm and 8 nm (*i*)a-Si:H-2 for (*n*)- and (*p*)-layers, respectively.

Table B.2: The *J*-*V* parameters of SHJ cells with different (*i*)a-Si:H layers and/or their combinations.

(*i*)-layers on (*n*)-/(*p*)-side	V_{OC} (mV)	J_{SC} (mA/cm^2)	*FF* (%)	η (%)
(*i*)-2/(*i*)-2	694.40 ± 4.67	36.92 ± 0.08	79.72 ± 0.46	20.44 ± 0.20
(*i*)-2/(*i*)-1+(*i*)-2	698.60 ± 5.27	37.01 ± 0.17	80.26 ± 0.29	20.75 ± 0.14
(*i*)-1+(*i*)-2/(*i*)-1+(*i*)-2	704.20 ± 2.28	37.15 ± 0.05	80.55 ± 0.33	21.07 ± 0.03

As seen in Table B.2, cells with bi-layer approaches exhibited overall improved *J*-*V* parameters as compared to single (*i*)a-Si:H-2 counterparts. The improvements can be

mainly ascribed to the better passivation quality that reduces losses induced by interface recombination.

B.3 Infrared spectra of (*i*)a-Si:H-1 and (*i*)a-Si:H-2

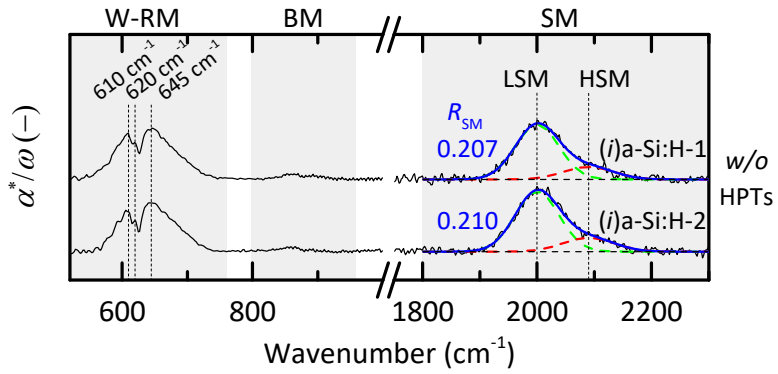

Figure B.3: Infrared spectra of (*i*)a-Si:H-1 and (*i*)a-Si:H-2 deposited at 160 °C. Both layers were symmetrically deposited on double-side-textured wafers with the structure sketch in Figure 7.1 (b), and the thickness of both layers is 20 nm in total on both sides of the substrate. These thicknesses are estimated based on the deposition rates calculated from flat samples. In the figure, W-RM stands for Si-H wagging-rocking modes, BM refers to Si-H polyhydrides bending modes, SM represents Si-H stretching modes. In the SM region, the green and red dashed lines represent the fitted Gaussian function for low-frequency SM (LSM) and high-frequency SM (HSM), respectively. The blue solid lines are the overall fittings. Note that these two samples in Figure B.3 were processed in different batches as compared to Figure 7.3(a).

B.4 FTIR analysis for (*i*)a-Si:H bi-layer with various thicknesses and HPTs

The microstructure and hydrogen-bonding configuration of bi-layer stacks deposited under 160 °C with various thicknesses were assessed by FTIR on dedicated samples as sketched in Figure 7.1 (b). Those (*i*)a-Si:H bi-layers consist of a 1-nm-thick (*i*)a-Si:H-1 layer with a (*i*)a-Si:H-2 layer featuring varied thicknesses. We also evaluated the effects of HPTs on the microstructural properties of the bi-layer stacks with various thicknesses. Note, the HPTs etch around 2 nm of the (*i*)a-Si:H bi-layer on each side of the c-Si wafer. The infrared spectra of different (*i*)a-Si:H bi-layers are presented in Figure B.4.

As seen in Figure B.4, with a thicker bi-layer, we noticed a progressively decreased absorption strength of the peak at around 610 cm^{-1}. Meanwhile, the signature of peaks at around 610 cm^{-1} and 620 cm^{-1} became less distinguishable for thicker layers as they started to merge with the third absorption peak centered at around 645 cm^{-1}. According to the model of a-Si:H film on c-Si proposed by M. Z. Burrows, et al. [309], it is reasonable to decompose our deposited (*i*)a-Si:H (free from epitaxial growth, see Chapter 6 [167]) into 'surface', 'bulk' and 'interface' components. It is well-known that both 'surface' and 'interface' layers are hydrogen-rich and void-rich as compared to the 'bulk' layer [262, 309–311]. With a thicker layer, the fraction of the 'bulk' component is higher as well, which imposes more impact on the measured infrared spectrum, thus, reflecting more the bulk properties of the a-Si:H. This is consistent with the microstructure

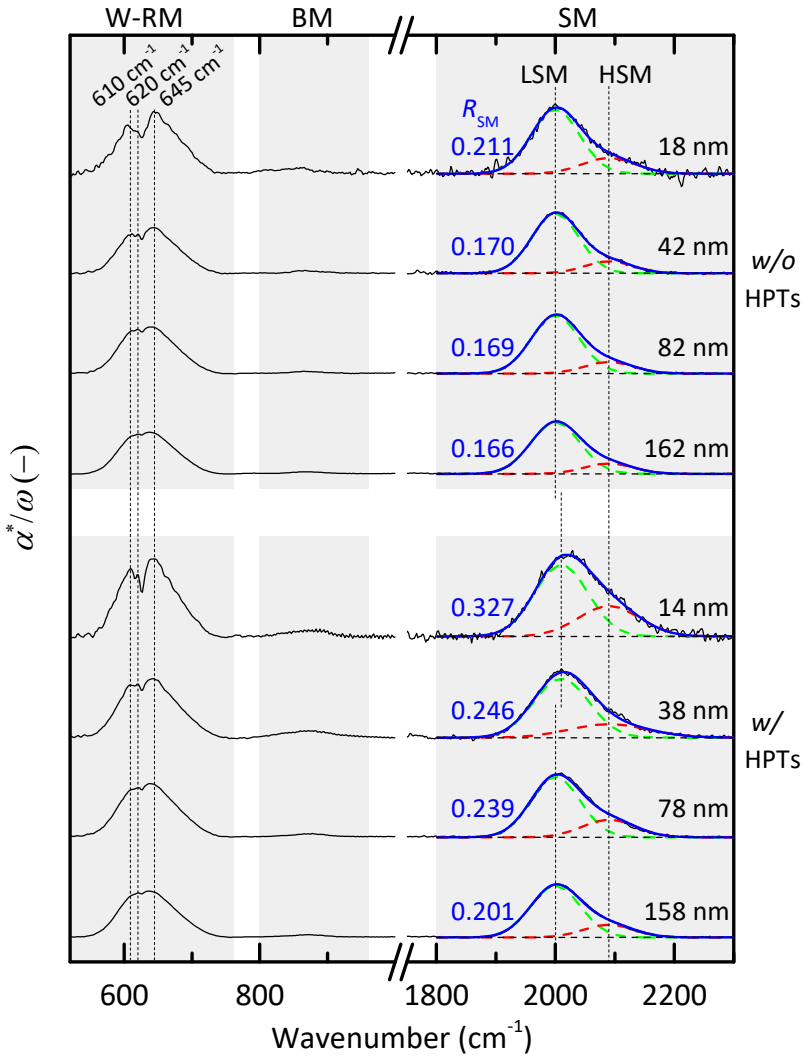

Figure B.4: The infrared spectra of (*i*)a-Si:H bi-layers deposited at 160 °C with (*w*/) or without (*w*/*o*) HPTs. The infrared spectra were normalized according to the thicknesses of (*i*)a-Si:H bi-layers as discussed in experimental details. Those (*i*)a-Si:H bi-layers consist of a 1-nm-thick (*i*)a-Si:H-1 layer with a (*i*)a-Si:H-2 layer featuring varied thicknesses. The indicated thickness numbers are the total thickness on both sides of the wafer. In the SM region, the green and red dashed lines represent the fitted Gaussian function for LSM and HSM, respectively. The blue solid lines are the overall fittings.

factor extracted from the SM, where thicker films tend to reach a lower limit of R_{SM}. One may also notice that the absorption strength is the highest for the thinnest films in both (*i*)a-Si:H bi-layers without and with HPTs series. This can be also ascribed to the reduced fraction of 'bulk' component with a thinner film. Indeed, a thinner (*i*)a-Si:H that

features a lower 'bulk' fraction should have relatively more void-rich and hydrogen-rich 'interface' or 'surface' layers, and thus a relatively higher density of volume deficiencies. This results in a lower average dielectric constant and a smaller proportionality constant of the dipole oscillation [456]. As a consequence, for a given hydrogen content, the absorption signal is enhanced for thinner films. Therefore, both R_{SM} and the change of absorption strength with varied thicknesses are pointing to the increased 'bulk' fractions in thicker films. Then it is logical to ascribe the peak at around 610 cm^{-1} to the 'surface' or 'interface' components of the (*i*)a-Si:H, and peaks at around 645 cm^{-1} (also 620 cm^{-1}) to the 'bulk' component.

Moreover, by comparing 'same' FTIR samples with $T_{(i)\text{a-Si:H}}$ = 160 °C without HPTs or with HPTs as shown in both Figure B.4 (Figure 7.3(b)) and Figure 7.3 (a), we observed quite similar R_{SM} but relatively different W-RM shapes even though they feature identical PECVD deposition conditions. Note that the series of samples in Figure B.4 were processed in different batches as compared to Figure 7.3 (a), and τ_{eff} values of FTIR samples in Figure B.4 were slightly lower than those in Figure 7.3 (a). Therefore, this observation implies that those absorption peaks around W-RM could be more sensitive to and more capable of revealing varied microstructural and interfacial properties of (*i*)a-Si:H layers as compared to those around the SM.

B.5 FBC-SHJ solar cells with electroplated Cu grid

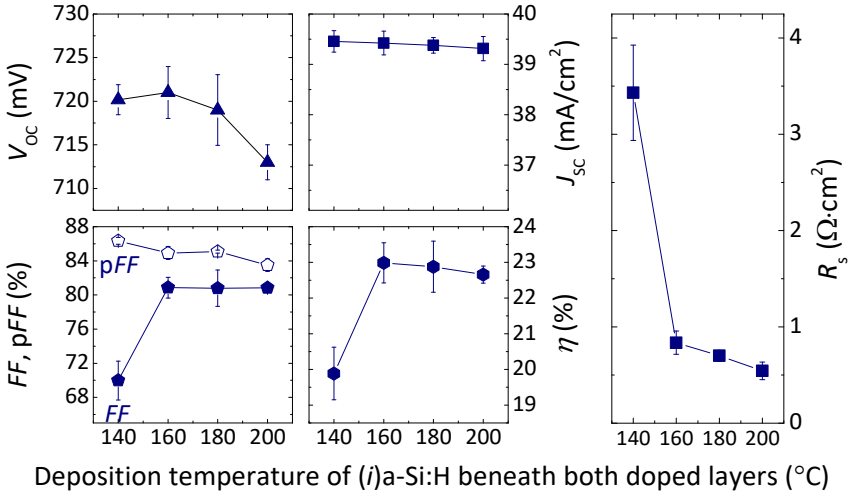

Figure B.5: The *J*-*V* parameters of FBC-SHJ solar cells prepared under various deposition temperatures of (*i*)a-Si:H bi-layer. Cells feature front-side electroplated Cu contact and rear-side thermally evaporated Ag contact. The results represent averaged parameters of six solar cells and the error bars represent the standard deviations.

We applied our optimized room-temperature Cu-electroplating metallization approach for cells with (*i*)a-Si:H deposited under various temperatures ($T_{(i)\text{a-Si:H}}$). Those cells also feature an additional 100-nm-thick SiO_x capping the front IWO to form a

double-layer anti-reflection coating [325, 429]. The cells are sketched in Figure 7.1 (d) and their *J*-*V* parameters are presented in Figure B.5. Besides, we also present in Figure B.5 the extracted series resistance (R_s) of solar cells based on p*FF* obtained from Suns-V_{OC} measurements.

As presented in Figure B.5, we observed similar *J*-*V* parameter trends to those cells with screen-printed Ag contacts as presented in Figure 7.5. Specifically, cells with higher $T_{(i)\text{a-Si:H}}$ exhibited lower V_{OC} values. Besides, the *FF* values were initially lower for cells with $T_{(i)\text{a-Si:H}}$ = 140 °C, then with increasing $T_{(i)\text{a-Si:H}}$, cells exhibited improved and saturated *FF* values. Accordingly, we also noticed lower extracted R_s values with increasing deposition temperatures of the (*i*)a-Si:H bi-layer. As for the J_{SC}, we observed rather minor effects of $T_{(i)\text{a-Si:H}}$. Overall, cells with $T_{(i)\text{a-Si:H}}$ of 160 °C to 180 °C tend to deliver the highest efficiencies due to their optimum V_{OC} and *FF* values.

B.6 Independently certified *I*-*V* curves

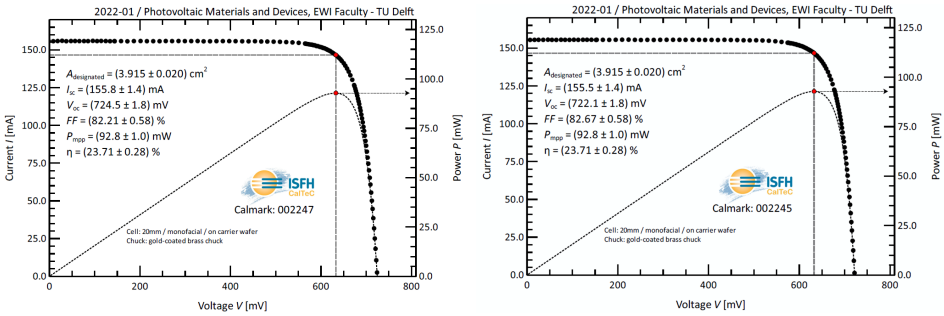

Figure B.6: The independently certified *I*-*V* characteristics and device parameters of the rear junction FBC-SHJ solar cells featuring (*i*)a-Si:H deposited at 160 °C (left) and 180 °C (right). Both solar cells feature the same layer stacks and fabrication process except for the deposition temperature of (*i*)a-Si:H layers on both sides. Both cells feature electroplated Cu front electrodes and SiO_x/IWO double-layer anti-reflection coating. The certifications were performed at ISFH CalTeC (Hamelin, Germany).

B.7 In-house measured *J*-*V* curve of the best solar cell

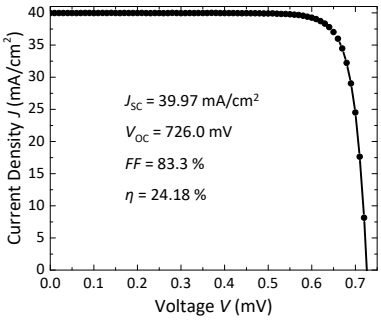

Figure B.7: The in-house measured *J*-*V* curve of the best rear-junction FBC-SHJ solar cells featuring (*i*)a-Si:H deposited at 160 °C. The cell features electroplated Cu front electrodes and SiO_x/IWO double-layer anti-reflection coating. The designated area of the solar cell is 3.92 cm^2.

C

SHJ bottom-cells for perovskite/c-Si tandem solar cells

This appendix is based on the Supporting Information of the following publication and the conference presentation:

Y. Zhao[1], K. Datta, N. Phung, A. E. A. Bracesco, V. Zardetto, G. Paggiaro, H. Liu, M. Fardousi, R. Santbergen, P. P. Moya, C. Han, G. Yang, J. Wang, D. Zhang, B. T. van Gorkom, T. P. A. van der Pol, M. Verhage, M. M. Wienk, W. M. M. Kessels, A. Weeber, M. Zeman, L. Mazzarella, M. Creatore, R. A. J. Janssen, and O. Isabella, "Optical simulation-aided design and engineering of monolithic perovskite/silicon tandem solar cells," *ACS Applied Energy Materials*, vol. 6, no. 10, pp. 5217–5229, 2023.

Y. Zhao, P. Procel, A. Smets, L. Mazzarella, C. Han, G. Yang, L. Cao, Z. Yao, D. Zhang, V. Zardetto, M. Najafi, A. Creatore, R. Janssen, S. Veenstra, G. Coletti, A. Weeber, M. Zeman, and O. Isabella, "Effects of (*i*)a-Si:H deposition temperature on high-efficiency silicon heterojunction solar cells for four-terminal tandem solar cells", *2022 8th World Conference on Photovoltaic Energy Conversion (WCPEC)*, Milan, Italy, oral presentation, 2022.

[1] co-first author with K. Datta

C.1 The effective lifetime of symmetrical samples with (*i*)/(*p*)-layers

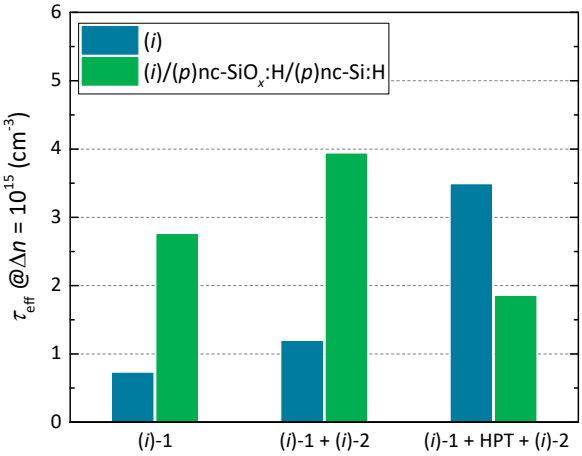

Figure C.1: The effective lifetime (τ_{eff}) of symmetrical samples with different (*i*)a-Si:H passivation approaches with (*p*)-layers (5 nm (*p*)nc-SiO$_x$:H + 16 nm (*p*)nc-Si:H).

C.2 The passivation quality before and after metallization

Table C.1: The τ_{eff}, iV_{OC} and i*FF* of solar cells before metallization and V_{OC} and *FF* of completed solar cells.

(*n*)-layers	With ITO on both sides (before metallization)			Completed solar cells	
	τ_{eff} @$\Delta n = 10^{15}$ cm^{-3} (ms)	iV_{OC} (mV)	i*FF* (%)	V_{OC} (mV)	*FF* (%)
(*n*)a-Si:H (5 nm)	2.06	710	82.8	704	80.7
(*n*)nc-Si:H (20 nm)	7.22	722	85.2	714	80.7
(*n*)nc-SiO$_x$:H (40 nm)	1.31	716	79.4	694	77.5

C.3 EQE spectra of single-junction single-side-textured solar cells

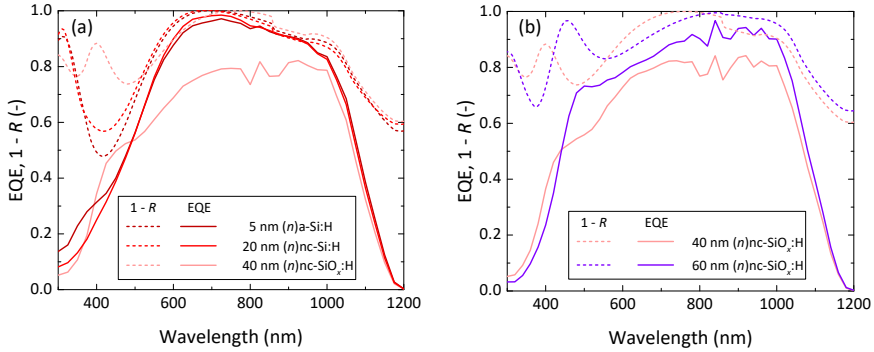

Figure C.2: EQE and 1 – reflectance (R) spectra of single-junction single-side-textured (front-side-flat and rear-side-textured) SHJ solar cells with (a) various front (n)-layers, and (b) 40 and 60 nm (n)nc-SiO$_x$:H layers. Solid lines represent EQE and dashed lines represent (1 – R). Note, for the cell with 40 nm (n)nc-SiO$_x$:H, the overall low EQE in the range from around 500 nm to 1000 nm is ascribed to significant recombination, which can be significantly suppressed by using a 60-nm-thick (n)nc-SiO$_x$:H layer as shown in figure (b).

C.4 The effects of (n)nc-SiO$_x$:H thickness on J-V parameters of solar cells

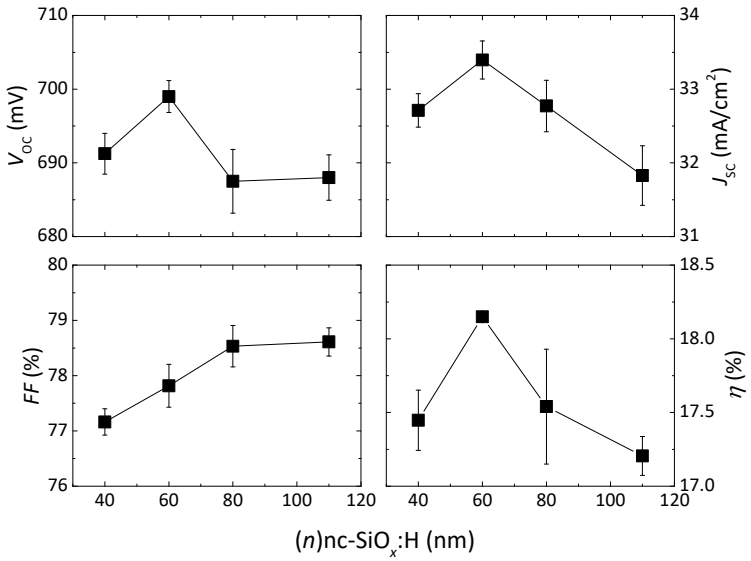

Figure C.3: The J-V parameters of single-junction single-side-textured SHJ solar cells with various thicknesses of front (n)nc-SiO$_x$:H layers. The results represent averaged parameters of three to five solar cells.

C.5 Effects of MgF_2 and C_{60} on the absorptance/EQE of the 2T tandem solar cells

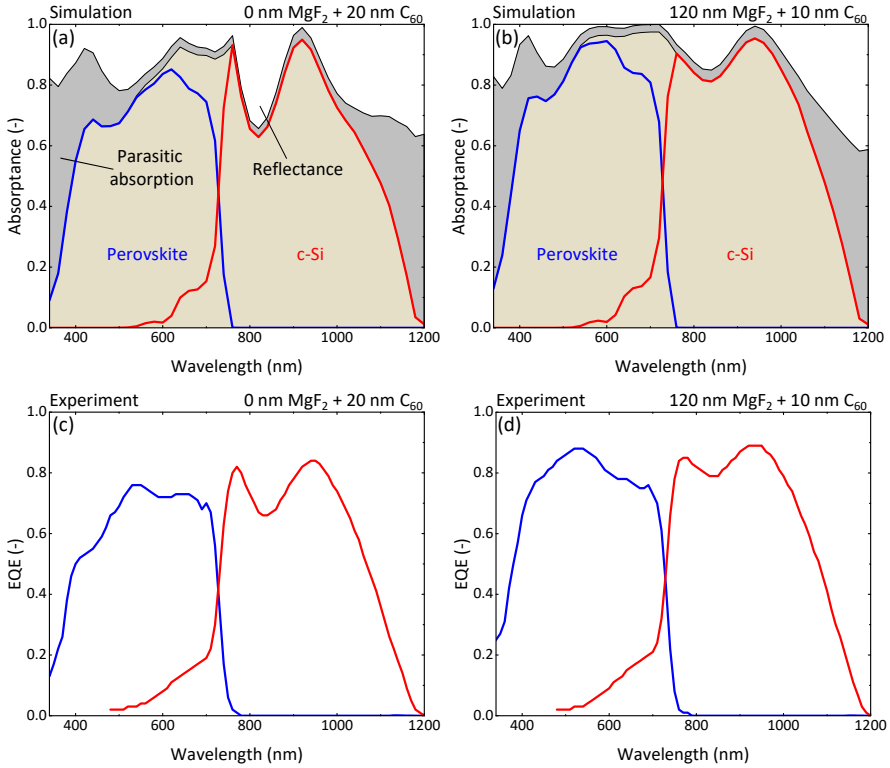

Figure C.4: Experimentally determined EQE and simulated absorptance spectra of tandem solar cells using (a) 0 nm MgF_2 and 20 nm C_{60}, or (b) 120 nm MgF_2 and 10 nm C_{60}. A 45 nm SnO_x layer was used in all cases.

C.6 The *J-V* curve and the EQE spectrum of the 25.1% 2T tandem solar cell

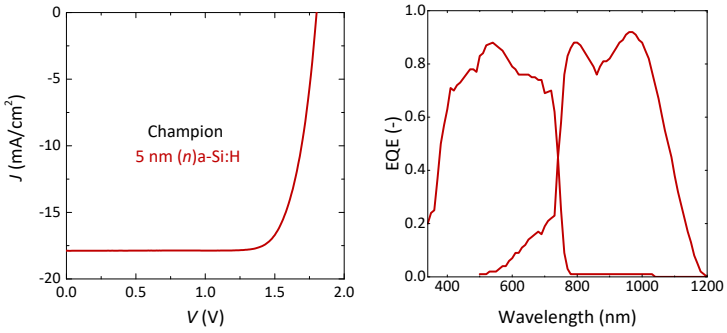

Figure C.5: The *J-V* curve (left) and the EQE spectrum (right) of the 25.1% 2T tandem solar cell.

C.7 The refractive indices of (*n*)-layers and absorbers in 2T tandem solar cells

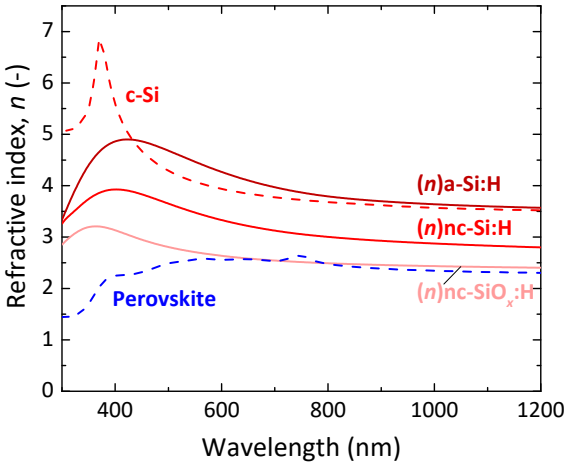

Figure C.6: Refractive indices of (*n*)-type layers and perovskite and c-Si active layers. The data of c-Si is taken from the literature [480].

C.8 Comparisons between simulated absorptance and measured EQE of 2T tandem solar cells

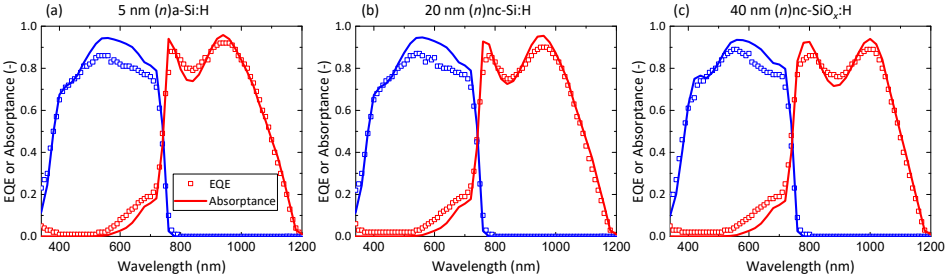

Figure C.7: Comparisons between the measured EQE and the simulated absorptance of 2T tandem solar cells with different (*n*)-layers. Open symbols represent measured EQE values, and the solid lines are simulated absorptance curves. The mismatches between the EQE and the simulated absorptance could be attributed to the following: choline chloride and 2PACz were not considered in the simulations due to difficulty in extracting their optical properties with nearly negligible thicknesses; the overestimated extinction coefficient of perovskite absorber thus the high simulated absorption of perovskite top cell; the non-ideal collection efficiency of charge carriers in real devices while the simulation considers only optical effects.

C.9 Light management of DST 2T tandem solar cells with various (*n*)-layers

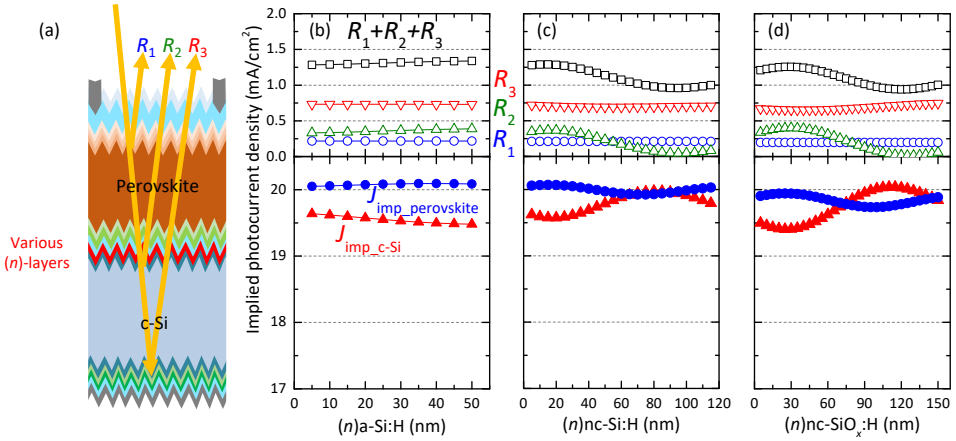

Figure C.8: Light management in double-side-textured monolithic tandem solar cells. (a) Schematic of the perovskite/SHJ tandem solar cell for optical simulations, and (b – d) implied photocurrent density of the perovskite top-cell, SHJ bottom-cell and reflected light as function of (*n*)-layer thickness and types of (*n*)-layer.

C.10 Comparisons between simulated absorptance and measured EQE of 4T tandem solar cells

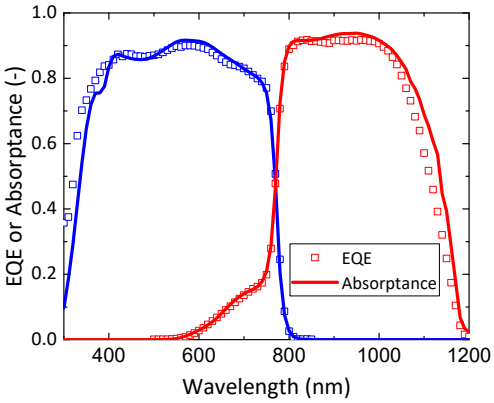

Figure C.9: Comparisons between the measured EQE and the simulated absorptance of 4T tandem solar cells. Open symbols represent measured EQE values, and the solid lines are simulated absorptance curves.

C.11 4T tandem solar cells with varying SiO_x thickness and OCL refractive index

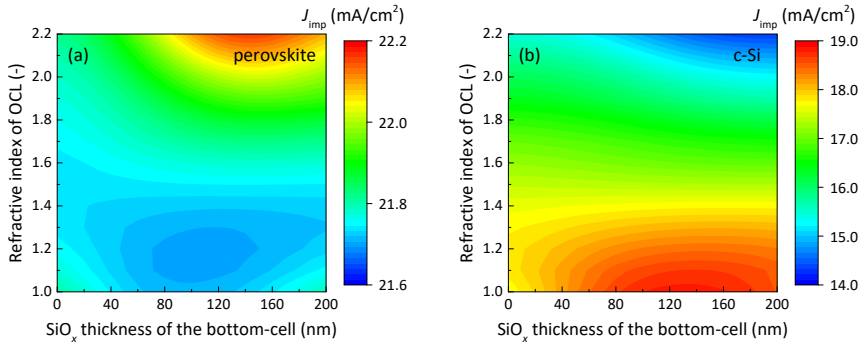

Figure C.10: The implied photocurrent density as function of SiO_x thickness of the bottom-cell and the refractive index of the optical coupling layer (OCL).

D

Transparent (*n*)nc-Si:H-based contacts for SHJ solar cells

D.1 The effects of (*i*)a-Si:H layer thickness on the *J*-*V* parameters of solar cells with (*n*)a-Si:H and (*n*)nc-Si:H (*n*)-contacts

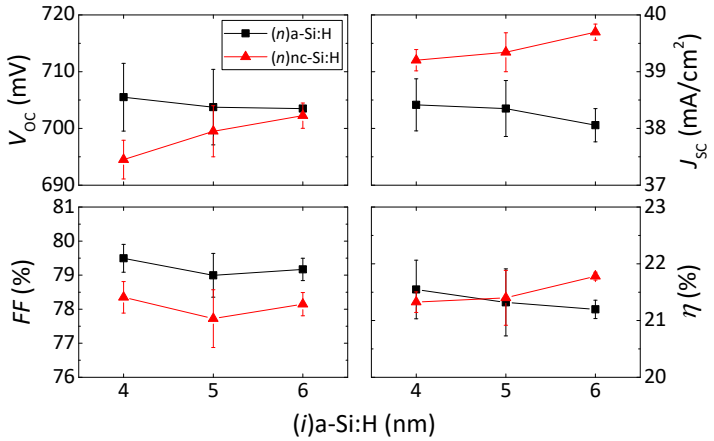

Figure D.1: The effects of (*i*)a-Si:H layer thickness on the *J*-*V* parameters of solar cells with (*n*)a-Si:H and (*n*)nc-Si:H (*n*)-contacts.

D.2 *J-V* parameters of solar cells with various (*n*)-contacts

Table D.1: *J-V* parameters of solar cells with various (*n*)-contacts. The structures of these solar cells resemble the design depicted in Figure 9.2 but with different thicknesses of (*i*)a-Si:H and (*n*)-contact on the front side. Optimized HPTs were applied for all devices. The results represent the averaged parameters of four solar cells and the best cell for each (*n*)-contact.

(*n*)nc-SiO$_x$:H-1 + (*n*)nc-Si:H + (*n*)a-Si:H		V_{OC} (mV)	J_{SC} (mA/cm^2)	*FF* (%)	η (%)
0 + 0 + 4 [a]	Average	722.8 ± 0.5	40.05 ± 0.09	82.66 ± 0.26	23.92 ± 0.09
	Best cell	723.0	40.16	82.74	24.01
0 + 3 + 2 [b]	Average	725.0 ± 1.4	39.98 ± 0.08	82.76 ± 0.40	23.99 ± 0.18
	Best cell	726.0	39.97	83.3	24.18
8 + 3 + 0 [b]	Average	723.3 ± 1.5	40.79 ± 0.12	77.61 ± 1.32	22.90 ± 0.45
	Best cell	725.0	40.83	78.55	23.24
8 + 3 + 1 [b]	Average	723.0 ± 0.8	40.39 ± 0.16	82.06 ± 0.28	23.96 ± 0.18
	Best cell	723.0	40.54	82.25	24.10
8 + 1 + 1 [b]	Average	721.8 ± 0.5	40.67 ± 0.03	81.45 ± 0.33	23.90 ± 0.11
	Best cell	722.0	40.68	81.83	24.02

[a]: 1 nm (*i*)a-Si:H-1 and 3 nm (*i*)a-Si:H-2 underneath (*n*)a-Si:H;
[b]: 1 nm (*i*)a-Si:H-1 and 5 nm (*i*)a-Si:H-2 underneath (*n*)-layers.

References

[1] Wikipedia.org, "Greenland ice sheet." https://en.wikipedia.org/wiki/Greenland_ ice_sheet. (Date accessed: 2023-05-28).

[2] Intergovernmental Panel on Climate Change (IPCC), "TAR Climate Change 2001: The Scientific Basis. Contribution of Working Group I to the Third Assessment Report of the Intergovernmental Panel on Climate Change," report, IPCC, Cambridge, 2001.

[3] J. Mouginot, E. Rignot, A. A. Bjørk, M. Van den Broeke, R. Millan, M. Morlighem, B. Noël, B. Scheuchl, and M. Wood, "Forty-six years of Greenland Ice Sheet mass balance from 1972 to 2018," *Proceedings of the national academy of sciences*, vol. 116, no. 19, pp. 9239–9244, 2019.

[4] National Aeronautics and Space Administration (NASA), "Vital signs of the planet-global temperature." https://climate.nasa.gov/vital-signs/global-temperature/, 2022. (Date accessed: 2022-12-01).

[5] National Aeronautics and Space Administration (NASA), "Understanding sea level." https://sealevel.nasa.gov/understanding-sea-level/global-sea-level/thermal-expansion, 2023. (Date accessed: 2023-07-07).

[6] O. Hoegh-Guldberg, D. Jacob, M. Taylor, M. Bindi, S. Brown, I. Camilloni, A. Diedhiou, R. Djalante, K. Ebi, F. Engelbrecht, J. Guiot, Y. Hijioka, S. Mehrotra, A. Payne, S. Seneviratne, A. Thomas, R. Warren, and G. Zhou, "Impacts of 1.5ºC Global Warming on Natural and Human Systems. In: Global Warming of 1.5°C," tech. rep., IPCC, 2018.

[7] United Nations, "Paris Agreement to the United Nations Framework Convention on Climate Change," tech. rep., United Nations, 2015.

[8] International Energy Agency (IEA), "Net Zero by 2050," tech. rep., IEA, 2021.

[9] Intergovernmental Panel on Climate Change (IPCC), "Climate Change 2022: Impacts, Adaptation and Vulnerability. Contribution of Working Group II Contribution to the Sixth Assessment Report of the Intergovernmental Panel on Climate Change," tech. rep., IPCC, 2022.

[10] International Energy Agency (IEA), "World Energy Outlook 2020," tech. rep., IEA, 2020.

[11] N. M. Haegel, P. Verlinden, M. Victoria, P. Altermatt, H. Atwater, T. Barnes, C. Breyer, C. Case, S. D. Wolf, C. Deline, M. Dharmrin, B. Dimmler, M. Gloeckler, J. C. Goldschmidt, B. Hallam, S. Haussener, B. Holder, U. Jaeger, A. Jaeger-Waldau, I. Kaizuka, H. Kikusato, B. Kroposki, S. Kurtz, K. Matsubara, S. Nowak, K. Ogimoto, C. Peter, I. M. Peters, S. Philipps, M. Powalla, U. Rau, T. Reindl, M. Roumpani, K. Sakurai, C. Schorn, P. Schossig, R. Schlatmann, R. Sinton, A. Slaoui, B. L. Smith, P. Schneidewind, B. Stanbery, M. Topic, W. Tumas, J. Vasi, M. Vetter, E. Weber, A. W. Weeber, A. Weidlich, D. Weiss, and A. W. Bett, "Photovoltaics at multi-terawatt scale: Waiting is not an option," *Science*, vol. 380, no. 6640, pp. 39–42, 2023.

[12] bp, "bp Statistical Review of World Energy," tech. rep., bp, 2022.

[13] Ember, "Global Electricity Review 2022," tech. rep., Ember, 2022.

[14] IEA Photovoltaic Power Systems Programme (PVPS), "Task 1 Strategic PV Analysis and Outreach: Snapshot of Global PV Markets 2023," tech. rep., IEA PVPS, 2023.

[15] International Renewable Energy Agency (IRENA), "Wind and Solar PV – what we need by 2050," tech. rep., IRENA, 2020.

[16] M. Ram, D. Bogdanov, A. Aghahosseini, A. Gulagi, A. Oyewo, M. Child, U. Caldera, K. Sadovskaia, J. Farfan, L. S. N. S. Barbosa, M. Fasihi, S. Khalili, B. Dalheimer, G. Gruber, T. Traber, F. De Caluwe, H. J. Fell, and C. Breyer, "Global energy system based on 100% renewable energy–power, heat, transport and desalination sectors," *Study by Lappeenranta University of Technology and Energy Watch Group, Lappeenranta, Berlin*, 2019.

[17] E. Becquerel, *La lumière, ses causes et ses effets*, vol. 1. Firmin Didot frères, fils et cie, 1867.

[18] A. H. Smets, K. Jager, O. Isabella, R. A. van Swaaij, and M. Zeman, *Solar energy: The physics and engineering of photovoltaic conversion technologies and systems*. UIT Cambridge Ltd. (September 1, 2016), 2016.

[19] W. Shockley and H. J. Queisser, "Detailed balance limit of efficiency of p-n junction solar cells," *Journal of applied physics*, vol. 32, no. 3, pp. 510–519, 1961.

[20] S. Rühle, "Tabulated values of the Shockley–Queisser limit for single junction solar cells," *Solar energy*, vol. 130, pp. 139–147, 2016.

[21] A. Richter, M. Hermle, and S. W. Glunz, "Reassessment of the Limiting Efficiency for Crystalline Silicon Solar Cells," *IEEE Journal of Photovoltaics*, vol. 3, no. 4, pp. 1184–1191, 2013.

[22] International Renewable Energy Agency (IRENA), "Renewable Power Generation Costs in 2021," tech. rep., IRENA, 2021.

[23] Verband Deutscher Maschinen- und Anlagenbau (VDMA), "International Technology Roadmap for Photovoltaic (13th Edition)," tech. rep., VDMA, 2022.

[24] G. Kavlak, J. McNerney, and J. E. Trancik, "Evaluating the causes of cost reduction in photovoltaic modules," *Energy policy*, vol. 123, pp. 700–710, 2018.

[25] International Energy Agency (IEA), "Renewables 2021: Analysis and forecast to 2026," tech. rep., IEA, 2021.

[26] Fraunhofer Institute for Solar Energy Systems (F-ISE), "Photovoltaics Report," tech. rep., Fraunhofer Institute for Solar Energy Systems (F-ISE), 2022.

[27] T. G. Allen, J. Bullock, X. Yang, A. Javey, and S. De Wolf, "Passivating contacts for crystalline silicon solar cells," *Nature Energy*, vol. 4, no. 11, pp. 914–928, 2019.

[28] T. Dullweber, H. Hannebauer, U. Baumann, T. Falcon, K. Bothe, S. Steckemetz, and R. Brendel, "Fine-line printed 5 busbar PERC solar cells with conversion efficiencies beyond 21%," in *29th EU PV Solar Energy Conference*, p. 621, 2014.

[29] A. Richter, R. Müller, J. Benick, F. Feldmann, B. Steinhauser, C. Reichel, A. Fell, M. Bivour, M. Hermle, and S. W. Glunz, "Design rules for high-efficiency both-sides-contacted silicon solar cells with balanced charge carrier transport and recombination losses," *Nature Energy*, vol. 6, no. 4, pp. 429–438, 2021.

[30] C. Ballif, F.-J. Haug, M. Boccard, P. J. Verlinden, and G. Hahn, "Status and perspectives of crystalline silicon photovoltaics in research and industry," *Nature Reviews Materials*, vol. 7, no. 8, pp. 597–616, 2022.

[31] A. Richter, J. Benick, F. Feldmann, A. Fell, M. Hermle, and S. W. Glunz, "n-type si solar cells with passivating electron contact: Identifying sources for efficiency limitations by wafer thickness and resistivity variation," *Solar Energy Materials and Solar Cells*, vol. 173, pp. 96–105, 2017.

[32] F. Feldmann, M. Simon, M. Bivour, C. Reichel, M. Hermle, and S. W. Glunz, "Efficient carrier-selective p- and n-contacts for Si solar cells," *Solar Energy Materials and Solar Cells*, vol. 131, pp. 100–104, 2014.

[33] S. Zhong, J. Dreon, Q. Jeangros, E. Aydin, S. De Wolf, F. Fu, M. Boccard, and C. Ballif, "Mitigating plasmonic absorption losses at rear electrodes in high-efficiency silicon solar cells using dopant-free contact stacks," *Advanced Functional Materials*, vol. 30, no. 5, p. 1907840, 2020.

[34] C. Battaglia, A. Cuevas, and S. De Wolf, "High-efficiency crystalline silicon solar cells: status and perspectives," *Energy & Environmental Science*, vol. 9, no. 5, pp. 1552–1576, 2016.

[35] K. H. Kim, C. S. Park, J. D. Lee, J. Y. Lim, J. M. Yeon, I. H. Kim, E. J. Lee, and Y. H. Cho, "Record high efficiency of screen-printed silicon aluminum back surface field solar cell: 20.29%," *Japanese Journal of Applied Physics*, vol. 56, no. 8S2, p. 08MB25, 2017.

[36] M. Hermle, F. Feldmann, M. Bivour, J. C. Goldschmidt, and S. W. Glunz, "Passivating contacts and tandem concepts: Approaches for the highest silicon-based solar cell efficiencies," *Applied Physics Reviews*, vol. 7, no. 2, p. 21305, 2020.

[37] A. W. Blakers, A. Wang, A. M. Milne, J. Zhao, and M. A. Green, "22.8% efficient silicon solar cell," *Applied Physics Letters*, vol. 55, no. 13, pp. 1363–1365, 1989.

[38] T. Dullweber and J. Schmidt, "Industrial silicon solar cells applying the passivated emitter and rear cell (PERC) concept—A review," *IEEE journal of photovoltaics*, vol. 6, no. 5, pp. 1366–1381, 2016.

[39] D. Kray, M. Hermle, and S. W. Glunz, "Theory and experiments on the back side reflectance of silicon wafer solar cells," *Progress in Photovoltaics: Research and Applications*, vol. 16, no. 1, pp. 1–15, 2008.

[40] A. Blakers, "Development of the PERC solar cell," *IEEE Journal of Photovoltaics*, vol. 9, no. 3, pp. 629–635, 2019.

[41] J. Zhao, A. Wang, and M. A. Green, "24% efficient PERL structure silicon solar cells," in *IEEE conference on photovoltaic specialists*, pp. 333–335, IEEE, 1990.

[42] J. Zhao, A. Wang, and M. A. Green, "24.5% Efficiency silicon PERT cells on MCZ substrates and 24.7% efficiency PERL cells on FZ substrates," *Progress in photovoltaics: research and applications*, vol. 7, no. 6, pp. 471–474, 1999.

[43] Verband Deutscher Maschinen- und Anlagenbau (VDMA), "International Technology Roadmap for Photovoltaic (14th Edition)," tech. rep., VDMA, 2023.

[44] M. A. Green, "The path to 25% silicon solar cell efficiency: History of silicon cell evolution," *Progress in Photovoltaics: Research and Applications*, vol. 17, pp. 183–189, may 2009.

[45] M. A. Green, E. D. Dunlop, J. Hohl-Ebinger, M. Yoshita, N. Kopidakis, K. Bothe, D. Hinken, M. Rauer, and X. Hao, "Solar cell efficiency tables (Version 60)," *Progress in Photovoltaics: Research and Applications*, vol. 30, pp. 687–701, jul 2022.

[46] Trina Solar, "210 PERC cell efficiency achieves 24.5%, Trina Solar breaks world record for the 24th time." https://www.trinasolar.com/en-glb/resources/newsroom/en210-perc-cell-efficiency-achieves-245-trina-solar-breaks-world-record-24th-time, 2022. (Date accessed: 2022-12-01).

[47] A. Richter, S. W. Glunz, F. Werner, J. Schmidt, and A. Cuevas, "Improved quantitative description of Auger recombination in crystalline silicon," *Physical Review B - Condensed Matter and Materials Physics*, vol. 86, no. 16, pp. 1–14, 2012.

[48] S. C. Baker-Finch, K. R. McIntosh, D. Yan, K. C. Fong, and T. C. Kho, "Near-infrared free carrier absorption in heavily doped silicon," *Journal of Applied Physics*, vol. 116, no. 6, p. 63106, 2014.

[49] D. Yan and A. Cuevas, "Empirical determination of the energy band gap narrowing in highly doped n+ silicon," *Journal of Applied Physics*, vol. 114, no. 4, p. 44508, 2013.

[50] D. Yan and A. Cuevas, "Empirical determination of the energy band gap narrowing in p+ silicon heavily doped with boron," *Journal of Applied Physics*, vol. 116, no. 19, p. 194505, 2014.

[51] M. Tanaka, M. Taguchi, T. Matsuyama, T. Sawada, S. Tsuda, S. Nakano, H. Hanafusa, and Y. Kuwano, "Development of new a-Si/c-Si heterojunction solar cells: ACJ-HIT (artificially constructed junction-heterojunction with intrinsic thin-layer)," *Japanese Journal of Applied Physics*, vol. 31, no. 11R, p. 3518, 1992.

[52] F. Feldmann, M. Bivour, C. Reichel, M. Hermle, and S. W. Glunz, "Passivated rear contacts for high-efficiency n-type Si solar cells providing high interface passivation quality and excellent transport characteristics," *Solar Energy Materials and Solar Cells*, vol. 120, no. PART A, pp. 270–274, 2014.

[53] U. Römer, R. Peibst, T. Ohrdes, B. Lim, J. Krügener, E. Bugiel, T. Wietler, and R. Brendel, "Recombination behavior and contact resistance of n+ and p+ poly-crystalline Si/mono-crystalline Si junctions," *Solar Energy Materials and Solar Cells*, vol. 131, no. October, pp. 85–91, 2014.

[54] H. Fujiwara, T. Kaneko, and M. Kondo, "Application of hydrogenated amorphous silicon oxide layers to c-Si heterojunction solar cells," *Applied Physics Letters*, vol. 91, no. 13, p. 133508, 2007.

[55] D. Pysch, M. Bivour, M. Hermle, and S. W. Glunz, "Amorphous silicon carbide heterojunction solar cells on p-type substrates," *Thin Solid Films*, vol. 519, no. 8, pp. 2550–2554, 2011.

[56] G. Nogay, J. Stuckelberger, P. Wyss, Q. Jeangros, C. Allebé, X. Niquille, F. Debrot, M. Despeisse, F.-J. Haug, P. Löper, and C. Ballif, "Silicon-rich silicon carbide hole-selective rear contacts for crystalline-silicon-based solar cells," *ACS applied materials & interfaces*, vol. 8, no. 51, pp. 35660–35667, 2016.

[57] G. Nogay, *Full-area passivating contacts with high and low thermal budgets: Solutions for high efficiency c-Si solar cells.* PhD thesis, École polytechnique fédérale de Lausanne, 2018.

[58] A. Ingenito, G. Nogay, Q. Jeangros, E. Rucavado, C. Allebé, S. Eswara, N. Valle, T. Wirtz, J. Horzel, T. Koida, M. Morales-Masis, M. Despeisse, F.-J. Haug, P. Löper, and C. Ballif, "A passivating contact for silicon solar cells formed during a single firing thermal annealing," *Nature Energy*, vol. 3, no. 9, pp. 800–808, 2018.

[59] M. Boccard and Z. C. Holman, "Amorphous silicon carbide passivating layers for crystalline-silicon-based heterojunction solar cells," *Journal of Applied Physics*, vol. 118, no. 6, p. 65704, 2015.

[60] M. W. M. van Cleef, F. A. Rubinelli, R. Rizzoli, R. Pinghini, R. E. I. Schropp, and W. F. van der Weg, "Amorphous silicon carbide/crystalline silicon heterojunction solar cells: a comprehensive study of the photocarrier collection," *Japanese journal of applied physics*, vol. 37, no. 7R, p. 3926, 1998.

[61] J. Stuckelberger, G. Nogay, P. Wyss, Q. Jeangros, C. Allebé, F. Debrot, X. Niquille, M. Ledinsky, A. Fejfar, M. Despeisse, F.-J. Haug, P. Löper, and C. Ballif, "Passivating electron contact based on highly crystalline nanostructured silicon oxide layers for silicon solar cells," *Solar Energy Materials and Solar Cells*, vol. 158, pp. 2–10, 2016.

[62] G. Yang, P. Guo, P. Procel, A. Weeber, O. Isabella, and M. Zeman, "Poly-crystalline silicon-oxide films as carrier-selective passivating contacts for c-si solar cells," *Applied Physics Letters*, vol. 112, no. 19, p. 193904, 2018.

[63] I. Mack, J. Stuckelberger, P. Wyss, G. Nogay, Q. Jeangros, J. Horzel, C. Allebé, M. Despeisse, F.-J. Haug, A. Ingenito, P. Löper, and C. Ballif, "Properties of mixed phase silicon-oxide-based passivating contacts for silicon solar cells," *Solar Energy Materials and Solar Cells*, vol. 181, pp. 9–14, 2018.

[64] G. Yang, C. Han, P. Procel, Y. Zhao, M. Singh, L. Mazzarella, M. Zeman, and O. Isabella, "Oxygen-alloyed poly-Si passivating contacts for high-thermal budget c-Si heterojunction solar cells," *Progress in Photovoltaics: research and applications*, vol. 30, no. 2, 2022.

[65] M. Singh, R. Santbergen, L. Mazzarella, A. Madrampazakis, G. Yang, R. Vismara, Z. Remes, A. Weeber, M. Zeman, and O. Isabella, "Optical characterization of poly-SiOx and poly-SiCx carrier-selective passivating contacts," *Solar Energy Materials and Solar Cells*, vol. 210, p. 110507, 2020.

[66] A. Ingenito, G. Nogay, J. Stuckelberger, P. Wyss, L. Gnocchi, C. Allebé, J. Horzel, M. Despeisse, F.-J. Haug, P. Löper, and C. Ballif, "Phosphorous-doped silicon carbide as front-side full-area passivating contact for double-side contacted c-Si solar cells," *IEEE Journal of Photovoltaics*, vol. 9, no. 2, pp. 346–354, 2018.

[67] H. Lin, M. Yang, X. Ru, G. Wang, S. Yin, F. Peng, C. Hong, M. Qu, J. Lu, L. Fang, C. Han, P. Procel, O. Isabella, P. Gao, Z. Li, and X. Xu, "Silicon heterojunction solar cells with up to 26.81% efficiency achieved by electrically optimized nanocrystalline-silicon hole contact layers," *Nature Energy*, 2023.

[68] K. Yoshikawa, H. Kawasaki, W. Yoshida, T. Irie, K. Konishi, K. Nakano, T. Uto, D. Adachi, M. Kanematsu, H. Uzu, and K. Yamamoto, "Silicon heterojunction solar cell with interdigitated back contacts for a photoconversion efficiency over 26%," *Nature Energy*, vol. 2, no. 5, p. 17032, 2017.

[69] JinkoSolar, "JinkoSolar's High-efficiency N-Type Monocrystalline Silicon Solar Cell Sets Our New Record with Maximum Conversion Efficiency of 26.4%." https://www.jinkosolar.com/en/site/newsdetail/1827, 2022. (Date accessed: 2023-05-23).

[70] F. Haase, C. Hollemann, S. Schäfer, A. Merkle, M. Rienäcker, J. Krügener, R. Brendel, and R. Peibst, "Laser contact openings for local poly-Si-metal contacts enabling 26.1%-efficient POLO-IBC solar cells," *Solar Energy Materials and Solar Cells*, vol. 186, pp. 184–193, 2018.

[71] Akcome, "Industrialized technology of high-efficiency hjt product and its challenges," in *5th International workshop on Silicon Heterojunction solar cells*, (Aix-les-bains, France), 2022.

[72] Canadian Solar, "Canadian Solar To Start Mass Production Of Topcon Modules With Power Output Up To 690w." http://investors.canadiansolar.com/news-releases/news-release-details/canadian-solar-start-mass-production-topcon-modules-power-output#: :text=Canadian Solar's TOPCon modules are,mainstream products in the market., 2022. (Date accessed: 2023-02-01).

[73] C. Battaglia, X. Yin, M. Zheng, I. D. Sharp, T. Chen, S. McDonnell, A. Azcatl, C. Carraro, B. Ma, R. Maboudian, R. M. Wallace, and A. Javey, "Hole selective MoOx contact for silicon solar cells," *Nano letters*, vol. 14, no. 2, pp. 967–971, 2014.

[74] J. Bullock, A. Cuevas, T. Allen, and C. Battaglia, "Molybdenum oxide MoOx: A versatile hole contact for silicon solar cells," *Applied Physics Letters*, vol. 105, no. 23, p. 232109, 2014.

[75] J. Geissbühler, J. Werner, S. Martin de Nicolas, L. Barraud, A. Hessler-Wyser, M. Despeisse, S. Nicolay, A. Tomasi, B. Niesen, S. De Wolf, and C. Ballif, "22.5% efficient silicon heterojunction solar cell with molybdenum oxide hole collector," *Applied Physics Letters*, vol. 107, no. 8, p. 81601, 2015.

[76] J. Dréon, Q. Jeangros, J. Cattin, J. Haschke, L. Antognini, C. Ballif, and M. Boccard, "23.5%-efficient silicon heterojunction silicon solar cell using molybdenum oxide as hole-selective contact," *Nano Energy*, vol. 70, p. 104495, 2020.

[77] M. Bivour, J. Temmler, H. Steinkemper, and M. Hermle, "Molybdenum and tungsten oxide: High work function wide band gap contact materials for hole selective contacts of silicon solar cells," *Solar Energy Materials and Solar Cells*, vol. 142, pp. 34–41, 2015.

[78] M. Mews, L. Korte, and B. Rech, "Oxygen vacancies in tungsten oxide and their influence on tungsten oxide/silicon heterojunction solar cells," *Solar Energy Materials and Solar Cells*, vol. 158, pp. 77–83, 2016.

[79] X. Yang, H. Xu, W. Liu, Q. Bi, L. Xu, J. Kang, M. N. Hedhili, B. Sun, X. Zhang, and S. De Wolf, "Atomic layer deposition of vanadium oxide as hole-selective contact for crystalline silicon solar cells," *Advanced Electronic Materials*, vol. 6, no. 8, p. 2000467, 2020.

[80] J. Bullock, M. Hettick, J. Geissbühler, A. J. Ong, T. Allen, C. M. Sutter-Fella, T. Chen, H. Ota, E. W. Schaler, S. De Wolf, C. Ballif, A. Cuevas, and A. Javey, "Efficient silicon solar cells with dopant-free asymmetric heterocontacts," *Nature Energy*, vol. 1, no. 3, pp. 1–7, 2016.

[81] G. Chistiakova, B. Macco, and L. Korte, "Low-temperature atomic layer deposited magnesium oxide as a passivating electron contact for c-Si-based solar cells," *IEEE Journal of Photovoltaics*, vol. 10, no. 2, pp. 398–406, 2020.

[82] Y. Wan, C. Samundsett, J. Bullock, T. Allen, M. Hettick, D. Yan, P. Zheng, X. Zhang, J. Cui, J. McKeon, A. Javey, and A. Cuevas, "Magnesium fluoride electron-selective contacts for crystalline silicon solar cells," *ACS applied materials & interfaces*, vol. 8, no. 23, pp. 14671–14677, 2016.

[83] S. Avasthi, W. E. McClain, G. Man, A. Kahn, J. Schwartz, and J. C. Sturm, "Hole-blocking titanium-oxide/silicon heterojunction and its application to photovoltaics," *Applied Physics Letters*, vol. 102, no. 20, p. 203901, 2013.

[84] X. Yang, P. Zheng, Q. Bi, and K. Weber, "Silicon heterojunction solar cells with electron selective TiOx contact," *Solar Energy Materials and Solar Cells*, vol. 150, pp. 32–38, 2016.

[85] W. Wang, L. Cai, L. Meng, N. Chen, H. Wei, Y. Hong, Y. Chen, L. Zeng, and Z. Liang, "Highly Stable Strontium Fluoride as a Thickness Tolerant Electron-Selective Contact for Dopant-Free Silicon Solar Cells," *Authorea*, 2023.

[86] L. Cao, P. Procel, A. Alcañiz, J. Yan, F. Tichelaar, E. Özkol, Y. Zhao, C. Han, G. Yang, Z. Yao, M. Zeman, R. Santbergen, L. Mazzarella, and O. Isabella, "Achieving 23.83% conversion efficiency in silicon heterojunction solar cell with ultra-thin MoOx hole collector layer via tailoring (i)a-Si: H/MoOx interface," *Progress in Photovoltaics: research and applications*, 2022.

[87] L. Mazzarella, A. Alcañiz, P. Procel, E. Kawa, Y. Zhao, U. Tiringer, C. Han, G. Yang, P. Taheri, M. Zeman, and O. Isabella, "Strategy to mitigate the dipole interfacial states in (i) a-si: H/moox passivating contacts solar cells," *Progress in Photovoltaics: research and applications*, vol. 29, no. 3, pp. 391–400, 2021.

[88] J. Bullock, Y. Wan, Z. Xu, S. Essig, M. Hettick, H. Wang, W. Ji, M. Boccard, A. Cuevas, and C. Ballif, "Stable dopant-free asymmetric heterocontact silicon solar cells with efficiencies above 20%," *ACS Energy Letters*, vol. 3, no. 3, pp. 508–513, 2018.

[89] J. Cho, N. Nawal, A. Hadipour, M. R. Payo, A. van der Heide, H. S. Radhakrishnan, M. Debucquoy, I. Gordon, J. Szlufcik, and J. Poortmans, "Interface analysis and intrinsic thermal stability of MoOx based hole-selective contacts for silicon heterojunction solar cells," *Solar Energy Materials and Solar Cells*, vol. 201, p. 110074, 2019.

[90] J. Cho, H. S. Radhakrishnan, R. Sharma, M. R. Payo, M. Debucquoy, A. van der Heide, I. Gordon, J. Szlufcik, and J. Poortmans, "Thermal stability improvement of metal oxide-based contacts for silicon heterojunction solar cells," *Solar Energy Materials and Solar Cells*, vol. 206, p. 110324, 2020.

[91] M. Bonnet-Eymard, M. Boccard, G. Bugnon, F. Sculati-Meillaud, M. Despeisse, and C. Ballif, "Optimized short-circuit current mismatch in multi-junction solar cells," *Solar energy materials and solar cells*, vol. 117, pp. 120–125, 2013.

[92] E. Köhnen, M. Jošt, A. B. Morales-Vilches, P. Tockhorn, A. Al-Ashouri, B. Macco, L. Kegelmann, L. Korte, B. Rech, R. Schlatmann, B. Stannowski, and S. Albrecht, "Highly efficient monolithic perovskite silicon tandem solar cells: analyzing the influence of current mismatch on device performance," *Sustainable Energy & Fuels*, vol. 3, no. 8, pp. 1995–2005, 2019.

[93] M. Jošt, E. Köhnen, A. B. Morales-Vilches, B. Lipovšek, K. Jäger, B. Macco, A. Al-Ashouri, J. Krč, L. Korte, B. Rech, R. Schlatmann, M. Topič, B. Stannowski, and S. Albrecht, "Textured interfaces in monolithic perovskite/silicon tandem solar cells: advanced light management

for improved efficiency and energy yield," *Energy & Environmental Science*, vol. 11, no. 12, pp. 3511–3523, 2018.

[94] J. Lehr, M. Langenhorst, R. Schmager, F. Gota, S. Kirner, U. Lemmer, B. S. Richards, C. Case, and U. W. Paetzold, "Energy yield of bifacial textured perovskite/silicon tandem photovoltaic modules," *Solar Energy Materials and Solar Cells*, vol. 208, p. 110367, 2020.

[95] M. T. Hörantner and H. J. Snaith, "Predicting and optimising the energy yield of perovskite-on-silicon tandem solar cells under real world conditions," *Energy and Environmental Science*, vol. 10, no. 9, pp. 1983–1993, 2017.

[96] M. H. Futscher and B. Ehrler, "Efficiency limit of perovskite/Si tandem solar cells," *ACS Energy Letters*, vol. 1, no. 4, pp. 863–868, 2016.

[97] G. Coletti, S. L. Luxembourg, L. J. Geerligs, V. Rosca, A. R. Burgers, Y. Wu, L. Okel, M. Kloos, F. J. K. Danzl, M. Najafi, D. Zhang, I. Dogan, V. Zardetto, F. Di Giacomo, J. Kroon, T. Aernouts, J. Hüpkes, C. H. Burgess, M. Creatore, R. Andriessen, and S. Veenstra, "Bifacial four-terminal perovskite/silicon tandem solar cells and modules," *ACS Energy Letters*, vol. 5, no. 5, pp. 1676–1680, 2020.

[98] L. Xu, F. Xu, J. Liu, X. Zhang, A. S. Subbiah, and S. De Wolf, "Bandgap optimization for bifacial tandem solar cells," *ACS Energy Letters*, vol. 0, no. 0, pp. 3114–3121, 0.

[99] R. Santbergen, H. Uzu, K. Yamamoto, and M. Zeman, "Optimization of Three-Terminal Perovskite/Silicon Tandem Solar Cells," *IEEE Journal of Photovoltaics*, vol. 9, no. 2, pp. 446–451, 2019.

[100] E. L. Warren, M. G. Deceglie, M. Rienäcker, R. Peibst, A. C. Tamboli, and P. Stradins, "Maximizing tandem solar cell power extraction using a three-terminal design," *Sustainable Energy & Fuels*, vol. 2, no. 6, pp. 1141–1147, 2018.

[101] E. L. Warren, W. E. McMahon, M. Rienacker, K. T. VanSant, R. C. Whitehead, R. Peibst, and A. C. Tamboli, "A taxonomy for three-terminal tandem solar cells," *ACS Energy Letters*, vol. 5, no. 4, pp. 1233–1242, 2020.

[102] P. Tockhorn, P. Wagner, L. Kegelmann, J.-C. Stang, M. Mews, S. Albrecht, and L. Korte, "Three-terminal perovskite/silicon tandem solar cells with top and interdigitated rear contacts," *ACS Applied Energy Materials*, vol. 3, no. 2, pp. 1381–1392, 2020.

[103] P. Wagner, P. Tockhorn, S. Hall, S. Albrecht, and L. Korte, "Performance of Monolithic Two- and Three-Terminal Perovskite/Silicon Tandem Solar Cells Under Varying Illumination Conditions," *Solar RRL*, vol. 7, p. 2200954, mar 2023.

[104] F. Gota, M. Langenhorst, R. Schmager, J. Lehr, and U. W. Paetzold, "Energy yield advantages of three-terminal perovskite-silicon tandem photovoltaics," *Joule*, vol. 4, no. 11, pp. 2387–2403, 2020.

[105] H. Schulte-Huxel, E. L. Warren, M. Schnabel, P. Stradins, D. Friedman, and A. C. Tamboli, "Iii-v/si tandem cell to module interconnection-comparison between different operation modes," in *2017 IEEE 44th Photovoltaic Specialist Conference (PVSC)*, pp. 2543–2547, IEEE, 2017.

[106] K. T. VanSant, A. C. Tamboli, and E. L. Warren, "Iii-v-on-si tandem solar cells," *Joule*, vol. 5, no. 3, pp. 514–518, 2021.

[107] R. France and C. Ballif, "Tandem solar cells," in *PV Academy, the 8th World Conference on Photovoltaic Energy Conversion(WCPEC-8)*, (Milan, Italy), 2022.

[108] Z. J. Yu, M. Leilaeioun, and Z. Holman, "Selecting tandem partners for silicon solar cells," *Nature Energy*, vol. 1, no. 11, p. 16137, 2016.

[109] National Renewable Energy Laboratory (NREL), "Best research-cell efficiency chart." https://www.nrel.gov/pv/interactive-cell-efficiency.html, 2023. (Date accessed: 2023-06-01).

[110] L.-L. Senaud, B. Kamino, J. Geissbühler, G. Christmann, G. Nogay, J. Zhao, F. Sahli, P. Wyss, D. L. Bätzner, D. Lachenal, Q. Jeangros, C. Ballif, and B. Paviet-Salomon, "High efficiency 3-terminal perovskite/silicon tandems based on tunnel junction ibc," in *the 8th World Conference on Photovoltaic Energy Conversion(WCPEC-8)*, (Milan, Italy), 2022.

[111] K. Yamamoto, H. Uzu, and D. Adachi, "High efficiency perovskite/hetero-junction crystalline silicon tandem solar cells," in *the 33rd International Photovoltaic Science and Engineering Conference(PVSEC-33)*, (Nagoya, Japan), 2022.

[112] K. Yamamoto, R. Mishima, H. Uzu, and D. Adachi, "High efficiency perovskite/heterojunction crystalline silicon tandem solar cells: towards industrial-sized cell and module," *Japanese Journal of Applied Physics*, vol. 62, no. SK, p. SK1021, 2023.

[113] B. Yan, Q. Hou, and J. Yao, "1245 mm*635 mm perovskite module passing full sequence of iec61215 and iec61730 and other characteristics in field operation," in *2023 40th European PV Solar Energy Conference and Exhibition (EUPVSEC)*, Lisbon, Portugal, 2023.

[114] Oxford PV, "Tandem cell production." https://www.oxfordpv.com/tandem-cell-production. (Date accessed: 2023-07-7).

[115] J. Werner, B. Niesen, and C. Ballif, "Perovskite/Silicon Tandem Solar Cells: Marriage of Convenience or True Love Story? – An Overview," *Advanced Materials Interfaces*, vol. 5, no. 1, pp. 1–19, 2018.

[116] F. Fu, J. Li, T. C. Yang, H. Liang, A. Faes, Q. Jeangros, C. Ballif, and Y. Hou, "Monolithic Perovskite-Silicon Tandem Solar Cells: From the Lab to Fab?," *Advanced Materials*, vol. 34, no. 24, p. 2106540, 2022.

[117] P. Tockhorn, J. Sutter, A. Cruz, P. Wagner, K. Jäger, D. Yoo, F. Lang, M. Grischek, B. Li, J. Li, O. Shargaieva, E. Unger, A. Al-Ashouri, E. Köhnen, M. Stolterfoht, D. Neher, R. Schlatmann, B. Rech, B. Stannowski, S. Albrecht, and C. Becker, "Nano-optical designs for high-efficiency monolithic perovskite–silicon tandem solar cells," *Nature Nanotechnology*, pp. 1–8, 2022.

[118] E. Raza and Z. Ahmad, "Review on two-terminal and four-terminal crystalline-silicon/perovskite tandem solar cells; progress, challenges, and future perspectives," *Energy Reports*, vol. 8, pp. 5820–5851, 2022.

[119] P. A. Basore, "Paths to future growth in photovoltaics manufacturing," *Progress in Photovoltaics: Research and Applications*, vol. 24, no. 7, pp. 1024–1031, 2016.

[120] D. B. Needleman, J. R. Poindexter, R. C. Kurchin, I. M. Peters, G. Wilson, and T. Buonassisi, "Economically sustainable scaling of photovoltaics to meet climate targets," *Energy & Environmental Science*, vol. 9, no. 6, pp. 2122–2129, 2016.

[121] S&P Global, "S&P Global Commodity Insights - PV Module Supply Chian Tracker 2022," 2022.

[122] PV Magazine, "World has installed 1tw of solar capacity." https://www.pv-magazine.com/2022/03/15/humans-have-installed-1-terawatt-of-solar-capacity/, 2022. (Date accessed: 2022-12-01).

[123] P. J. Verlinden, "Future challenges for photovoltaic manufacturing at the terawatt level," *Journal of Renewable and Sustainable Energy*, vol. 12, no. 5, p. 53505, 2020.

[124] T. Mishima, M. Taguchi, H. Sakata, and E. Maruyama, "Development status of high-efficiency HIT solar cells," *Solar Energy Materials and Solar Cells*, vol. 95, no. 1, pp. 18–21, 2011.

[125] S. De Wolf, A. Descoeudres, Z. C. Holman, and C. Ballif, "High-efficiency Silicon Heterojunction Solar Cells: A Review," *Green*, vol. 2, no. 1, 2012.

[126] A. H. T. Le, R. Basnet, D. Yan, W. Chen, J. P. Seif, and Z. Hameiri, "Temperature dependence of polysilicon passivating contact and its device performance," in *2020 47th IEEE Photovoltaic Specialists Conference (PVSC)*, pp. 1020–1023, IEEE, 2020.

[127] C. Han, G. Yang, P. Procel, D. O'Connor, Y. Zhao, A. Gopalakrishnan, X. Zhang, M. Zeman, L. Mazzarella, and O. Isabella, "Controllable simultaneous bifacial Cu-plating for high efficiency crystalline silicon solar cells," *Solar RRL*, vol. 6, no. 6, p. 2100810, 2022.

[128] J. Haschke, O. Dupré, M. Boccard, and C. Ballif, "Silicon heterojunction solar cells : Recent technological development and practical aspects - from lab to industry," *Solar Energy Materials and Solar Cells*, vol. 187, pp. 140–153, 2018.

[129] D. Adachi, J. L. Hernández, and K. Yamamoto, "Impact of carrier recombination on fill factor for large area heterojunction crystalline silicon solar cell with 25.1% efficiency," *Applied Physics Letters*, vol. 107, p. 233506, dec 2015.

[130] PV Magazine, "Huasun achieves 25.26% efficiency for heterojunction solar cell." https://www.pv-magazine.com/2021/07/13/huasun-achieves-25-26-efficiency-for-heterojunction-solar-cell/, 2021. (Date accessed: 2023-03-31).

[131] M. Yang, X. Ru, S. Yin, C. Hong, F. Peng, M. Qu, J. Lu, L. Fang, and X. Xu, "Over 26% efficiency shj solar cell using nanocrystalline silicon oxide window layer," in *the 8th World Conference on Photovoltaic Energy Conversion (WCPEC-8)*, (Milan, Italy), 2022.

[132] X. Ru, M. Qu, J. Wang, T. Ruan, M. Yang, F. Peng, W. Long, K. Zheng, H. Yan, and X. Xu, "25.11% efficiency silicon heterojunction solar cell with low deposition rate intrinsic amorphous silicon buffer layers," *Solar Energy Materials and Solar Cells*, vol. 215, p. 110643, 2020.

[133] T. Sawada, N. Terada, S. Tsuge, T. Baba, T. Takahama, K. Wakisaka, S. Tsuda, and S. Nakano, "High-efficiency of a-Si/c-Si Heterojunction Solar Cell," *WCPEC-1*, vol. 2, pp. 1219–1226, 1994.

[134] M. Taguchi, K. Kawamoto, S. Tsuge, T. Baba, H. Sakata, M. Morizane, K. Uchihashi, N. Nakamura, S. Kiyama, and O. Oota, "HITTM cells—high-efficiency crystalline Si cells with novel structure," *Progress in Photovoltaics: Research and Applications*, vol. 8, no. 5, pp. 503–513, 2000.

[135] H. Sakala, T. Nakai, T. Babe, M. Tajuchi, S. Tsuge, K. Uchihashi, and S. Klyama, "20.7% Highest Efficiency Large Area (100.5 cm2) HITTM Cell," in *28th IEEE PVSC*, pp. 7–12, 2000.

[136] M. Taguchi, A. Terakawa, E. Maruyama, and M. Tanaka, "Obtaining a higher Voc in HIT cells," *Progress in Photovoltaics: Research and Applications*, vol. 13, no. 6, pp. 481–488, 2005.

[137] T. Kinoshita, D. Fujishima, A. Yano, A. Ogane, S. Tohoda, K. Matsuyama, Y. Nakamura, N. Tokuoka, H. Kanno, H. Sakata, M. Taguchi, and E. Maruyama, "The Approaches for High Efficiency HITTM Solar Cell with Very Thin (<100 μm) Silicon Wafer over 23%," in *26th European Photovoltaic Solar Energy Conference and Exhibition*, pp. 871 – 874, 2011.

[138] M. Taguchi, A. Yano, S. Tohoda, K. Matsuyama, Y. Nakamura, T. Nishiwaki, K. Fujita, and E. Maruyama, "24.7% Record efficiency HIT solar cell on thin silicon wafer," *IEEE Journal of Photovoltaics*, vol. 4, no. 1, pp. 96–99, 2014.

[139] K. Masuko, M. Shigematsu, T. Hashiguchi, D. Fujishima, M. Kai, N. Yoshimura, T. Yamaguchi, Y. Ichihashi, T. Mishima, N. Matsubara, T. Yamanishi, T. Takahama, M. Taguchi, E. Maruyama, and S. Okamoto, "Achievement of More Than 25% Conversion Efficiency With Crystalline Silicon Heterojunction Solar Cell," *IEEE Journal of Photovoltaics*, vol. 4, no. 6, pp. 1433–1435, 2014.

[140] Y. Tsunomura, Y. Yoshimine, M. Taguchi, T. Baba, T. Kinoshita, H. Kanno, H. Sakata, E. Maruyama, and M. Tanaka, "Twenty-two percent efficiency HIT solar cell," *Solar Energy Materials and Solar Cells*, vol. 93, no. 6-7, pp. 670–673, 2009.

[141] W. van Sark, L. Korte, and F. Roca, *Physics and technology of amorphous-crystalline heterostructure silicon solar cells*. Springer, 2012.

[142] C. Ballif, S. De Wolf, A. Descoeudres, and Z. C. Holman, "Amorphous silicon/crystalline silicon heterojunction solar cells," in *Semiconductors and Semimetals*, vol. 90, pp. 73–120, Elsevier, 2014.

[143] S. Noguchi, H. Iwata, and K. Sano, "Photovoltaic device, US5213628A," 1993.

[144] S. K. Chunduri and M. Schmela, "Heterojunction Solar Technology 2023 - Working Hard on Cost Reduction," tech. rep., TaiyangNews, 2023.

[145] R. V. K. Chavali, S. De Wolf, and M. A. Alam, "Device physics underlying silicon heterojunction and passivating-contact solar cells: A topical review," *Progress in Photovoltaics: Research and Applications*, vol. 26, no. 4, pp. 241–260, 2018.

[146] Z. Sun, X. Chen, Y. He, J. Li, J. Wang, H. Yan, and Y. Zhang, "Toward Efficiency Limits of Crystalline Silicon Solar Cells: Recent Progress in High-Efficiency Silicon Heterojunction Solar Cells," *Advanced Energy Materials*, vol. 12, no. 23, p. 2200015, 2022.

[147] Y. Liu, Y. Li, Y. Wu, G. Yang, L. Mazzarella, P. Procel-Moya, A. C. Tamboli, K. Weber, M. Boccard, O. Isabella, X. Yang, and B. Sun, "High-efficiency silicon heterojunction solar cells: materials, devices and applications," *Materials Science and Engineering: R: Reports*, vol. 142, p. 100579, 2020.

[148] A. Razzaq, T. G. Allen, W. Liu, Z. Liu, and S. De Wolf, "Silicon heterojunction solar cells: Techno-economic assessment and opportunities," *Joule*, vol. 6, no. 3, pp. 514–542, 2022.

[149] Y. Zhang, M. Kim, L. Wang, P. Verlinden, and B. Hallam, "Design considerations for multi-terawatt scale manufacturing of existing and future photovoltaic technologies: challenges and opportunities related to silver, indium and bismuth consumption," *Energy & Environmental Science*, vol. 14, no. 11, pp. 5587–5610, 2021.

[150] P. Procel, G. Yang, O. Isabella, and M. Zeman, "Theoretical evaluation of contact stack for high efficiency IBC-SHJ solar cells," *Solar Energy Materials and Solar Cells*, vol. 186, pp. 66–77, 2018.

[151] P. Procel, H. Xu, A. Saez, C. Ruiz-Tobon, L. Mazzarella, Y. Zhao, C. Han, G. Yang, M. Zeman, and O. Isabella, "The role of heterointerfaces and subgap energy states on transport mechanisms in silicon heterojunction solar cells," *Progress in Photovoltaics: research and applications*, vol. 28, no. 9, pp. 935–945, 2020.

[152] W. E. Spear and P. G. Le Comber, "Substitutional doping of amorphous silicon," *Solid state communications*, vol. 17, no. 9, pp. 1193–1196, 1975.

[153] W. Rehm, R. Fischer, J. Stuke, and H. Wagner, "Photo and dark conductivity of doped amorphous silicon," *physica status solidi (b)*, vol. 79, pp. 539–547, feb 1977.

[154] S. G. Greenbaum, W. E. Carlos, and P. C. Taylor, "Local bonding arrangements of boron in doped hydrogenated amorphous silicon," *Journal of applied physics*, vol. 56, no. 6, pp. 1874–1877, 1984.

[155] S. De Wolf and M. Kondo, "Boron-doped a-Si:H/c-Si interface passivation: Degradation mechanism," *Applied Physics Letters*, vol. 91, p. 112109, sep 2007.

[156] Z. Holman, A. Descoeudres, L. Barraud, F. Fernandez, J. Seif, S. De Wolf, and C. Ballif, "Current Losses at the Front of Silicon Heterojunction Solar Cells," *IEEE Journal of Photovoltaics*, vol. 2, no. 1, pp. 7–15, 2012.

[157] H. Fujiwara and M. Kondo, "Effects of a-Si: H layer thicknesses on the performance of a-Si: H/c-Si heterojunction solar cells," *Journal of Applied Physics*, vol. 101, no. 5, p. 54516, 2007.

[158] A. Janotta, R. Janssen, M. Schmidt, T. Graf, M. Stutzmann, L. Görgens, A. Bergmaier, G. Dollinger, C. Hammerl, S. Schreiber, and B. Stritzker, "Doping and its efficiency in a-SiO x: H," *Physical Review B*, vol. 69, no. 11, p. 115206, 2004.

[159] D. Zhang, D. Deligiannis, G. Papakonstantinou, R. A. van Swaaij, and M. Zeman, "Optical enhancement of silicon heterojunction solar cells with hydrogenated amorphous silicon carbide emitter," *IEEE Journal of Photovoltaics*, vol. 4, no. 6, pp. 1326–1330, 2014.

[160] L. Mazzarella, S. Kirner, B. Stannowski, L. Korte, B. Rech, and R. Schlatmann, "p-type microcrystalline silicon oxide emitter for silicon heterojunction solar cells allowing current densities above 40 mA/cm2," *Applied Physics Letters*, vol. 106, p. 23902, jan 2015.

[161] L. Mazzarella, A. B. Morales-Vilches, L. Korte, R. Schlatmann, and B. Stannowski, "Versatility of nanocrystalline silicon films: From thin-film to perovskite/c-Si tandem solar cell applications," *Coatings*, vol. 10, no. 8, p. 759, 2020.

[162] Y. Xu, Z. Hu, H. Diao, Y. Cai, S. Zhang, X. Zeng, H. Hao, X. Liao, E. Fortunato, and R. Martins, "Heterojunction solar cells with n-type nanocrystalline silicon emitters on p-type c-Si wafers," *Journal of Non-Crystalline Solids*, vol. 352, no. 9, pp. 1972–1975, 2006.

[163] J. P. Seif, A. Descoeudres, G. Nogay, S. Hanni, S. M. De Nicolas, N. Holm, J. Geissbuhler, A. Hessler-Wyser, M. Duchamp, R. E. Dunin-Borkowski, M. Ledinsky, S. De Wolf, and C. Ballif, "Strategies for Doped Nanocrystalline Silicon Integration in Silicon Heterojunction Solar Cells," *IEEE Journal of Photovoltaics*, vol. 6, no. 5, pp. 1132–1140, 2016.

[164] G. Nogay, J. Seif, Y. Riesen, A. Tomasi, Q. Jeangros, N. Wyrsch, F.-J. Haug, S. De Wolf, and C. Ballif, "Nanocrystalline Silicon Carrier Collectors for Silicon Heterojunction Solar Cells and Impact on Low-Temperature Device Characteristics," *IEEE Journal of Photovoltaics*, vol. 6, no. 6, pp. 1654–1662, 2016.

[165] L. V. Mercaldo, E. Bobeico, I. Usatii, M. Della Noce, L. Lancellotti, L. Serenelli, M. Izzi, M. Tucci, and P. D. Veneri, "Potentials of mixed-phase doped layers in p-type Si heterojunction solar cells with ZnO: Al," *Solar Energy Materials and Solar Cells*, vol. 169, pp. 113–121, 2017.

[166] L. Antognini, V. Paratte, J. Haschke, J. Cattin, J. Dréon, M. Lehmann, L.-L. Senaud, Q. Jeangros, C. Ballif, and M. Boccard, "Influence of the Dopant Gas Precursor in P-Type Nanocrystalline Silicon Layers on the Performance of Front Junction Heterojunction Solar Cells," *IEEE Journal of Photovoltaics*, vol. 11, no. 4, pp. 944–956, 2021.

[167] Y. Zhao, L. Mazzarella, P. Procel, C. Han, F. D. Tichelaar, G. Yang, A. Weeber, M. Zeman, and O. Isabella, "Ultra-thin electron collectors based on nc-Si: H for high-efficiency silicon heterojunction solar cells," *Progress in Photovoltaics: research and applications*, vol. 30, no. 8, pp. 809–822, 2022.

[168] P. Cuony, M. Marending, D. T. L. Alexander, M. Boccard, G. Bugnon, M. Despeisse, and C. Ballif, "Mixed-phase p-type silicon oxide containing silicon nanocrystals and its role in thin-film silicon solar cells," *Applied Physics Letters*, vol. 97, p. 213502, nov 2010.

[169] A. Lambertz, V. Smirnov, T. Merdzhanova, K. Ding, S. Haas, G. Jost, R. E. I. Schropp, F. Finger, and U. Rau, "Microcrystalline silicon–oxygen alloys for application in silicon solar cells and modules," *Solar Energy Materials and Solar Cells*, vol. 119, pp. 134–143, 2013.

[170] O. Gabriel, S. Kirner, M. Klingsporn, F. Friedrich, B. Stannowski, and R. Schlatmann, "On the plasma chemistry during plasma enhanced chemical vapor deposition of microcrystalline silicon oxides," *Plasma Processes and Polymers*, vol. 12, no. 1, pp. 82–91, 2015.

[171] S. Kirner, S. Neubert, C. Schultz, O. Gabriel, B. Stannowski, B. Rech, and R. Schlatmann, "Quadruple-junction solar cells and modules based on amorphous and microcrystalline silicon with high stable efficiencies," *Japanese Journal of Applied Physics*, vol. 54, no. 8S1, p. 08KB03, 2015.

[172] A. Richter, L. Zhao, F. Finger, and K. Ding, "Nano-composite microstructure model for the classification of hydrogenated nanocrystalline silicon oxide thin films," *Surface and Coatings Technology*, vol. 295, pp. 119–124, 2016.

[173] L. Mazzarella, A. B. Morales-Vilches, M. Hendrichs, S. Kirner, L. Korte, R. Schlatmann, and B. Stannowski, "Nanocrystalline n-Type Silicon Oxide Front Contacts for Silicon Heterojunction Solar Cells: Photocurrent Enhancement on Planar and Textured Substrates," *IEEE Journal of Photovoltaics*, vol. 8, no. 1, pp. 70–78, 2017.

[174] A. Richter, V. Smirnov, A. Lambertz, K. Nomoto, K. Welter, and K. Ding, "Versatility of doped nanocrystalline silicon oxide for applications in silicon thin-film and heterojunction solar cells," *Solar Energy Materials and Solar Cells*, vol. 174, pp. 196–201, 2018.

[175] Y. Zhao, L. Mazzarella, P. Procel, C. Han, G. Yang, A. Weeber, M. Zeman, and O. Isabella, "Doped hydrogenated nanocrystalline silicon oxide layers for high-efficiency c-Si heterojunction solar cells," *Progress in Photovoltaics: Research and Applications*, vol. 28, no. 5, pp. 425–435, 2020.

[176] P. Roca i Cabarrocas, N. Layadi, T. Heitz, B. Drévillon, and I. Solomon, "Substrate selectivity in the formation of microcrystalline silicon: Mechanisms and technological consequences," *Applied Physics Letters*, vol. 66, pp. 3609–3611, jun 1995.

[177] M. Tzolov, F. Finger, R. Carius, and P. Hapke, "Optical and transport studies on thin microcrystalline silicon films prepared by very high frequency glow discharge for solar cell applications," *Journal of Applied Physics*, vol. 81, no. 11, pp. 7376–7385, 1997.

[178] J. Koh, A. S. Ferlauto, P. I. Rovira, C. R. Wronski, and R. W. Collins, "Evolutionary phase diagrams for plasma-enhanced chemical vapor deposition of silicon thin films from hydrogen-diluted silane," *Applied physics letters*, vol. 75, no. 15, pp. 2286–2288, 1999.

[179] D. Neamen, *Semiconductor Physics and Devices*. McGraw-Hill Education, fourth ed., 2012.

[180] S. D. Stranks, R. L. Z. Hoye, D. Di, R. H. Friend, and F. Deschler, "The physics of light emission in halide perovskite devices," *Advanced materials*, vol. 31, no. 47, p. 1803336, 2019.

[181] E. M. Hutter, M. C. Gélvez-Rueda, A. Osherov, V. Bulović, F. C. Grozema, S. D. Stranks, and T. J. Savenije, "Direct–indirect character of the bandgap in methylammonium lead iodide perovskite," *Nature materials*, vol. 16, no. 1, pp. 115–120, 2017.

[182] M. A. Green, "Solar cells: operating principles, technology, and system applications," *Englewood Cliffs*, 1982.

[183] J. I. Pankove, *Optical processes in semiconductors*. Courier Corporation, 1975.

[184] W. Shockley and W. T. Read Jr, "Statistics of the recombinations of holes and electrons," *Physical review*, vol. 87, no. 5, p. 835, 1952.

[185] R. N. Hall, "Electron-hole recombination in germanium," *Physical review*, vol. 87, no. 2, p. 387, 1952.

[186] A. G. Aberle, "Surface passivation of crystalline silicon solar cells: a review," *Progress in Photovoltaics: Research and Applications*, vol. 8, no. 5, pp. 473–487, 2000.

[187] W. D. Eades and R. M. Swanson, "Calculation of surface generation and recombination velocities at the Si-SiO2 interface," *Journal of applied Physics*, vol. 58, no. 11, pp. 4267–4276, 1985.

[188] A. G. Aberle, S. Glunz, and W. Warta, "Impact of illumination level and oxide parameters on Shockley–Read–Hall recombination at the Si-SiO2 interface," *Journal of Applied Physics*, vol. 71, no. 9, pp. 4422–4431, 1992.

[189] A. B. Sproul, "Dimensionless solution of the equation describing the effect of surface recombination on carrier decay in semiconductors," *Journal of Applied Physics*, vol. 76, no. 5, pp. 2851–2854, 1994.

[190] J. Brody, A. Rohatgi, and A. Ristow, "Review and comparison of equations relating bulk lifetime and surface recombination velocity to effective lifetime measured under flash lamp illumination," *Solar energy materials and solar cells*, vol. 77, no. 3, pp. 293–301, 2003.

[191] D. K. Schroder, *Semiconductor material and device characterization*. John Wiley & Sons, 2006.

[192] A. Cuevas, Y. Wan, D. Yan, C. Samundsett, T. Allen, X. Zhang, J. Cui, and J. Bullock, "Carrier population control and surface passivation in solar cells," *Solar energy materials and solar cells*, vol. 184, pp. 38–47, 2018.

[193] J. Schmidt, B. Veith, and R. Brendel, "Effective surface passivation of crystalline silicon using ultrathin Al2O3 films and Al2O3/SiNx stacks," *physica status solidi (RRL)–Rapid Research Letters*, vol. 3, no. 9, pp. 287–289, 2009.

[194] Z. C. Holman, M. Filipič, A. Descoeudres, S. De Wolf, F. Smole, M. Topič, and C. Ballif, "Infrared light management in high-efficiency silicon heterojunction and rear-passivated solar cells," *Journal of Applied Physics*, vol. 113, no. 1, p. 013107, 2013.

[195] H. W. Deckman, C. R. Wronski, H. Witzke, and E. Yablonovitch, "Optically enhanced amorphous silicon solar cells," *Applied Physics Letters*, vol. 42, no. 11, pp. 968–970, 1983.

[196] H. Sai and T. Matsui, "Toward tco-free silicon heterojunction solar cells: Effect of tco layers in electrical transport and stability," *Solar RRL*, p. 2300290, 2023.

[197] M. A. Green, E. D. Dunlop, M. Yoshita, N. Kopidakis, K. Bothe, G. Siefer, and X. Hao, "Solar cell efficiency tables (version 62)," *Progress in Photovoltaics: Research and Applications*, vol. 31, no. 7, pp. 651–663, 2023.

[198] M. Bivour, S. Schröer, M. Hermle, and S. W. Glunz, "Silicon heterojunction rear emitter solar cells: Less restrictions on the optoelectrical properties of front side TCOs," *Solar Energy Materials and Solar Cells*, vol. 122, pp. 120–129, 2014.

[199] J. Haschke, G. Christmann, C. Messmer, M. Bivour, M. Boccard, and C. Ballif, "Lateral transport in silicon solar cells," *Journal of Applied Physics*, vol. 127, no. 11, p. 114501, 2020.

[200] C. Han, R. Santbergen, M. van Duffelen, P. Procel, Y. Zhao, G. Yang, X. Zhang, M. Zeman, L. Mazzarella, and O. Isabella, "Towards bifacial silicon heterojunction solar cells with reduced TCO use," *Progress in Photovoltaics: Research and Applications*, vol. 30, no. 7, pp. 750–762, 2022.

[201] P. Procel Moya, H. Xu, L. Mazzarella, L.-L. Senaud, B. Paviet-Salomon, H. Sivaramakrishnan Radhakrishna, M. Filipic, M. Xu, M. Boccard, A. Fioretti, R. Monnard, J.-C. Stang, P. Wagner, D. Meza, D. Lachenal, B. Strahm, W. Duan, A. Lambertz, A. Fejfar, K. Ding, M. Despeisse, I. Gordon, L. Korte, C. Ballif, O. Isabella, and M. Zeman, "On the Correlation between Contact Resistivity and High Efficiency in (IBC-) SHJ Solar Cells," in *36th European Photovoltaic Solar Energy Conference and Exhibition*, pp. 251–254, 2019.

[202] T. F. Schulze, L. Korte, F. Ruske, and B. Rech, "Band lineup in amorphous/crystalline silicon heterojunctions and the impact of hydrogen microstructure and topological disorder," *Physical Review B*, vol. 83, no. 16, p. 165314, 2011.

[203] U. Wurfel, A. Cuevas, and P. Wurfel, "Charge carrier separation in solar cells," *IEEE Journal of Photovoltaics*, vol. 5, no. 1, pp. 461–469, 2015.

[204] A. Cuevas, T. Allen, J. Bullock, Y. Wan, D. Yan, and X. Zhang, "Skin care for healthy silicon solar cells," in *2015 IEEE 42nd Photovoltaic Specialist Conference (PVSC)*, pp. 1–6, IEEE, 2015.

[205] M. Ieong, P. M. Solomon, S. E. Laux, H.-S. Wong, and D. Chidambarrao, "Comparison of raised and Schottky source/drain MOSFETs using a novel tunneling contact model," in *International Electron Devices Meeting 1998. Technical Digest (Cat. No. 98CH36217)*, pp. 733–736, IEEE, 1998.

[206] S. M. Sze and K. K. Ng, *Physics of Semiconductor Devices*. John Wiley & Sons, 2006.

[207] F. Jiménez-Molinos, F. Gámiz, A. Palma, P. Cartujo, and J. A. López-Villanueva, "Direct and trap-assisted elastic tunneling through ultrathin gate oxides," *Journal of Applied Physics*, vol. 91, no. 8, pp. 5116–5124, 2002.

[208] W. Goes, Y. Wimmer, A.-M. El-Sayed, G. Rzepa, M. Jech, A. L. Shluger, and T. Grasser, "Identification of oxide defects in semiconductor devices: A systematic approach linking DFT to rate equations and experimental evidence," *Microelectronics Reliability*, vol. 87, pp. 286–320, 2018.

[209] T. F. Schulze, L. Korte, E. Conrad, M. Schmidt, and B. Rech, "Electrical transport mechanisms in a-Si: H/c-Si heterojunction solar cells," *Journal of Applied Physics*, vol. 107, no. 2, p. 23711, 2010.

[210] L. Zhao, C. L. Zhou, H. L. Li, H. W. Diao, and W. J. Wang, "Design optimization of bifacial HIT solar cells on p-type silicon substrates by simulation," *Solar Energy Materials and Solar Cells*, vol. 92, no. 6, pp. 673–681, 2008.

[211] K. U. Ritzau, M. Bivour, S. Schröer, H. Steinkemper, P. Reinecke, F. Wagner, and M. Hermle, "TCO work function related transport losses at the a-Si:H/TCO-contact in SHJ solar cells," *Solar Energy Materials and Solar Cells*, vol. 131, pp. 9–13, 2014.

[212] R. Gogolin, M. Turcu, R. Ferr, J. Clemens, N.-p. Harder, R. Brendel, and J. Schmidt, "Analysis of Series Resistance Losses in a-Si:H/c-Si Heterojunction Solar Cells," *IEEE Journal of Photovoltaics*, vol. 4, no. 5, pp. 1169–1176, 2018.

[213] A. Palma, A. Godoy, J. A. Jimenez-Tejada, J. E. Carceller, and J. A. Lopez-Villanueva, "Quantum two-dimensional calculation of time constants of random telegraph signals in metal-oxide–semiconductor structures," *Physical Review B*, vol. 56, no. 15, p. 9565, 1997.

[214] M. Bivour, S. Schröer, and M. Hermle, "Numerical analysis of electrical TCO/a-Si:H(p) contact properties for silicon heterojunction solar cells," *Energy Procedia*, vol. 38, pp. 658–669, 2013.

[215] D. Lachenal, P. Papet, B. Legradic, R. Kramer, T. Kössler, L. Andreetta, N. Holm, W. Frammelsberger, D. L. Baetzner, B. Strahm, L. Senaud, J. Schüttauf, A. Descoeudres, G. Christmann, S. Nicolay, M. Despeisse, B. Paviet-Salomon, and C. Ballif, "Optimization of tunnel-junction IBC solar cells based on a series resistance model," *Solar Energy Materials and Solar Cells*, vol. 200, p. 110036, 2019.

[216] D. K. Schroder and D. L. Meier, "Solar cell contact resistance—A review," *IEEE Transactions on electron devices*, vol. 31, no. 5, pp. 637–647, 1984.

[217] D. Lachenal, D. Baetzner, W. Frammelsberger, B. Legradic, J. Meixenberger, P. Papet, B. Strahm, and G. Wahli, "Heterojunction and passivated contacts: a simple method to extract both n/tco and p/tco contacts resistivity," *Energy Procedia*, vol. 92, pp. 932–938, 2016.

[218] A. Onno, C. Chen, P. Koswatta, M. Boccard, and Z. C. Holman, "Passivation, conductivity, and selectivity in solar cell contacts: Concepts and simulations based on a unified partial-resistances framework," *Journal of Applied Physics*, vol. 126, no. 18, p. 183103, 2019.

[219] M. Stutzmann, "The defect density in amorphous silicon," *Philosophical Magazine B*, vol. 60, no. 4, pp. 531–546, 1989.

[220] R. A. Street, *Hydrogenated Amorphous Silicon*. Cambridge: Cambridge University Press, 1991.

[221] M. Zeman, "Advanced amorphous silicon solar cell technologies," *Thin film solar cells: fabrication, characterization and applications*, pp. 1–66, 2006.

[222] R. E. Norberg, D. J. Leopold, and P. A. Fedders, "Non-bonded hydrogen in a-Si:H," *Journal of Non-Crystalline Solids*, vol. 227-230, pp. 124–127, 1998.

[223] A. H. M. Smets, W. M. M. Kessels, and M. C. M. Van de Sanden, "Vacancies and voids in hydrogenated amorphous silicon," *Applied physics letters*, vol. 82, no. 10, pp. 1547–1549, 2003.

[224] A. H. M. Smets and M. C. M. Van De Sanden, "Relation of the Si-H stretching frequency to the nanostructural Si-H bulk environment," *Physical Review B*, vol. 76, no. 7, p. 73202, 2007.

[225] O. Vetterl, F. Finger, R. Carius, P. Hapke, L. Houben, O. Kluth, A. Lambertz, A. Mück, B. Rech, and H. Wagner, "Intrinsic microcrystalline silicon: A new material for photovoltaics," *Solar Energy Materials and Solar Cells*, vol. 62, no. 1-2, pp. 97–108, 2000.

[226] J. Müllerová, P. Šutta, G. Van Elzakker, M. Zeman, and M. Mikula, "Microstructure of hydrogenated silicon thin films prepared from silane diluted with hydrogen," *Applied Surface Science*, vol. 254, no. 12, pp. 3690–3695, 2008.

[227] T. Itoh, K. Yamamoto, K. Ushikoshi, S. Nonomura, and S. Nitta, "Characterization and role of hydrogen in nc-Si: H," *Journal of non-crystalline solids*, vol. 266, pp. 201–205, 2000.

[228] D. C. Marra, E. A. Edelberg, R. L. Naone, and E. S. Aydil, "Silicon hydride composition of plasma-deposited hydrogenated amorphous and nanocrystalline silicon films and surfaces," *Journal of Vacuum Science & Technology A: Vacuum, Surfaces, and Films*, vol. 16, no. 6, pp. 3199–3210, 1998.

[229] S. Lebib and P. Roca i Cabarrocas, "Effects of ion energy on the crystal size and hydrogen bonding in plasma-deposited nanocrystalline silicon thin films," *Journal of Applied Physics*, vol. 97, no. 10, p. 104334, 2005.

[230] S. Lee, J. K. Arch, S. J. Fonash, and C. R. Wronski, "The mobility gaps in a-Si: H and its effects on solar cell performance," in *IEEE Conference on Photovoltaic Specialists*, pp. 1624–1629, IEEE, 1990.

[231] J. Tauc, "Optical properties and electronic structure of amorphous Ge and Si," *Materials research bulletin*, vol. 3, no. 1, pp. 37–46, 1968.

[232] C. R. Wronski, S. Lee, M. Hicks, and S. Kumar, "Internal photoemission of holes and the mobility gap of hydrogenated amorphous silicon," *Physical review letters*, vol. 63, no. 13, p. 1420, 1989.

[233] C. R. Wronski, "Review of direct measurements of mobility gaps in a-Si: H using internal photoemission," *Journal of non-crystalline solids*, vol. 141, pp. 16–23, 1992.

[234] A. Funde, N. A. Bakr, D. Kamble, R. Hawaldar, D. Amalnerkar, and S. Jadkar, "Influence of hydrogen dilution on structural, electrical and optical properties of hydrogenated nanocrystalline silicon (nc-si: H) thin films prepared by plasma enhanced chemical vapour deposition (pe-cvd)," *Solar Energy Materials and Solar Cells*, vol. 92, no. 10, pp. 1217–1223, 2008.

[235] W. Li, D. Xia, H. Wang, and X. Zhao, "Hydrogenated nanocrystalline silicon thin film prepared by rf-pecvd at high pressure," *Journal of Non-Crystalline Solids*, vol. 356, no. 44-49, pp. 2552–2556, 2010.

[236] S. Liu, X. Zeng, W. Peng, H. Xiao, W. Yao, X. Xie, C. Wang, and Z. Wang, "Improvement of amorphous silicon nip solar cells by incorporating double-layer hydrogenated nanocrystalline silicon structure," *Journal of non-crystalline solids*, vol. 357, no. 1, pp. 121–125, 2011.

[237] G. B. Tong, Z. Aspanut, M. R. Muhamad, and S. A. Rahman, "Optical properties and crystallinity of hydrogenated nanocrystalline silicon (nc-si: H) thin films deposited by rf-pecvd," *Vacuum*, vol. 86, no. 8, pp. 1195–1202, 2012.

[238] B. Yan, G. Yue, J. Yang, and S. Guha, "On the bandgap of hydrogenated nanocrystalline silicon intrinsic materials used in thin film silicon solar cells," *Solar energy materials and solar cells*, vol. 111, pp. 90–96, 2013.

[239] Z. Hu, X. Liao, H. Diao, Y. Cai, S. Zhang, E. Fortunato, and R. Martins, "Hydrogenated p-type nanocrystalline silicon in amorphous silicon solar cells," *Journal of Non-Crystalline Solids*, vol. 352, no. 9-20, pp. 1900–1903, 2006.

[240] B. Delley and E. Steigmeier, "Quantum confinement in si nanocrystals," *Physical Review B*, vol. 47, no. 3, p. 1397, 1993.

[241] W. E. Spear and P. G. L. Comber, "Electronic properties of substitutionally doped amorphous Si and Ge," *Philosophical Magazine*, vol. 33, no. 6, pp. 935–949, 1976.

[242] J. C. Knights, "Characterization of plasma-deposited amorphous Si: H thin films," *Japanese Journal of Applied Physics*, vol. 18, no. S1, p. 101, 1979.

[243] Y.-M. Li, I. An, H. V. Nguyen, C. R. Wronski, and R. W. Collins, "Thin-film coalescence in hydrogenated amorphous silicon probed by spectroscopic ellipsometry with millisecond-scale resolution," *Physical review letters*, vol. 68, no. 18, p. 2814, 1992.

[244] C. C. Tsai, J. G. Shaw, B. Wacker, and J. C. Knights, "Film growth mechanisms of amorphous silicon in diode and triode glow discharge systems," *MRS Online Proceedings Library (OPL)*, vol. 95, 1987.

[245] A. Matsuda, "Growth mechanism of microcrystalline silicon obtained from reactive plasmas," *Thin Solid Films*, vol. 337, no. 1-2, pp. 1–6, 1999.

[246] E. Bustarret, M. A. Hachicha, and M. Brunel, "Experimental determination of the nanocrystalline volume fraction in silicon thin films from Raman spectroscopy," *Applied Physics Letters*, vol. 52, no. 20, pp. 1675–1677, 1988.

[247] E. C. Freeman and W. Paul, "Infrared vibrational spectra of rf-sputtered hydrogenated amorphous silicon," *Physical Review B*, vol. 18, no. 8, p. 4288, 1978.

[248] E. C. Freeman and W. Paul, "Optical constants of rf sputtered hydrogenated amorphous Si," *Physical Review B*, vol. 20, no. 2, p. 716, 1979.

[249] T. D. Moustakas, H. P. Maruska, and R. Friedman, "Properties and photovoltaic applications of microcrystalline silicon films prepared by rf reactive sputtering," *Journal of applied physics*, vol. 58, no. 2, pp. 983–986, 1985.

[250] S. Logothetidis and G. Kiriakidis, "Optical properties and structure of microcrystalline hydrogenated silicon prepared by radio-frequency magnetron sputtering," *Journal of applied physics*, vol. 64, no. 5, pp. 2389–2398, 1988.

[251] P. Roca i Cabarrocas, "Deposition Techniques and Processes Involved in the Growth of Amorphous and Microcrystalline Silicon Thin Films - Physics and Technology of Amorphous-Crystalline Heterostructure Silicon Solar Cells," in *Physics and Technology of Amorphous-Crystalline Heterostructure Silicon Solar Cells* (W. G. J. H. M. van Sark, L. Korte, and F. Roca, eds.), pp. 131–160, Berlin, Heidelberg: Springer Berlin Heidelberg, 2012.

[252] J. P. M. Schmitt, "Fundamental mechanisms in silane plasma decompositions and amorphous silicon deposition," *Journal of Non-Crystalline Solids*, vol. 59, pp. 649–657, 1983.

[253] A. Gallagher, "Surface Reactions in Discharge and CVD Deposition of Silane," *MRS Online Proceedings Library (OPL)*, vol. 70, 1986.

[254] A. Matsuda, K. Nomoto, Y. Takeuchi, A. Suzuki, A. Yuuki, and J. Perrin, "Temperature dependence of the sticking and loss probabilities of silyl radicals on hydrogenated amorphous silicon," *Surface Science*, vol. 227, no. 1-2, pp. 50–56, 1990.

[255] J. Perrin, Y. Takeda, N. Hirano, Y. Takeuchi, and A. Matsuda, "Sticking and recombination of the SiH3 radical on hydrogenated amorphous silicon: The catalytic effect of diborane," *Surface Science*, vol. 210, no. 1-2, pp. 114–128, 1989.

[256] A. Matsuda and K. Tanaka, "Investigation of the growth kinetics of glow-discharge hydrogenated amorphous silicon using a radical separation technique," *Journal of applied physics*, vol. 60, no. 7, pp. 2351–2356, 1986.

[257] W. M. M. Kessels, A. H. M. Smets, D. C. Marra, E. S. Aydil, D. C. Schram, and M. C. M. van de Sanden, "On the growth mechanism of a-Si: H," *Thin Solid Films*, vol. 383, no. 1-2, pp. 154–160, 2001.

[258] A. von Keudell and J. R. Abelson, "Direct insertion of SiH 3 radicals into strained Si-Si surface bonds during plasma deposition of hydrogenated amorphous silicon films," *Physical Review B*, vol. 59, no. 8, p. 5791, 1999.

[259] W. Widdra, S. I. Yi, R. Maboudian, G. A. D. Briggs, and W. H. Weinberg, "Adsorption, abstraction, and pairing of atomic hydrogen on Si (100)-(2× 1)," *Physical review letters*, vol. 74, no. 11, p. 2074, 1995.

[260] H. Shirai, J.-i. H. J.-i. Hanna, and I. S. I. Shimizu, "Role of atomic hydrogen during growth of hydrogenated amorphous silicon in the "chemical annealing"," *Japanese journal of applied physics*, vol. 30, no. 4B, p. L679, 1991.

[261] E. Amanatides, S. Stamou, and D. Mataras, "Gas phase and surface kinetics in plasma enhanced chemical vapor deposition of microcrystalline silicon: The combined effect of rf power and hydrogen dilution," *Journal of Applied Physics*, vol. 90, no. 11, pp. 5786–5798, 2001.

[262] J. Robertson, "Deposition mechanism of hydrogenated amorphous silicon," *Journal of Applied Physics*, vol. 87, no. 5, pp. 2608–2617, 2000.

[263] S. Hamma and P. Roca i Cabarrocas, "In situ correlation between the optical and electrical properties of thin intrinsic and n-type microcrystalline silicon films," *Journal of Applied Physics*, vol. 81, no. 11, pp. 7282–7288, 1997.

[264] P. Roca i Cabarrocas, "New approaches for the production of nano-, micro-, and polycrystalline silicon thin films," *physica status solidi (c)*, vol. 1, no. 5, pp. 1115–1130, 2004.

[265] P. Roca i Cabarrocas, "Plasma enhanced chemical vapor deposition of amorphous, polymorphous and microcrystalline silicon films," *Journal of non-crystalline solids*, vol. 266, pp. 31–37, 2000.

[266] A. Matsuda, "Formation kinetics and control of microcrystallite in μc-Si:H from glow discharge plasma," *Journal of Non-Crystalline Solids*, vol. 59-60, no. PART 2, pp. 767–774, 1983.

[267] K. Nomoto, Y. Urano, J. L. Guizot, G. Ganguly, and A. Matsuda, "Role of hydrogen atoms in the formation process of hydrogenated microcrystalline silicon," *Japanese journal of applied physics*, vol. 29, no. 8A, p. L1372, 1990.

[268] M. Katiyar and J. R. Abelson, "Investigation of hydrogen induced phase transition from a-Si: H to μc-Si: H using real time infrared spectroscopy," *Materials Science and Engineering: A*, vol. 304, pp. 349–352, 2001.

[269] C. C. Tsai, G. B. Anderson, R. Thompson, and B. Wacker, "Control of silicon network structure in plasma deposition," *Journal of Non-Crystalline Solids*, vol. 114, no. PART 1, pp. 151–153, 1989.

[270] I. Solomon, B. Drévillon, H. Shirai, and N. Layadi, "Plasma deposition of microcrystalline silicon: the selective etching model," *Journal of non-crystalline solids*, vol. 164, pp. 989–992, 1993.

[271] N. Layadi, P. Roca i Cabarrocas, B. Drévillon, and I. Solomon, "Real-time spectroscopic ellipsometry study of the growth of amorphous and microcrystalline silicon thin films prepared by alternating silicon deposition and hydrogen plasma treatment," *Physical Review B*, vol. 52, no. 7, p. 5136, 1995.

[272] K. Nakamura, K. Yoshino, S. Takeoka, and I. Shimizu, "Roles of atomic hydrogen in chemical annealing," *Japanese Journal of Applied Physics*, vol. 34, no. 2R, pp. 442–449, 1995.

[273] S. Sriraman, S. Agarwal, E. S. Aydil, and D. Maroudas, "Mechanism of hydrogen-induced crystallization of amorphous silicon," *Nature*, vol. 418, no. 6893, pp. 62–65, 2002.

[274] P. Roca i Cabarrocas, Y. Djeridane, V. Bui, Y. Bonnassieux, and A. Abramov, "Critical issues in plasma deposition of microcrystalline silicon for thin film transistors," *Solid-state electronics*, vol. 52, no. 3, pp. 422–426, 2008.

[275] N. Chaâbane, P. Roca i Cabarrocas, and H. Vach, "Trapping of plasma produced nanocrystalline si particles on a low temperature substrate," *Journal of non-crystalline solids*, vol. 338, pp. 51–55, 2004.

[276] J. E. Gerbi and J. R. Abelson, "Deposition of microcrystalline silicon: Direct evidence for hydrogen-induced surface mobility of Si adspecies," *Journal of Applied Physics*, vol. 89, no. 2, pp. 1463–1469, 2001.

[277] K. Saitoh, M. Kondo, M. Fukawa, T. Nishimiya, A. Matsuda, W. Futako, and I. Shimizu, "Role of the hydrogen plasma treatment in layer-by-layer deposition of microcrystalline silicon," *Applied physics letters*, vol. 71, no. 23, pp. 3403–3405, 1997.

[278] J. J. Boland and G. N. Parsons, "Bond selectivity in silicon film growth," *Science*, vol. 256, no. 5061, pp. 1304–1306, 1992.

[279] J. Perrin, "Plasma and surface reactions during a-Si: H film growth," *Journal of non-crystalline solids*, vol. 137, pp. 639–644, 1991.

[280] B. Kalache, A. I. Kosarev, R. Vanderhaghen, and P. Roca i Cabarrocas, "Ion bombardment effects on microcrystalline silicon growth mechanisms and on the film properties," *Journal of Applied physics*, vol. 93, no. 2, pp. 1262–1273, 2003.

[281] P. Roca i Cabarrocas, Y. Djeridane, T. Nguyen-Tran, E. Johnson, A. Abramov, and Q. Zhang, "Low temperature plasma synthesis of silicon nanocrystals: a strategy for high deposition rate and efficient polymorphous and microcrystalline solar cells," *Plasma Physics and Controlled Fusion*, vol. 50, no. 12, p. 124037, 2008.

[282] S. Kasouit, J. Damon-Lacoste, R. Vanderhaghen, and P. Roca i Cabarrocas, "Contribution of plasma generated nanocrystals to the growth of microcrystalline silicon thin films," *Journal of Non-Crystalline Solids*, vol. 338, pp. 86–90, 2004.

[283] K.-H. Kim, E. V. Johnson, A. G. Kazanskii, M. V. Khenkin, and P. Roca i Cabarrocas, "Unravelling a simple method for the low temperature synthesis of silicon nanocrystals and monolithic nanocrystalline thin films," *Scientific Reports*, vol. 7, no. 1, p. 40553, 2017.

[284] Q. Brulin, N. Ning, and H. Vach, "Hydrogen-induced crystallization of amorphous silicon clusters in a plasma reactor," *Journal of non-crystalline solids*, vol. 352, no. 9-20, pp. 1055–1058, 2006.

[285] P. Roca i Cabarrocas, T. Nguyen-Tran, Y. Djeridane, A. Abramov, E. Johnson, and G. Patriarche, "Synthesis of silicon nanocrystals in silane plasmas for nanoelectronics and large area electronic devices," *Journal of Physics D: Applied Physics*, vol. 40, no. 8, p. 2258, 2007.

[286] P. Roca i Cabarrocas, A. F. i Morral, and Y. Poissant, "Growth and optoelectronic properties of polymorphous silicon thin films," *Thin Solid Films*, vol. 403, pp. 39–46, 2002.

[287] N. Chaâbane, V. Suendo, H. Vach, and P. Roca i Cabarrocas, "Soft landing of silicon nanocrystals in plasma enhanced chemical vapor deposition," *Applied physics letters*, vol. 88, no. 20, 2006.

[288] S. Usui and M. Kikuchi, "Properties of heavily doped GD- Si with low resistivity," *Journal of Non-Crystalline Solids*, vol. 34, no. 1, pp. 1–11, 1979.

[289] W. Germer, "Microcrystalline silicon thin films for sensor applications," *Sensors and Actuators*, vol. 7, no. 2, pp. 135–142, 1985.

[290] R. A. Street, "Doping and the Fermi energy in amorphous silicon," *Physical Review Letters*, vol. 49, no. 16, p. 1187, 1982.

[291] M. Stutzmann, D. K. Biegelsen, and R. A. Street, "Detailed investigation of doping in hydrogenated amorphous silicon and germanium," *Physical Review B*, vol. 35, no. 11, p. 5666, 1987.

[292] S. Nishida, H. Tasaki, M. Konagai, and K. Takahashi, "Highly conductive and wide band gap amorphous-microcrystalline mixed-phase silicon films prepared by photochemical vapor deposition," *Journal of applied physics*, vol. 58, no. 4, pp. 1427–1431, 1985.

[293] A. Wang and G. Lucovsky, "Intrinsic microcrystalline silicon deposited by remote PECVD: a new thin-film photovoltaic material," in *IEEE Conference on Photovoltaic Specialists*, pp. 1614–1618, IEEE, 1990.

[294] P. Alpuim, V. Chu, and J. P. Conde, "Electronic and structural properties of doped amorphous and nanocrystalline silicon deposited at low substrate temperatures by radio-frequency plasma-enhanced chemical vapor deposition," *Journal of Vacuum Science & Technology A: Vacuum, Surfaces, and Films*, vol. 21, no. 4, pp. 1048–1054, 2003.

[295] J. I. Pankove, D. E. Carlson, J. E. Berkeyheiser, and R. O. Wance, "Neutralization of shallow acceptor levels in silicon by atomic hydrogen," *Physical review letters*, vol. 51, no. 24, p. 2224, 1983.

[296] N. M. Johnson, C. Herring, and D. J. Chadi, "Interstitial hydrogen and neutralization of shallow-donor impurities in single-crystal silicon," *Physical Review Letters*, vol. 56, no. 7, p. 769, 1986.

[297] X. L. Jiang, Y. L. He, and H. L. Zhu, "The effect of passivation of boron dopants by hydrogen in nano-crystalline and micro-crystalline silicon films," *Journal of Physics: Condensed Matter*, vol. 6, no. 3, p. 713, 1994.

[298] H. Tan, P. Babal, M. Zeman, and A. H. M. Smets, "Wide bandgap p-type nanocrystalline silicon oxide as window layer for high performance thin- film silicon multi-junction solar cells," *Solar Energy Materials and Solar Cells*, vol. 132, pp. 597–605, 2015.

[299] B. Paviet-Salomon, A. Tomasi, D. Lachenal, N. Badel, G. Christmann, L. Barraud, A. Descoeudres, J. Geissbühler, A. Faes, Q. Jeangros, J. P. Seif, S. Nicolay, B. Strahm, S. De Wolf, C. Ballif, and M. Despeisse, "Interdigitated back contact silicon heterojunction solar cells featuring an interband tunnel junction enabling simplified processing," *Solar Energy*, no. January, 2018.

[300] P. Cuony, D. T. L. Alexander, I. Perez-Wurfl, M. Despeisse, G. Bugnon, M. Boccard, T. Söderström, A. Hessler-Wyser, C. Hébert, and C. Ballif, "Silicon Filaments in Silicon Oxide for Next-Generation Photovoltaics," *Advanced Materials*, vol. 24, pp. 1182–1186, mar 2012.

[301] Y. Hou, E. Aydin, M. D. Bastiani, C. Xiao, F. H. Isikgor, D.-J. Xue, B. Chen, H. Chen, B. Bahrami, A. H. Chowdhury, A. Johnston, S.-W. Baek, Z. Huang, M. Wei, Y. Dong, J. Troughton, R. Jalmood, A. J. Mirabelli, T. G. Allen, E. V. Kerschaver, M. I. Saidaminov, D. Baran, Q. Qiao, K. Zhu, S. D. Wolf, and E. H. Sargent, "Efficient tandem solar cells with solution-processed perovskite on textured crystalline silicon," *Science*, vol. 367, no. 6482, pp. 1135–1140, 2020.

[302] J. J. Boland, "Structure of the H-saturated Si (100) surface," *Physical review letters*, vol. 65, no. 26, p. 3325, 1990.

[303] B. Demaurex, R. Bartlome, J. P. Seif, J. Geissbühler, D. T. L. Alexander, Q. Jeangros, C. Ballif, and S. De Wolf, "Low-temperature plasma-deposited silicon epitaxial films: Growth and properties," *Journal of Applied Physics*, vol. 116, no. 5, p. 53519, 2014.

[304] D. H. Levi, C. W. Teplin, E. Iwaniczko, Y. Yan, T. H. Wang, and H. M. Branz, "Real-time spectroscopic ellipsometry studies of the growth of amorphous and epitaxial silicon for photovoltaic applications," *Journal of Vacuum Science & Technology A: Vacuum, Surfaces, and Films*, vol. 24, no. 4, pp. 1676–1683, 2006.

[305] U. K. Das, M. Z. Burrows, M. Lu, S. Bowden, and R. W. Birkmire, "Surface passivation and heterojunction cells on Si (100) and (111) wafers using dc and rf plasma deposited Si:H thin films," *Applied Physics Letters*, vol. 92, no. 6, pp. 90–93, 2008.

[306] P. Roca i Cabarrocas, R. Cariou, and M. Labrune, "Low temperature plasma deposition of silicon thin films: From amorphous to crystalline," *Journal of Non-Crystalline Solids*, vol. 358, no. 17, pp. 2000–2003, 2012.

[307] T. de Vrijer and A. H. M. Smets, "Advanced textured monocrystalline silicon substrates with high optical scattering yields and low electrical recombination losses for supporting crack-free nano-to poly-crystalline film growth," *Energy Science & Engineering*, vol. 9, no. 8, pp. 1080–1089, 2021.

[308] P. Roca i Cabarrocas, N. Layadi, B. Drevillon, and I. Solomon, "Microcrystalline silicon growth by the layer-by-layer technique: long term evolution and nucleation mechanisms," *Journal of Non-Crystalline Solids*, vol. 198-200, pp. 871–874, 1996.

[309] M. Z. Burrows, U. K. Das, R. L. Opila, S. De Wolf, and R. W. Birkmire, "Role of hydrogen bonding environment in a-Si:H films for c-Si surface passivation," *Journal of Vacuum Science & Technology A: Vacuum, Surfaces, and Films*, vol. 26, no. 4, pp. 683–687, 2008.

[310] H. Fujiwara, Y. Toyoshima, M. Kondo, and A. Matsuda, "Interface-layer formation mechanism in a-Si: H thin-film growth studied by real-time spectroscopic ellipsometry and infrared spectroscopy," *Physical Review B*, vol. 60, no. 19, p. 13598, 1999.

[311] H. Fujiwara, M. Kondo, and A. Matsuda, "Depth profiling of silicon–hydrogen bonding modes in amorphous and microcrystalline Si: H thin films by real-time infrared spectroscopy and spectroscopic ellipsometry," *Journal of applied physics*, vol. 91, no. 7, pp. 4181–4190, 2002.

[312] Y. Zhao, P. Procel, C. Han, L. Mazzarella, G. Yang, A. Weeber, M. Zeman, and O. Isabella, "Design and optimization of hole collectors based on nc-SiOx: H for high-efficiency silicon heterojunction solar cells," *Solar Energy Materials and Solar Cells*, vol. 219, p. 110779, 2021.

[313] Y. Zhao, P. Procel, A. Smets, L. Mazzarella, C. Han, G. Yang, L. Cao, Z. Yao, A. Weeber, M. Zeman, and O. Isabella, "Effects of (i)a-Si: H deposition temperature on high-efficiency silicon heterojunction solar cells," *Progress in Photovoltaics: research and applications*, 2022.

[314] F. Finger, P. Hapke, M. Luysberg, R. Carius, H. Wagner, and M. Scheib, "Improvement of grain size and deposition rate of microcrystalline silicon by use of very high frequency glow discharge," *Applied Physics Letters*, vol. 65, pp. 2588–2590, nov 1994.

[315] H. Umishio, H. Sai, T. Koida, and T. Matsui, "Nanocrystalline-silicon hole contact layers enabling efficiency improvement of silicon heterojunction solar cells: Impact of nanostructure evolution on solar cell performance," *Progress in Photovoltaics: Research and Applications*, vol. 29, no. 3, pp. 344–356, 2021.

[316] A. M. Funde, N. A. Bakr, D. K. Kamble, R. R. Hawaldar, D. P. Amalnerkar, and S. R. Jadkar, "Influence of hydrogen dilution on structural, electrical and optical properties of hydrogenated nanocrystalline silicon (nc-Si: H) thin films prepared by plasma enhanced chemical vapour deposition (PE-CVD)," *Solar Energy Materials and Solar Cells*, vol. 92, no. 10, pp. 1217–1223, 2008.

[317] C.-Z. Chen, S.-H. Qiu, C.-Q. Liu, Y.-D. Wu, P. Li, C.-Y. Yu, and X.-y. Lin, "Low temperature fast growth of nanocrystalline silicon films by rf-PECVD from SiH4/H2 gases: microstructural characterization," *Journal of Physics D: Applied Physics*, vol. 41, no. 19, p. 195413, 2008.

[318] A. N. Fioretti, M. Boccard, R. Monnard, and C. Ballif, "Low-temperature p-type microcrystalline silicon as carrier selective contact for silicon heterojunction solar cells," *IEEE Journal of Photovoltaics*, vol. 9, no. 5, pp. 1158–1165, 2019.

[319] J. Gope, S. Kumar, A. Parashar, P. N. Dixit, C. M. S. Rauthan, O. S. Panwar, D. N. Patel, and S. C. Agarwal, "Amorphous and nanocrystalline silicon made by varying deposition pressure in PECVD process," *Journal of Non-Crystalline Solids*, vol. 355, no. 45-47, pp. 2228–2232, 2009.

[320] N. Pellaton Vaucher, B. Rech, D. Fischer, S. Dubail, M. Goetz, H. Keppner, N. Wyrsch, C. Beneking, O. Hadjadj, V. Shklover, and A. Shah, "Controlled nucleation of thin microcrystalline layers for the recombination junction in a-Si stacked cells," *Solar Energy Materials and Solar Cells*, vol. 49, no. 1-4, pp. 27–33, 1997.

[321] L. Mazzarella, S. Kirner, O. Gabriel, S. S. Schmidt, L. Korte, B. Stannowski, B. Rech, and R. Schlatmann, "Nanocrystalline silicon emitter optimization for Si-HJ solar cells: Substrate selectivity and CO2 plasma treatment effect," *Physica Status Solidi (A) Applications and Materials Science*, vol. 214, no. 2, p. 1532958, 2017.

[322] L. Mazzarella, *Nanocrystalline Silicon and Silicon Oxide Contact Layers For Silicon Heterojunction Solar Cells*. PhD thesis, DER TECHNISCHEN UNIVERSITÄT BERLIN, 2017.

[323] G. Yang, P. Guo, P. Procel, G. Limodio, A. Weeber, O. Isabella, and M. Zeman, "High-efficiency black IBC c-Si solar cells with poly-Si as carrier-selective passivating contacts," *Solar Energy Materials and Solar Cells*, vol. 186, pp. 9–13, 2018.

[324] D. Deligiannis, S. Alivizatos, A. Ingenito, D. Zhang, M. van Sebille, R. A. C. M. M. van Swaaij, and M. Zeman, "Wet-chemical Treatment for Improved Surface Passivation of Textured Silicon Heterojunction Solar Cells," *Energy Procedia*, vol. 55, pp. 197–202, 2014.

[325] C. Han, Y. Zhao, L. Mazzarella, R. Santbergen, A. Montes, P. Procel, G. Yang, X. Zhang, M. Zeman, and O. Isabella, "Room-temperature sputtered tungsten-doped indium oxide for improved current in silicon heterojunction solar cells," *Solar Energy Materials and Solar Cells*, vol. 227, p. 111082, 2021.

[326] P. Babál, *Doped nanocrystalline silicon oxide for use as (intermediate) reflecting layers in thin-film silicon solar cells*. PhD thesis, Technische Universiteit Delft, 2014.

[327] C. Han, L. Mazzarella, Y. Zhao, G. Yang, P. Procel, M. Tijssen, A. Montes, L. Spitaleri, A. Gulino, X. Zhang, O. Isabella, and M. Zeman, "High-mobility Hydrogenated Fluorine-doped Indium Oxide Film for Passivating Contacts c-Si Solar Cells," *ACS Applied Materials & Interfaces*, vol. 11, no. 49, pp. 45586–45595, 2019.

[328] C. Han, G. Yang, A. Montes, P. Procel, L. Mazzarella, Y. Zhao, S. Eijt, H. Schut, X. Zhang, M. Zeman, and O. Isabella, "Realizing the Potential of RF-Sputtered Hydrogenated Fluorine-Doped Indium Oxide as Electrode Materials for Ultrathin SiOx/Poly-Si Passivating Contacts," *ACS Applied Energy Materials*, vol. 3, no. 9, pp. 8606–8618, 2020.

[329] Fraunhofer Institute for Solar Energy Systems (F-ISE), "Innovative fine-line screen printing metallization reduces silver consumption for solar cell contacts." https://www.ise.fraunhofer.de/en/press-media/press-releases/2019/innovative-fine-line-screen-printing-metallization-reduces-silver-consumption-for-solar-cell-contacts.html, 2019. (Date accessed: 2022-12-01).

[330] D. Deligiannis, *Surface passivation for silicon heterojunction solar cells*. PhD thesis, Technische Universiteit Delft, 2017.

[331] G. Limodio, Y. De Groot, G. Van Kuler, L. Mazzarella, Y. Zhao, P. Procel, G. Yang, O. Isabella, and M. Zeman, "Copper-plating metallization with alternative seed layers for c-Si solar cells embedding carrier-selective passivating contacts," *IEEE journal of photovoltaics*, vol. 10, no. 2, pp. 372–382, 2019.

[332] C. Han, *High-Mobility TCO-Based Contacting Schemes for c-Si Solar Cells*. PhD thesis, Technische Universiteit Delft, 2022.

[333] H. Fujiwara, *Spectroscopic ellipsometry: principles and applications*. John Wiley & Sons, 2007.

[334] H. Fujiwara and R. W. Collins, *Spectroscopic ellipsometry for photovoltaics*, vol. 1. Springer, 2018.

[335] J. A. Sap, O. Isabella, K. Jäger, and M. Zeman, "Extraction of optical properties of flat and surface-textured transparent conductive oxide films in a broad wavelength range," *Thin Solid Films*, vol. 520, no. 3, pp. 1096–1101, 2011.

[336] W.Theiss Hardware and Software, "Scout technical manual." https://www.mtheiss.com/. (Date accessed: 2020-09-09).

[337] S. K. O'Leary, S. R. Johnson, and P. K. Lim, "The relationship between the distribution of electronic states and the optical absorption spectrum of an amorphous semiconductor: An empirical analysis," *Journal of applied physics*, vol. 82, no. 7, pp. 3334–3340, 1997.

[338] A. A. Langford, M. L. Fleet, B. P. Nelson, W. A. Lanford, and N. Maley, "Infrared absorption strength and hydrogen content of hydrogenated amorphous silicon," *Physical Review B*, vol. 45, no. 23, pp. 13367–13377, 1992.

[339] E. Bhattacharya and A. H. Mahan, "Microstructure and the light-induced metastability in hydrogenated amorphous silicon," *Applied physics letters*, vol. 52, no. 19, pp. 1587–1589, 1988.

[340] M. H. Brodsky, M. Cardona, and J. J. Cuomo, "Infrared and Raman spectra of the silicon-hydrogen bonds in amorphous silicon prepared by glow discharge and sputtering," *Physical Review B*, vol. 16, no. 8, p. 3556, 1977.

[341] H. Shanks, C. J. Fang, L. Ley, M. Cardona, F. J. Demond, and S. Kalbitzer, "Infrared spectrum and structure of hydrogenated amorphous silicon," *physica status solidi (b)*, vol. 100, no. 1, pp. 43–56, 1980.

[342] N. Maley, "Critical investigation of the infrared-transmission-data analysis of hydrogenated amorphous silicon alloys," *Physical Review B*, vol. 46, no. 4, p. 2078, 1992.

[343] G. Lucovsky, R. J. Nemanich, and J. C. Knights, "Structural interpretation of the vibrational spectra of a-Si: H alloys," *Physical Review B*, vol. 19, no. 4, p. 2064, 1979.

[344] J. H. Parker Jr, D. W. Feldman, and M. Ashkin, "Raman scattering by silicon and germanium," *Physical Review*, vol. 155, no. 3, p. 712, 1967.

[345] Z. Iqbal and S. Veprek, "Raman scattering from hydrogenated microcrystalline and amorphous silicon," *Journal of Physics C: Solid State Physics*, vol. 15, no. 2, p. 377, 1982.

[346] C. Droz, *Thin film microcrystalline silicon layers and solar cells: microstructure and electrical performances*. PhD thesis, Université de Neuchâtel, 2003.

[347] C. Smit, R. Van Swaaij, H. Donker, A. Petit, W. M. M. Kessels, and M. C. M. Van de Sanden, "Determining the material structure of microcrystalline silicon from Raman spectra," *Journal of applied physics*, vol. 94, no. 5, pp. 3582–3588, 2003.

[348] L.-L. Senaud, *Electrical Losses Mitigation in Silicon Heterojunction Solar Cells*. PhD thesis, École polytechnique fédérale de Lausanne, 2021.

[349] A. T. Voutsas, M. K. Hatalis, J. Boyce, and A. Chiang, "Raman spectroscopy of amorphous and microcrystalline silicon films deposited by low-pressure chemical vapor deposition," *Journal of Applied Physics*, vol. 78, no. 12, pp. 6999–7006, 1995.

[350] H. Nagel, C. Berge, and A. G. Aberle, "Generalized analysis of quasi-steady-state and quasi-transient measurements of carrier lifetimes in semiconductors," *Journal of Applied Physics*, vol. 86, no. 11, pp. 6218–6221, 1999.

[351] R. A. Sinton and A. Cuevas, "Contactless determination of current–voltage characteristics and minority-carrier lifetimes in semiconductors from quasi-steady-state photoconductance data," *Applied Physics Letters*, vol. 69, no. 17, pp. 2510–2512, 1996.

[352] D. Pysch, A. Mette, and S. W. Glunz, "A review and comparison of different methods to determine the series resistance of solar cells," *Solar Energy Materials and Solar Cells*, vol. 91, no. 18, pp. 1698–1706, 2007.

[353] R. A. Sinton and A. Cuevas, "A quasi-steady-state open-circuit voltage method for solar cell characterization," in *Proceedings of the 16th European photovoltaic solar energy conference*, vol. 1152, p. 4, 2000.

[354] M. J. Kerr, A. Cuevas, and R. A. Sinton, "Generalized analysis of quasi-steady-state and transient decay open circuit voltage measurements," *Journal of applied physics*, vol. 91, no. 1, pp. 399–404, 2002.

[355] National Renewable Energy Laboratory (NREL), "Reference air mass 1.5 spectra." https://www.nrel.gov/grid/solar-resource/spectra-am1.5.html. (Date accessed: 2022-03-16).

[356] J. Hohl-Ebinger, G. Siefer, and W. Warta, "Non-linearity of solar cells in spectral response measurements," in *22rd European Photovoltaic Solar Energy Conference, Milan, Italy*, p. 422, 2007.

[357] B. H. Hamadani, A. Shore, H. W. Yoon, and M. Campanelli, "Nonlinear response of silicon solar cells," in *2017 IEEE 44th Photovoltaic Specialist Conference (PVSC)*, pp. 437–440, IEEE, 2017.

[358] K. Yoshikawa, W. Yoshida, T. Irie, H. Kawasaki, K. Konishi, H. Ishibashi, T. Asatani, D. Adachi, M. Kanematsu, H. Uzu, and K. Yamamoto, "Exceeding conversion efficiency of 26% by heterojunction interdigitated back contact solar cell with thin film Si technology," *Solar Energy Materials and Solar Cells*, vol. 173, pp. 37–42, 2017.

[359] S. Y. Herasimenka, W. J. Dauksher, and S. G. Bowden, ">750 mV open circuit voltage measured on 50 μ m thick silicon heterojunction solar cell," *Applied Physics Letters*, vol. 103, p. 053511, jul 2013.

[360] R. Martins, A. Macarico, I. Ferreira, R. Nunes, A. Bicho, and E. Fortunato, "Highly conductive and highly transparent n-type microcrystalline silicon thin films," *Thin Solid Films*, vol. 303, no. 1-2, pp. 47–52, 1997.

[361] P. Keblinski, S. R. Phillpot, D. Wolf, and H. Gleiter, "Amorphous structure of grain boundaries and grain junctions in nanocrystalline silicon by molecular-dynamics simulation," *Acta materialia*, vol. 45, no. 3, pp. 987–998, 1997.

[362] J. Sritharathikhun, H. Yamamoto, S. Miyajima, A. Yamada, and M. Konagai, "Optimization of amorphous silicon oxide buffer layer for high-efficiency p-type hydrogenated microcrystalline silicon oxide/n-type crystalline silicon heterojunction solar cells," *Japanese Journal of Applied Physics*, vol. 47, no. 11R, p. 8452, 2008.

[363] K. Nakada, S. Miyajima, and M. Konagai, "Application of n-type microcrystalline silicon oxide as back reflector of crystalline silicon heterojunction solar cells," *Japanese Journal of Applied Physics*, vol. 54, no. 8, p. 82301, 2015.

[364] J. Koh, H. Fujiwara, R. J. Koval, C. R. Wronski, and R. W. Collins, "Real time spectroscopic ellipsometry studies of the nucleation and growth of p-type microcrystalline silicon films on amorphous silicon using B2H6, B(CH3)3 and BF3 dopant source gases," *Journal of Applied Physics*, vol. 85, pp. 4141–4153, apr 1999.

[365] J. Wolff, R. Carius, and F. Finger, "Preparation of microcrystalline silicon seed-layers with defined structural properties," *Thin Solid Films*, vol. 427, pp. 46–50, 2003.

[366] J.-h. Zhou, K. Ikuta, T. Yasuda, T. Umeda, S. Yamasaki, K. Tanaka, and J.-h. Zhou, "Growth of amorphous-layer-free microcrystalline silicon on insulating glass substrates by plasma-enhanced chemical vapor deposition," *Applied Physics Letters*, vol. 1534, no. 1997, pp. 1–4, 2003.

[367] M. Mews, T. F. Schulze, N. Mingirulli, and L. Korte, "Hydrogen plasma treatments for passivation of amorphous-crystalline silicon-heterojunctions on surfaces promoting epitaxy," *Applied Physics Letters*, vol. 102, no. 12, p. 122106, 2013.

[368] A. Descoeudres, L. Barraud, S. De Wolf, B. Strahm, D. Lachenal, C. Guérin, Z. C. Holman, F. Zicarelli, B. Demaurex, J. Seif, J. Holovsky, and C. Ballif, "Improved amorphous/crystalline silicon interface passivation by hydrogen plasma treatment," *Applied Physics Letters*, vol. 99, p. 123506, sep 2011.

[369] K. Pangal, J. C. Sturm, S. Wagner, and T. H. Büyüklimanli, "Hydrogen plasma enhanced crystallization of hydrogenated amorphous silicon films," *Journal of Applied Physics*, vol. 85, no. 3, pp. 1900–1906, 1999.

[370] J. Dutta, U. Kroll, P. Chabloz, A. Shah, A. A. Howling, J. Dorier, and C. Hollenstein, "Dependence of intrinsic stress in hydrogenated amorphous silicon on excitation frequency in a plasma-enhanced chemical vapor deposition process," *Journal of Applied Physics*, vol. 72, pp. 3220–3222, oct 1992.

[371] A. Lambertz, T. Grundler, and F. Finger, "Hydrogenated amorphous silicon oxide containing a microcrystalline silicon phase and usage as an intermediate reflector in thin-film silicon solar cells," *Journal of Applied Physics*, vol. 109, p. 113109, jun 2011.

[372] M. Kondo, M. Fukawa, L. Guo, and A. Matsuda, "High rate growth of microcrystalline silicon at low temperatures," *Journal of Non-Crystalline Solids*, vol. 266-269, pp. 84–89, 2000.

[373] I. Kaiser, N. H. Nickel, and W. Fuhs, "Hydrogen-mediated structural changes of amorphous and microcrystalline silicon," *Physical Review B*, vol. 58, no. 4, pp. 1718–1721, 1998.

[374] S. Nunomura, I. Sakata, and K. Matsubara, "In-situ detection of interface defects in a-Si:H/c-Si heterojunction during plasma processing," *Applied Physics Express*, vol. 12, no. 5, p. 51006, 2019.

[375] W. Beyer and M. S. A. Ghazala, "Absorption strengths of Si-H vibrational modes in hydrogenated silicon," *MRS Online Proceedings Library Archive*, vol. 507, p. 601, 1998.

[376] H. Fujiwara, M. Kondo, and A. Matsuda, "Stress-induced nucleation of microcrystalline silicon from amorphous phase," *Japanese journal of applied physics*, vol. 41, no. 5R, p. 2821, 2002.

[377] J. Harbison, A. Williams, and D. Lang, "Effect of silane dilution on intrinsic stress in glow discharge hydrogenated amorphous silicon films," *Journal of applied physics*, vol. 55, no. 4, pp. 946–951, 1984.

[378] S. Sheng, H. Hao, H. Diao, X. Zeng, Y. Xu, X. Liao, and T. L. Monchesky, "XPS depth profiling study of n/TCO interfaces for p-i-n amorphous silicon solar cells," *Applied Surface Science*, vol. 253, no. 3, pp. 1677–1682, 2006.

[379] M. Gao, Y. Wan, Y. Li, B. Han, W. Song, F. Xu, L. Zhao, and Z. Ma, "Effective Passivation and Tunneling Hybrid a-SiOx(In) Layer in ITO/n-Si Heterojunction Photovoltaic Device," *ACS Applied Materials and Interfaces*, vol. 9, no. 20, pp. 17565–17575, 2017.

[380] A. Klein, C. Körber, A. Wachau, F. Säuberlich, Y. Gassenbauer, S. P. Harvey, D. E. Proffit, and T. O. Mason, "Transparent conducting oxides for photovoltaics: Manipulation of fermi level, work function and energy band alignment," *Materials*, vol. 3, no. 11, pp. 4892–4914, 2010.

[381] S. M. De Nicolás, D. Muñoz, A. S. Ozanne, N. Nguyen, and P. J. Ribeyron, "Optimisation of doped amorphous silicon layers applied to heterojunction solar cells," *Energy Procedia*, vol. 8, pp. 226–231, 2011.

[382] R. Rößler, C. Leendertz, L. Korte, N. Mingirulli, and B. Rech, "Impact of the transparent conductive oxide work function on injection-dependent a-Si: H/c-Si band bending and solar cell parameters," *Journal of Applied Physics*, vol. 113, no. 14, p. 144513, 2013.

[383] J. Temmler, M. Bivour, H. Steinkemper, and M. Hermle, "Boron doped a-SiC: H front layers for silicon heterojunction cells," in *Proc. 29th Euro. Photovolt. Sol. Energy Conf. Exhib.*, pp. 481–483, 2014.

[384] J. Sritharathikhun, F. Jiang, S. Miyajima, A. Yamada, and M. Konagai, "Optimization of p-type hydrogenated microcrystalline silicon oxide window layer for high-efficiency crystalline silicon heterojunction solar cells," *Japanese Journal of Applied Physics*, vol. 48, no. 10R, p. 101603, 2009.

[385] J. Haschke, R. Monnard, L. Antognini, J. Cattin, A. A. Abdallah, B. Aïssa, M. M. Kivambe, N. Tabet, M. Boccard, and C. Ballif, "Nanocrystalline silicon oxide stacks for silicon heterojunction solar cells for hot climates," *AIP Conference Proceedings*, vol. 1999, p. 30001, aug 2018.

[386] L. Mazzarella, A. B. Morales-Vilches, L. Korte, R. Schlatmann, and B. Stannowski, "Ultra-thin nanocrystalline n-type silicon oxide front contact layers for rear-emitter silicon heterojunction solar cells," *Solar Energy Materials and Solar Cells*, vol. 179, pp. 386–391, 2018.

[387] D. Qiu, W. Duan, A. Lambertz, K. Bittkau, P. Steuter, Y. Liu, A. Gad, M. Pomaska, U. Rau, and K. Ding, "Front contact optimization for rear-junction SHJ solar cells with ultra-thin n-type nanocrystalline silicon oxide," *Solar Energy Materials and Solar Cells*, vol. 209, p. 110471, 2020.

[388] C. Lei, C.-W. Peng, J. Zhong, H. Li, M. Yang, K. Zheng, X. Qu, C. Yu, Y. Li, and X. Xu, "Phosphorus treatment to promote crystallinity of the microcrystalline silicon front contact layers for highly efficient heterojunction solar cells," *Solar Energy Materials and Solar Cells*, vol. 209, p. 110439, 2020.

[389] K. Ding, U. Aeberhard, F. Finger, and U. Rau, "Silicon heterojunction solar cell with amorphous silicon oxide buffer and microcrystalline silicon oxide contact layers," *physica status solidi (RRL) – Rapid Research Letters*, vol. 6, pp. 193–195, may 2012.

[390] S. Dhar, S. Mandal, G. Das, S. Mukhopadhyay, P. P. Ray, C. Banerjee, and A. K. Barua, "Silicon heterojunction solar cells with novel fluorinated n-type nanocrystalline silicon oxide emitters on p-type crystalline silicon," *Japanese Journal of Applied Physics*, vol. 54, no. 8S1, p. 08KD03, 2015.

[391] S. Kirner, L. Mazzarella, L. Korte, B. Stannowski, B. Rech, and R. Schlatmann, "Silicon Heterojunction Solar Cells with Nanocrystalline Silicon Oxide Emitter: Insights into Charge Carrier Transport," *IEEE Journal of Photovoltaics*, vol. 5, no. 6, pp. 1601–1605, 2015.

[392] H. A. Gatz, J. K. Rath, M. A. Verheijen, W. M. M. Kessels, and R. E. I. Schropp, "Silicon heterojunction solar cell passivation in combination with nanocrystalline silicon oxide emitters," *physica status solidi (a)*, vol. 213, pp. 1932–1936, jul 2016.

[393] D. L. Meier and D. K. Schroder, "Contact resistance: Its measurement and relative importance to power loss in a solar cell," *IEEE Transactions on Electron Devices*, vol. 31, no. 5, pp. 647–653, 1984.

[394] R. J. Handy, "Theoretical analysis of the series resistance of a solar cell," *Solid-State Electronics*, vol. 10, no. 8, pp. 765–775, 1967.

[395] A. Cruz, E.-C. Wang, A. B. Morales-Vilches, D. Meza, S. Neubert, B. Szyszka, R. Schlatmann, and B. Stannowski, "Effect of front TCO on the performance of rear-junction silicon heterojunction solar cells: Insights from simulations and experiments," *Solar Energy Materials and Solar Cells*, vol. 195, pp. 339–345, 2019.

[396] C. Messmer, M. Bivour, C. Luderer, L. Tutsch, J. Schön, and M. Hermle, "Influence of Interfacial Oxides at TCO/Doped Si Thin Film Contacts on the Charge Carrier Transport of Passivating Contacts," *IEEE Journal of Photovoltaics*, vol. 10, no. 2, pp. 343–350, 2020.

[397] M. A. Leilaeioun, W. Weigand, M. Boccard, J. Y. Zhengshan, K. Fisher, and Z. C. Holman, "Contact resistivity of the p-type amorphous silicon hole contact in silicon heterojunction solar cells," *IEEE Journal of Photovoltaics*, vol. 10, no. 1, pp. 54–62, 2019.

[398] S. Y. Lee, H. Choi, H. Li, K. Ji, S. Nam, J. Choi, S. W. Ahn, H. M. Lee, and B. Park, "Analysis of a-Si:H/TCO contact resistance for the Si heterojunction back-contact solar cell," *Solar Energy Materials and Solar Cells*, vol. 120, no. PART A, pp. 412–416, 2014.

[399] Synopsys, "Sentaurus Device User," tech. rep., Synopsys, 2013.

[400] P. Muralidharan, M. A. Leilaeioun, W. Weigand, Z. C. Holman, S. M. Goodnick, and D. Vasileska, "Understanding Transport in Hole Contacts of Silicon Heterojunction Solar Cells by Simulating TLM Structures," *IEEE Journal of Photovoltaics*, vol. 10, no. 2, pp. 363–371, 2020.

[401] M. R. Page, E. Iwaniczko, Y. Q. Xu, L. Roybal, F. Hasoon, Q. Wang, and R. S. Crandall, "Amorphous/crystalline silicon heterojunction solar cells with varying i-layer thickness," *Thin Solid Films*, vol. 519, no. 14, pp. 4527–4530, 2011.

[402] M. Mikolášek, M. Nemec, M. Vojs, J. Jakabovič, V. Řeháček, D. Zhang, M. Zeman, and L. Harmatha, "Electrical transport mechanisms in amorphous/crystalline silicon heterojunction: Impact of passivation layer thickness," *Thin Solid Films*, vol. 558, pp. 315–319, 2014.

[403] A. B. Morales-Vilches, L. Mazzarella, M. Hendrichs, L. Korte, R. Schlatmann, and B. Stannowski, "Nanocrystalline vs. amorphous n-type silicon front surface field layers in silicon heterojunction solar cells: Role of thickness and oxygen content," in *33rd European Photovoltaic Solar Energy Conference and Exhibition*, pp. 715–719, 2017.

[404] B. M. Monroy, A. Remolina Millán, M. F. Garcia-Sanchez, A. Ponce, M. Picquart, and G. Santana, "Structure and optical properties of silicon nanocrystals embedded in amorphous silicon thin films obtained by PECVD," *Journal of Nanomaterials*, vol. 2011, pp. 1–9, 2011.

[405] M. Kondo, Y. Toyoshima, A. Matsuda, and K. Ikuta, "Substrate dependence of initial growth of microcrystalline silicon in plasma-enhanced chemical vapor deposition," *Journal of applied physics*, vol. 80, no. 10, pp. 6061–6063, 1996.

[406] T. Watahiki, T. Furuhata, T. Matsuura, T. Shinagawa, Y. Shirayanagi, T. Morioka, T. Hayashida, Y. Yuda, S. Kano, and Y. Sakai, "Rear-emitter Si heterojunction solar cells with over 23% efficiency," *Applied Physics Express*, vol. 8, no. 2, p. 21402, 2015.

[407] H. P. Zhou, M. Xu, S. Xu, L. L. Liu, C. X. Liu, L. C. Kwek, and L. X. Xu, "Hydrogen-plasma-induced Rapid, Low-Temperature Crystallization of μm-thick a-Si: H Films," *Scientific reports*, vol. 6, no. 1, pp. 1–8, 2016.

[408] D. P. Pham, S. Kim, S. Kim, S. Lee, A. H. T. Le, J. Park, and J. Yi, "Ultra-thin stack of n-type hydrogenated microcrystalline silicon and silicon oxide front contact layer for rear-emitter silicon heterojunction solar cells," *Materials Science in Semiconductor Processing*, vol. 96, pp. 1–7, 2019.

[409] R. Santbergen, T. Meguro, T. Suezaki, G. Koizumi, K. Yamamoto, and M. Zeman, "GenPro4 optical model for solar cell simulation and its application to multijunction solar cells," *IEEE journal of photovoltaics*, vol. 7, no. 3, pp. 919–926, 2017.

[410] M. Bailly, J. V. Carpenter, Z. Holman, and S. Bowden, "Substrate dependent growth of microcrystalline silicon," in *2014 IEEE 40th Photovoltaic Specialist Conference (PVSC)*, pp. 1201–1205, IEEE, 2014.

[411] H. Wernerus, M. Bivour, L. Kroely, M. Hermle, and W. Wolke, "Characterization of ultra-thin μc-Si:H films for silicon heterojunction solar cells," *Energy Procedia*, vol. 55, pp. 310–319, 2014.

[412] D. G. Ast and M. H. Brodsky, "Thickness and temperature dependence of the conductivity of phosphorus-doped hydrogenated amorphous silicon," *Philosophical Magazine B*, vol. 41, no. 3, pp. 273–285, 1980.

[413] S. Hasegawa, S. Shimizu, and Y. Kurata, "Thickness dependences of properties of p-and b-doped hydrogenated amorphous silicon: I. dark conductivity and photoconductivity," *Philosophical Magazine B*, vol. 49, no. 5, pp. 511–519, 1984.

[414] S. Hasegawa, S. Shimizu, and Y. Kurata, "Thickness dependences of properties of P-and B-doped hydrogenated amorphous silicon: II. ESR, hydrogen vibrational spectra and optical absorption," *Philosophical Magazine B*, vol. 49, no. 5, pp. 521–532, 1984.

[415] T. Matsumoto, J.-i. Suzuki, M. Ohnuma, Y. Kanemitsu, and Y. Masumoto, "Evidence of quantum size effect in nanocrystalline silicon by optical absorption," *Physical review B*, vol. 63, no. 19, p. 195322, 2001.

[416] J. C. Knights, R. A. Street, and G. Lucovsky, "Electronic and structural properties of plasma-deposited a-Si: O: H-The story of O2," *Journal of Non-Crystalline Solids*, vol. 35, pp. 279–284, 1980.

[417] H. Richter, Z. P. Wang, and L. Ley, "The one phonon Raman spectrum in microcrystalline silicon," *Solid State Communications*, vol. 39, no. 5, pp. 625–629, 1981.

[418] I. H. Campbell and P. M. Fauchet, "The effects of microcrystal size and shape on the one phonon Raman spectra of crystalline semiconductors," *Solid State Communications*, vol. 58, no. 10, pp. 739–741, 1986.

[419] J. Zi, H. Büscher, C. Falter, W. Ludwig, K. Zhang, and X. Xie, "Raman shifts in Si nanocrystals," *Applied Physics Letters*, vol. 69, no. 2, pp. 200–202, 1996.

[420] W. Wei, G. Xu, J. Wang, and T. Wang, "Raman spectra of intrinsic and doped hydrogenated nanocrystalline silicon films," *Vacuum*, vol. 81, no. 5, pp. 656–662, 2007.

[421] H. Kaya, T. Imura, T. Kusao, A. Hiraki, O. Nakamura, Y. Okayasu, and M. Matsumura, "Evaluation of boron and phosphorus doping microcrystalline silicon films," *Japanese Journal of Applied Physics*, vol. 23, no. 8A, p. L549, 1984.

[422] S. Guha, J. Yang, P. Nath, and M. Hack, "Enhancement of open circuit voltage in high efficiency amorphous silicon alloy solar cells," *Applied Physics Letters*, vol. 49, no. 4, pp. 218–219, 1986.

[423] S. Wang, V. Smirnov, T. Chen, B. Holländer, X. Zhang, S. Xiong, Y. Zhao, and F. Finger, "Effects of oxygen incorporation in solar cells with a-SiOx: H absorber layer," *Japanese journal of applied physics*, vol. 54, no. 1, p. 11401, 2014.

[424] K.-J. Chang and D. J. Chadi, "Theory of hydrogen passivation of shallow-level dopants in crystalline silicon," *Physical review letters*, vol. 60, no. 14, p. 1422, 1988.

[425] K. Bergman, M. Stavola, S. J. Pearton, and J. Lopata, "Donor-hydrogen complexes in passivated silicon," *Physical Review B*, vol. 37, no. 5, p. 2770, 1988.

[426] A. Tomasi, B. Paviet-Salomon, Q. Jeangros, J. Haschke, G. Christmann, L. Barraud, A. Descoeudres, J. PeterSeif, S. Nicolay, M. Despeisse, S. De Wolf, and C. Ballif, "Simple processing of back-contacted silicon heterojunction solar cells using selective-area crystalline growth," *Nature Energy*, vol. 2, no. 5, pp. 1–8, 2017.

[427] X. Qu, Y. He, M. Qu, T. Ruan, F. Chu, Z. Zheng, Y. Ma, Y. Chen, X. Ru, X. Xu, H. Yan, L. Wang, Y. Zhang, X. Hao, Z. Hameiri, Z.-G. Chen, L. Wang, and K. Zheng, "Identification of embedded nanotwins at c-Si/a-Si:H interface limiting the performance of high-efficiency silicon heterojunction solar cells," *Nature Energy*, vol. 6, no. 2, pp. 194–202, 2021.

[428] J. Geissbühler, S. De Wolf, B. Demaurex, J. P. Seif, D. T. L. Alexander, L. Barraud, and C. Ballif, "Amorphous/crystalline silicon interface defects induced by hydrogen plasma treatments," *Applied Physics Letters*, vol. 102, no. 23, p. 231604, 2013.

[429] D. Zhang, I. A. Digdaya, R. Santbergen, R. Van Swaaij, P. Bronsveld, M. Zeman, J. A. M. Van Roosmalen, and A. W. Weeber, "Design and fabrication of a SiOx/ITO double-layer antireflective coating for heterojunction silicon solar cells," *Solar Energy Materials and Solar Cells*, vol. 117, pp. 132–138, 2013.

[430] J. Yu, J. Li, Y. Zhao, A. Lambertz, T. Chen, W. Duan, W. Liu, X. Yang, Y. Huang, and K. Ding, "Copper metallization of electrodes for silicon heterojunction solar cells: Process, reliability and challenges," *Solar Energy Materials and Solar Cells*, vol. 224, p. 110993, 2021.

[431] H. Sai, P.-W. Chen, H.-J. Hsu, T. Matsui, S. Nunomura, and K. Matsubara, "Impact of intrinsic amorphous silicon bilayers in silicon heterojunction solar cells," *Journal of Applied Physics*, vol. 124, no. 10, p. 103102, 2018.

[432] S. De Wolf and M. Kondo, "Abruptness of a-Si:H/c-Si interface revealed by carrier lifetime measurements," *Applied Physics Letters*, vol. 90, no. 4, pp. 1–4, 2007.

[433] S.-K. Kim, J. C. Lee, S.-J. Park, Y.-J. Kim, and K. H. Yoon, "Effect of hydrogen dilution on intrinsic a-Si: H layer between emitter and Si wafer in silicon heterojunction solar cell," *Solar energy materials and solar cells*, vol. 92, no. 3, pp. 298–301, 2008.

[434] J. Ge, Z. Ling, J. Wong, T. Mueller, and a.G. Aberle, "Optimisation of Intrinsic a-Si:H Passivation Layers in Crystalline-amorphous Silicon Heterojunction Solar Cells," *Energy Procedia*, vol. 15, no. 2011, pp. 107–117, 2012.

[435] D. Deligiannis, R. Vasudevan, A. H. M. Smets, R. A. van Swaaij, and M. Zeman, "Surface passivation of c-Si for silicon heterojunction solar cells using high-pressure hydrogen diluted plasmas," *AIP Advances*, vol. 5, no. 9, p. 97165, 2015.

[436] Y. Zhang, C. Yu, M. Yang, L.-R. Zhang, Y.-C. He, J.-Y. Zhang, X.-X. Xu, Y.-Z. Zhang, X.-M. Song, and H. Yan, "Significant Improvement of Passivation Performance by Two-Step Preparation of Amorphous Silicon Passivation Layers in Silicon Heterojunction Solar Cells," *Chinese Physics Letters*, vol. 34, no. 3, p. 038101, 2017.

[437] S. N. Granata, T. Bearda, F. Dross, I. Gordon, J. Poortmans, and R. Mertens, "Effect of an in-situ H2 plasma pretreatment on the minority carrier lifetime of a-Si:H (i) passivated crystalline silicon," *Energy Procedia*, vol. 27, pp. 412–418, 2012.

[438] L. Zhang, W. Guo, W. Liu, J. Bao, J. Liu, J. Shi, F. Meng, and Z. Liu, "Investigation of positive roles of hydrogen plasma treatment for interface passivation based on silicon heterojunction solar cells," *Journal of Physics D: Applied Physics*, vol. 49, no. 16, p. 165305, 2016.

[439] A. Soman, U. Nsofor, U. Das, T. Gu, and S. Hegedus, "Correlation between in situ diagnostics of the hydrogen plasma and the interface passivation quality of hydrogen plasma post-treated a-Si: H in silicon heterojunction solar cells," *ACS applied materials & interfaces*, vol. 11, no. 17, pp. 16181–16190, 2019.

[440] M. Xu, C. Wang, T. Bearda, E. Simoen, H. S. Radhakrishnan, I. Gordon, W. Li, J. Szlufcik, and J. Poortmans, "Dry passivation process for silicon heterojunction solar cells using hydrogen plasma treatment followed by in situ a-Si: H deposition," *IEEE Journal of Photovoltaics*, vol. 8, no. 6, pp. 1539–1545, 2018.

[441] A. Neumüller, O. Sergeev, S. J. Heise, S. Bereznev, O. Volobujeva, J. F. L. Salas, M. Vehse, and C. Agert, "Improved amorphous silicon passivation layer for heterojunction solar cells with post-deposition plasma treatment," *Nano Energy*, vol. 43, pp. 228–235, 2018.

[442] S. M. Karabanov and M. A. Reginevich, "Impact of Hydrogen Plasma Treatment on Intrinsic Amorphous Silicon Bilayers in Silicon Heterojunction Solar Cells," in *2021 IEEE International Conference on Environment and Electrical Engineering and 2021 IEEE Industrial and Commercial Power Systems Europe (EEEIC/I&CPS Europe)*, pp. 1–5, IEEE, 2021.

[443] K.-S. Lee, C. B. Yeon, S. J. Yun, K. H. Jung, and J. W. Lim, "Improved surface passivation using dual-layered a-Si: H for silicon heterojunction solar cells," *ECS Solid State Letters*, vol. 3, no. 3, p. P33, 2014.

[444] F. A. Bin Mohd Zulkifly, Y. Shiratori, K. Nakada, and S. Miyajima, "Impact of bilayer structures on the surface passivation quality of high-rate-sputtered hydrogenated amorphous silicon for silicon heterojunction solar cells," *Progress in Photovoltaics: Research and Applications*, vol. 28, no. 9, pp. 971–976, 2020.

[445] W. Liu, L. Zhang, R. Chen, F. Meng, W. Guo, J. Bao, and Z. Liu, "Underdense a-Si: H film capped by a dense film as the passivation layer of a silicon heterojunction solar cell," *Journal of Applied Physics*, vol. 120, no. 17, p. 175301, 2016.

[446] H. Sai, H.-J. Hsu, P.-W. Chen, P.-L. Chen, and T. Matsui, "Intrinsic amorphous silicon bilayers for effective surface passivation in silicon heterojunction solar cells: a comparative study of interfacial layers," *physica status solidi (a)*, vol. 218, no. 9, p. 2000743, 2021.

[447] S. Dauwe, J. Schmidt, and R. Hezel, "Very low surface recombination velocities on p-and n-type silicon wafers passivated with hydrogenated amorphous silicon films," in *Conference Record of the Twenty-Ninth IEEE Photovoltaic Specialists Conference, 2002.*, pp. 1246–1249, IEEE, 2002.

[448] B. Macco, J. Melskens, N. J. Podraza, K. Arts, C. Pugh, O. Thomas, and W. M. M. Kessels, "Correlating the silicon surface passivation to the nanostructure of low-temperature a-Si: H after rapid thermal annealing," *Journal of Applied Physics*, vol. 122, no. 3, p. 35302, 2017.

[449] B. Demaurex, S. De Wolf, A. Descoeudres, Z. Charles Holman, and C. Ballif, "Damage at hydrogenated amorphous/crystalline silicon interfaces by indium tin oxide overlayer sputtering," *Applied Physics Letters*, vol. 101, no. 17, p. 171604, 2012.

[450] Z. Wu, L. Zhang, W. Liu, R. Chen, Z. Li, F. Meng, and Z. Liu, "Role of hydrogen in modifying a-Si: H/c-Si interface passivation and band alignment for rear-emitter silicon heterojunction solar cells," *Journal of Materials Science: Materials in Electronics*, vol. 31, no. 12, pp. 9468–9474, 2020.

[451] C. Luderer, D. Kurt, A. Moldovan, M. Hermle, and M. Bivour, "Intrinsic layer modification in silicon heterojunctions: Balancing transport and surface passivation," *Solar Energy Materials and Solar Cells*, vol. 238, p. 111412, 2022.

[452] S. Nunomura, I. Sakata, H. Sakakita, K. Koga, and M. Shiratani, "Real-time monitoring of surface passivation of crystalline silicon during growth of amorphous and epitaxial silicon layer," *Journal of Applied Physics*, vol. 128, no. 3, p. 33302, 2020.

[453] A. H. Mahan, D. L. Williamson, B. P. Nelson, and R. S. Crandall, "Small-angle X-ray scattering studies of microvoids in a-SiC: H and a-Si: H," *Solar Cells*, vol. 27, no. 1-4, pp. 465–476, 1989.

[454] K. Gotoh, M. Wilde, S. Kato, S. Ogura, Y. Kurokawa, K. Fukutani, and N. Usami, "Hydrogen concentration at a-Si: H/c-Si heterointerfaces—The impact of deposition temperature on passivation performance," *AIP Advances*, vol. 9, no. 7, p. 75115, 2019.

[455] T. F. Schulze, H. N. Beushausen, C. Leendertz, A. Dobrich, B. Rech, and L. Korte, "Interplay of amorphous silicon disorder and hydrogen content with interface defects in amorphous/crystalline silicon heterojunctions," *Applied Physics Letters*, vol. 96, no. 25, p. 252102, 2010.

[456] A. Smakula, "Über erregung und entfärbung lichtelektrisch leitender alkalihalogenide," *Zeitschrift für Physik*, vol. 59, no. 9, pp. 603–614, 1930.

[457] C. Manfredotti, F. Fizzotti, M. Boero, P. Pastorino, P. Polesello, and E. Vittone, "Influence of hydrogen-bonding configurations on the physical properties of hydrogenated amorphous silicon," *Physical Review B*, vol. 50, no. 24, p. 18046, 1994.

[458] C. J. Fang, K. J. Gruntz, L. Ley, M. Cardona, F. J. Demond, G. Müller, and S. Kalbitzer, "The hydrogen content of a-Ge: H and a-Si: H as determined by IR spectroscopy, gas evolution and nuclear reaction techniques," *Journal of Non-Crystalline Solids*, vol. 35, pp. 255–260, 1980.

[459] M. Cardona, "Vibrational spectra of hydrogen in silicon and germanium," *Physica Status Solidi. B, Basic Research*, vol. 118, no. 2, pp. 463–481, 1983.

[460] Y. Xu, X. Liao, G. Kong, X. Zeng, Z. Hu, H. Diao, and S. Zhang, "Microstructure characterization of transition films from amorphous to nanocrocrystalline silicon," *Journal of crystal growth*, vol. 256, no. 1-2, pp. 27–32, 2003.

[461] G.-F. Hou, X.-H. Geng, X.-D. Zhang, J. Sun, J.-J. Zhang, and Y. Zhao, "Evolution of infrared spectra and optical emission spectra in hydrogenated silicon thin films prepared by VHF-PECVD," *Chinese Physics B*, vol. 20, no. 7, p. 77802, 2011.

[462] R. A. Street, C. C. Tsai, J. Kakalios, and W. B. Jackson, "Hydrogen diffusion in amorphous silicon," *Philosophical Magazine B*, vol. 56, no. 3, pp. 305–320, 1987.

[463] R. A. Street, "Hydrogen diffusion and electronic metastability in amorphous silicon," *Physica B: Condensed Matter*, vol. 170, no. 1-4, pp. 69–81, 1991.

[464] W. Beyer, "Hydrogen effusion: a probe for surface desorption and diffusion," *Physica B: Condensed Matter*, vol. 170, no. 1-4, pp. 105–114, 1991.

[465] S. De Wolf and M. Kondo, "Surface passivation properties of stacked doped PECVD a-Si: H layers for hetero-structure c-Si solar cells," in *2006 IEEE 4th World Conference on Photovoltaic Energy Conference (WCPEC-4)*, vol. 2, pp. 1469–1472, IEEE, 2006.

[466] S. De Wolf and M. Kondo, "Nature of doped a-Si:H/c-Si interface recombination," *Journal of Applied Physics*, vol. 105, no. 10, p. 103707, 2009.

[467] T. F. Schulze, C. Leendertz, N. Mingirulli, L. Korte, and B. Rech, "Impact of Fermi-level dependent defect equilibration on Voc of amorphous/crystalline silicon heterojunction solar cells," *Energy Procedia*, vol. 8, pp. 282–287, 2011.

[468] J. P. Mailoa, C. D. Bailie, E. C. Johlin, E. T. Hoke, A. J. Akey, W. H. Nguyen, M. D. McGehee, and T. Buonassisi, "A 2-terminal perovskite/silicon multijunction solar cell enabled by a silicon tunnel junction," *Applied Physics Letters*, vol. 106, p. 121105, mar 2015.

[469] M. Jošt, L. Kegelmann, L. Korte, and S. Albrecht, "Monolithic perovskite tandem solar cells: a review of the present status and advanced characterization methods toward 30% efficiency," *Advanced Energy Materials*, vol. 10, no. 26, p. 1904102, 2020.

[470] X. Y. Chin, D. Turkay, J. A. Steele, S. Tabean, S. Eswara, M. Mensi, P. Fiala, C. M. Wolff, A. Paracchino, K. Artuk, D. Jacobs, Q. Guesnay, F. Sahli, G. Andreatta, M. Boccard, Q. Jeangros, and C. Ballif, "Interface passivation for 31.25%-efficient perovskite/silicon tandem solar cells," *Science*, vol. 381, no. 6653, pp. 59–63, 2023.

[471] S. Mariotti, E. Köhnen, F. Scheler, K. Sveinbjörnsson, L. Zimmermann, M. Piot, F. Yang, B. Li, J. Warby, A. Musiienko, D. Menzel, F. Lang, S. Keßler, I. Levine, D. Mantione, A. Al-Ashouri, M. S. Härtel, K. Xu, A. Cruz, J. Kurpiers, P. Wagner, H. Köbler, J. Li, A. Magomedov, D. Mecerreyes, E. Unger, A. Abate, M. Stolterfoht, B. Stannowski, R. Schlatmann, L. Korte, and S. Albrecht, "Interface engineering for high-performance, triple-halide perovskite-silicon tandem solar cells," *Science*, vol. 381, no. 6653, pp. 63–69, 2023.

[472] K. Datta, *Mixed-Halide Perovskite Semiconductors for Multijunction Photovoltaics*. PhD thesis, Technische Universiteit Eindhoven, 2022.

[473] Y. Jiang, I. Almansouri, S. Huang, T. Young, Y. Li, Y. Peng, Q. Hou, L. Spiccia, U. Bach, and Y.-B. Cheng, "Optical analysis of perovskite/silicon tandem solar cells," *Journal of Materials Chemistry C*, vol. 4, no. 24, pp. 5679–5689, 2016.

[474] L. Mazzarella, Y. Lin, S. Kirner, A. B. Morales-Vilches, L. Korte, S. Albrecht, E. Crossland, B. Stannowski, C. Case, H. J. Snaith, and R. Schlatmann, "Infrared light management using a nanocrystalline silicon oxide interlayer in monolithic perovskite/silicon heterojunction tandem solar cells with efficiency above 25%," *Advanced Energy Materials*, vol. 9, no. 14, p. 1803241, 2019.

[475] R. Santbergen, R. Mishima, T. Meguro, M. Hino, H. Uzu, J. Blanker, K. Yamamoto, and M. Zeman, "Minimizing optical losses in monolithic perovskite/c-Si tandem solar cells with a flat top cell," *Optics Express*, vol. 24, no. 18, pp. A1288–A1299, 2016.

[476] Y. Zhao, K. Datta, N. Phung, A. E. A. Bracesco, V. Zardetto, G. Paggiaro, H. Liu, M. Fardousi, R. Santbergen, P. P. Moya, C. Han, G. Yang, J. Wang, D. Zhang, B. T. van Gorkom, T. P. A. van der Pol, M. Verhage, M. M. Wienk, W. M. M. Kessels, A. Weeber, M. Zeman, L. Mazzarella, M. Creatore, R. A. J. Janssen, and O. Isabella, "Optical Simulation-Aided Design and Engineering of Monolithic Perovskite/Silicon Tandem Solar Cells," *ACS Applied Energy Materials*, vol. 6, no. 10, pp. 5217–5229, 2023.

[477] J. Werner, L. Barraud, A. Walter, M. Bräuninger, F. Sahli, D. Sacchetto, N. Tétreault, B. Paviet-Salomon, S. J. Moon, C. Allebé, M. Despeisse, S. Nicolay, S. De Wolf, B. Niesen, and C. Ballif, "Efficient Near-Infrared-Transparent Perovskite Solar Cells Enabling Direct Comparison of 4-Terminal and Monolithic Perovskite/Silicon Tandem Cells," *ACS Energy Letters*, vol. 1, no. 2, pp. 474–480, 2016.

[478] D. Zhang, K. Datta, V. Zardetto, S. Veenstra, G. Coletti, and R. A. J. Janssen, "Validated Method for Evaluating the Four-Terminal Perovskite/Si Tandem Cell Performance and its Efficiency Potential," *Solar RRL*, vol. 7, p. 2200914, feb 2023.

[479] D. Zhang, M. Najafi, V. Zardetto, M. Dörenkämper, X. Zhou, S. Veenstra, L. J. Geerligs, T. Aernouts, and R. Andriessen, "High efficiency 4-terminal perovskite/c-Si tandem cells," *Solar Energy Materials and Solar Cells*, vol. 188, pp. 1–5, 2018.

[480] M. A. Green and M. J. Keevers, "Optical properties of intrinsic silicon at 300 K," *Progress in Photovoltaics: Research and Applications*, vol. 3, pp. 189–192, jan 1995.

[481] P. B. Johnson and R. W. Christy, "Optical Constants of the Noble Metals," *Physical Review B*, vol. 6, pp. 4370–4379, dec 1972.

[482] H. Liu, "Optimization of Hydrogenated Amorphous Si Layer for Si Heterojunction Solar Cells," master thesis, Technische Universiteit Delft, 2020.

[483] G. Paggiaro, "Optimizations of high-efficiency silicon heterojunction solar cells for tandem applications," master thesis, Technische Universiteit Delft, 2021.

[484] J. Xu, C. C. Boyd, J. Y. Zhengshan, A. F. Palmstrom, D. J. Witter, B. W. Larson, R. M. France, J. Werner, S. P. Harvey, and E. J. Wolf, "Triple-halide wide–band gap perovskites with suppressed phase segregation for efficient tandems," *Science*, vol. 367, no. 6482, pp. 1097–1104, 2020.

[485] K. Datta, B. Branco, Y. Zhao, V. Zardetto, N. Phung, A. Bracesco, L. Mazzarella, M. M. Wienk, M. Creatore, O. Isabella, and R. A. J. Janssen, "Efficient Continuous Light-Driven Electrochemical Water Splitting Enabled by Monolithic Perovskite-Silicon Tandem Photovoltaics," *Advanced Materials Technologies*, vol. 8, no. 2, p. 2201131, 2023.

[486] F. Sahli, B. A. Kamino, J. Werner, M. Bräuninger, B. Paviet-Salomon, L. Barraud, R. Monnard, J. P. Seif, A. Tomasi, Q. Jeangros, A. Hessler-Wyser, S. De Wolf, M. Despeisse, S. Nicolay, B. Niesen, and C. Ballif, "Improved Optics in Monolithic Perovskite/Silicon Tandem Solar Cells with a Nanocrystalline Silicon Recombination Junction," *Advanced Energy Materials*, vol. 8, no. 6, p. 1701609, 2018.

[487] Y. Zhao, M. Fardousi, R. Santbergen, K. Datta, A. E. A. Bracesco, D. Zhang, A. Weeber, M. Zeman, L. Mazzarella, M. Creatore, R. A. Janssen, and O. Isabella, "Optical simulation-aided design and optimization of shj bottom subcells for high-efficiency monolithic perovskite/c-si tandem solar cells," in *SiliconPV2023*, (Delft, the Netherlands), 2023.

[488] F. Peña Camargo, P. Caprioglio, F. Zu, E. Gutierrez-Partida, C. M. Wolff, K. Brinkmann, S. Albrecht, T. Riedl, N. Koch, D. Neher, and M. Stolterfoht, "Halide Segregation versus Interfacial Recombination in Bromide-Rich Wide-Gap Perovskite Solar Cells," *ACS Energy Letters*, vol. 5, pp. 2728–2736, jul 2020.

[489] E. L. Unger, L. Kegelmann, K. Suchan, D. Sörell, L. Korte, and S. Albrecht, "Roadmap and roadblocks for the band gap tunability of metal halide perovskites," *Journal of Materials Chemistry A*, vol. 5, no. 23, pp. 11401–11409, 2017.

[490] M. Stolterfoht, C. M. Wolff, J. A. Márquez, S. Zhang, C. J. Hages, D. Rothhardt, S. Albrecht, P. L. Burn, P. Meredith, T. Unold, and D. Neher, "Visualization and suppression of interfacial recombination for high-efficiency large-area pin perovskite solar cells," *Nature Energy*, vol. 3, no. 10, pp. 847–854, 2018.

[491] M. Stolterfoht, P. Caprioglio, C. M. Wolff, J. A. Márquez, J. Nordmann, S. Zhang, D. Rothhardt, U. Hörmann, Y. Amir, A. Redinger, L. Kegelmann, F. Zu, S. Albrecht, N. Koch, T. Kirchartz, M. Saliba, T. Unold, and D. Neher, "The impact of energy alignment and interfacial recombination on the internal and external open-circuit voltage of perovskite solar cells," *Energy & environmental science*, vol. 12, no. 9, pp. 2778–2788, 2019.

[492] R. D. J. Oliver, P. Caprioglio, F. Peña-Camargo, L. R. V. Buizza, F. Zu, A. J. Ramadan, S. G. Motti, S. Mahesh, M. M. McCarthy, J. H. Warby, Y.-H. Lin, N. Koch, S. Albrecht, L. M. Herz, M. B. Johnston, D. Neher, M. Stolterfoht, and H. J. Snaith, "Understanding and suppressing non-radiative losses in methylammonium-free wide-bandgap perovskite solar cells," *Energy & Environmental Science*, vol. 15, no. 2, pp. 714–726, 2022.

[493] F. H. Isikgor, F. Furlan, J. Liu, E. Ugur, M. K. Eswaran, A. S. Subbiah, E. Yengel, M. De Bastiani, G. T. Harrison, S. Zhumagali, C. T. Howells, E. Aydin, M. Wang, N. Gasparini, T. G. Allen, A. ur Rehman, E. Van Kerschaver, D. Baran, I. McCulloch, T. D. Anthopoulos, U. Schwingenschlögl, F. Laquai, and S. De Wolf, "Concurrent cationic and anionic perovskite defect passivation enables 27.4% perovskite/silicon tandems with suppression of halide segregation," *Joule*, vol. 5, no. 6, pp. 1566–1586, 2021.

[494] S. Chen, X. Xiao, H. Gu, and J. Huang, "Iodine reduction for reproducible and high-performance perovskite solar cells and modules," *Science Advances*, vol. 7, no. 10, p. eabe8130, 2021.

[495] A. Al-Ashouri, E. Köhnen, B. Li, A. Magomedov, H. Hempel, P. Caprioglio, J. A. Márquez, A. B. M. Vilches, E. Kasparavicius, J. A. Smith, N. Phung, D. Menzel, M. Grischek, L. Kegelmann, D. Skroblin, C. Gollwitzer, T. Malinauskas, M. Jošt, G. Matič, B. Rech, R. Schlatmann, M. Topič, L. Korte, A. Abate, B. Stannowski, D. Neher, M. Stolterfoht, T. Unold, V. Getautis, and S. Albrecht, "Monolithic perovskite/silicon tandem solar cell with > 29% efficiency by enhanced hole extraction," *Science*, vol. 370, pp. 1300–1309, dec 2020.

[496] A. Al-Ashouri, A. Magomedov, M. Roß, M. Jošt, M. Talaikis, G. Chistiakova, T. Bertram, J. A. Márquez, E. Köhnen, E. Kasparavičius, S. Levcenco, L. Gil-Escrig, C. J. Hages, R. Schlatmann, B. Rech, T. Malinauskas, T. Unold, C. A. Kaufmann, L. Korte, G. Niaura, V. Getautis, and S. Albrecht, "Conformal monolayer contacts with lossless interfaces for perovskite single junction and monolithic tandem solar cells," *Energy and Environmental Science*, vol. 12, no. 11, pp. 3356–3369, 2019.

[497] I. Levine, A. Al-Ashouri, A. Musiienko, H. Hempel, A. Magomedov, A. Drevilkauskaite, V. Getautis, D. Menzel, K. Hinrichs, T. Unold, S. Albrecht, and T. Dittrich, "Charge transfer rates and electron trapping at buried interfaces of perovskite solar cells," *Joule*, vol. 5, no. 11, pp. 2915–2933, 2021.

[498] E. Aktas, N. Phung, H. Köbler, D. A. González, M. Méndez, I. Kafedjiska, S.-H. Turren-Cruz, R. Wenisch, I. Lauermann, A. Abate, and E. Palomares, "Understanding the perovskite/self-assembled selective contact interface for ultra-stable and highly efficient p–i–n perovskite solar cells," *Energy & Environmental Science*, vol. 14, no. 7, pp. 3976–3985, 2021.

[499] J. T. DuBose and P. V. Kamat, "Hole Trapping in Halide Perovskites Induces Phase Segregation," *Accounts of Materials Research*, vol. 3, no. 7, pp. 761–771, 2022.

[500] X. Zheng, B. Chen, J. Dai, Y. Fang, Y. Bai, Y. Lin, H. Wei, X. C. Zeng, and J. Huang, "Defect passivation in hybrid perovskite solar cells using quaternary ammonium halide anions and cations," *Nature Energy*, vol. 2, p. 17102, jul 2017.

[501] K. O. Brinkmann, T. Becker, F. Zimmermann, C. Kreusel, T. Gahlmann, M. Theisen, T. Haeger, S. Olthof, C. Tückmantel, M. Günster, T. Maschwitz, F. Göbelsmann, C. Koch, D. Hertel, P. Caprioglio, F. Peña-Camargo, L. Perdigón-Toro, A. Al-Ashouri, L. Merten, A. Hinderhofer, L. Gomell, S. Zhang, F. Schreiber, S. Albrecht, K. Meerholz, D. Neher, M. Stolterfoht, and T. Riedl, "Perovskite–organic tandem solar cells with indium oxide interconnect," *Nature 2022 604:7905*, vol. 604, pp. 280–286, apr 2022.

[502] Y. Shao, Y. Yuan, and J. Huang, "Correlation of energy disorder and open-circuit voltage in hybrid perovskite solar cells," *Nature Energy*, vol. 1, no. 1, pp. 1–6, 2016.

[503] Z. Liu, J. Siekmann, B. Klingebiel, U. Rau, and T. Kirchartz, "Interface Optimization via Fullerene Blends Enables Open-Circuit Voltages of 1.35 V in CH3NH3Pb (I0.8Br0.2)3 Solar Cells," *Advanced Energy Materials*, vol. 11, no. 16, p. 2003386, 2021.

[504] M. De Bastiani, A. J. Mirabelli, Y. Hou, F. Gota, E. Aydin, T. G. Allen, J. Troughton, A. S. Subbiah, F. H. Isikgor, J. Liu, L. Xu, B. Chen, E. Van Kerschaver, D. Baran, B. Fraboni, M. F. Salvador, U. W. Paetzold, E. H. Sargent, and S. De Wolf, "Efficient bifacial monolithic perovskite/silicon tandem solar cells via bandgap engineering," *Nature Energy*, vol. 6, no. 2, pp. 167–175, 2021.

[505] Y. Zhao, P. Procel, A. Smets, L. Mazzarella, C. Han, G. Yang, L. Cao, Z. Yao, D. Zhang, V. Zardetto, M. Najafi, M. Creatore, R. A. J. Janssen, S. Veenstra, G. Coletti, A. Weeber, M. Zeman, and O. Isabella, "Effects of (i)a-si:h deposition temperature on high-efficiency silicon heterojunction solar cells for four-terminal tandem solar cells," in *the 8th World Conference on Photovoltaic Energy Conversion (WCPEC-8)*, (Milan, Italy), 2022.

[506] Y. Zhao, R. Santbergen, D. Zhang, M. Najafi, S. Veenstra, G. Coletti, A. Weeber, M. Zeman, L. Mazzarella, and O. Isabella, "Optical design strategies for high-efficiency monofacial and bifacial four-terminal perovskite-silicon tandem modules," in *SiliconPV2023*, (Delft, the Netherlands), 2023.

[507] D. Deligiannis, V. Marioleas, R. Vasudevan, C. C. G. Visser, R. A. van Swaaij, and M. Zeman, "Understanding the thickness-dependent effective lifetime of crystalline silicon passivated with a thin layer of intrinsic hydrogenated amorphous silicon using a nanometer-accurate wet-etching method," *Journal of Applied Physics*, vol. 119, no. 23, p. 235307, 2016.

[508] A. A. Howling, J. Dorier, C. Hollenstein, U. Kroll, and F. Finger, "Frequency effects in silane plasmas for plasma enhanced chemical vapor deposition," *Journal of Vacuum Science & Technology A: Vacuum, Surfaces, and Films*, vol. 10, no. 4, pp. 1080–1085, 1992.

[509] M. Heintze and R. Zedlitz, "New diagnostic aspects of high rate a-Si: H deposition in a VHF plasma," *Journal of non-crystalline solids*, vol. 198, pp. 1038–1041, 1996.

[510] T. Mueller, S. Schwertheim, and W. R. Fahrner, "Application of wide-bandgap hydrogenated amorphous silicon oxide layers to heterojunction solar cells for high quality passivation," in *2008 33rd IEEE Photovoltaic Specialists Conference*, pp. 1–6, IEEE, 2008.

[511] J. Peter Seif, A. Descoeudres, M. Filipič, F. Smole, M. Topič, Z. Charles Holman, S. De Wolf, and C. Ballif, "Amorphous silicon oxide window layers for high-efficiency silicon heterojunction solar cells," *Journal of Applied Physics*, vol. 115, no. 2, 2014.

[512] D. Deligiannis, J. Van Vliet, R. Vasudevan, R. A. C. M. M. Van Swaaij, and M. Zeman, "Passivation mechanism in silicon heterojunction solar cells with intrinsic hydrogenated amorphous silicon oxide layers," *Journal of Applied Physics*, vol. 121, no. 8, 2017.

[513] K. Jiang, W. Liu, Y. Yang, Z. Yan, S. Huang, Z. Li, X. Li, L. Zhang, and Z. Liu, "Functions of oxygen atoms in hydrogenated amorphous silicon oxide layers for rear-emitter silicon heterojunction solar cells," *Journal of Materials Science: Materials in Electronics*, vol. 33, no. 1, pp. 416–426, 2022.

[514] E. Kobayashi, Y. Watabe, T. Yamamoto, and Y. Yamada, "Cerium oxide and hydrogen codoped indium oxide films for high-efficiency silicon heterojunction solar cells," *Solar Energy Materials and Solar Cells*, vol. 149, pp. 75–80, 2016.

[515] K. L. Chopra, S. Major, and D. K. Pandya, "Transparent conductors—a status review," *Thin solid films*, vol. 102, no. 1, pp. 1–46, 1983.

[516] J. E. Medvedeva, "Combining optical transparency with electrical conductivity: challenges and prospects," *Transparent Electronics: From Synthesis to Applications*, vol. 29, 2010.

[517] M. Morales-masis, S. D. Wolf, R. Woods-robinson, J. W. Ager, and C. Ballif, "Transparent Electrodes for Efficient Optoelectronics," *Advanced Electronic Materials*, vol. 3, no. 5, p. 1600529, 2017.

[518] A. Cruz, D. Erfurt, P. Wagner, A. B. Morales-Vilches, F. Ruske, R. Schlatmann, and B. Stannowski, "Optoelectrical analysis of TCO+ Silicon oxide double layers at the front and rear side of silicon heterojunction solar cells," *Solar Energy Materials and Solar Cells*, vol. 236, p. 111493, 2022.

[519] Z. C. Holman, A. Descoeudres, S. De Wolf, and C. Ballif, "Record infrared internal quantum efficiency in silicon heterojunction solar cells with dielectric/metal rear reflectors," *IEEE Journal of Photovoltaics*, vol. 3, no. 4, pp. 1243–1249, 2013.

[520] M. Boccard, L. Antognini, V. Paratte, J. Haschke, M. Truong, J. Cattin, J. Dréon, W. Lin, L.-L. Senaud, and B. Paviet-Salomon, "Hole-selective front contact stack enabling 24.1%-efficient silicon heterojunction solar cells," *IEEE Journal of Photovoltaics*, vol. 11, no. 1, pp. 9–15, 2020.

[521] H. Sai, H. Umishio, and T. Matsui, "Very thin (56 μm) silicon heterojunction solar cells with an efficiency of 23.3% and an open circuit voltage of 754 mV," *Solar RRL*, vol. 5, no. 11, p. 2100634, 2021.

[522] Y. Zhao, P. Procel, C. Han, L. Cao, G. Yang, E. Özkol, A. Alcañiz, K. Kovačević, G. Limodio, R. Santbergen, A. Smets, A. Weeber, M. Zeman, L. Mazzarella, and O. Isabella, "Strategies for realizing high-efficiency silicon heterojunction solar cells," *Solar Energy Materials and Solar Cells*, vol. 258, p. 112413, 2023.

[523] E. Kobayashi, S. De Wolf, J. Levrat, G. Christmann, A. Descoeudres, S. Nicolay, M. Despeisse, Y. Watabe, and C. Ballif, "Light-induced performance increase of silicon heterojunction solar cells," *Applied Physics Letters*, vol. 109, no. 15, 2016.

[524] E. Kobayashi, S. De Wolf, J. Levrat, A. Descoeudres, M. Despeisse, F.-J. Haug, and C. Ballif, "Increasing the efficiency of silicon heterojunction solar cells and modules by light soaking," *Solar Energy Materials and Solar Cells*, vol. 173, pp. 43–49, 2017.

[525] J. Cattin, L.-L. Senaud, J. Haschke, B. Paviet-Salomon, M. Despeisse, C. Ballif, and M. Boccard, "Influence of light soaking on silicon heterojunction solar cells with various architectures," *IEEE Journal of Photovoltaics*, vol. 11, no. 3, pp. 575–583, 2021.

[526] W. Liu, J. Shi, L. Zhang, A. Han, S. Huang, X. Li, J. Peng, Y. Yang, Y. Gao, J. Yu, K. Jiang, X. Yang, Z. Li, W. Zhao, J. Du, X. Song, J. Yin, J. Wang, Y. Yu, Q. Shi, Z. Ma, H. Zhang, J. Ling, L. Xu, J. Kang, F. Xu, J. Liu, H. Liu, Y. Xie, F. Meng, S. De Wolf, F. Laquai, Z. Di, and Z. Liu, "Light-induced activation of boron doping in hydrogenated amorphous silicon for over 25% efficiency silicon solar cells," *Nature Energy*, vol. 7, no. 5, pp. 427–437, 2022.

[527] Y. Zhao, L. Mazzarella, P. Procel Moya, O. Isabella, and M. Zeman, "Electron transport layer- and/or hole transport layer-free silicon heterojunction solar cells, NL2028691B1; WO2023/287279A1," 2021.

[528] P. Procel Moya, G. Yang, M. Zeman, O. Isabella, and L. Mazzarella, "Transparent passivated contacts for Si solar cells, NL2024024B1; EP4046205A1; WO2021075956A1," 2019.

[529] P. Procel Moya and O. Isabella, "Localized passivated contacts for solar cells, P100803NL00," 2022.

[530] Y. Smirnov, L. Schmengler, R. Kuik, P. Repecaud, M. Najafi, D. Zhang, M. Theelen, E. Aydin, S. Veenstra, and S. De Wolf, "Scalable pulsed laser deposition of transparent rear electrode for perovskite solar cells," *Advanced Materials Technologies*, vol. 6, no. 2, p. 2000856, 2021.

[531] Z. Lu, F. Meng, Y. Cui, J. Shi, Z. Feng, and Z. Liu, "High quality of IWO films prepared at room temperature by reactive plasma deposition for photovoltaic devices," *Journal of physics D: applied physics*, vol. 46, no. 7, p. 75103, 2013.

[532] H. Liu, Y. Gong, H. Diao, X. Jia, L. Zhao, W. Wang, W. Wang, and J. Zong, "Comparative study on IWO and ICO transparent conductive oxide films prepared by reactive plasma deposition for copper electroplated silicon heterojunction solar cell," *Journal of Materials Science: Materials in Electronics*, vol. 33, no. 8, pp. 5000–5008, 2022.

[533] H. Steinkemper, F. Feldmann, M. Bivour, and M. Hermle, "Numerical simulation of carrier-selective electron contacts featuring tunnel oxides," *IEEE Journal of Photovoltaics*, vol. 5, no. 5, pp. 1348–1356, 2015.

[534] P. Procel, G. Yang, O. Isabella, and M. Zeman, "Numerical simulations of IBC solar cells based on poly-Si carrier-selective passivating contacts," *IEEE Journal of Photovoltaics*, vol. 9, no. 2, pp. 374–384, 2019.

[535] P. Procel, P. Löper, F. Crupi, C. Ballif, and A. Ingenito, "Numerical simulations of hole carrier selective contacts in p-type c-Si solar cells," *Solar Energy Materials and Solar Cells*, vol. 200, p. 109937, 2019.

[536] S. D. Wolf and E. Aydin, "Tandems have the power," *Science*, vol. 381, no. 6653, pp. 30–31, 2023.

[537] K. Shimakawa, "Percolation-controlled electronic properties in microcrystalline silicon: effective medium approach," *Journal of non-crystalline solids*, vol. 266, pp. 223–226, 2000.

Acknowledgement

The past roughly seven years, including my initiation into photovoltaics through my master of science program and conducting my master thesis at the Photovoltaic Materials and Devices group, feel like a mere glance. After repeated self-reflection, I conclude that these years have truly brought me a life-changing experience, which has greatly enhanced my self-awareness and empowered me to embark on further explorations. Besides the personal growth achieved during my pursuit of the PhD, it has also been a delightful and fulfilling journey, and I sincerely appreciate the guidance, support and encouragement I received along the way from everyone who contributed to them.

First and foremost, I am profoundly grateful to my promoters, Prof. dr. Arthur Weeber, Prof. dr. ir. Olindo Isabella and Prof. dr. Miro Zeman, for placing your trust in me and providing me with the opportunity to pursue my PhD. I am truly fortunate to have you as my supervisors, as you consistently provide invaluable guidance, constructive feedback and detailed advice for shaping my research direction, refining my research ideas and enhancing the quality of my work. The open discussions that we always had greatly contributed to a joyful, transparent and efficient research and working environment for me. During the period around 2019 when I was progressively improving the efficiency of solar cells almost every few weeks, your greeting in the corridor would often be like: "Hi Yifeng, is there another higher efficiency to share?" This is just an example that I gratefully perceived as a recognition of my efforts and a source that continuously fueled my enthusiasm for pushing the performance of solar cells further. Furthermore, I admire your dedication to educating the younger generation of engineers and researchers in the field of PV, thereby contributing to a more sustainable society. This also deepens my understanding of the true purpose of education.

I would like to express my enormous appreciation to the members of my thesis committee, Prof. dr. Ferdinand Grozema, Prof. dr. Pere Roca i Cabarrocas, Prof. dr. Stefaan De Wolf and Dr. Paola Delli Veneri. Thank you very much for graciously accepting our invitation to be the committee member and for investing your time in thoroughly reviewing this thesis. I am extremely grateful for your invaluable insights, thoughtful comments and guidance that have enhanced the quality of my PhD thesis. Your expertise and diverse perspectives have also greatly enriched my understanding of my PhD topic. I would like to also thank Prof. dr. ir. Pavol Bauer for being the reserved committee member.

I would like to extend my heartfelt thanks to my daily supervisor Dr. Luana Mazzarella, and the 'Shi Fu', Dr. Paul Procel. Both of you consistently offered your unwavering support and inspiration throughout these years. I deeply value your mentorship, especially those constant scientific discussions we engaged in, whether they were in offices, while walking around the campus, or during coffee breaks. These discussions assisted me in comprehending better the results and sparked numerous research ideas to be explored further. Whenever I measured solar cells, you would eagerly join me to witness and celebrate every possible little efficiency improvement resulting from the ideas that came out from our discussions. Moreover, I truly appreciate your emotional support during some challenging times, as you acted not just as mentors but also as experienced and understanding friends. Last but not least, I have always relied on both of you to review the initial drafts of my manuscripts, ensuring a clear and coherent story is presented. I would like to thank Dr. Filiberto Ricciardella, the partner of Luana, for sometimes 'being involved' in our scientific discussions and for enjoying relaxed moments together. Last but not least, I am extremely delighted to become Sophie's 'Uncle Zhao'.

I consider myself very lucky to have had the opportunity to collaborate with Dr. Can Han on an almost daily basis. Your consistent reliability, professionalism, collaborative spirit and passion for exploratory research inspired me to learn from you. The mutual trust we placed in each other set up a strong foundation for achieving remarkable results, including the demonstration of the best-performing crystalline silicon solar cells within the group, and within the Netherlands. Thanks to you, I also improved my ability to use Chinese to describe professional terms related to PV, as I started learning all these terms from the invaluable 'Solar Energy' book written by our group.

Since the beginning of my internship and master thesis project in the group, Dr. Guangtao Yang, a true master in the lab, has been an excellent mentor. You guided me to know the lab from scratch and improved my practical skills by generously sharing your expertise. Your calm personality, open-mindedness, patience, and willingness to offer assistance both professionally and personally make you a mentor not only in research but also in life. I would like to extend my appreciation to your partner, Wei Cui, for her warm and constant support in life. The time we spent together, including the moments when I occasionally took care of the boys, allowed me to gain a unique perspective on getting to know the Netherlands.

I would like to express my sincere appreciation to Dr. Rudi Santbergen for providing detailed guidance in utilizing the GenPro4 optical simulation model for my research in single-junction and tandem solar cells. I cherish the days when we were in the same offices and the open discussions we had on various topics. You speak always calmly and with great patience, which is a trait I hope I can acquire with time.

My immense thanks go to Prof. dr. Arno Smets for the very insightful discussions regarding the FTIR study of (*i*)a-Si:H layers. During these discussions, I was impressed by your extensive and solid theoretical background, as well as your rich practical experience. Notably, I could sense your pure scientifically-driven passion to comprehend the results as we delved deeper into our discussions.

I would like to convey my sincere thanks to Dr. Frans D. Tichelaar for performing TEM and EDX measurements on SHJ solar cells with thin (*n*)-contacts. Your professionalism has provided significant insights into the question that I had in my mind: are there any observable nanocrystals in such a 3-nm-thick (*n*)nc-Si:H layer? Despite the seemingly negative answer, thanks to your very sharp observation, we discovered other intriguing findings, including unexpected interfacial oxidation at (*n*)nc-Si:H/ITO interface and Si atoms stacking faults on top of the c-Si substrate. These observations facilitated optimization strategies that further enhanced the performance of our solar cells.

I am truly grateful to have had Martijn Tijssen, Stefaan Heirman, Daragh O'Connor and Remko Koornneef guaranteeing consistent technical support throughout my PhD project. Your extensive expertise and unwavering dedication ensured the smooth operation of the labs. It was a fulfilling experience collaborating with all of you, and I greatly appreciated your prompt response to my lab-related concerns (of course, during working hours). The technical insights you have shared with me through our discussions have been invaluable for expanding my understanding of the experimental process and equipment utilized in my research. I always remember once Martijn jokingly said, "Yifeng, hold your horse!", in response to my flurry of messages sent within a short time regarding an issue I encountered in the lab. This response later became a mindset reminding me to stay cool whenever a problem arise, instead of getting overwhelmed by thoughts of process delays or unacceptable setbacks. Sometimes, the equipment also needs to take a break, just like we do.

I also want to express my sincere gratitude to Dr. Engin Özkol for the numerous collaborations and enjoyable coffee time we had together. It seemed that you intentionally left the group during almost my entire PhD project to Helmholtz-Zentrum Berlin, perhaps because, as you often said, "Yifeng is the only one who can wake me up early on Sunday morning and make me go to the

lab." Putting this joke aside, the joint initial development of nc-SiO$_x$:H layers for SHJ solar cells (included in the reference cluster of Figure 9.1), the passivation optimization for black silicon and your insightful introduction of plasma physics to me, have been beneficial for my research. You did not trust the automation in AMIGO, choosing instead to operate it manually in the lab while impressing me with your fast speed in playing the minesweeper.

Two are better than one when it comes to energy transition. I came up with this statement while cooperating with partners within the Joint Solar Program III (JSP III) project. I would like to first acknowledge the funding provided by the NWO JSP III project. I am sincerely grateful to my colleagues at the Eindhoven University of Technology and TNO Eindhoven for your expertise on perovskite solar cells that significantly advanced this PhD project. Especially, many thanks go to Prof. dr. René Janssen, Prof. dr. Mariadriana Creatore, Dr. Kunal Datta, Dr. Nga Phung, Andrea Bracesco and Bruno Branco, mainly for the fruitful and constructive discussions and productive collaborations we had while developing 2T tandem solar cells and their applications in solar-to-hydrogen water-splitting systems. The contributions from other colleagues at the Eindhoven University of Technology, namely, Dr. Junke Wang, Dr. Bas T. van Gorkom, Tom P. A. van der Pol, Michael Verhage, Dr. Martijn M. Wienk, Prof. dr. Wilhelmus M. M. Kessels, were also crucial in understanding and fabrication of 2T tandem solar cells. I would also like to express my sincere gratitude to colleagues at TNO Eindhoven, namely, Dr. Sjoerd Veenstra, Dr. Gianluca Coletti, Dr. Dong Zhang, Dr. Valerio Zardetto, Dr. Mehrdad Najafi and colleagues from imec mainly for successfully realizing the over 30%-efficient 4T tandem solar cell. Dr. Dong Zhang and Dr. Valerio Zardetto also contributed to the development of 2T tandem solar cells. Collaborating with all of you has been an incredibly rewarding and pleasant experience. Moreover, I would like to also acknowledge all other JSPIII project partners, including but not limited to AMOLF (Prof. dr. Erik Garnett, Prof. dr. Albert Polman, Dr. Esther Alarcon Llado, Dr. Hongyu Sun and Yorick Bleiji), and the University of Amsterdam (Prof. dr. Peter Schall and Dr. Yingying Tang) for valuable knowledge exchange throughout this project. My thanks also go to Petra Manshanden and Eric Kossen at TNO Petten for instructing me on advanced solar cell characterizations with procedures similar to that of the calibration institute and advanced screen-printing using industrial tools, respectively. I would like to acknowledge Dr. Martin Ledinský from the Institute of Physics of the Czech Academy of Sciences for the measurements and discussion on the crystallinity of very thin (p)nc-SiO$_x$:H.

I would like to also thank the staff members of Else Kooi Laboratory, including Dr. Paolo Sberna, Tom Scholtes, Robert Verhoeven, Dr. Gregory Pandraud, Loek Steenweg, Silvana Milosavljevic, Dr. Hitham Amin Hassan, Dr. Johannes van Wingerden, Dr. Bruno Morana, Dr. Aleksandar Jović, Mario Laros, Vinod Narain, Bianca Knot, Vincent van Croonenburg and others, for your kind support and enlightening inter-disciplinary discussions.

There is one thing in common among members of the PVMD group, and that is the willingness to help others and share their knowledge, this made the time with them truly inspirational and enjoyable and made me feel part of the group. My sincere appreciation first goes to Mark Vielvoije, Marieke Bijl, Sharmila Rattansingh, Margot Witteveen-Visser, Carla Jager, Ilona van der Wenden, Claudia de Kooter and Ellen Schwencke-Karlas for your always timely assistance and managing various administrative tasks. Hi Mark, can you notice anything related to Zelda in this report?

I would like to express my gratitude to Dr. René van Swaaij for your openness, and for providing rich and unique insights during our discussions. I also cherish the time I have spent together with Prof. dr. Ivan Gordon during the 5$^{\text{th}}$ International Workshop on Silicon Heterojunction solar cells in Aix-les-Bains and with Dr. Malte Ruben Vogt after the 8$^{\text{th}}$ World Conference on Photovoltaic Energy Conversion conferences in Milan. I appreciate the coffee breaks I had with Dr. Hesan Ziar and Dr. Patrizio Manganiello, during which I often found motivation and inspiration. I would like to express my gratitude to Tim Velzeboer, Dr. Mehmet Karaman and Dr. Engin Özkol for patiently addressing my questions throughout the Applied Vacuum Technology course, and also

for the enjoyable coffee breaks we had together.

Time flies, and perhaps one notable indication is the pile of PhD thesis hard copies resting on my office desk. I would like to thank all my officemates for creating a positive and harmonious working environment. It was a great pleasure working alongside many creative researchers and I value the friendship we have formed during our time together. Thank you to Dr. Rudi Santbergen, Manvika Singh, Dr. Daniele Scirè, Dr. Yudai Yamashita, Yilong Zhou, Maarten Verkou, Youri Blom and Dr. Zain Ul Abdin. Yudai, I sincerely appreciate your hospitality in Tokyo, and I truly enjoyed the photos you posted, particularly those astonishing ones capturing the fireworks. I hold our friendship in high regard. Yilong, thank you for always offering your help whenever needed, for the thoughtful talks we had and for organizing the very enjoyable laser tag event. Youri, my younger Dutch 'brother', your consistent daily questions to me have convinced me that you will accomplish your PhD project with great success.

Besides, I am fortunate that I have had so many reliable, experienced and supportive colleagues, with whom we have also shared many delightful moments. I appreciate Dr. Yilei Tian for providing guidance and insights on Raman spectroscopy measurements, and for generously sharing your experience on both professional and personal aspects of life with me. My appreciation also goes to Dr. Robin Vismara for offering advice on debugging my optical simulations and for the training on the Lambda spectrophotometer. Thanks to Dr. Gianluca Limodio (the biggest boss), I had my first published peer-reviewed article (co-authored). Moreover, I like that you spread positive vibes through your constant state of relaxation and joy. I would like to thank Dr. Nasim Rezaei for sharing her expertise on spectroscopic ellipsometry. I frequently recall Dr. Paula Perez Rodriguez's words to me in 2018: "It is not healthy to use AMOR for four days per week". This serves as a reminder to myself to prioritize work-life balance. I appreciate Dr. Thierry de Vrijer for our scientific discussions on layer optimizations in AMIGO. Thank you Dr. Klaas Bakker for your kind help during my visit to TNO Eindhoven. I would also like to thank Dr. Andres Calcabrini for sharing his knowledge on optimizing the processing parameters of the laser cutter when it just arrived.

I extend my sincere gratitude to Liqi Cao and Katarina Kovačević for co-supervising the master students during my absence in the lab and for their consistent dedication to ensure the smooth and reproducible operation of low-thermal budget solar cell baseline, as well as advancing this technology even further. Thank you, Liqi, for the precious moments we have spent together, especially, those on road cycling. You rode over 20 km to buy an inner tire and rescue me from a situation with a flat tire in the middle of nowhere. In short, I extend my best wishes to both of you for resounding success in your respective PhD projects! Moreover, I would like to acknowledge Dr. Carlos M. Ruiz Tobon, Dr. Mirco Muttillo, Juan Camilo Ortiz Lizcano, Ana Rita Bento Montes, Dr. Zameer Ahamd, Dr. Zhirong Yao, Dr. Dimitrios Deligiannis, Dr. Fai Tong Si, Dr. Yuan Gao, Arturo Martinez Lopez, Alba Alcañiz Moya, David van Nijen, Jin Yan, Dr. Chengjian Xu, Afshin Nazer, Sho Aonuki, Federica Saitta, Haoxu Wang, Jonathan Henzel, Yingwen Zhao, Wenxian Wang, Bernardus Zijlstra, Shuang Hao, Govind Padmakumar, Reinder Boekhoff, Alex Katsikogiannis and Dr. Moumita Rana. As former or present members of the PVMD group, you have made contributions in many ways, whether they were professional or personal, big or small, to the accomplishment of my PhD project. Thank you and wish you all the best!

Surely, I would like to take a moment to express my appreciation to the master students I have supervised and co-supervised. Thank you to Hanchen Liu, Chaofeng Li, Giulia Paggiaro, Mohua Fardousi, Katarina Kovačević, Yi Zheng, Narasimha Raju Pusapati, Maria Magalhães, Sebastian Smits and Flip Reutelingsperger. Working with you has been both a pleasure and a fulfilling experience. Your findings and discoveries have directly or indirectly contributed to my PhD project. I am proud in witnessing your accomplishments and growth throughout our collaboration, and I am delighted to see your ongoing pursuit of your dreams all over the world. I genuinely hope that you continue to love what you do and find joy in every aspect of life!

My dear friend, Peiqing Guo, or Guo Lao Ban (boss), thanks for being such a wonderful friend since the beginning of our master program in Delft. We have shared countless joyful and thoughtful moments together, especially, our 'virtual' meetups via VR to play Table Tennis and Golf during the challenging COVID time not only provided me with a source of enjoyment but also expanded my horizons beyond academia. Let's continue to be companions on our life journey, just like the incredible time we spent in Texel, Düsseldorf and Azores alongside your partner, Dr-to-be Shengqing Xiao.

I would also like to thank Dr. Yue Zhang and PDEng. Rong Yu, I cherish the precious memories and delicious food we had both in Delft and Maastricht. Yue, I truly admire your courage to embrace change and the successful completion of your PhD project on cryogenic electron microscopy of biological samples. Hope our friendship can thrive and grow even further! Best wishes to both of you!

Dr-to-be Jin Tang, thank you for your special visit from Helsinki to Delft and for our frank exchange of feelings about life and PhD in these years. I deeply value our friendship. I would like to express my gratitude to all my friends for their care and help over these years, and especially, thank you Zhimin Zhou for the memorable travel together to Napels, thank you Dr-to-be Jian Li for generously sharing life and work experience, as well as being a gracious host in Eindhoven, thank you Dr. Boyao Zhang for delivering buckets of paint I needed in urgent. My special thank goes to Yiyi Chen for kindly sharing your beautifully and artistically designed Chinese character 'Fu (福)', symbolizing luck and blessing, with me for celebrating every Chinese new year. My appreciation also goes to Dr. Qiang Liu, Wei Yuan and Shilong Fu.

When I was composing this acknowledgement, I scrolled through the photo album on my phone, hoping to pick up some distant memories. To my delightful surprise (or perhaps, as expected), the majority of my photo album was filled with moments captured alongside you, my beloved partner, Yiran Zhao. Your constant company has been a source of immense comfort and strength throughout this journey. We have grown together, shared weal and woe, and provided unwavering support to each other. Your lighthearted and humorous spirit has consistently brought joy and relaxation to our shared moments. Simply put, being with you is an absolute pleasure, and I am deeply grateful beyond words for your love and support, and above all, you are always right. I look forward to extending our journey together even further, as I have truly cherished being a chef at home and crafting meals for you! I would also like to extend my heartfelt gratitude to Yiran's parents for their genuine care and consistent support, making me feel loved and accepted.

During the last year of my bachelor study in China, my mother, Li Song, sent me a long text message. In this message, she expressed her support for my decision to study abroad, and mentioned 'A man's ambitions should reach far and wide.' Mom, I am immensely grateful that your vision, unconditional support, and faith in me have been instrumental in helping me to achieve this significant milestone that also belongs to you. I extend my heartfelt gratitude to Uncle Liu for his support and care throughout the years. I am really fortunate that I have such an incredibly united family, from my grandparents to my aunts, uncles, cousins and their partners, and even my young nephews have shown their support in many forms. You have been pillars of strength in my life, standing by me throughout this journey and sharing the joys of my accomplishments. My deepest admiration goes to my father, Wenbin Zhao. You are an exceptional role model in every dimension of my life, and your greatness perpetually stands unparalleled in my thoughts.

Lastly, it is truly fantastic how artificial intelligence has rapidly evolved in recent years and turned what once seemed unattainable into reality. Just like those developing artificial intelligence, the developments made in many other fields, such as renewable energy technologies and medical research, reflect the brilliance of all scientists dedicated to advancing and improving our world. Their collective efforts are reshaping our future, and they deserve our profound gratitude for making the extraordinary a part of our everyday lives.

List of Publications

First-authored peer-reviewed journal articles

1. **Y. Zhao**, P. Procel, C. Han, L. Cao, G. Yang, E. Özkol, A. Alcañiz, K. Kovačević, G. Limodio, R. Santbergen, A. Smets, A. Weeber, M. Zeman, L. Mazzarella and O. Isabella, "Strategies for realizing high-efficiency silicon heterojunction solar cells", *Solar Energy Materials and Solar Cells*, vol. 258, p. 112413, 2023.

2. **Y. Zhao**[1], K. Datta, N. Phung, A. E. A. Bracesco, V. Zardetto, G. Paggiaro, H. Liu, M. Fardousi, R. Santbergen, P. Procel Moya, C. Han, G. Yang, J. Wang, D. Zhang, B. T. van Gorkom, T. P. A. van der Pol, M. Verhage, M. M. Wienk, W. M. M. Kessels, A. Weeber, M. Zeman, L. Mazzarella, M. Creatore, R. A. J. Janssen, and O. Isabella, "Optical simulation-aided design and engineering of monolithic perovskite/silicon tandem solar cells," *ACS Applied Energy Materials*, vol. 6, no. 10, pp. 5217–5229, 2023.

3. K. Datta, B. Branco, **Y. Zhao**[2], V. Zardetto, N. Phung, A. Bracesco, L. Mazzarella, M. M. Wienk, M. Creatore, and O. Isabella, "Efficient Continuous Light-Driven Electrochemical Water Splitting Enabled by Monolithic Perovskite-Silicon Tandem Photovoltaics," *Advanced Materials Technologies*, vol. 8, no. 2, p. 2201131, 2023.

4. **Y. Zhao**, P. Procel, A. Smets, L. Mazzarella, C. Han, G. Yang, L. Cao, Z. Yao, A. Weeber, M. Zeman, and O. Isabella, "Effects of (*i*)a-Si: H deposition temperature on high-efficiency silicon heterojunction solar cells," *Progress in Photovoltaics: research and applications*, 2022.

5. **Y. Zhao**, L. Mazzarella, P. Procel, C. Han, F. D. Tichelaar, G. Yang, A. Weeber, M. Zeman, and O. Isabella, "Ultra-thin electron collectors based on nc-Si:H for high-efficiency silicon heterojunction solar cells," *Progress in Photovoltaics: research and applications*, vol. 30, no. 8, pp. 809–822, 2022.

6. **Y. Zhao**, P. Procel, C. Han, L. Mazzarella, G. Yang, A. Weeber, M. Zeman, and O. Isabella, "Design and optimization of hole collectors based on nc-SiO_x:H for high-efficiency silicon heterojunction solar cells," *Solar Energy Materials and Solar Cells*, vol. 219, p. 110779, 2021.

7. **Y. Zhao**, L. Mazzarella, P. Procel, C. Han, G. Yang, A. Weeber, M. Zeman, and O. Isabella, "Doped hydrogenated nanocrystalline silicon oxide layers for high-efficiency c-Si heterojunction solar cells," *Progress in Photovoltaics: Research and Applications*, vol. 28, no. 5, pp. 425–435, 2020.

Co-authored peer-reviewed journal articles

1. Z. Yao, G. Yang, C. Han, P. Procel Moya, E. Özkol, J. Yan, **Y. Zhao**, L. Cao, R. van Swaaij, L. Mazzarella and O. Isabella, "Poly-SiO_x passivating contacts with plasma-assisted N_2O oxidation of silicon (PANO-SiO_x)," *Solar RRL*, in press, 2023.

2. M. Singh, K. Datta, A. Amarnath, F. Wagner, **Y. Zhao**, G. Yang, A. Bracesco, N. Phung, D. Zhang, V. Zardetto, M. Najafi, S. C. Veenstra, G. Coletti, L. Mazzarella, M. Creatore, M. M.

[1] co-first author with K. Datta

[2] co-first author with K. Datta and B. Branco

Wienk, R. A. J. Janssen, A. W. Weeber, M. Zeman, and O. Isabella, "Crystalline silicon solar cells with thin poly-SiOx carrier-selective passivating contacts for perovskite/c-Si tandem applications", *Progress in Photovoltaics: research and applications*, in press, 2023.

3. G. Yang, R. Gram, P. Procel, C. Han, Z. Yao, M. Singh, **Y. Zhao**, L. Mazzarella, M. Zeman, and O. Isabella, "Will SiOx-pinholes for SiOx/poly-Si passivating contact enhance the passivation quality?" *Solar Energy Materials and Solar Cells*, vol. 252, p. 112200, 2023.
4. L. Cao, P. Procel, A. Alcañiz, J. Yan, F. Tichelaar, E. Özkol, **Y. Zhao**, C. Han, G. Yang, Z. Yao, M. Zeman, R. Santbergen, L.Mazzarella, and O. Isabella, "Achieving 23.83% conversion efficiency in silicon heterojunction solar cell with ultra-thin MoOx hole collector layer via tailoring (i)a-Si: H/MoOx interface," *Progress in Photovoltaics: research and applications*, 2022.
5. T. de Vrijer, D. van Nijen, H. Parasramka, P. A. Procel Moya, **Y. Zhao**, O. Isabella, and A. H. M. Smets, "The fundamental operation mechanisms of nc-SiOX ≥ 0: H based tunnel recombination junctions revealed," *Solar Energy Materials and Solar Cells*, vol. 236, p. 111501, 2022.
6. C. Han, G. Yang, P. Procel, D. O'Connor, **Y. Zhao**, A. Gopalakrishnan, X. Zhang, M. Zeman, L.Mazzarella, and O. Isabella, "Controllable simultaneous bifacial Cuplating for high efficiency crystalline silicon solar cells," *Solar RRL*, vol. 6, no. 6, p. 2100810, 2022.
7. G. Yang, C. Han, P. Procel, **Y. Zhao**, M. Singh, L. Mazzarella, M. Zeman, and O. Isabella, "Oxygen-alloyed poly-Si passivating contacts for high-thermal budget c-Si heterojunction solar cells," *Progress in Photovoltaics: research and applications*, vol. 30, no. 2, pp. 141-151, 2022.
8. C.Han, R. Santbergen, M. van Duffelen, P. Procel, **Y. Zhao**, G. Yang, X. Zhang, M. Zeman, L. Mazzarella, and O. Isabella, "Towards bifacial silicon heterojunction solar cells with reduced TCO use," *Progress in Photovoltaics: Research and Applications*, vol. 30, no. 7, pp. 750–762, 2022.
9. L. Mazzarella, A. Alcañiz, P. Procel, E. Kawa, **Y. Zhao**, U. Tiringer, C. Han, G. Yang, P. Taheri, M. Zeman, and O. Isabella, "Strategy to mitigate the dipole interfacial states in (i)a-si: H/MoOx passivating contacts solar cells," *Progress in Photovoltaics: research and applications*, vol. 29, no. 3, pp. 391–400, 2021.
10. C. Han, **Y. Zhao**, L. Mazzarella, R. Santbergen, A. Montes, P. Procel, G. Yang, X. Zhang, M. Zeman, and O. Isabella, "Room-temperature sputtered tungsten-doped indium oxide for improved current in silicon heterojunction solar cells," *Solar Energy Materials and Solar Cells*, vol. 227, p. 111082, 2021.
11. C. Han, G. Yang, A. Montes, P. Procel, L. Mazzarella, **Y. Zhao**, S. Eijt, H. Schut, X. Zhang, M. Zeman, and O. Isabella, "Realizing the Potential of RF-Sputtered Hydrogenated Fluorine-Doped Indium Oxide as Electrode Materials for Ultrathin SiOx/Poly-Si Passivating Contacts," *ACS Applied Energy Materials*, vol. 3, no. 9, pp. 8606–8618, 2020.
12. P. Procel, H. Xu, A. Saez, C. Ruiz-Tobon, L. Mazzarella, **Y. Zhao**, C. Han, G. Yang, M. Zeman, and O. Isabella, "The role of heterointerfaces and subgap energy states on transport mechanisms in silicon heterojunction solar cells," *Progress in Photovoltaics: research and applications*, vol. 28, no. 9, pp. 935–945, 2020.
13. E. Özkol, P. Procel, **Y. Zhao**, L. Mazzarella, R. Medlin, P. Šutta, O. Isabella, M. Zeman, "Effective Passivation of Black Silicon Surfaces via Plasma-Enhanced Chemical Vapor Deposition Grown Conformal Hydrogenated Amorphous Silicon Layer," *Physica Status Solidi - Rapid Research Letter*, vol. 14, no. 1, 2020.

14. C. Han, L. Mazzarella, **Y. Zhao**, G. Yang, P. Procel, M. Tijssen, A. Montes, L. Spitaleri, A. Gulino, X. Zhang, O. Isabella, and M. Zeman, "High-mobility Hydrogenated Fluorine-doped Indium Oxide Film for Passivating Contacts c-Si Solar Cells," *ACS Applied Materials & Interfaces*, vol. 11, no. 49, pp. 45586–45595, 2019.
15. G. Limodio, Y. De Groot, G. Van Kuler, L. Mazzarella, **Y. Zhao**, P. Procel, G. Yang, O. Isabella, and M. Zeman, "Copper-plating metallization with alternative seed layers for c-Si solar cells embedding carrier-selective passivating contacts," *IEEE journal of photovoltaics*, vol. 10, no. 2, pp. 372–382, 2019.
16. G. Limodio, G. D'Herouville, L. Mazzarella, **Y. Zhao**, G. Yang, O. Isabella, and M. Zeman, "High temperature oxidation pre-treatment of textured c-Si wafers passivated by a-Si: H," *Materials Science in Semiconductor Processing*, vol. 97, pp. 67-70, 2019.

Conference Proceedings

1. **Y. Zhao**, P. Procel, A. H. M. Smets, L. Mazzarella, C. Han, L. Cao, G. Yang, Z. Yao, A. Weeber, M. Zeman, and O. Isabella, "Effects of (i) a-Si: H deposition temperature on passivation quality and performance of high-efficiency silicon heterojunction solar cells", *2022 IEEE 49th Photovoltaics Specialists Conference (PVSC)*, Philadelphia, PA, USA, pp. 0484-0484, 2022.
2. D. Scirè, M. Bonadonna, **Y. Zhao**, P. Procel, O. Isabella, M. Zeman, R. Macaluso, M. Mosca, and I. Crupi, "Analysis of Transition Metal Oxides based Heterojunction Solar Cells with S-shaped JV curves", *2020 AEIT International Annual Conference (AEIT)*, Catania, Italy, pp. 1-6, 2020.
3. L. Mazzarella, A. Alcañiz-Moya, E. Kawa, P. Procel, **Y. Zhao**, C. Han, G. Yang, M. Zeman, and O. Isabella, "Strategy to mitigate the dipole interfacial states in (i)a-Si:H/MoOx passivating contacts solar cells", *2020 47th IEEE Photovoltaic Specialists Conference (PVSC)*, Calgary, AB, Canada, pp. 0405-0407, 2020.
4. M. Zeman, G. Yang, P. Procel Moya, G. Limodio, **Y. Zhao**, A. Weeber, and O. Isabella, "High-efficiency crystalline silicon solar cell architectures", *2018 12th International Conference on Advanced Semiconductor Devices and Microsystems (ASDAM)*, Smolenice, Slovakia, pp. 1-6, 2018.

Patent applications

1. P. Procel Moya, **Y. Zhao**, L. Cao, K. Kovačević and O. Isabella, "Simplified processing of interdigitated-back-contacted silicon heterojunction solar cells", the Netherlands, NL2033406.
2. **Y. Zhao**, L. Mazzarella, P. A. Procel Moya, O. Isabella and M. Zeman, "Electron Transport Layer- and/or Hole Transport Layer-Free Silicon HeteroJunction Solar Cells", the Netherlands, NL2028691B1; WO2023287279A1.

First-authored conference contributions

1. **Y. Zhao**, M. Fardousi, R. Santbergen, K. Datta, A.E.A. Bracesco, D. Zhang, A. Weeber, M. Zeman, L. Mazzarella, M. Creatore, R. A. J. Janssen, and O. Isabella, "Optical simulation-aided design and optimization of SHJ bottom subcells for high-efficiency monolithic perovskite/c-Si tandem solar cells", *2023 40th European PV Solar Energy Conference and Exhibition (EUPVSEC)*, Lisbon, Portugal, poster presentation, 2023.

2. **Y. Zhao**, R. Santbergen, D. Zhang, V. Zardetto, M. Najafi, S. Veenstra, G. Coletti, A. Weeber, M. Zeman, L. Mazzarella, and O. Isabella, *2023 40th European PV Solar Energy Conference and Exhibition (EUPVSEC)*, Lisbon, Portugal, poster presentation, 2023.
3. **Y. Zhao**, D. Zhang, V. Zardetto, M. Najafi, R. Santbergen, M. Creatore, R. Janssen, S. Veenstra, G. Coletti, A. Weeber, M. Zeman, L. Mazzarella, and O. Isabella, "High-efficiency 4-terminal perovskite-silicon tandem solar cell and optical design strategies for monofacial and bifacial 4-terminal tandem modules", *2023 Sunday*, Ede, the Netherlands, oral presentation, 2023. [3]
4. **Y. Zhao**, R. Santbergen, D. Zhang, M. Najafi, S. Veenstra, G. Coletti, A. Weeber, M. Zeman, L. Mazzarella, and O. Isabella, "Optical design strategies for high-efficiency monofacial and bifacial four-terminal perovskite-silicon tandem modules", *2023 13th International Conference on Crystalline Silicon Photovoltaics (SiliconPV)*, Delft, the Netherlands, poster presentation, 2023.
5. **Y. Zhao**, M. Fardousi, R. Santbergen, K. Datta, A.E.A. Bracesco, D. Zhang, A. Weeber, M. Zeman, L. Mazzarella, M. Creatore, R. A. J. Janssen, and O. Isabella, "Optical simulation-aided design and optimization of SHJ bottom subcells for high-efficiency monolithic perovskite/c-Si tandem solar cells", *2023 13th International Conference on Crystalline Silicon Photovoltaics (SiliconPV)*, Delft, the Netherlands, oral presentation, 2023.
6. **Y. Zhao**, P. Procel, C. Han, L. Mazzarella, L. Cao, G. Yang, R. Santbergen, K. Kovačević, A. Alcañiz, G. Limodio, E. Özkol, A. Smets, A. Weeber, M. Zeman, and O. Isabella, "Strategies for realizing high-efficiency silicon heterojunction solar cells featuring reduced consumption of indium and silver", *2023 13th International Conference on Crystalline Silicon Photovoltaics (SiliconPV)*, Delft, the Netherlands, oral presentation, 2023. [4]
7. **Y. Zhao**, C. Han, P. Procel, A. Smets, L. Mazzarella, G. Yang, L. Cao, Z. Yao, A. Weeber, M. Zeman, and O. Isabella, "Effects of (i)a-Si:H deposition temperature and strategies to reduce In-based TCO and Ag use in high-efficiency SHJ solar cells", *2022 33rd International Photovoltaic Science and Engineering Conference (PVSEC)*, Nagoya, Japan, oral presentation, 2022.
8. **Y. Zhao**, P. Procel, A. Smets, L. Mazzarella, C. Han, G. Yang, L. Cao, Z. Yao, D. Zhang, V. Zardetto, M. Najafi, M. Creatore, R. Janssen, S. Veenstra, G. Coletti, A. Weeber, M. Zeman, and O. Isabella, 'Effects of (i)a-Si:H deposition temperature on high efficiency silicon heterojunction solar cells for four-terminal tandem solar cells', *2022 8th World Conference on Photovoltaic Energy Conversion (WCPEC)*, Milan, Italy, oral presentation, 2022. [5]
9. **Y. Zhao**, K. Datta, A.E.A. Bracesco, N. Phung, V. Zardetto, M. Creatore, R. Janssen, A. Weeber, M. Zeman, L. Mazzarella, and O. Isabella, "Development of 2T SHJ-perovskite tandem solar cells", *Annual Symposium: Light Management, Materials Design and Fabrication for Photovoltaics (LMPV)*, Amsterdam, the Netherlands, poster presentation, 2022.
10. **Y. Zhao**, P. Procel, A. Smets, L. Mazzarella, C. Han, G. Yang, L. Cao, Z. Yao, A. Weeber, M. Zeman, and O. Isabella, "Effects of (i)a-Si:H deposition temperature on high-efficiency silicon heterojunction solar cells", *2022 IEEE 49th Photovoltaics Specialists Conference (PVSC)*, Philadelphia, PA, USA, oral presentation, 2022.
11. **Y. Zhao**, G. Paggiaro, H. Liu, P. Procel, G. Yang, A. Weeber, M. Zeman, L. Mazzarella, and O. Isabella, "Design and optimizations of silicon heterojunction solar cells for high-efficiency

[3] Invited talk.
[4] This work received the 'SiliconPV Award'.
[5] This work received the 'Student Award'.

monolithic perovskite/c-Si tandem applications", *2021 MRS Fall Meeting and Exhibit (MRS)*, Online, oral presentation, 2021.

12. **Y. Zhao**, L. Mazzarella, P. Procel, C. Han, F. D. Tichelaar, G. Yang, A.Weeber, M. Zeman, and O. Isabella, "Ultra-thin electron collectors based on nc-Si:H for high-efficiency silicon heterojunction solar cells", *2021 38th European PV Solar Energy Conference and Exhibition (EUPVSEC)*, Online, oral presentation, 2021.

13. **Y. Zhao**, L.Mazzarella, P.Procel, C.Han, G. Yang, A. Weeber, M. Zeman, and O. Isabella, "Optimization strategies for electron collectors based on nc-SiOx:H for high-efficiency silicon heterojunction solar cells", *2021 11th International Conference on Crystalline Silicon Photovoltaics (SiliconPV)*, Online, poster presentation, 2021.

14. **Y. Zhao**, P. Procel, C. Han, L. Mazzarella, G. Yang, A. Weeber, M. Zeman, and O. Isabella, "Design and optimization of hole collectors based on nc-SiOx:H for high-efficiency silicon heterojunction solar cells", *2020 37th European PV Solar Energy Conference and Exhibition (EUPVSEC)*, Online, oral presentation, 2020.

15. **Y. Zhao**, P. Procel, C. Han, L. Mazzarella, G. Yang, A. Weeber, M. Zeman, and O. Isabella, "Design and optimization of positive-charge carrier collectors based on nc-SiOx:H for high-efficiency silicon heterojunction solar cells", *2020 10th International Conference on Crystalline Silicon Photovoltaics (SiliconPV)*, Online, oral presentation, 2020.

16. **Y. Zhao**, P. Procel, L. Mazzarella, C. Han, G. Yang, O. Isabella, A. Weeber, and M. Zeman, "Positive-charge carrier collections in low-temperature c-Si heterojunction solar cells", *2019 Sunday*, Bussum, the Netherlands, poster presentation, 2019.

17. **Y. Zhao**, L. Mazzarella, P. Procel, G. Yang, C. Han, G. Limodio, O. Isabella, A. Weeber, and M. Zeman, "Opto-electrical optimization of nc-SiOx:H layers for silicon heterojunction solar cells", *2019 9th International Conference on Crystalline Silicon Photovoltaics (SiliconPV)*, Leuven, Belgium, poster presentation, 2019.

18. **Y. Zhao**, E. Özkol, P. Procel, G. Yang, L. Mazzarella, O. Isabella, A. Weeber, and M. Zeman, "Contact stack evaluation and process development of IBC-SHJ solar cells", *2018 MRS Fall Meeting and Exhibit (MRS)*, Boston, MA, USA, oral presentation, 2018.

Curriculum Vitæ

Yifeng ZHAO

Aug. 2018 – Jan. 2023	**Ph.D. candidate** in photovoltaic materials and devices *Delft University of Technology, Delft, the Netherlands* **Thesis:** Hydrogenated nanocrystalline silicon-based layers for silicon heterojunction and perovskite/c-Si tandem solar cells **Promotors:** Prof. dr. A. W. Weeber Prof. dr. ir. O. Isabella Prof. dr. M. Zeman
Aug. 2016 – June 2018	**M.Sc. Sustainable Energy Technology** (cum laude) *Delft University of Technology, Delft, the Netherlands* **Thesis:** Contact stack evaluation for SHJ solar cells and process development of IBC-SHJ solar cells **Supervisor:** Prof. dr. ir. O. Isabella
Sept. 2012 – July 2016	**B.Sc. Environmental Science** *Northwest Agriculture & Forestry University, Yangling, China* **Thesis:** The removal of lead, vanadium and methylene blue in solution by glutaraldehyde cross-linked chitosan modified graphene oxide **Supervisor:** Prof. dr. X. Yin
July 2014 – Aug. 2014	**Undergraduate Research Exchange Program** *University of Nebraska-Lincoln, Lincoln, the United States* **Research:** Comparison of different microwave-assisted digestion methods of nano-sliver for inductively coupled plasma mass spectrometry analysis **Supervisor:** Prof. dr. D. D. Snow